1-1-2013

A New Class of Solid Oxide Metal-Air Redox Batteries for Advanced Stationary Energy Storage

Xuan Zhao
University of South Carolina - Columbia

A New Class Of Solid Oxide Metal-Air Redox Batteries For Advanced Stationary Energy Storage

by

Xuan Zhao

Bachelor of Science
Huazhong University of Science and Technology, 2008

Master of Science
Huazhong University of Science and Technology, 2011

Submitted in Partial Fulfillment of the Requirements

For the Degree of Doctor of Philosophy in

Mechanical Engineering

College of Engineering and Computing

University of South Carolina

2013

Accepted by:

Kevin Huang, Major Professor

Kenneth Reifsnider, Committee Member

Xinyu Huang, Committee Member

John Weidner, Committee Member

Lacy Ford, Vice Provost and Dean of Graduate Studies

ACKNOWLEDGEMENTS

I would like to express my deepest gratitude to my advisor Dr. Kevin Huang for his outstanding guidance, meticulous caring, extreme patience and continuous financial support for my research. I cannot show how much honored I felt when Dr. Huang assigned me this dissertation project – a work to bridge the solid oxide fuel cell technology and energy storage for the stationary energy storage applications. I would also like to thank my committee members: Dr. Kenneth Reifsnider, Dr. John Weidner, and Dr. Xinyu Huang. Without their insightful and constructive suggestions, I cannot finish my dissertation.

I would also like to thank all my previous and current lab colleagues, especially for Dr. Xue Li, Dr. Nansheng Xu and Dr. Yunhui Gong, for their extensive hands-on trainings on fuel cell fabrication and numerous helpful comments; Dr. Lingling Zhang for helps on chemical orders. I would also like to thank Dr. Meng Guo and his supervisor Dr. Ralph White for their kind help on the numerical modeling works to justify the theoretical prediction and experimental results of my project.

Finally, I would like to thank my family, including my parents, my patient boyfriend and my dearest uncle's. Without their years' love, complete understanding and strong support, I could not be so determined and joyful to finish these challenging tasks.

ABSTRACT

Cost-effective and large-scale energy storage technologies are a key enabler of grid modernization. Among energy storage technologies currently being researched, developed and deployed, rechargeable batteries are unique and important that can offer a myriad of advantages over the conventional large scale siting- and geography- constrained pumped-hydro and compressed-air energy storage systems. However, current rechargeable batteries still need many breakthroughs in material optimization and system design to become commercially viable for stationary energy storage.

This PhD research project investigates the energy storage characteristics of a new class of rechargeable solid oxide metal-air redox batteries (SOMARBs) that combines a regenerative solid oxide fuel cell (RSOFC) and hydrogen chemical-looping component. The RSOFC serves as the "electrical functioning unit", alternating between the fuel cell and electrolysis mode to realize discharge and charge cycles, respectively, while the hydrogen chemical-looping component functions as an energy storage unit (ESU), performing electrical-chemical energy conversion in situ via a H_2/H_2O-mediated metal/metal oxide redox reaction. One of the distinctive features of the new battery from conventional storage batteries is the ESU that is physically separated from the electrodes of RSOFC, allowing it to freely expand and contract without impacting the mechanical

integrity of the entire battery structure. This feature also allows an easy switch in the chemistry of this battery. Other features include state-of-charge independent EMF, O^{2-}-enabled high rate and high capacity storage, independent design of power and energy, scalability, sustainability and safety.

The materials selection for ESU is critical to energy capacity, round-trip efficiency and cost effectiveness of the new battery. Me-MeO_x redox couples with favorable thermodynamics and kinetics are highly preferable. The preliminary theoretical analysis suggests that Fe-based redox couples can be a promising candidate for operating at both high and low temperatures. Therefore, the Fe-based redox-couple systems have been selected as the baseline for this study, the constituted battery of which is termed solid oxide iron-air redox battery (or SOFeARB).

The first objective of this PhD work is aimed at demonstrating the proof-of-concept. By combining a commercial anode-supported tubular RSOFC and Fe-based redox couple, the first generation SOFeARB operated at 800^{o}C has been demonstrated to produce an energy capacity of 348Wh/kg-Fe and round-trip efficiency of 91.5% over twenty stable charge/discharge cycles. Further system optimization leads to an 800^{o}C-SOFeARB comprised of a commercial electrolyte-supported planar RSOFC and Fe-based redox couple; this configuration has become a standard testing system for later studies. The 800^{o}C planar SOFeARBs have been investigated under various current densities and cycle durations. The results show that metal utilization plays a determining role in balancing the energy capacity and round-trip efficiency. Increasing metal utilization increases the energy

capacity, but at the expense of lowered round-trip efficiency. From an engineering perspective, a strategy can be laid out to operate the battery at a low metal utilization (e.g., overloading the low-cost Fe-based ESU materials) as a means of achieving the required energy/power rating while retaining a high round-trip efficiency. From a computational perspective, a multi-physics-based model has also been constructed and satisfactorily verified with the experimental results obtained under high current densities.

The second objective of this work is to lower the operating temperature of SOMARBs to intermediate temperature (IT) range (e.g. 550-650^{o}C). Two changes were made in order to enable operation at IT range: introduction of optimized Sr- and Mg- doped $LaGaO_3$ (LSGM) based RSOFC by tape-casting and infiltration techniques, and optimization of morphology of ESU through innovative synthesis methods. The optimized battery can reach a round-trip efficiency as high as 82.5% and specific energy 91% of the theoretical value in the IT range.

The third objective of this work is to improve the cyclic durability and stability of IT-SOFeARBs. The results show that the performance, reversibility and stability of a 550^{o}C-SOFeARB can be significantly improved by nanostructuring energy storage materials synthesized from a low-cost carbothermic reaction. The 100-cycle test explicitly shows an improvement of 12.5%, 27.8% and 214% in specific energy, round-trip efficiency and stability, respectively, over the baseline battery. A more thorough investigation shows that current density has a more pronounced effect on the round-trip efficiency than the cycle duration, implying that operating a SOMARB under a relatively

lower current density for a longer cyclic duration is a favorable testing condition to achieve a required energy storage capacity.

The fourth objective of this work is to explore metal-air chemistries other than Fe-air. The two new metal-air chemistries of choice are W-air and Mo-air. The selection of W and Mo as the redox metals is based on their faster kinetic rate and higher specific densities per oxygen than the Fe-based counterparts. Each battery was electrochemically compared with the baseline SOFeARB at a specific temperature. The results show that these heavy metals based SOMARBs can indeed produce higher energy density (capacity per unit volume) than the baseline battery SOFeARB by allowing more mass loading and higher oxygen storage capacity. The better kinetic rates also lead to a higher cycle efficiency and cycle stability.

In summary, this dissertation work demonstrates a new energy storage mechanism that has great potential for stationary applications. The new storage battery has been studied in the perspectives of theoretical assessment, materials development, parametric optimization, and test methodology. According to these systematic investigations, a set of standard testing and characterization protocols has been configured for future testing of larger systems. Thermodynamics and kinetics have constantly been employed to guide materials selection and electrochemical testing. The experimental results are often found consistent with the theoretical predictions.

TABLE OF CONTENTS

LIST OF TABLES

LIST OF FIGURES

LIST OF SYMBOLS

E_N	Nernst potential.
SE	Specific energy.
Q	Specific charge.
ED	Energy density.
CD	Charge density.
RC	Rate capacity.
η_{rt}	RTE.
t_{Me}	Full discharge time.
U_{Me}	Metal utilization.
U_{Fe}	Iron utilization.
ΔG	The change of Gibbs Free Energy of the metal-air reaction.
K	Equilibrium constant of the metal-air reaction.
n	Electron number.
F	Faraday's constant.
P	The oxygen partial pressure in air (=0.21atm).
P_{O_2}	The actual oxygen partial pressure in fuel-electrode chamber
M_{Me}	The formula weight of metal in the ESU.

V_{Me}	The actual volume of the metal in the ESU
S_{RSOFC}	The active electrode area of RSOFC
ρ_{Me}	The specific density of the metal
W_{Me}	The actual weight of the metal in the ESU
I_d	The galvanic discharge current
Q_{Me}	The measured specific charge
t_{Me}	Actual cycle time
J_{max}	Maximum current density
Q_{max}	Maximum specific charge
q_{max}	Maximum charge density
x	Oxygen stoichiometry in MeO_x
S_{ESU}	Specific surface area of the redox materials
m_{ESU}	The actual weight of ESU
Mo	The atomic weight of oxygen (=16g/mol)
Δm	The mass change of the ESU per area
K_p	The parabolic rate constant of redox kinetics
ρ_{ESU}	The density of the redox materials in ESU
j	The applied current density
$A_{\partial\Omega_E}$	Area of the RSOFC boundary.
c_i	Molar concentration of gas phase species i

$\bar{c}_i$ Mean molar concentration of species i in the CST

$c_{i,f}$ Mean molar concentration of species i at the gas outlet boundary

c_{Fe} Total amount of Fe and FeO per unit bulk volume of ESU

$\underline{\mathbf{d}}_k$ Diffusive driving force acting on species k

$D_{i,j}$ Maxwell- Stefan diffusivities

$\widetilde{D}_{i,k}$ Multi-component Fick diffusivities

$\widetilde{D}_{i,k}^{eff}$ Effective multi-component Fick diffusivities

E Voltage of the battery

$E_{\text{eq},n}$ Equilibrium potential of the anode

$E_{\text{eq},p}$ Equilibrium potential of the cathode

$E_{\text{eq},n}^{\theta}$ Standard-state equilibrium potential for anode

i_{app} Applied current density on the battery

i_n Electrochemical current densities for the anode of RSOFC

i_p Electrochemical current densities for the cathode of RSOFC

$i_{n,0}$ Exchange current density for the anode

$i_{p,0}$ Exchange current density for the cathode

$i_{n,0}^{\text{ref}}$ Reference-state exchange current density

$\underline{\underline{\mathbf{I}}}$ Identity matrix

$\underline{\mathbf{j}}_i$ Diffusive mass flux vector for species i

k Rate constant for the forward regenerative reaction

k^{-1} Rate constant for the reverse regenerative reaction

M_{Fe} Molar mass of Fe

M_{FeO} Molar mass of FeO

M_k Molar mass for gas phase species k

M_n Mean molar mass of gas mixture

$\underline{\mathbf{n}}$ Unit normal vector pointing out of the RSOFC boundary

n_{Fe} Amount of Fe

n_{FeO} Amount of FeO

$\underline{\mathbf{N}}_i$ Total mass flux of species i

p Modified pressure

p_A Absolute pressure

p_{ref} Reference pressure

Q_{br} Volumetric mass source for the gas phase

Q_f Volumetric flow rate of the gas phase at the gas outlet boundary

r_i Volumetric molar reaction rate of species

R Universal gas constant

R_i Volumetric mass source of species i

t Time

T Temperature

$\underline{\mathbf{u}}$ Velocity vector of the fluid flow.

U Full-cell Nernst potential of the battery.

U_0 Normal inflow velocity at the gas inlet boundary

V_R Volume of the CST

V_{ESU} Bulk volume of ESU

x_k Mole fraction of species k

α_a Anodic transfer coefficient for the anode

β_a Anodic transfer coefficient for the cathode

ε_p Porosity of the ESU

$\varepsilon_{p,0}$ Initial porosity of the ESU

ϕ_n Solid phase electric potential of the anode

ϕ_p Solid phase electric potential of the cathode

η Over voltage of the battery

κ_{br} Permeability of porous media

μ Viscosity of gas phase

ρ Density of domain gas phase

ρ_{Fe} Density of Fe

ρ_{FeO} Density of FeO

τ Mean residence time of CST

ω_i Mass fraction of species i

ξ_{Fe} Conversion for Fe to FeO

$\xi_{Fe,0}$ Initial conversion for Fe to FeO

$\partial\Omega_{E}$	Symbol for the RSOFC boundary
$\partial\Omega_{in}$	Symbol for the gas inlet boundary
∇	The gradient operator
i	Index for gaseous species ($i=1$ for hydrogen and $i=2$ for steam)
k	Dummy index for species

List of Abbreviations

AFC……...Alkaline Fuel Cell

CAES……..Compressed Air Energy Storage

CFD……..Computational Fluid Dynamics

CSE……..Charge Specific Energy

CST……Continuous Stirred Tank

DSE……Discharge Specific Energy

EES……Electrical Energy Storage

EFU…….Electrical Functioning Unit

ESU……Energy Storage Unit

ERB……Electrochemical Rechargeable Batteries

FESEM…….Field Emission Scanning Electron Microscope

GDC…….....Gd- Doped CeO_2

HCL…….Hydrogen Chemical Looping

HESS……...Hydrogen-based Energy storage system

HSFES…….High-speed Fly Wheels Energy Storage

HT…….High Temperature

ICBs……...Iron/chromium Flow Batteries

IRBs…….Iron Redox Flow Batteries

IT……...Intermediate Temperature

LABs……..Lead-Acid Batteries

LDC……..La- doped CeO_2

LSCF……Sr- and Fe- doped $LaCoO_3$

LSGM……..Sr-and Mg-doped $LaGaO_3$

LSM…….Sr- doped $LaMnO_3$

Me/MeO_x……. Metal/Metal oxide

MCFC……Molten Carbonate Fuel Cell

MTSE……...Maximum Theoretical Specific Energy

MTED……...Maximum Theoretical Energy Density

NAS……Sodium Sulfur Battery

Ni-MH……Nickel-Metal Hydride

PEMFC……Polymer Electrolyte Membrane Fuel Cell

PHES……Pumped Hydroelectric Energy Storage

PSBs……...Polysulphide/bromine Flow Batteries

PXRD……Powder X-ray Diffraction

RFBs……Redox Flow Batteries

RSOFC……..Regenerative Solid Oxide Fuel Cell

RTE…….Round Trip Efficiency

SCES……...Supercapacitors Energy Storage

SDC…….Sm- doped CeO_2

SEM……..Scanning Electron Microscope

SMES……..…Superconducting Magnetic Energy Storage

SOEC…….…….Solid Oxide Electrolytsis Cell

SOFC…….……..Solid Oxide Fuel Cell

SOFeARB…….Solid Oxide Fe-air Redox Battery

SOFeCARB……...Solid Oxide Fe/C-air Redox Battery

SOMARB……Solid Oxide Metal-air Redox Battery

SOMoARB……..Solid Oxide Mo-air Redox Battery

SORFB……...Solid Oxide Redox Flow Battery

SOWARB……..Solid Oxide W-air Redox Battery

SSC……..Sr- doped $SmCoO_3$

sscm…….standard cubic centimeter per minute

TPBs……Three Phase Boundaries

VRBs……..Vanadium Redox Flow Batteries

VBBS……..Vanadium/bromine Flow Batteries

XRD……...X-ray Diffraction

YSZ…….Yttria Stabilized ZrO_2

ZBB……..Zinc/bromine Flow Batteries

ZEBRA……...“Zeolite Battery Research Africa”,

Sodium-nickel-chlorite battery

CHAPTER 1

OVERVIEW OF THE STATE-OF-ART STATIONARY ELECTRICAL ENERGY STORAGE TECHNOLOGIES

1.1 INTRODUCTION

Cost-effective and large-scale energy storage technologies are a key enabler of grid modernization, addressing the electric grid's most pressing needs by improving its stability and resiliency. Investment in energy storage is essential for keeping pace with the increasing demands for electricity arising from continued growth in U. S. productivity, shifts in and continued expansion of national cultural imperatives (e.g., emergence of the distributed grid and electric vehicles), and the projected increase in renewable energy sources.

Today's electricity transmitted and distributed across electric grid is generated from both fossil and non-fossil based power plants; the former accounts for 68% of the total electricity generated, while the latter (consisting of nuclear, hydroelectric and renewable) constitutes the rest 32%. Figure 1.1 shows the distribution of all types of power generation methods currently being used to support our society.

Among all the types of energy production, renewables are the fastest growing

resources being developed, primarily due to its natural abundance, wide accessibility and environmental friendliness. In recent years, the electricity generation from renewable resources has grown at an annual rate of 3.1% [1], and the renewable share in the world's electricity generation is projected to increase from 19% in 2008 to 23% in 2035 [2].

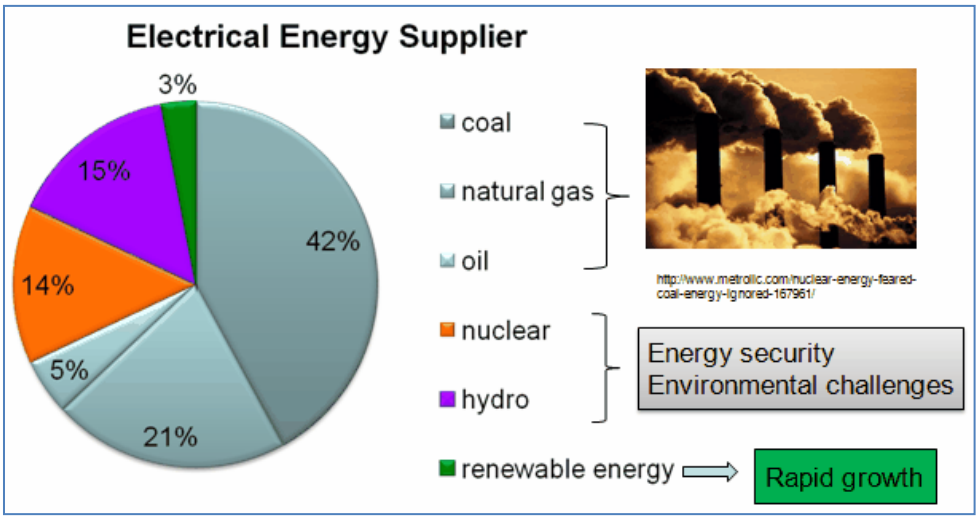

Figure 1.1 Distribution of current electrical energy production methods [3].

A key to harnessing energy from renewable resources efficiently and reliably lies in the availability of a technology that is capable of leveling off the intermittency presented by renewable energy resources to electric grid. The technology of competence is electrical energy storage (EES).

An EES device functions as a buffer between energy supply and demand. When electricity is in excess, it is stored in EES devices for later use when electricity is in demand. With such a basic functionality, EES devices can find important applications in the area of ensuring grid stability and reliability [4-7]. In general, the grid applications for EES

technologies can be loosely divided into power applications and energy management applications, which are differentiated based on storage discharge duration. Technology used for power applications are typically used for short duration, ranging from fractions of a second to approximately one hour, to address faults and operational issues that cause disturbances, such as voltage sags and swells, impulses, and flickers. Technology used for energy management applications store excess electricity during periods of low demand for use during periods of high demand. These devices are typically for longer durations of more than one hour to serve functions that include reducing peak load and integrating renewable energy sources. Figure 1.2 illustrates typical applications of EES in electric grid, all of which aim at ensuring the grid stability and reliability.

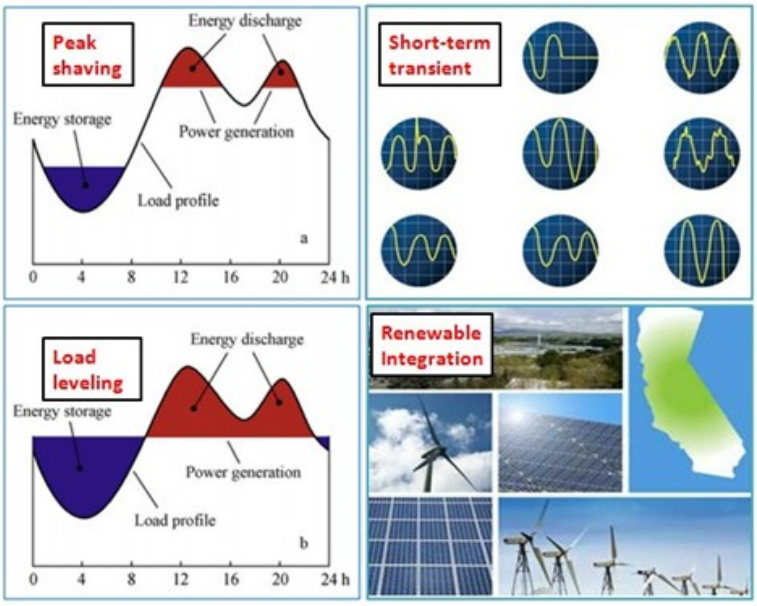

Figure 1.2 Application of EES devices in electric grid

1.2 EES PERFORMANCE METRICS

Establishment of performance metrics is necessary for evaluating EES technologies and finding suitable applications in the EES market. The following summarizes the primary parameters important to my research project on storage batteries.

- Energy capacity: the total amount of electrical energy stored by the EES technology, which is usually measured in kilowatt-hours (kWh) or mega-joules (MJ).
- Specific energy: the amount of energy stored in a given system per unit mass (kWh/kg or MJ/kg).
- Energy density: the amount of energy stored in a given system per unit volume (kWh/L or MJ/L).
- Power capacity: the rate of energy output in a short time-scale (kW or MW).
- Round-trip efficiency (RTE): the ratio of the energy output during the discharge to the energy input during the charge
- Response time: the time taken by the EES device to provide the needed energy
- Cycle life: the lifetime of EES subject to repeated discharge-charge cycles
- Cost of energy storage: the cost per unit energy stored in unit of $/kWh.
- Scalability/manufacturability: the ability for EES device to be scaled up and

manufactured at a large scale

- Sustainability: the availability of the materials used in the EES to last over a meaningfully long period of time
- Environmental impact: whether the materials and operation of ESS device have negative impact on the environment and humans
- Safety: safe operation over a meaningfully long period of time

1.3 THE STATE-OF-ART EES TECHNOLOGIES

EES technologies provide methods for reversible conversion of electricity into other forms of energy. These forms of energy include [8]:

- potential energy (e.g., elevated water reservoirs)
- kinetic energy (e.g., compressed air, flywheels)
- magnetic energy (e.g., superconducting inductors)
- electrical charges (e.g., capacitors/supercapacitors)
- chemical/electrochemical energy (e.g., rechargeable batteries)

The following discusses in detail about the principles and characteristics of these EES technologies.

1.3.1 Pumped Hydroelectric Energy Storage (PHES)

Pumped hydroelectric energy storage (PHES) is by far the most mature and largest storage technology available. United States alone own approximately 40 PHES stations with a total capacity of ~20GW. Worldwide, there are hundreds of PHES stations operating with a total capacities of 127GW [9].

Typically, a PHES is equipped with reversible pumps/generators connecting an upper and a lower reservoir (Figure 1.3). During off-peak electric demand, water is pumped from the lower reservoir to the higher one by utilizing relatively cheap electricity from the grid. During peak hours, water is then released from the upper reservoir to generate power for higher price.

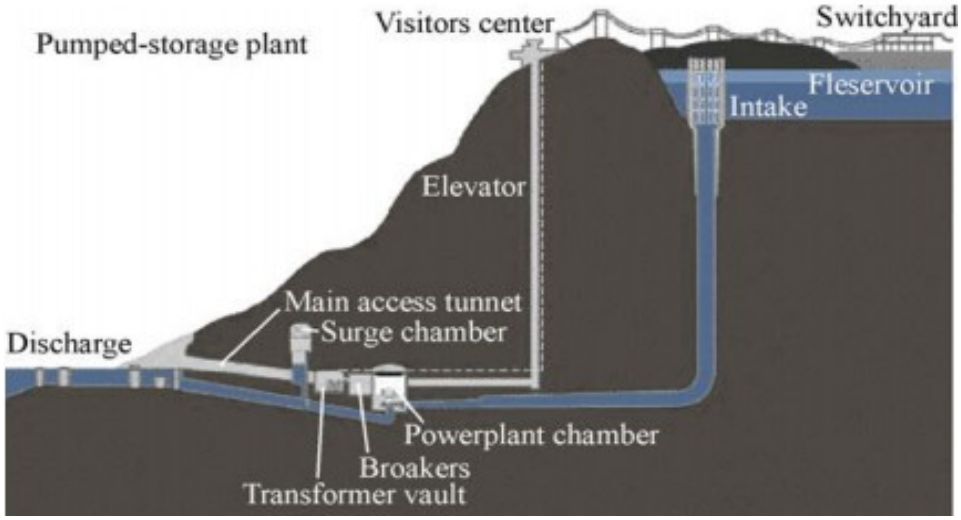

Figure 1.3 A typical layout of a pumped hydroelectric energy storage facility [10].

A typical PHES facility has 300 m of hydraulic head, and the energy storage capacity

(kWh) is a function of the reservoir volume and hydraulic head. In reality, facilities are usually designed with the greatest hydraulic head possible rather than largest upper reservoir primarily due to the cost consideration.

PHES has a relatively fast reaction time and a large storage capacity. It seems that PHES is very clean and environmentally friendly since only water is used as the energy storage medium. However, reality is quite the opposite. Corrosion is a big challenge for the PHES facilities since salty water is usually used in the PHES systems [11]. DOE's recent report shows that hydropower can also impact the fish spawning, change the water quality and flow, affect the normal life of humans, flora, and fauna [12]. Moreover, PHES is highly geographically specific [9, 12]. The suitable site that needs two large reservoirs with enough hydraulic head is rather rare, and always located in remote places such as mountainous areas. Therefore, the initial investment of PHES is high, and the power grid to which PHES is connected is always in far distance.

1.3.2 Compressed Air Energy Storage (CAES)

Compressed air energy storage (CAES) is another mature and large energy storage system. A typical CAES facility consists of a power motor that drives an air compressor, a high-pressure turbine, a low-pressure turbine, and a generator, as shown in Figure 1.4.

At off-peak time, inexpensive power is taken from the grid and used to pump free air into the underground reservoir at a high pressure. The pressurized air is stored underground

for use during peak hours. At peak time, the compressed air is released from the reservoir and used to drive the turbines to generate electricity.

Like PHES, CAES can be manufactured and assembled at very large scales. It has been primarily targeted storing excess energy generated by wind and solar power [7]. Typical power capacities for a CAES system range from 50 to 300MW [13]. The cycle life is only limited by the mechanical fatigue of the cylinders, and cycling of 10,000 times has been demonstrated [7]. Fast response time is another feature of CAES; it needs only 9 min for emergency start and can be stabilized within 12 min.

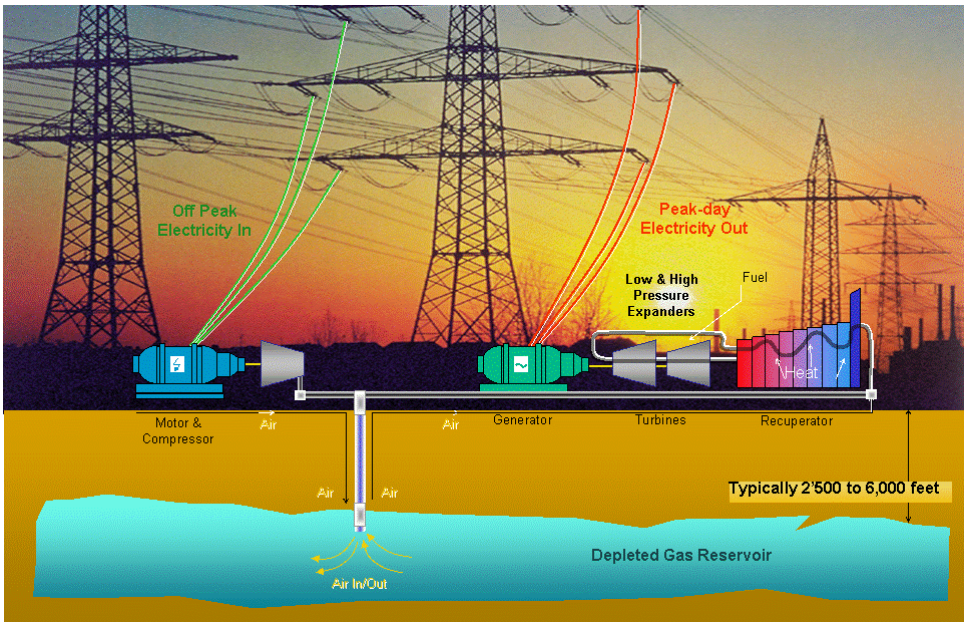

Figure 1.4 Compressed Air Energy Storage (CAES) system [13].

The major limitation of CAES is its geological preference; it has to be built on large underground reservoirs. Another concern is low efficiency; analysis has shown that only about 10-20% of total input energy is converted to useful form of energy [14]. The major

energy lose arises from heat loss and air leakage.

1.3.3 High-Speed Fly-wheels Energy Storage (HSFES)

A long-lasting yet overlooked storage technology, high speed flywheel (e.g., spindles and CVT transmissions), has been revisited for energy storage applications in recent years [6, 15]. The off-peak and inexpensive electricity can be stored in the form of kinetic energy by high-speed flywheels, which can be later converted back to electricity when demand is high at peak time. The energy can remain in its kinetic state for as long as needed.

To store electrical energy, a disc inside a casing spins at high angular velocity converts electricity into kinetic energy. Conversely, kinetic energy is converted back to electricity as the angular velocity decreases. The cross-section of a typical flywheel system is shown in Figure 1.5. To create a complete flywheel system that is efficient for energy storage, several components are required: a flywheel, casing, bearings and seals, power transmissions, and vacuum and system controls. The stored kinetic energy can be calculated by:

$$E_{Kinetic} = I\omega^2 \tag{1.1}$$

where I is the moment of inertia of the disc, and ω is the angular velocity.

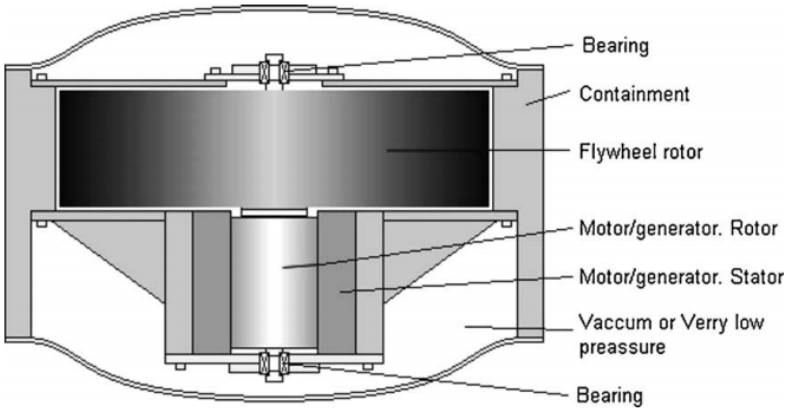

Figure 1.5 Cross-section of typical flywheel system [15].

This classic mechanical marvel has very fast response time, long lifetime under constant cycling, very high power, reasonable energy densities and greater-than 85% efficiency [15]. Besides, it is a rather clean and environmentally benign technology. However, flywheels require materials that can withstand its high angular momentum. They also need complicated and heavy equipment to function properly. In general, flywheels cost more than batteries in initial investment, despite requiring less maintenance. Overall, design complexities, transmission requirements, the initial high investment, system size and weight are the primary barriers for HSFES.

1.3.4 Superconducting Magnetic Energy Storage (SMES)

Superconducting Magnetic Energy Storage (SMES) is a unique technology that stores electrical energy directly into electric current without energy loss. This is achieved when a direct current (DC) passes through the cryogenically cooled superconducting inductor coils (-270^{o}C) [7]. Since there is no resistance presented by the coils, no energy losses is

expected during the energy conversion [10].

SMES is charged by increasing the DC current within the coils rectified from alternating current (AC); during the discharge, DC current is converted from the coils back to AC. To maintain the superconducting state of the inductor, the coils need to be immersed in liquid helium.

The typical SMES system consists of three major components: a superconducting coil, a cryostat system, and a power conversion system, see Figure 1.6. The energy density (ED) of a magnetic field is given by

$$ED_{(SMES)} = \frac{1}{2}\mu H^2 = \frac{1}{2}LI^2 \tag{1.2}$$

where, μ is the permeability of the storage medium, H is the strength of the magnetic field, L is the inductance of the coil, and I is the current passing through the coil.

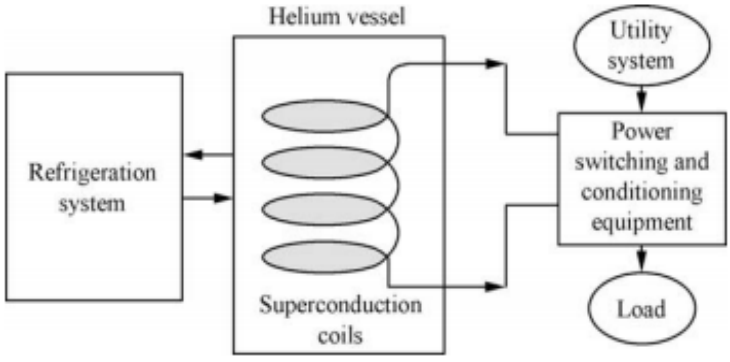

Figure 1.6 Schematic showing a typical SMES system[10].

Because there is nearly no ohmic resistance in the coils, cycle efficiencies of SMES

systems are extremely high, ranging from 90% [16] to 99% [17], even for a short period (<1 min for full discharge). SMES also exhibits a very rapid response (around a few milliseconds) and a long cycle life (> 20 years if there is no degradation in the magnet) [11].

SMES systems have already been installed in US, Japan and Europe for short-term transient applications [7, 10]. Most of the installations are in the range of 280-830 MWh capacity with high power outputs (up to 2.5 MW) [18]. The major challenges for SMES are the cost and environmental issues associated with extremely low temperature and strong magnetic field.

1.3.5 Supercapacitors Energy Storage (SCES)

The capacitors store energy as electrical charges between two parallel electrodes separated by a dielectric medium. The energy within a capacitor is given by

$$E = \frac{1}{2} C V^2 \tag{1.3}$$

where E is the energy stored within the capacitor, V is the voltage applied, and C is the capacitance given by

$$C = \frac{A}{d} \varepsilon_r \varepsilon_0 \tag{1.4}$$

where A is the area of the parallel electrodes, d is the distance between the two electrodes,

ε_r is the relative permittivity or dielectric constant, and ε_o is the permittivity of free space. Therefore, to increase the energy stored within a capacitor, the voltage or capacitance must be increased. The voltage is limited by the maximum energy field strength.

Like batteries, supercapacitors store electrical charges inside microstructure of electrodes. They are electrochemical cells, but without redox reactions taking place at the electrodes. A supercapacitor contains two conductor electrodes, one electrolyte and a porous membrane, where ion-transfer across the two electrodes occurs. A schematic of supercapacitors can be seen in Figure 1.7.

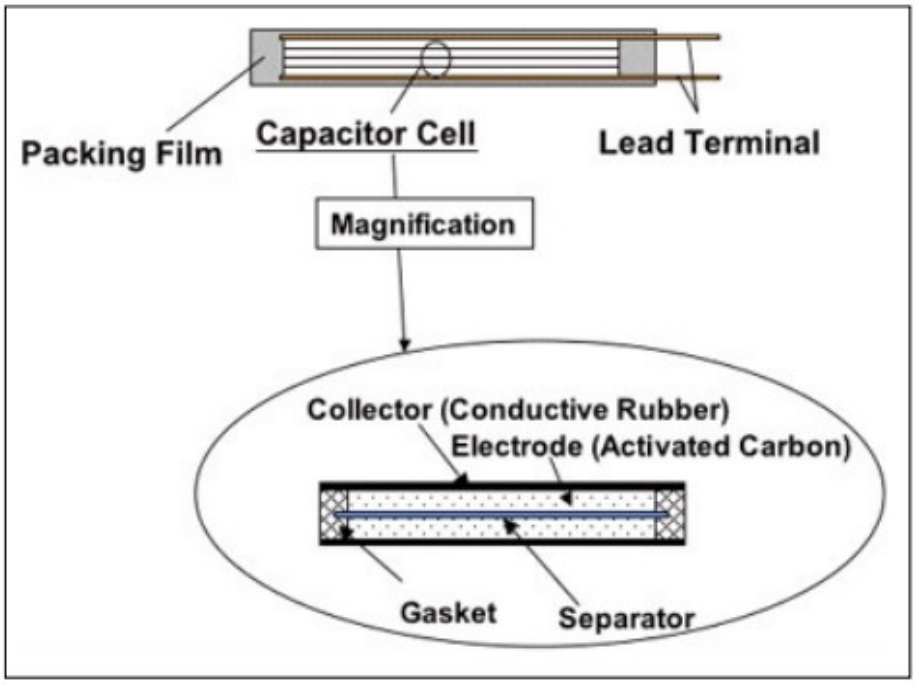

Figure 1.7 Components of a supercapacitor energy storage device [11].

With no energy conversion taking place, the charge-discharge process of SCES is highly efficient and reversible. Some supercapacitors are fabricated by using thin film

polymers for dielectric layer and carbon nanotube electrodes [19]. They use polarized liquid layers between conducting ionic electrolyte and a conducting electrode to increase the capacitance. They can be connected in series or in parallel. Such systems have energy densities of 20MJ/m^3 to 70 MJ/m^3, with a cycle efficiency of 95% [19, 20].

The response time of capacitors/supercapacitors is in millisecond time-scale, and thus they can be extremely useful for voltage regulation, frequency control, and other power quality applications. However, the stored energy in capacitors discharges itself at ~5% per day, so the stored energy has to be consumed within a very short time frame [7].

1.3.6 Hydrogen-based Energy Storage System (HESS)

Hydrogen as an important energy carrier has an outstanding energy value on a unit mass basis due to its low molecular weight and high molar heat value. It reacts with oxygen, either by combustion or in fuel cells, to give off energy, with only water as the product.

However, hydrogen does not exist on earth naturally and has to be produced. Hydrogen can be generated in several ways: by extraction from fossil fuels, gasification of biomass, and by means of water electrolysis, or photocatalysis using renewable energy such as solar or wind power. So far, fossil-fuel derived hydrogen is the least expensive technology to produce hydrogen, accounting for 95% of bulk hydrogen production in the world. Water electrolysis makes up nearly 4% hydrogen production, but relatively inefficient and costly.

When hydrogen is produced and not in immediate use, it needs to be stored. Historically, hydrogen has been stored in states of gas, liquid and solid. Gaseous hydrogen can always been compressed in gas cylinders at a typical pressure of 350 bar; this requires high-pressure gas cylinders. Liquid hydrogen needs to be stored in cryogenic tanks; it is inefficient since the liquefaction itself consumes roughly 20% of the recoverable energy along with about 2% evaporated [21]. Therefore, the search for cost effective and safe alternative hydrogen storage methods has garnered much attention in recent years. Storage of hydrogen in solids is leading the effort.

The principle of hydrogen storage in solids is primarily based on reversible chemisorption and physisorption processes. Two categories of hydrogen storage solids show high storage capacity: metal hydrides [22, 23] and highly porous solids (*e.g*. active carbon [24, 25], zeolites [25, 26] and polymers [27-29]). More recently, metal-organic frameworks [30, 31] have emerged as a new class of hydrogen storage materials based on physisorption due to their flexibility in designing functionalized porous structures with low density.

The stored hydrogen can be used directly in hydrogen fuel cells, which is a well-known electrochemical conversion device that produces electricity at a much higher efficiency. When fuel cell is operated in the electrolysis mode, hydrogen can be generated by splitting water using electricity. A Regenerative Fuel Cell System (RFCS) can realize the H_2 production and storage simultaneously. A typical RFCS as shown in Figure 1.8

composes of the following components: a water electrolyzer system, a fuel cell system, a hydrogen storage system and a power conversion system.

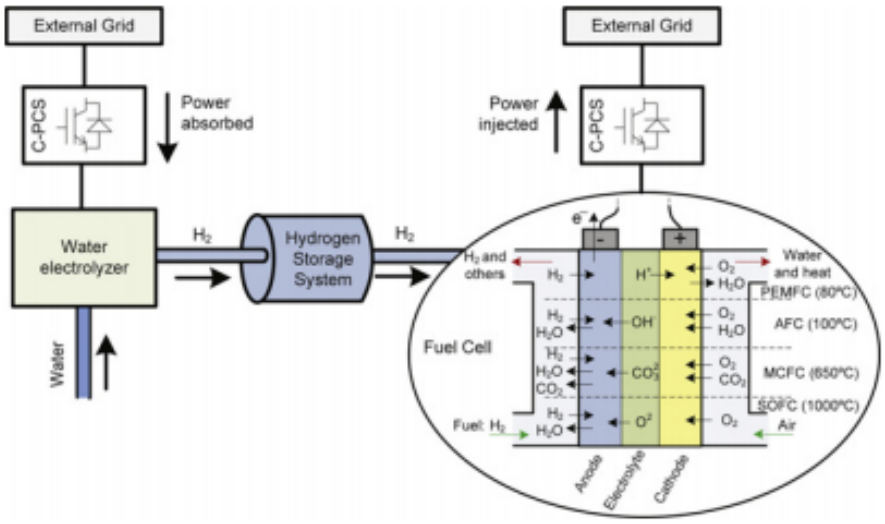

Figure 1.8 A typical configuration diagram of RFCS [8].

As seen in Figure 1.8, water electrolyzer and hydrogen fuel cell are two key components of RFCS. The water electrolyzer can be made from an aqueous alkaline electrolyte [32], a polymer electrolyte membrane [33], and a solid oxide electrolyte [34]. Similarly, there are also many types of fuel cells for stationary and distributed applications, depending on the electrolyte material employed, *e.g.* the Polymer Electrolyte Membrane Fuel Cell (PEMFC), Alkaline Fuel Cell (AFC), Molten Carbonate Fuel Cell (MCFC) and Solid Oxide Fuel Cell (SOFC), *etc* [35].

The power capacity and energy storage capacity of RFCS are separable. Due to their modular nature, high energy systems (e.g., >100 MWh) and high peak power (>10 MW)

can be achieved simultaneously through varying electrode surface area and hydrogen storage capacity. The major drawback of RFCS is its low energy efficiency, primarily caused by the low-efficiency hydrogen storage system, a “bottle-neck” subsystem that limits the overall efficiency, despite the use of higher efficiency fuel cell and electrolyzer systems.

1.3.7 Electrochemical rechargeable batteries (ERB)

Among all of the available EES mechanisms, the most promising technology for stationary applications is electrochemical rechargeable batteries capable of efficiently and reversibly converting electrical-chemical energy. Many forms of ERBs have been developed in the past decades, but only a few (e.g., lead-acid, metal hydrides batteries) have been demonstrated in grid application. The well-known lithium-ion batteries developed for portable applications are facing technical and economical impasses for large-scale stationary applications due to their low rate capacity and safety concerns [36]. Batteries that are deemed suitable for stationary EES include lead-acid, metal hydrides, redox flow batteries and sodium-sulfur batteries. In this subchapter, we review these four primary stationary batteries along with some newly emerging storage batteries.

1.3.7.1 Lead-Acid Batteries

Lead-acid batteries (LABs) are the earliest and most commonly used storage battery even invented. The lead-acid battery was first invented in 1859 by G. Plante [6]. LABs in

recent versions are more or less simplified variations of the early form. The changes were found in the chemical nature of the active electrode materials, different electrolyte compositions and designs to achieve better performances. The positive electrode is composed of PbO_2, while negative electrode is sponge Pb. The electrolyte is H_2SO_4 aqueous solution. During the discharge, both electrodes are reacted to form $PbSO_4$. During the charge, both electrodes return to their original states. The electrochemical reactions as well as the global reaction are given by

$$\text{Cathode: } PbO_2 + 4H^+ + 2e^- \underset{charge}{\overset{discharge}{\rightleftarrows}} Pb^{2+} + 2H_2O \tag{1.5}$$

$$Pb^{2+} + SO_4^{2-} \underset{charge}{\overset{discharge}{\rightleftarrows}} PbSO_4 \tag{1.6}$$

$$\text{Anode: } Pb \underset{charge}{\overset{discharge}{\rightleftarrows}} Pb^{2+} + 2e^- \tag{1.7}$$

$$Pb^{2+} + SO_4^{2-} \underset{charge}{\overset{discharge}{\rightleftarrows}} PbSO_4 \tag{1.8}$$

$$\text{Overall: } Pb + PbO_2 + 2H_2SO_4 \underset{charge}{\overset{discharge}{\rightleftarrows}} 2PbSO_4 + 2H_2O \tag{1.9}$$

There are two types of LABs: flooded batteries and valve-regulated batteries. The flooded batteries are consisted of two electrodes that are made by lead plates which are soaked in a mixture of water (65%) and sulphuric acid (35%). The valve-regulated batteries are sealed with a pressure regulating valve, which eliminates air penetration as well as allows hydrogen venting. A typical lead-acid battery structure is shown in Figure 1.9.

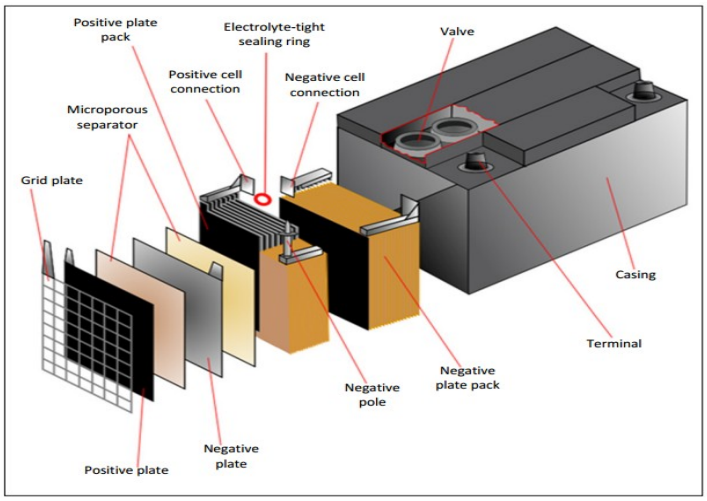

Figure 1.9 A typical structure of LABs [11].

This mature battery technology has dominated the stationary energy storage market for the last century. In 1988, a 10 MW/40 MWh flooded lead-acid system was installed at the Chino substation of Southern California Edison Company for load leveling [4]. Lead-acid battery's success is attributed to many of its features including technological maturity, long life span (up to 15 years), long cyle life (1200-1800 cycles, depending on the depth of discharge), fast response, good DC-DC efficiency (e.g., 75% to 85%), and low self-discharge rate (e..g., <0.1%/day). It can also be used both for power applications (in seconds) and energy applications (up to 8 hours) [8, 11].

The major limitation of lead-acid battery is high maintenance cost since it is highly sensitive to the environment. The typical operating temperature for a lead acid battery is 27^{o}C; however, a temperature change of 5^{o}C or more can significantly shorten the lifetime of the battery.

1.3.7.2 Ni-Cd and Ni-Metal Hydride Batteries

1.3.7.2.1 Ni-Cd Batteries

Ni-Cd batteries are a type of alkaline (liquid KOH) based battery first invented in 1950 [8]. The cathode is nickel hydroxide and the anode is metallic cadmium. During the discharge, the nickel oxyhydroxide combines with water and electrons, producing nickel hydroxide and hydroxide ions at the cathode. Cadmium hydroxide is formed at the anode. During the charge, the reactions are reversed. The electrode reactions and overall reaction of the Ni-Cd batteries are expressed by

$$\text{Cathode: } 2NiO(OH) + 2H_2O + 2e^- \underset{Charge}{\overset{Discharge}{\rightleftharpoons}} 2Ni(OH)_2 + 2OH^- \tag{1.10}$$

$$\text{Anode: } Cd + 2OH^- \underset{Charge}{\overset{Discharge}{\rightleftharpoons}} Cd(OH)_2 + 2e^- \tag{1.11}$$

$$\text{Overall: } 2NiO(OH) + Cd + 2H_2O \underset{Charge}{\overset{Discharge}{\rightleftharpoons}} 2Ni(OH)_2 + Cd(OH)_2 \tag{1.12}$$

There are two typical configurations of Ni-Cd batteries: vented (Figure 1.10 (a)) form for portable equipment and sealed (Figure1.10 (b)) form for general industrial applications.

Ni-Cd batteries can sustain high discharge rates without adversely affecting capacity. Ni-Cd batteries have good characteristics with respect to its long cycle life (>3500 cycles), along with low maintenance cost [8, 11]. Due to greater demand for battery-powered portable devices, Ni-Cd batteries experienced a boom during the last quarter of the twentieth century. Recently, Ni-Cd batteries have been used to store solar energy because

they can withstand higher temperatures than lead-acid batteries. Ni-Cd batteries can also be used for large-scale stationary storage, for example, a 27 MW unit assembled with 13,760 nickel-cadmium cells was installed in Alaska [6].

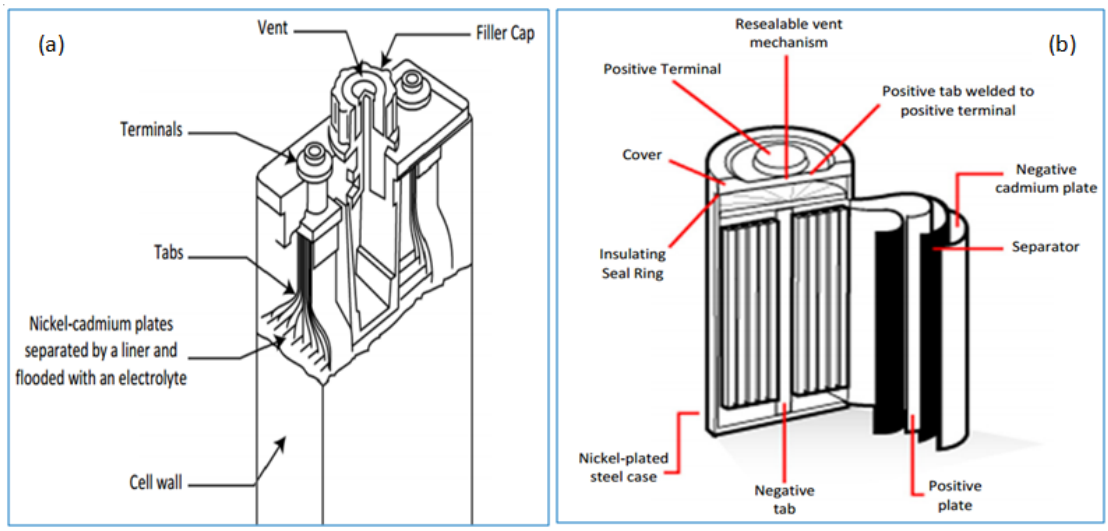

Figure 1.10 Structures of (a) vented and (b) sealed Ni-Cd battery.

However, the toxic heavy metal Cd can cause health harzards to human body, which has phased out this battery from the storage battery market as other higher energy density and more envirnmentally friedly batteries emerge in recent years.

1.3.7.2.2 Ni-Metal Hydride Batteries

The nickel-metal hydride technology (Ni-MH) was developed to replace Ni-Cd batteries [37]. The positive electrode of the Ni-MH is nickel hydroxide, a well developed cathode material with the same composition as that in Ni-Cd battery. The electrolyte is also alkaline based aqueous solution. The active material for negative electrode is actually

hydrogen, which is stored in the metal-hydride structure. The following reactions show the working principle of a typical Ni-MH battery:

Cathode: $\beta - NiOOH + H_2O + e^- \underset{Charge}{\overset{Discharge}{\rightleftharpoons}} Ni(OH)_2 + OH^-$ (1.13)

Anode: $MH + OH^- \underset{Charge}{\overset{Discharge}{\rightleftharpoons}} M + H_2O + e^-$ (1.14)

Overall reaction: $MH + \beta - NiOOH \underset{Charge}{\overset{Discharge}{\rightleftharpoons}} M + Ni(OH)_2$ (1.15)

Due to a higher energy densities (3 times of the Ni-Cd batteries), higher capability and longer cycle life, the Ni-MH has been widely used in many portable devices as well as some of the latest generation of hybrid electric vehicles. However, the nickel electrode still suffers from low energy density, high self-discharge rate (e.g., 2% to 5% loss per month) and the 'memory effect' of incomplete discharge prior to a new recharge. Moreover, Ni-MH batteries are not as durable as some other types; its lifespan is around 500-1000 cycles, with a broad variation on how the batteries are used. Another problem is the poor scalability. If one battery is fully discharged before the other batteries in a same stack, it causes "polarity reversal" effect where the other batteries in the stack drive the drained cell in a reversal direction. Lastly, Ni-MH batteries suffer from dramatically reduced performance in cold conditions, which limits their outdoor application.

1.3.7.3 Redox Flow Batteries

Redox flow batteries (RFBs) are an emerging storage technology. They are comprised

of two different aqueous electrolytes contained in separate tanks and pumped through the electrochemical cell where the electrode reactions occur. The electrolytes flowing through the cathode and anode are often termed anolyte and catholyte. Figure 1.11 shows a generic RFB system. During the discharge, an anolyte solution flows through a porous electrode and reacts to generate electrons, which flow through the external circuitry. The charge-carrying species are then transported to a separator dividing the anolyte and catholyte solutions:

Anode: $$A^{(n-x)+} \underset{charge}{\overset{discharge}{\rightleftharpoons}} A^{n+} + xe^{-} (n > x) \tag{1.16}$$

Cathode: $$B^{(m+y)+} \underset{charge}{\overset{discharge}{\rightleftharpoons}} B^{m+} - ye^{-} \tag{1.17}$$

RFBs have several key features of energy storage. Instead of storing the electrochemical reactants within the electrode, the reactants are dissolved in electrolytic solutions and stored in external tanks. Therefore, the electrodes do not need to undergo physical changes. The decoupling of storage and electrode reaction in RFB system is a major advantage. The power and energy outputs in RFBs are independent variables since the power is determined by the electrode size and the amount of energy stored depends on the tank size and solution concentration [8, 11, 38].

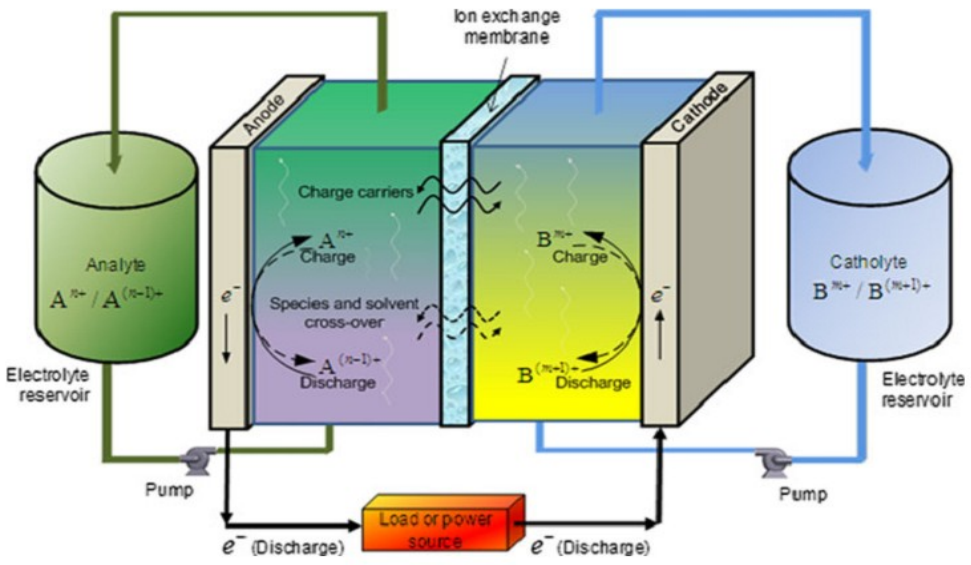

Figure 1.11 Operation principle of Flow Battery Energy Storage system [38].

Current RFBs can be classified according to the anolyte and catholyte chemistries into: iron/chromium flow batteries (ICBs), polysulphide/bromine flow batteries (PSBs), all vanadium redox flow batteries (VRBs), vanadium/bromine flow batteries (VBBs), zinc/bromine flow batteries (ZBB), vanadium/cerium flow batteries, soluble lead-acid batteries (e.g. lead-carbon batteries), all iron redox flow batteries (IRBs), *etc* [39, 40]. Among these RFBs, VRB, PSB, ICB and ZBB are more commercially ready, Table 1.1 compares the major characteristics of these four RFBs.

Most of the RFBs are mainly operated with an aqueous electrolyte. The operating voltage and energy density are limited due to the confinement of working temperature and hydrogen evolution. In addition, high costs, usage of toxic materials, and high self-discharge rate resulted from leakage shunt current are the just few factors hindering a widespread deployment of the RFB technology.

Table 1.1 Comparison of storage characteristics of four typical RFBs

Type	OCV(V)	SED(Wh/kg)	Discharge time(h)	Self-discharge % per month at 20°C	Cycle life	RTE
VRB	1.4	15(29)	4-12	5-10	5000	70-80%
PSB	1.5	20(41)	4-12	5-10	2000	60-70%
ICB	1.18	<10	4-12	-	2000	70-80%
ZBB	1.8	65(429)	2-5	12-15	2000	65-75%

1.3.7.4 Sodium-Sulfur and ZEBRA Batteries

1.3.7.4.1 Sodium-Sulfur Batteries

Among all the existing storage batteries, sodium sulfur battery (NAS) technology is by far best suited for large-scale stationary applications. This type of battery is unique in ways that it operates at higher rate capacity and elevated temperature (350°C), employing a solid Na^+ conducting electrolyte, a liquid Na negative and sulfur positive electrode with the storage capacity variable with the extent of Na-S reaction product.

A NAS battery uses sodium and sulfur for the negative and positive electrodes, respectively, and a Na^+ conducting β-alumina ceramic as the electrolyte. Figure 1.12 illustrates the working principle of a typical NAS battery. During the discharge, the

metallic Na is oxidized to Na^+, while the S cathode is reduced to S^{2-}. The electrolyte transports Na^+ from the anode to the cathode where they combine with sulfur anions and produce sodium polysulfide Na_2S_x. During the charge, the reaction occurs in a reversal manner. The reactions involved in the NAS battery is given by

Anode: $$Na \underset{Charge}{\overset{Discharge}{\rightleftarrows}} Na^+ + e^- \tag{1.18}$$

Cathode: $$xS + e^- \underset{Charge}{\overset{Discharge}{\rightleftarrows}} S_x^- \tag{1.19}$$

Overall: $$2Na + xS \underset{Charge}{\overset{Discharge}{\rightleftarrows}} Na_2S_x \tag{1.20}$$

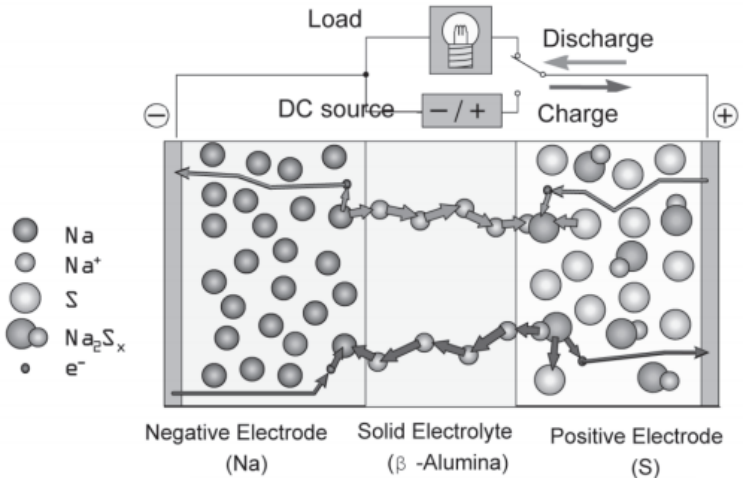

Figure 1.12 A schematic of the working principle of NAS battery [41].

NAS batteries operate at a temperature around 350°C in order to keep the electrode materials in a molten state, reducing the resistance for Na^+ transport from electrolyte, and retaining a fast electrode kinetic rate. Therefore, NAS batteries are usually designed in a tubular manner where the sodium is normally contained in an interior cavity formed by an electrolyte tube (see Figure 1.13).

The key advantages of NAS batteries include high energy density, high rate capacity, negligible self-discharge, high RTE (~85%), high cycle life and good sustainability. It can meet either the short-term or long-term discharge applications. The flexibility makes it superior over many other batteries for energy management and power quality applications. However, the electrode materials have a very high reactivity in liquid state, so the safety issue is of a great concern. Another drawback of this battery is its inability to thermal cycling. Finally, the EMF of NAS batteries varies with the state-of-charge.

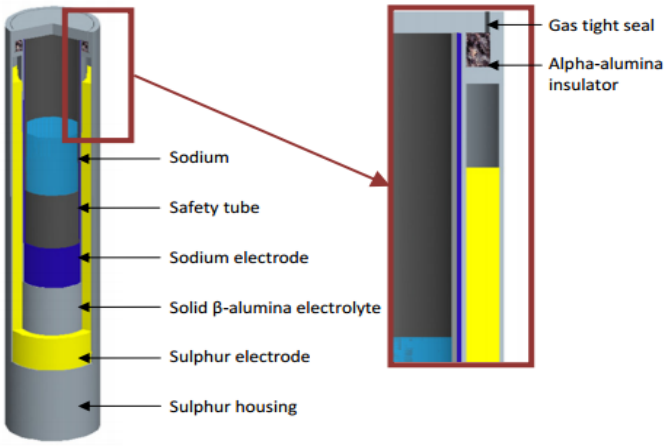

Figure 1.13 Typical structure of a NAS battery [11].

1.3.7.4.2 Sodium-nickel-chlorite (ZEBRA)

An improved version NAS battery was invented in South Africa; ZEBRA stands for "Zeolite Battery Research Africa" [42, 43]. The general configuration of ZEBRA is similar to NAS battery in negative electrode and electrolyte: liquid sodium as the negative electrode and β"-Al_2O_3 as the electrolyte. The difference lies in the positive electrode.

ZEBRA uses solid $NiCl_2$ positive electrode and a second liquid electrolyte, $NaAlCl_4$ [44]. Figure 1.14 shows its configuration and global reaction [43].

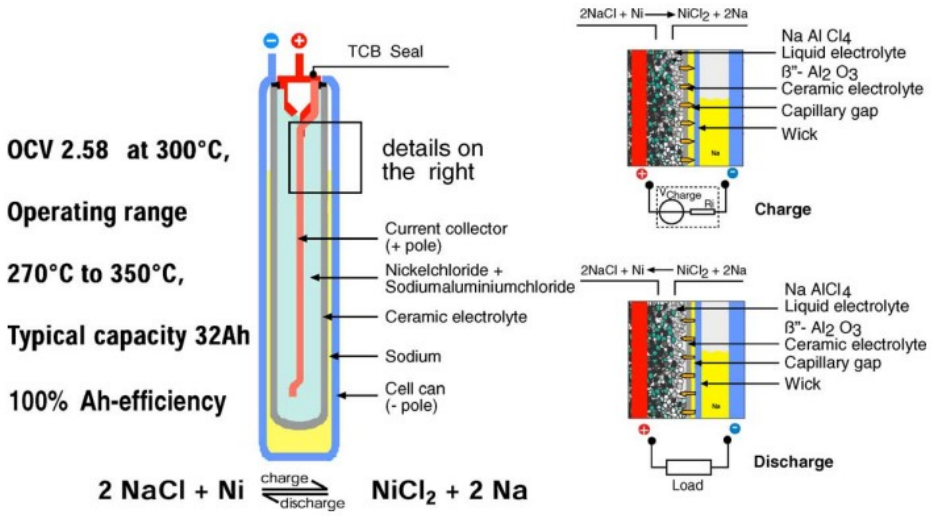

Figure 1.14 Structure of a typical ZEBRA battery and reactions [43].

The liquid salt $NaAlCl_4$ is significant to ZEBRA's robustness since ceramic is usually vulnerable to small cracks or even breakage. $NaAlCl_4$ contacts with the liquid sodium and reacts to form salt and aluminum during the discharge:

$$NaAlCl_4 + 3Na \leftrightarrow 4NaCl + Al \tag{1.21}$$

The charge capacity of the ZEBRA cell is determined by the quantity of NaCl salt in the cathode. In the event that a cell is overcharged, the liquid $NaAlCl_4$ can serve as a "sodium reservoir" following the reversible equation:

$$NaAlCl_4 + Ni \leftrightarrow 2Na + 2AlCl_3 + NiCl_2 \tag{1.22}$$

The working temperature of ZEBRA ranges from 270 to 350^{o}C, and the OCV is

around 2.61V per cell. The theoretical specific energy density of individual cell is 790 Wh/kg, which is slightly greater than that of NAS cells, 760 Wh/kg [44]. Safety tests in Switzerland showed that these batteries are much safer than NAS cells, and do not represent a significant risk under simulated crash conditions during transportation application [43]. The major obstacles facing ZEBRA include thermal cycling ability and cost issue.

1.3.7.5 Liquid Metal Batteries

Compared with solid electrodes, liquid electrodes can tolerate much higher level of mechanical stresses. The self-segregating nature of liquid electrodes and electrolytes naturally provides an option for manufacturing a liquid battery. However, there are no viable liquids found at room temperature for such a structured battery. Using liquid metals at elevated temperature becomes another option. Early work on liquid metal batteries demonstrated high energy density with a variety of chemistries. For example, the Li/Bi cell operating between 380^{o}C and 485^{o}C yielded a 2.2A/cm^2 current density along with a maximum power density of 570mW/cm^2 at 0.6V; the Li/Te cell operating at 475^{o}C yielded a 2.2A/cm^2 current density and a maximum power density of 1000mW/cm^2 at 0.9V [45, 46]. However, the use of prohibitively expensive metalloids (such as Bi and Te) as the positive electrode limits the real application of those batteries. The solubility of negative electrode metal (e.g. Li or Na) in the electrolyte causes a noticeable self-discharge current density (~40 mA/cm^2).

In 2011, a new class of liquid metal batteries operating at high temperature was demonstrated in MIT [47]. In this type of batteries, a negative metal electrode of A (A = Li, Be, Na, Mg, K, Ca), a molten salt electrolyte (e.g. $MgCl_2$−KCl−NaCl), and a positive electrode of B (B = Sn, Sb, Pb, Bi) are utilized. Due to density differences and immiscibility of A, electrolyte and B, the salt and metal phases stratify into three distinct layers. During the discharge, A is oxidized to A^{x+} ($A \rightarrow A^{x+} + xe^-$) at the negative electrode, which dissolves into the electrolyte while the electrons are released into the external circuit. Meanwhile, at the positive electrode A^{x+} ions in the electrolyte are reduced to A ($A^{x+} + xe^- \rightarrow A$), which is deposited into the B electrode to form a liquid metal alloy (A-B) with receiving electrons from the external circuitry.

The reverse reactions occur when the battery is charged. Charging and discharging of the battery are accompanied by volumetric changes in the liquid electrodes. The difference in the chemical potentials of pure A (μA) and A dissolved in B [μA(in B)] generates a voltage that can be expressed as:

$$E_{cell} = \frac{RT}{2F} \ln\left[\frac{a_{A(inB)}}{a_A}\right] \tag{1.23}$$

The schematic of an Mg-Sb battery is shown in Figure 1.15.

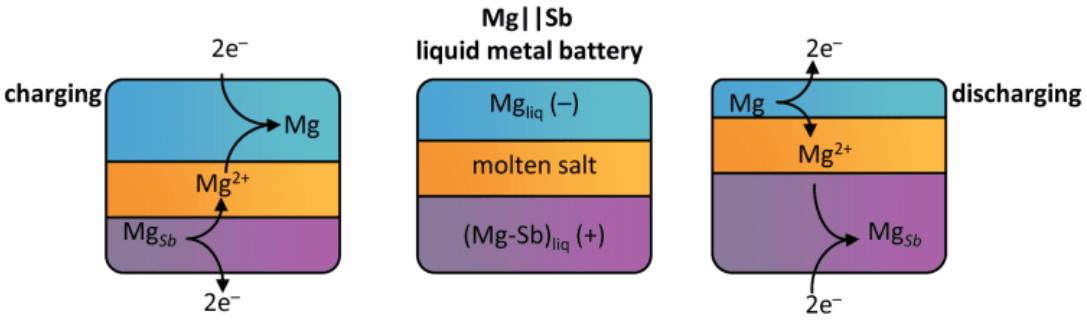

Figure 1.15 Working principle of a new liquid metal Mg-Sb battery [47].

This cost-effective battery has demonstrated 69% DC-DC energy efficiency at rates ranging from 50 to 200mA/cm^2. Due to its low cost and good performance, Bill Gates has invested $15M to fund Liquid Metal Battery Corp. for large-scale grid energy storage application [48]. The major challenges of the battery include corrosion, thermal cyclability, low EMF (0.4V~0.6V) dependent on state-of-charge.

1.3.7.6 Metal Air Batteries

Metal-Air battery can be deemed as a special fuel cell using metal as the fuel and air as the oxidant. Since 1960s, considerable work has been carried out to develop commercial metal-air batteries. The development of metal-air batteries experienced a halt due to material problems at air electrode, thermal management, and etc [49]. Recent advances in the performance and stability of air cathodes [50, 51] and improved anode materials [52-54], along with their extremely high energy density nature have spurred a great interest to revisit this old technology for energy storage.

Traditional metal-air batteries can be divided into two types according to their

electrolytes. One is based on an aqueous electrolyte, and the other is based on a water sensitive aprotic solvents.

Among the existing metal-air batteries, Al-air, Fe-air and Zn-air batteries use aqueous electrolytes. The generic battery reactions for M-air (M=Al or Fe) are

$$\text{Anode: } Me + xOH^- \underset{Charge}{\overset{Discharge}{\rightleftharpoons}} Me(OH)_x + xe^- \tag{1.24}$$

$$\text{Cathode: } O_2 + 2H_2O + 4e^- \underset{Charge}{\overset{Discharge}{\rightleftharpoons}} 4OH^- \tag{1.25}$$

$$\text{Overall: } Me + \frac{x}{4}O_2 + \frac{x}{2}H_2O \underset{Charge}{\overset{Discharge}{\rightleftharpoons}} Me(OH)_x \tag{1.26}$$

Zn-air battery differs from the Al-air and Fe-air counterparts in that $Zn(OH)_4^{2-}$ forms at the anode compartment and gradually decomposes into ZnO in the fluid. In Figure 1.16, the working principle of zinc-air battery is demonstrated.

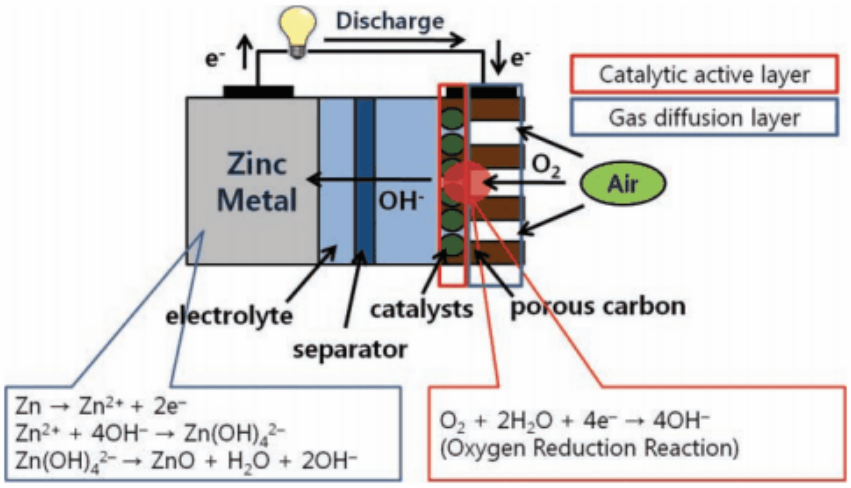

Figure 1.16 Working principle of zinc-air battery using an aqueous electrolyte [55].

Lithium-air batteries are typically based on aprotic electrolytes that conduct Li^+-ions,

but aqueous based electrolytes have also been reported recently. To circumvent the problems of electrolyte stability, a number of Li-air battery configurations have been investigated and shown in Figure 1.17. The overall reactions can be expressed by:

$$2Li + O_2 \underset{Charge}{\overset{Discharge}{\rightleftharpoons}} Li_2O_2 \qquad (1.27)$$

or

$$4Li + O_2 \underset{Charge}{\overset{Discharge}{\rightleftharpoons}} 2Li_2O \qquad (1.28)$$

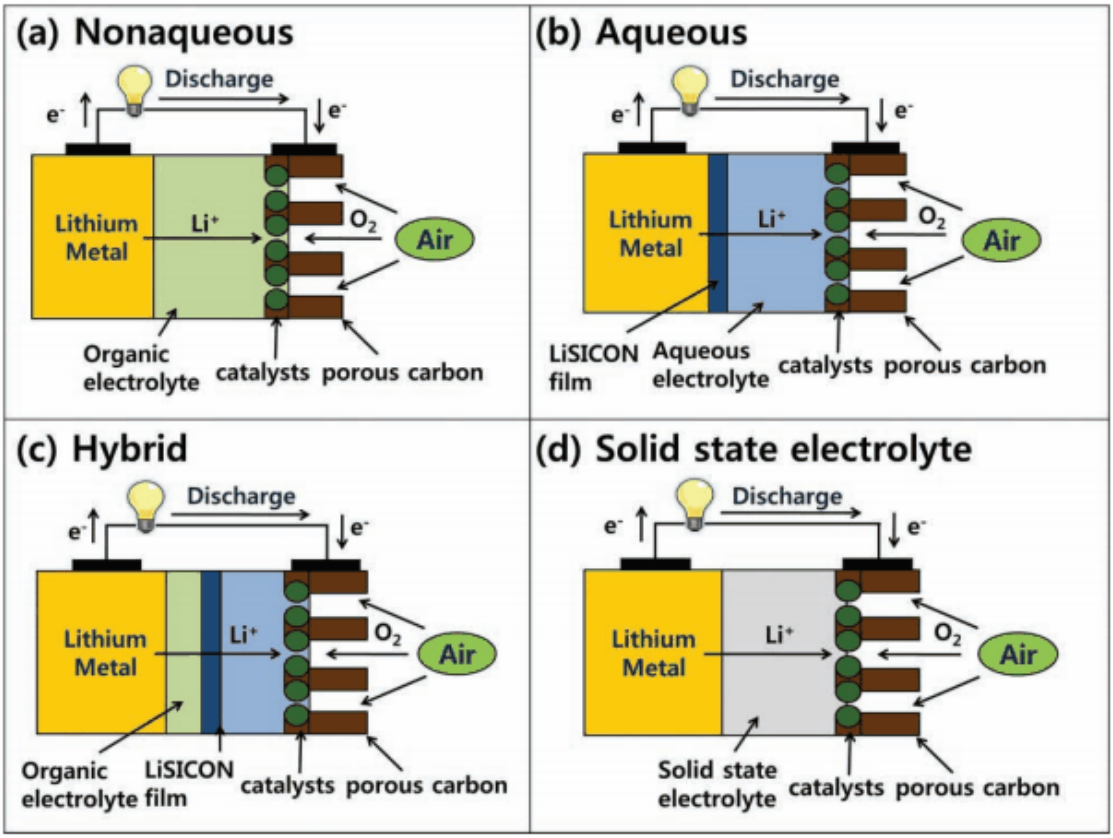

Figure 1.17 Schematic cell configurations for four different types of Li-air battery [55].

Despite the promised high energy density, the Li-air battery is being seriously

challenged as a commercial product due to the decomposition of electrolyte, air electrode clogging, all of which leads to poor rechargeability and inferior energy output [56-58]. Another hurdle facing Li-air battery is the high cost (>$600/kWh) due to special packaging and internal overcharge protection circuits. Although many manufacturers offer refueling units for Zn-air battery, where the consumed metal is mechanically replaced and processed separately, fewer developers offer a fully electrically rechargeable Zn-air battery. Rechargeable metal-air batteries that are under development have a lifetime of only a few hundred cycles (for Zn-air) and the efficiency is below 50% [10]. All these issues call for discovery of new materials and innovative design for metal-air batteries.

1.3.8 Summary

EES is a reversible energy conversion system that transforms electrical energy into other forms of energy (*e.g.*, kinetic, potential and chemical, *etc*). Its ability to store electricity for later use makes it an ideal buffer for balancing demand and supply of electrical energy. The principal requirements for a grid-scale energy storage system include fast response, high energy storage capacity, high power capacity, high rate capacity, high round-trip efficiency, long cycle life, safety, sustainability and scalability, all of which have a great impact on the final product cost.

Electrochemical energy storage such as rechargeable batteries is more flexible to integrate into a smart grid than geographically selective technologies like PHES and CAES.

Although many types of batteries have been proposed, they together contribute to less than 1% of the total energy production [59], implying that many breakthroughs in system design and materials optimization are needed.

Among the state-of-art batteries, RFBs and NAS/ZEBRA stand out to be the most suitable technologies for grid energy storage. RFBs are flexible in system design for either power or energy application, making it a valuable asset for grid application. The high power/energy densities and fast and deep discharge/charge cycling capability have positioned the NAS/ZEBRA as a front runner in the commercial development of grid-scale energy storage batteries. However, low energy density, short shelf life, use of toxic materials and high costs are the primary barriers to the commercialization of RFBs technology. The inability to sustain thermal cycling, high manufacturing cost as well as unsafe nature are the impasses for NAS/ZEBRA technology to overcome.

Besides the relatively new RFBs and NAS/ZEBRA technologies, metal-air batteries are receiving growing attention in recent years due to their extremely high energy density, inexhaustible cathode reactants and potential cost reduction. However, metal-air batteries are facing many challenges in materials development and system design. Meeting these challenges with materials discovery, new battery chemistry and innovative design are of critical importance to commercialize the high-potential metal-air rechargeable batteries. My PhD research is aimed to develop a new metal-air rechargeable battery with a new chemistry. In the following subchapters, a novel Solid Oxide Metal Air Battery (SOMARB)

system based on Solid Oxide Fuel Cell (SOFC) and Hydrogen Chemical Looping (HCL) technologies is explained as a novel EES mechanism suitable for stationary storage.

CHAPTER 2

A NEW SOLID OXIDE METAL AIR REDOX BATTERY (SOMARB): PRINCIPLES AND PROMISES

2.1 BACKGROUND

2.1.1 Regenerative SOFCs

Fuel cell has been known in scientific world for more than 170 years since German-Swiss scientist Christian Friedrich Schönbein first asserted the possibility of a fuel cell that combined hydrogen and oxygen in 1839 [60]. The first SOFC was demonstrated more than one century later in 1940s [61, 62]. However, it was not until 1980s that the first reversible SOFC (RSOFC) was operated as both power and hydrogen generators [63].

RSOFC is a high-temperature electrical-chemical conversion device. Based on electrochemical principle (unlimited by the Carnot cycle), it can reversibly convert the stored chemical energy in hydrocarbon fuels including H_2 to electrical energy and split water and CO_2 into H_2 and CO with DC electrical energy input at high energy conversion efficiency. It is possible that the reversible conversion between chemical and electrical energy in RSOFCs can be utilized as a means of storing energy provided that the consumed

and generated fuel (e.g., H_2) by RSOFCs are properly stored during the charge-discharge cycles. Figure 2.1 shows a typical RSOFC configuration.

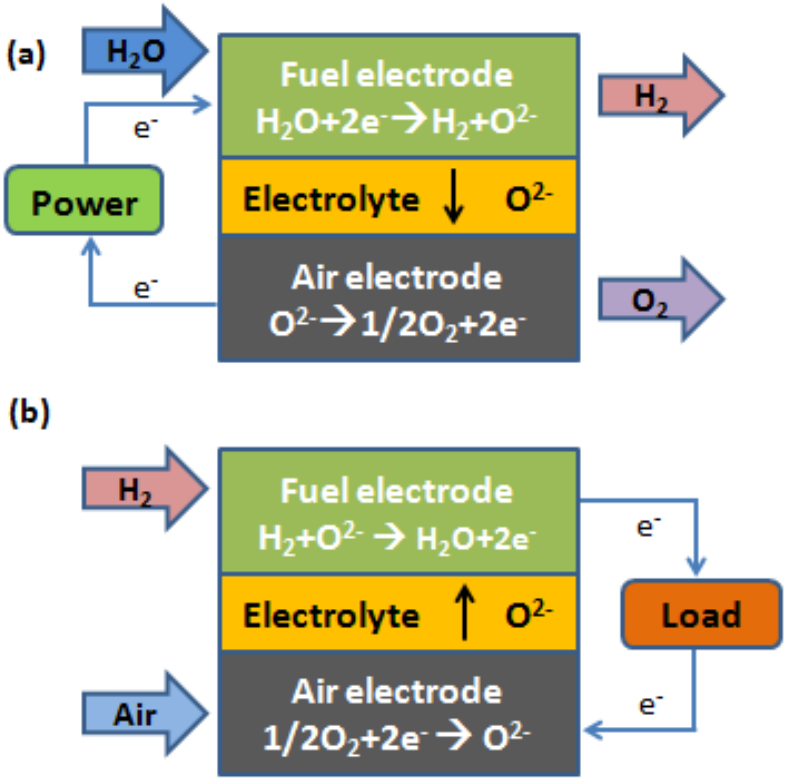

Figure 2.1 RSOFC in (a) Electrolysis mode; (b) fuel cell mode.

An operational SOFC demands for a constant supply of H_2 for continuous power generation; this would require large-capacity hydrogen separation and storage facility to support it. Similarly, a solid oxide electrolysis cell (or SOEC) requires a constant supply of H_2O for its operation. A bulky storage facility for $H_{2(g)}$ would compromise the compact nature of a RSOFC. Therefore, there is an incentive to convert the bulky hydrogen production and storage into a more compacted form for the application of RSOFCs.

Storing hydrogen in solids offers a volume-effective solution for a compact RSOFC. However, due to the high operating temperature of RSOFCs (600^{o}C-1000^{o}C), most of the current hydrogen-storage solids are not suited for the application. Storing energy in chemically stable metal/metal oxide redox couples at high temperatures has been demonstrated as a more efficient alternative in today's metal-steam hydrogen chemical looping process [64].

2.1.2 Steam-Metal Hydrogen Chemical Looping (HCL)

Hydrogen can be produced from water, an abundant resource on the earth, by chemically reacting a reactive metal with steam [3, 64, 65]. During the process, pure hydrogen is generated by oxidizing the metal with steam as shown in eq. (2.1). After all metal is converted into oxide, a reverse reaction will be needed to regenerate the metal by introducing hydrogen or other reducing agents, which completes a chemical looping process

$$xMe + yH_2O \leftrightarrow Me_xO_y + yH_2 \tag{2.1}$$

E*q*. (2.1) depicts a reaction between a gas and solid, which makes the separation of hydrogen relatively easy for chemical-looping systems [66]. The unique advantage of such a chemical looping process lies in its ability to indirectly store hydrogen in the form of reduced solid metals, a volume-effective way to store chemical energy.

Oxygen carrier metals are vital for chemical looping in a hydrogen production process.

An oxygen carrier is selected primarily based on its ability to transport oxygen from water to fuel. Currently, only metals that possess favorable thermodynamic equilibrium are considered as a prospective oxygen carrier. The metals are usually mixed with inert ceramic oxides to prevent agglomeration during operation, thus enhancing the recyclability. Common sintering inhibitor oxides include Al_2O_3, SiO_2, TiO_2 and ZrO_2 (stabilized with Y_2O_3).

The metals that have been investigated as oxygen carriers are Mn, Fe, Co, Ni, W and Cu, and alloys formed among them. A metal/metal oxide redox couple is selected for chemical looping according to its thermodynamic equilibrium, recyclability, synthesis method, and resistance to attrition. Since the chemical looping reaction occurs usually at high temperatures, the melting point of the metal/metal oxide redox couple also needs to be considered. If the melting point of an oxygen carrier is within the range of operation temperature, agglomeration and decrease in reactivity would be likely to occur during the reaction. Table 2.1 lists the melting points of some common metals and their oxides. Among those metals, Mn, Fe, Ni, and W have high melting points in both reduced and oxidized forms whereas the melting points of Cu-based carriers are generally low.

Table 2.1 Melting points of some metals and metal oxides

Metal (or lower valency metal oxide) / higher valency metal oxide	Melting point of lower valence metal oxides or metal (^oC)	Melting point of higher valence metal oxides (^oC)
Ti/Ti_3O_2	1668	-
V/V_2O_3	1910	1940
Cr/Cr_2O_3	1907	2435
MnO/Mn_3O_4	1945	1567
Mn/MnO	1246	1945
Fe_3O_4/Fe_2O_3	1597	1566
FeO/Fe_3O_4	1377	1597
Fe/FeO	1538	1377
Co/CoO	1495	1933
Ni/NiO	1455	1955
Cu_2O/CuO	1235	1326
Cu/Cu_2O	1085	1235
WO_2/WO_3	1700	1473
W/WO_2	3422	1700
MoO_2/MoO_3	1100	795
Mo/MoO_2	2623	1100

*data taken from Wikipedia

An important thermodynamic criterion for metal/metal-oxide redox couple selection is the ratio of oxygen to metal (O/M) in a metal oxide. A higher O/M ratio implies a higher oxygen capacity, and therefore a higher hydrogen production capacity. Therefore, W/WO_3 redox couple is conceived to have a higher capacity than Ni/NiO for hydrogen production.

2.1.3 The Early Concept of RSOFC Energy Storage

The combination of a RSOFC with a metal/metal oxide redox couple for energy storage was first proposed in 1996 in a patent filed by two Westinghouse engineers Dr. Arnold Isenberg and Dr. Roswell Ruka. In their patent as schematically illustrated in Figure 2.2, bundles of cathode-supported RSOFCs were integrated with a Fe/FeO redox-couple bed [67]. The H_2O produced during the fuel-cell mode (discharge) was led to oxidize Fe in the redox-couple bed to produce H_2 for a sustainable fuel cell operation. Reversely, the H_2 electrically split from H_2O during the electrolysis mode (charge) of RSOFC was utilized to reduce FeO back to Fe. The configuration shown in Figure 2.2 becomes the foundation of our new "solid oxide metal air redox battery" that is built upon an anode support instead of cathode. However, this patent has never drawn enough attention due to the low power density inherited from cathode-supported tubular SOFCs and system complexity.

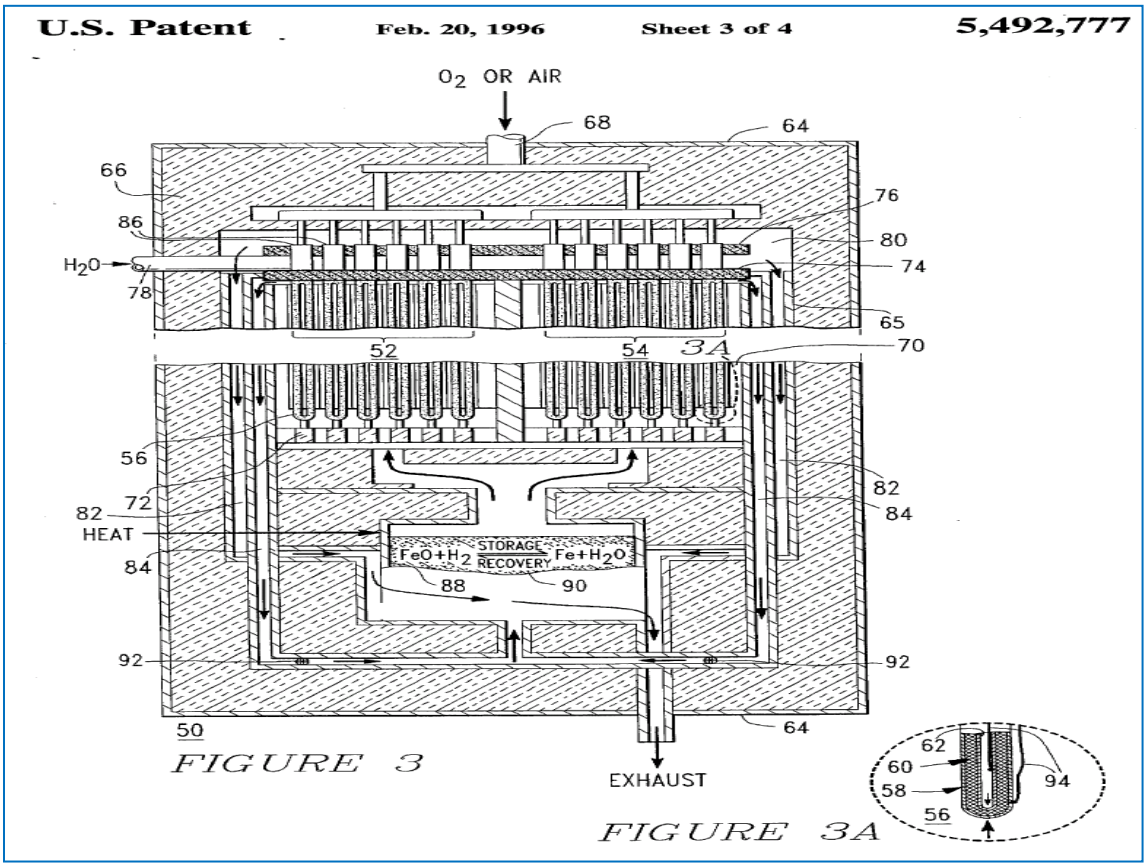

Figure 2.2 Early Westinghouse's concept on an electrochemical energy conversion and storage system based on RSOFC and hydrogen chemical looping [67].

2.2 WORKING PRINCIPLE OF THE ADVANCED SOMARB

My Ph.D. research aims to demonstrate, develop and optimize a novel "solid oxide metal air redox battery (SOMARB)" based on an anode supported tubular RSOFC and HCL technologies for large-scale grid storage.

Our design of SOMARB consists of a RSOFC as the electrical functioning unit and a metal/metal oxide (Me/MeO_x) redox couple as the energy storage medium (ESU). As previously discussed, RSOFC either works as a solid oxide fuel cell or a solid oxide electrolyzer. At the fuel electrode, a closed loop is created to ensure energy transfer through

electrochemical reaction and chemical equilibrium among H_2-H_2O-Me-MeO_x. The air electrode is open to the atmosphere containing inexhaustible cathode reactant - air. Figure 2.3 shows schematically the working principle of the SOMARB. During the charge cycle, MeO_x is reduced into Me by H_2 that is generated by splitting H_2O in RSOFC, and the produced H_2O proceeds towards RSOFC for continued electrochemical splitting. During the discharge cycle, Me is oxidized to form MeO_x and H_2 by H_2O that is continually supplied from electrochemical oxidation of H_2 produced from the metal-steam reaction in RSOFC functioning as a fuel cell. During the cycles, the reactant gas H_2O-H_2 is continuously circulating in the close-loop.

The reaction loop during the discharge and charge cycles (reactions (1)-(4) in Figure 2.3) can be generalized as:

$$\begin{array}{ccc} H_{2(g)}+O^{2-} & \underset{charge}{\overset{discharge}{\rightleftharpoons}} & H_2O_{(g)}+2e^- \\ \Big\downarrow\Big\uparrow \; discharge \;/\; charge & & \Big\uparrow\Big\downarrow \; charge \;/\; discharge \\ x\,H_{2(g)}+MeO_{x(s)} & \underset{discharge}{\overset{charge}{\rightleftharpoons}} & xH_2O_{(g)}+Me_{(s)} \end{array} \qquad (2.2)$$

During the discharge and charge cycles, the reactions at the air-electrode are:

$$\frac{1}{2}O_2 + 2e^- \underset{charge}{\overset{discharge}{\rightleftharpoons}} O^{2-} \qquad (2.3)$$

By combining reactions (2.2) and (2.3), the global reaction of the battery becomes:

$$Me + \frac{x}{2} O_2 \underset{charge}{\overset{discharge}{\rightleftharpoons}} MeOx \qquad (2.4)$$

It is evident that the new battery is essentially a metal-air battery, although its working manner resembles a redox flow battery and has also been previously termed “solid oxide redox flow battery” (SORFB) [68].

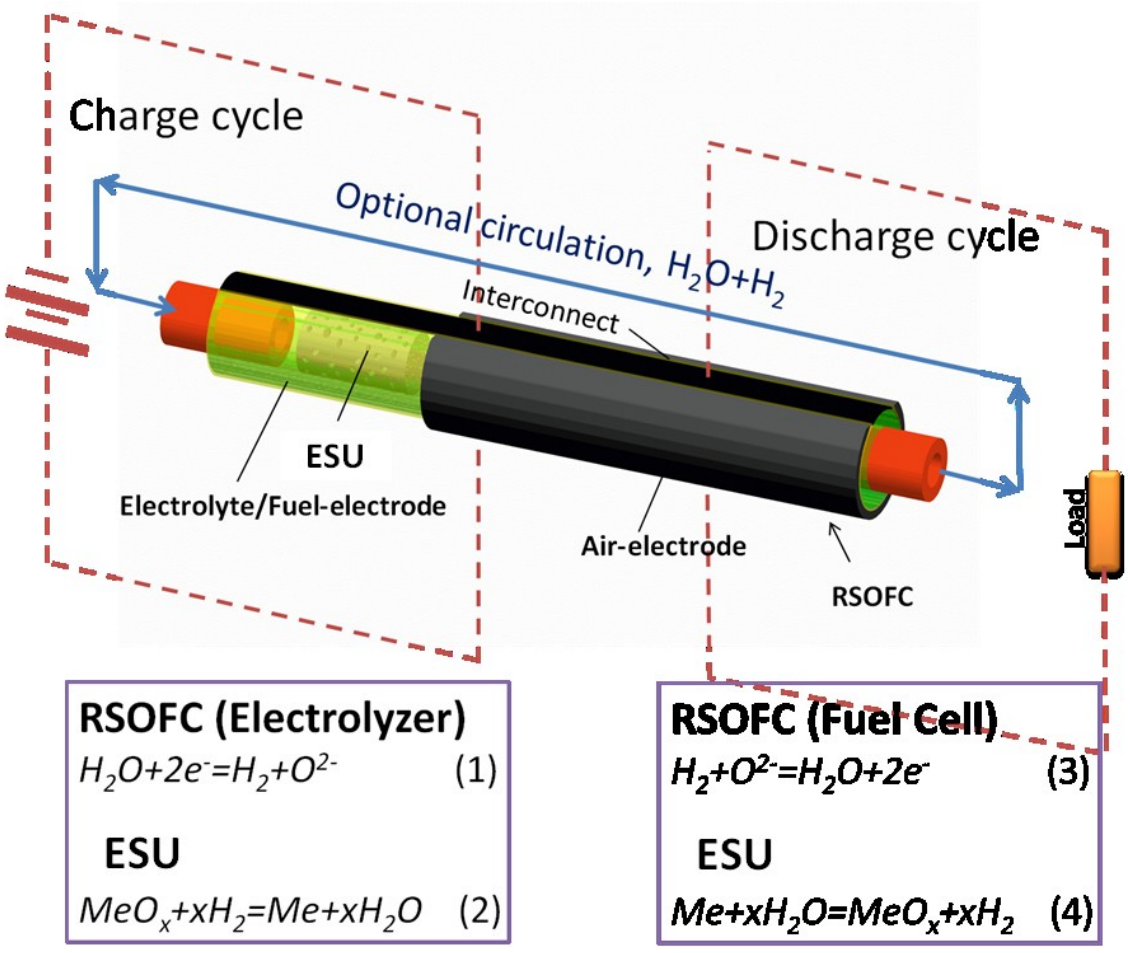

Figure 2.3 Working principle of the new metal-air battery based on an anode-supported tubular RSOFC.

2.3 KEY FEATURES OF THE SOMARB

A number of features of the new SOMARB are conceived distinguishable from other

batteries for large-scale stationary energy storage.

- Energy can be designed independently with power to meet applications with either power or energy focus.

- The fuel electrode and ESU are physically separated, enabling a faster charge-discharge cycle without the concerns of structural damages as commonly encountered in conventional storage batteries.

- The direction of the reversible redox reaction in the ESU is driven by the partial pressures of H_2 and H_2O in the fuel-electrode chamber. When the partial pressure of hydrogen is above the equilibrium value, reduction is dominant, and vice versa. Under the open-circuit condition, H_2-H_2O mixture equilibrates with Me and MeO_x at fixed thermodynamic partial pressures and is uniform across the fuel-electrode chamber. Under the current-loading conditions, however, the H_2 and H_2O concentrations near the surface of RSOFC are different from those at the surface of Me-MeO_x redox couple; the latter is constantly fixed by the redox reaction shown in eq. (2.4) at a constant temperature. This situation is schematically illustrated in Figure 2.4 (a)-(c). Since the pH_2/pH_2O of the reactant gas entering the RSOFC remains constant during the cycle, the energy storage process is accomplished by a corresponding change in the mass ratio of Me and MeO, m_{Me}/m_{MeO}, which is precisely regulated by the H_2/H_2O-mediated redox reaction.

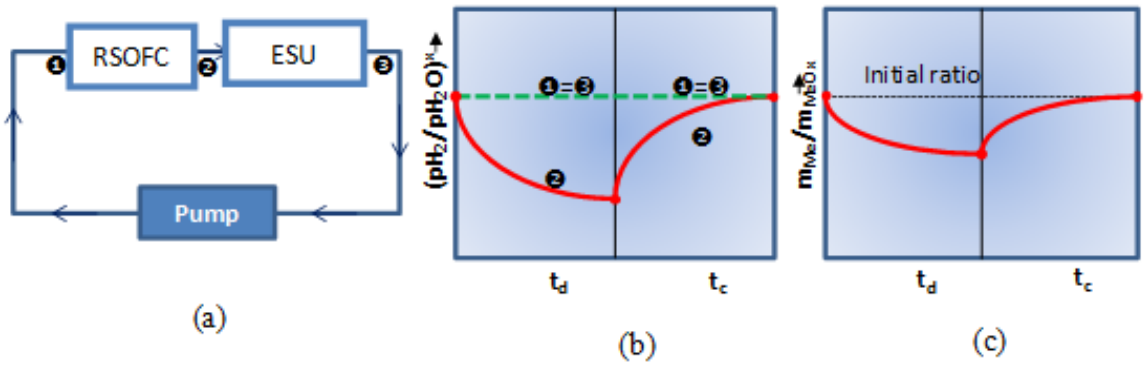

(a) (b) (c)

Figure 2.4 Schematic illustrations of (a) gas flow blocks among three major components; (b) pH_2/pH_2O variations at locations ❶=❸ and ❷ with the cycle; (c) variations of mass ratio of Me to MeO_x in the ESU with the cycle. td and tc are times for discharge and charge, respectively.

- A fixed pH_2/pH_2O at a fixed temperature leads to a fixed EMF in a concentration cell like SOMARB. Such a state-of-the-charge independent EMF feature is advantageous over NAS/ZEBRA batteries and liquid metal batteries, in which the active species is directly formed into or extracted from the electrode structure, leading to a process-dependent EMF.

- Different from most of the traditional rechargeable batteries that rely on single-electron charge transfer limited by single-charge electrolytes employed (e.g. Li^+, H^+ or Na^+ [41, 55, 69]), the new battery presents a double-electron transfer process enabled by the solid O^{2-} electrolyte, promising a higher storage-capacity at a higher rate. This is a valuable asset to rapidly harvest energy from renewable sources when the natural high energy flux is available.

- It can be thermally cycled without the concerns of structural damages as commonly

encountered in conventional high-temperature liquid metal batteries.

- It is sustainable, cost-effective, and environmental-friendly due to the use of earth-abundant, inexpensive, and environmentally benign redox couple energy storage materials.

- It can be easily scaled up to larger systems from an engineering perspective. Similar stack design of large class tubular SOFCs has been previously demonstrated.

- The overall system is operationally safe regardless of rates of cycles.

- Different from the early Westinghouse's design, anode-supported tubular RSOFCs on which the SOMARB is based, can achieve higher power density due to lower resistance. Moreover, internal containment of ESU materials offered by the anode-supported tubular design can potentially provide high volume-specific energy capacity with a much smaller footprint.

2.4 KEY METRICS OF THE SOMARB

As an EES mechanism, the performance of the SOMARB is evaluated with a range of metrics. The equations in Table 2.2 quantify the key metrics of the SOMARB to be evaluated in this research.

Table 2.2 Equations for quantifying the key metrics of the SOMARB

Metric	Equation		*No.*
E_N (V)	$E_N = -\frac{\Delta G}{nF} = \frac{RT}{nF} lnK = \frac{RT}{nF} ln \frac{P}{P_{O_2}}$	(theoretical)	(2.5)
SE (J/kg)	$SE^* = -\frac{\Delta G}{1000 \times 3600 \cdot M_{Me}}$	(theoretical)	(2.6)
	$SE = \int_{t_1}^{t_2} (I_d V_d(t) / m_{Me}) dt$	(measured)	(2.7)
SC (C/kg)	$Q^* = \frac{W_{Me}}{M_{Me}} \cdot 2x \cdot F$	(theoretical)	(2.8)
	$Q = I_d \cdot t_d / m_{Me}$	(measured)	(2.9)
ED (J/m^3)	$ED^* = -\frac{\Delta G}{1000 \times 3600 \cdot M_{Me}} \cdot \rho_{Me}$	(theoretical)	(2.10)
	$ED = \int_{t_1}^{t_2} (I_d V_d(t) / V_{Me}) dt$	(measured)	(2.11)
CD (C/m^3)	$CD^* = \frac{W_{Me}}{M_{Me}} \cdot 2x \cdot F \cdot \rho_{Me}$	(theoretical)	(2.12)
	$CD = I_d \cdot t_d / V_{Me}$	(measured)	(2.13)
RC (C/m^2)	$RC = I_d \cdot t_d / S_{RSOFC}$	(measured)	(2.14)
t_{Me} (s)	$t_{Me}^* = \frac{Q_{Me}^*}{I_d}$	(theoretical)	(2.15)
U_{Me} (%)	$U_{Me} = \frac{Q_{Me}}{Q_{Me}^*} = \frac{t_{Me}}{t_{Me}^*}$	(theoretical)	(2.16)

2.5 SUMMARY

A new EES mechanism -SOMARB- has been developed from RSOFC and chemical looping technologies. The new battery consists of a RSOFC and an ESU. During the discharge and charge cycles, the RSOFC alternates between fuel cell mode and electrolyzer mode, and simultaneously, the ESU stores energy via a H_2/H_2O mediated metal/metal oxide redox reaction. The new SOMARB can produce a high energy capacity at a high rate, endure multiple thermal cycling, and operate in a cost-effective, environmentally-friendly, sustainable, scalable, and safe manner. A profound advantage of the battery is the decoupled fuel electrode and ESU design, which allows faster charge-discharge cycles without concerning structural damages as commonly encountered in conventional storage batteries.

CHAPTER 3

FUNDAMENTALS OF ESU REDOX COUPLE SELECTION

There are two factors determining the overall performance of a SOMARB: electrical performance of RSOFC and redox reversibility of ESU material. While enhancing the performance of a RSOFC has been a broadly studied subject of the fuel cell research, selecting adequate ESU materials for the SOMARB is a new research frontier. A primary guideline for selecting redox-couple based ESU materials follows thermodynamic and kinetic principles with a goal to maximize the thermodynamic values and kinetic rates. Secondary considerations include cost effectiveness, sustainability, environmental impact and safety. In this chapter, we will focus on analyzing from a theoretical perspective a variety of metal-metal-oxide redox couples for the SOMARB.

3.1 THE PHASE DIAGRAM APPROACH

According to eq. (2.2) to eq. (2.4), the overall performance of the new battery depends on the chemistry of metal/metal-oxide redox couples. Therefore, the selection and determination of the redox couple compositions is critical. The first step to select a chemically stable redox couple is to examine the phase diagram. Taking Fe-O system as

an example, Figure 3.1 indicates that there are two sets of redox couple existed in Fe-O system over a temperature window of 500-800°C: Fe-FeO operating at >600°C and Fe-Fe_3O_4 operating at ≤600°C.

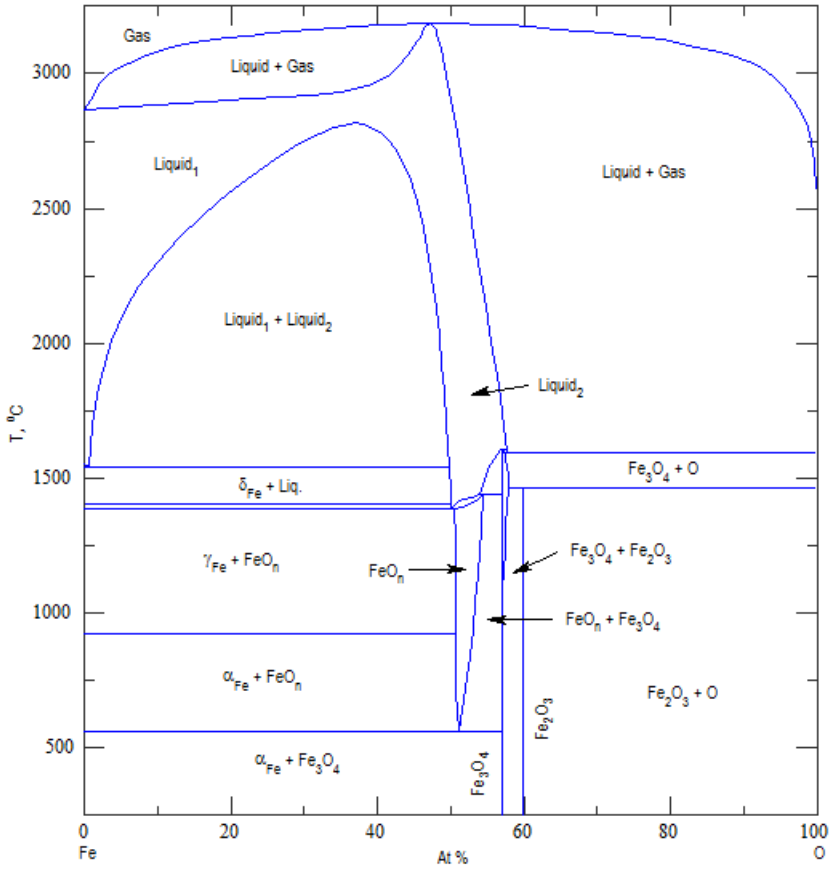

Figure 3.1 Phase diagram of Fe-O system[70, 71].

The phase stability diagram of Fe-O-H system in Figure 3.2 further confirms the temperature-dependent phase relationship shown in Figure 3.1, *i.e.*, prevalent Fe-FeO equilibrium at >600°C and Fe-Fe_3O_4 at ≤600°C. Additional useful information displayed in Figure 3.2 is that the pH_2/pH_2O ratio is only dependent on temperature, which implies a

fixed E_N for a concentration cell with air as the oxidant at a given temperature.

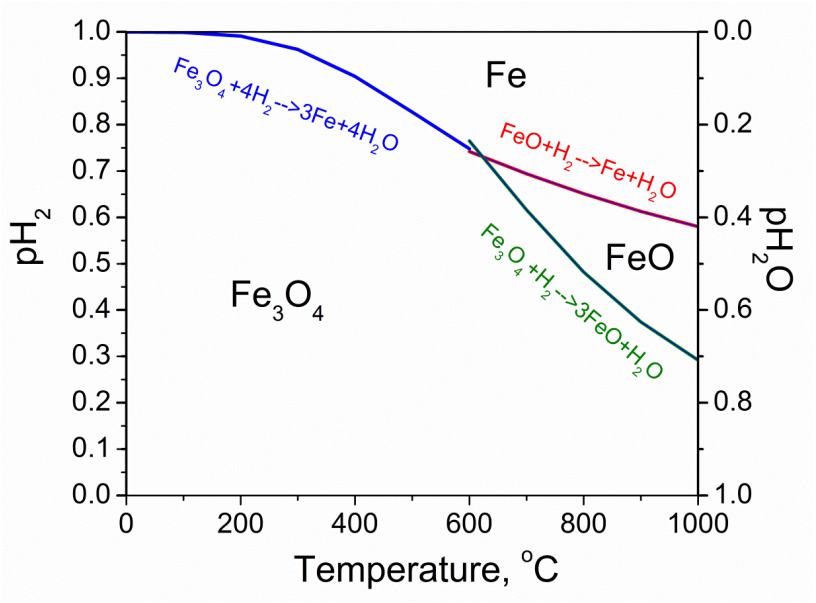

Figure 3.2 Phase stability domain of Fe-O-H system as a function of temperature[71].

According to Gibb's phase rule, there should be a fixed EMF at a given temperature in the presence of two discrete phases for an isobaric binary system as discussed above. Figure 3.3 shows the theoretical EMF calculated on the basis of Fe-FeO and Fe-Fe_3O_4 redox couples. For instance, the EMF at 550°C corresponding to Fe-Fe_3O_4 equilibrium is 1.067 V, while it is 0.970 V at 800°C, corresponding to Fe-FeO equilibrium. Conversely, if the EMF is measurable as a function of temperature, it can also be used to confirm the phase relationship predicted by Figures. 3.1 and 3.2. Later experimental results justify this prediction very well.

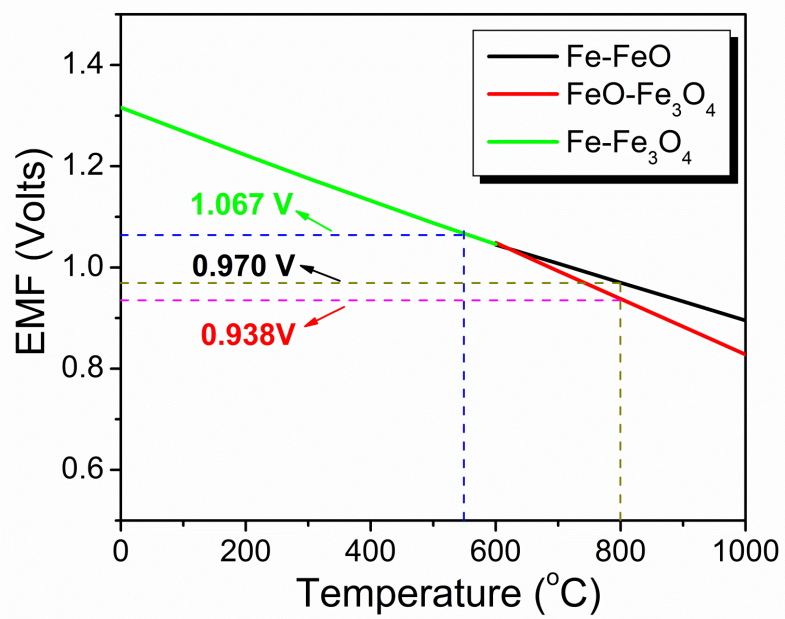

Figure 3.3 Theoretical EMFs of Fe-FeO_x redox couples as a function of temperature[71].

As we discussed in Chapter 2, one key feature of SOMARB is the decoupled design of electrodes and ESU, which avoids volume expansion-contraction of electrodes during electrical cycles. Besides, this feature also allows the new metal-air chemistry to be explored conveniently by simply changing the type of redox couple in ESU. Therefore, we should also look into the phase diagram of other Me/MeO_x redox couples. According to the phase diagram of tungsten-oxygen system shown in Figure 3.4, W-WO_2 is the stable redox couple for energy storage within the temperature window of interest. Similarly, Mo-MoO_2 is the stable redox couple for Mo-based ESU, according to the phase diagram of Mo-oxygen system shown in Figure 3.5.

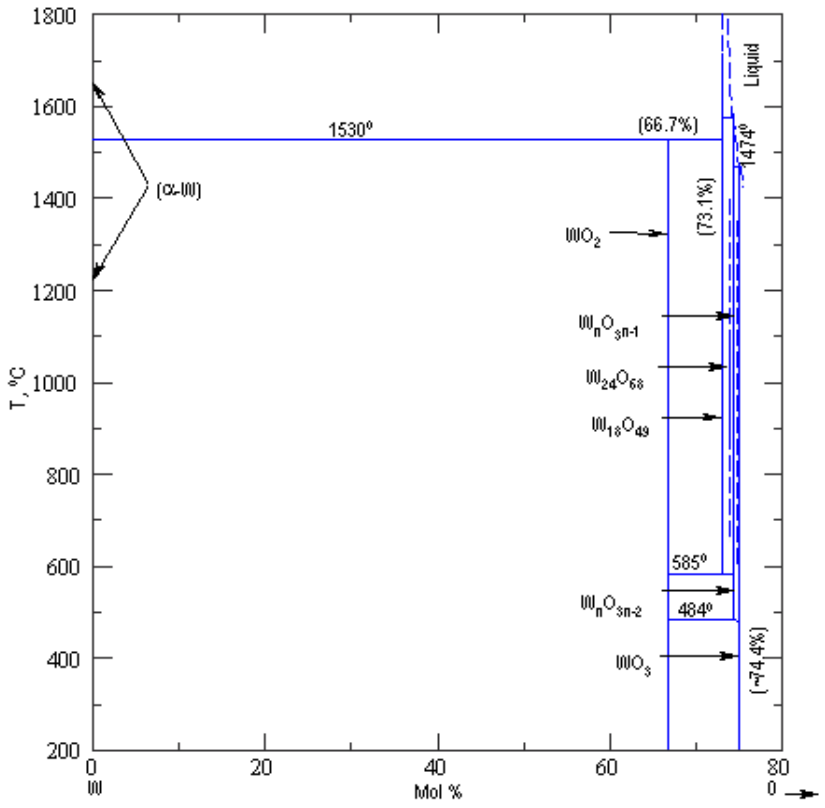

Figure 3.4 Phase diagram of the tungsten-oxygen system[72].

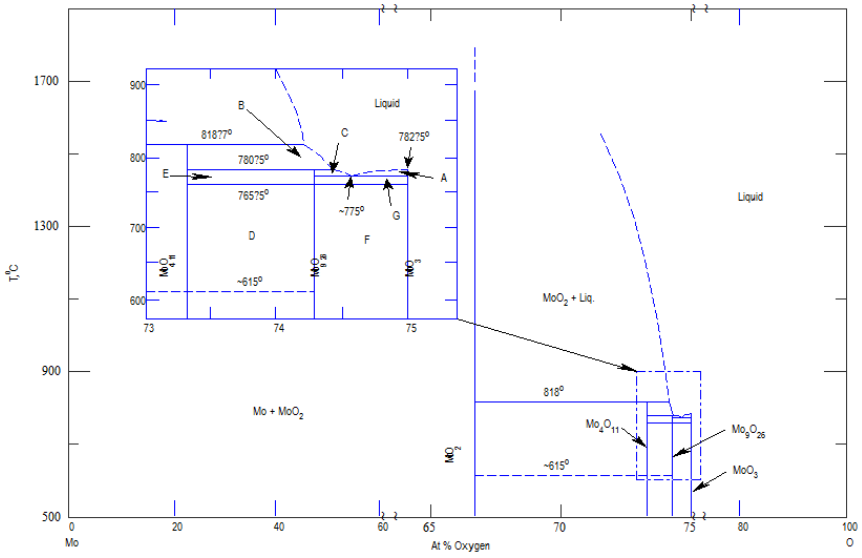

Figure 3.5 Phase Diagram of the Mo-O system[73].

In the following, Ti-, V-, Cr, Mn-, Fe-, Co-, Ni-, Cu-, Mo-, and W- based ESU redox couples would be evaluated from a thermodynamic as well as a perspective. According to their individual phase diagrams,[70, 72-80] the stable redox couples are Ti-Ti_3O_2,[74] V-V_2O_3,[75] Cr-Cr_2O_3,[76] Mn-MnO,[77] Fe-Fe_3O_4 (intermediate temperature)/Fe-FeO (high temperature),[70] Co-CoO,[78] Ni-NiO,[79] Cu-Cu_2O,[80] Mo-MoO_2 [73]and W-WO_2,[72] respectively.

3.2 THE THERMODYNAMIC APPROACH

The thermodynamic properties of metal/metal oxide redox couples determine the maximal voltage (or Nernst potential E_N) and maximum theoretical specific energy (MTSE) and maximum theoretical energy density (MTED) achievable by a SOMARB. Figure 3.6 compares these three important quantities among aforementioned transition-metal and oxide redox couples. The equation for E_N is given by eq. (2.5). The MTSE and MTED calculations follow:

$$MTSE = \frac{\Delta G}{1000\times 3600 \cdot M_{Me}} \tag{3.1}$$

$$MTED = \frac{\Delta G}{1000\times 3600 \cdot M_{Me}} \cdot \rho_{Me} \tag{3.2}$$

Clearly, among these redox couples, Ti-Ti_3O_2 exhibit the highest E_N; V-V_2O_3 has the highest MTSE; and Cr-Cr_2O_3 has the highest MTED. The Cu-Cu_2O redox couple has the lowest E_N, MTSE and MTED. As the temperature decreases, EMF, MTSE and MTED all increase. These trends are more pronounced for Fe-FeO_x based ESU, because the redox

couple Fe-Fe_3O_4 at T⩽600°C has a higher E_N, MTSE and MTED than its counterpart Fe-FeO at T>600°C due to a greater oxygen content in the oxide.

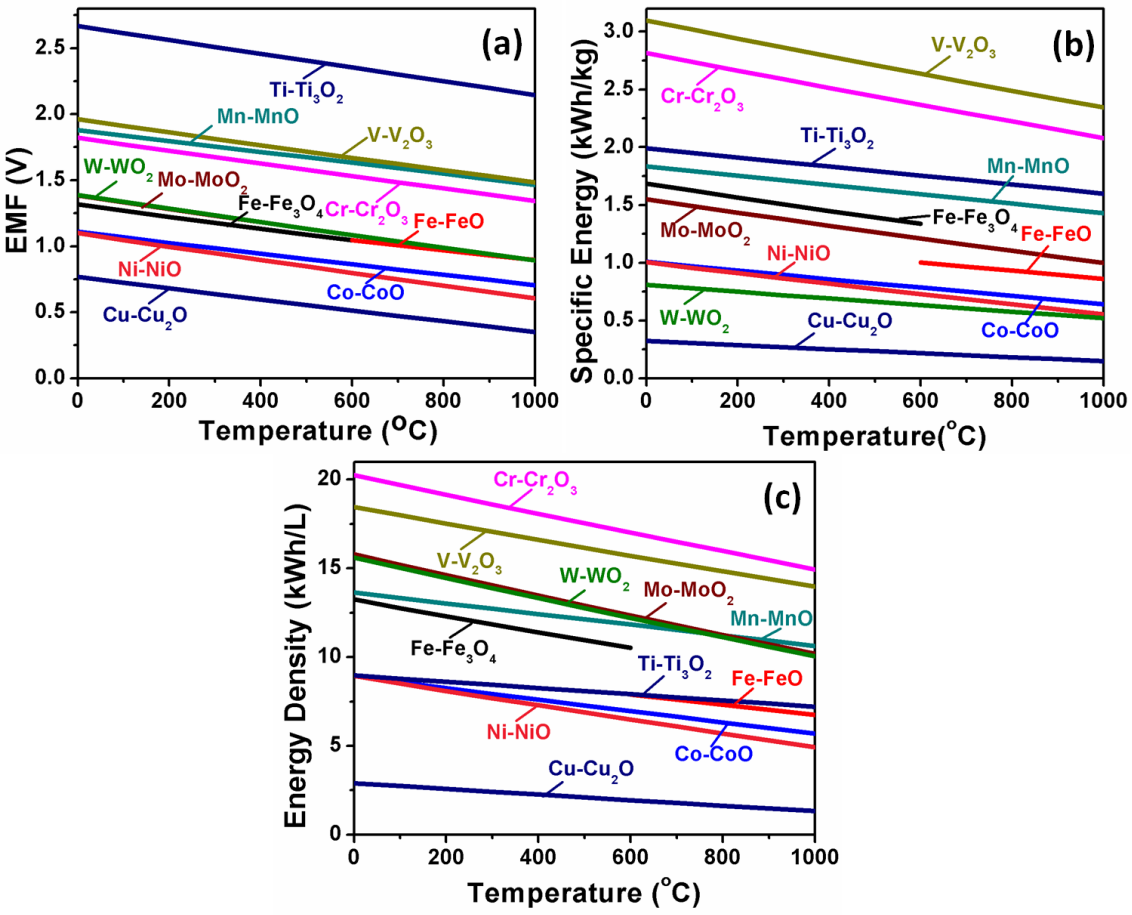

Figure 3.6 Comparisons of (a) E_N, (b) MTSE and (c) MTED among several transition metal-oxide redox-couples calculated for various temperatures.

3.3 THE KINETIC APPROACH

When further compared redox kinetics of these Metal/Metal oxide (Me/MeO_x), we found that several redox couples, for example, Ti-Ti_3O_2, V-V_2O_3, Cr-Cr_2O_3, Mn-MnO, are not able to store sufficient amount of charge carried over and mediated by H_2-H_2O gas due to their unfavorable redox kinetics, despite of their thermodynamic advantages.

Kinetic theory concerned with oxidation of a metal and reduction of a metal oxide generally deals with the relationship between the change of mass and time. Among these relationships, linear or parabolic relationship or a hybrid of the two has been widely reported. It is generally accepted that the linear kinetics is dominant at the early stage when many reactive sites are available for reaction whereas the parabolic kinetics is prevalent at later stage when the reactive sites are limited. In this study, the time scale is varied from 10 minutes to 10 hours. Therefore, parabolic kinetics is a more adequate theory to describe the metal oxidation and oxide reduction processes

$$(\Delta m)^2 = K_p \cdot t \tag{3.3}$$

where Δm is the mass change of the ESU, g/cm^2; K_p is the parabolic rate constant of redox kinetics, g^2/cm^4/sec; t is the time, sec.

In the SOMARB, the oxidation rate of metal is indirectly related to the maximum specific charge (Q_{max}, Ah/g) and the maximum charge density (q_{max}, Ah/L), which follow:

$$Q_{max} = \frac{\Delta m \cdot S_{ESU}}{3600 \cdot M_O} \cdot 2F \cdot x \tag{3.4}$$

$$q_{max} = \frac{\Delta m \cdot S_{ESU}}{3600 \cdot M_O} \cdot 2F \cdot x \cdot \rho_{ESU} \tag{3.5}$$

where M_o is the atomic weight of oxygen, 16 g/mol; x is the oxygen stoichiometry of MeO_x; S_{ESU} is the specific surface area of the redox materials in ESU, cm^2/g; ρ_{ESU} is the

density of the redox materials in ESU, g/cm^3. To be conservative, we chose the density values of metal oxides instead of the metals for the calculation of q_{max}. Substituting eq. (3.3) into eq. (3.4) and eq. (3.5), respectively, leads to Q_{max} and q_{max}:

$$Q_{max} = \frac{2F \cdot x \cdot \sqrt{K_p \cdot t}}{3600 \cdot M_O} \cdot S_{ESU} \tag{3.6}$$

$$q_{max} = \frac{2F \cdot x \cdot \sqrt{K_p \cdot t}}{3600 \cdot M_O} \cdot S_{ESU} \cdot \rho_{ESU} \tag{3.7}$$

The equivalent maximum current density, J_{max} (A/cm^2), of RSOFC then equals:

$$J_{max} = \frac{3600 \cdot Q_{max}}{t \cdot S_{RSOFC}} \cdot m_{ESU} = \frac{3600 \cdot q_{max}}{t \cdot S_{RSOFC}} \cdot \frac{m_{ESU}}{\rho_{ESU}} = \frac{2F \cdot x \cdot \sqrt{K_p / t}}{M_O \cdot S_{RSOFC}} \cdot (S_{ESU} \cdot m_{ESU}) \tag{3.8}$$

The J_{max}, Q_{max} as well as q_{max} among those aforementioned transition metal-metal oxide redox couples at 800^{o}C and 550^{o}C achievable for each transition metal redox couple are plotted in Figure 3.7. It should be noted that $(S_{ESU} \cdot m_{ESU})/S_{RSOFC}$ is set to 10/1 at 800^{o}C and 1000/1 at 550^{o}C as a conservative measure for all the calculations. Due to the scarcity of kinetic rate constants related to metal oxidation in H_2O-H_2 mixture, all the k_p values were collected from experiments conducted in air (otherwise pointed out). Table 3.1 lists these K_p values and their sources. The rate of metal oxidation in steam is expected to be higher than that in air because the former has a faster surface kinetics and produces a relatively more porous scale than the latter [81]. Therefore, the calculations are deemed conservative.

Among all the redox couples analyzed, Fe/FeO_x and $W\text{-}WO_2$ and $Mo\text{-}MoO_2$ stand out to be the most kinetically favorable redox couples with high current density, high specific charge and high charge density. In addition, Fe-based, W-based and Mo-based ESU redox couples are all important industrial materials with abundant storage on the earth, and they are non-toxic and environmentally friendly. Therefore, my dissertation first selected the most cost-effective solid oxide iron air battery (SOFeARB) containing Fe-based ESU (Fe-FeO at 800^{o}C and $Fe\text{-}Fe_3O_4$ at 550^{o}C) as a model system to study the energy storage characteristics of this class of SOMARBs operated at high temperature (=800^{o}C) and at intermediate temperature (=550^{o}C). Solid oxide tungsten air battery (SOWARB) operated at 800^{o}C and solid oxide molybdenum air battery (SOMoARB) operated at 550^{o}C have also been investigated to exploit the kinetic advantages inherited from W/WO_2 and Mo/MoO_2 redox couples predicted by Figure 3.7.

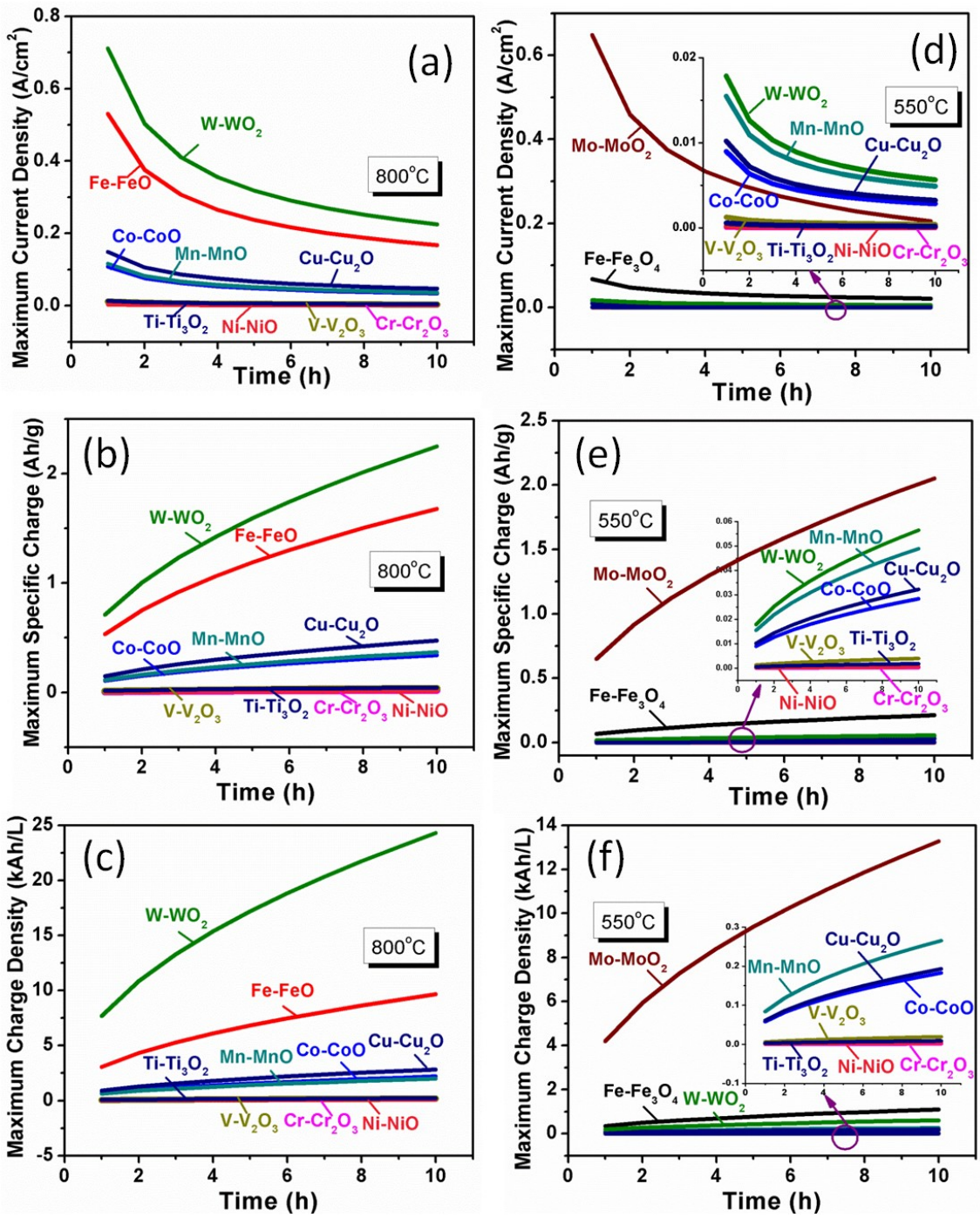

Figure 3.7 Comparisons of (a) maximum current density and (b) maximum specific charge and (c) maximum charge density among several transition metal-oxide redox-couples at 800°C and these corresponding values in (d), (e), and (f) at 550°C. (Note: $(S_{ESU} \cdot m_{ESU})/A_{RSOFC}$ are set to 10/1 and 1000/1 as a realistic ratio after comparing with the experimental data).

Table 3.1 Origins and calculation methods for K_p values

ESUs	Equations for K_p ($g^2/cm^4/s$)	Ref
Ti-Ti_3O_2	K_p=0.16 exp (-45,000/R/T), 550-850°C	[82]
V-V_2O_3	K_p=1.3×10^{-3} exp(-30,700/R/T), 400-600°C (in O_2) K_p=0.94×10^{-5} exp(-31,400/R/T), 600-900°C (in N_2)	[83]
Cr-Cr_2O_3	K_p=61.5 exp (-64,630/R/T)	[84-86]
Mn-MnO	K_p=1.95×10^{-3} exp (-28,300/R/T), 400-1200°C	[87]
Fe-FeO **Fe-Fe_3O_4**	K_p=0.37 exp(-33,000/R/T), 500-1100°C	[88]
Co-CoO	K_p=4.1×10^{-6} exp(-20,000/R/T), 400-700°C K_p=6.4×10^4 exp(-65,500/R/T), 700-1200°C	[89, 90]
Ni-NiO	K_p=8×10^{-4} exp(-41,200/R/T), 400-850°C	[91]
Cu-Cu_2O	K_p= 1.5×10^{-5} exp(-20,140/R/T), 300-550°C K_p= 0.266 exp(-37,700/R/T), 550-900°C	[88]
Mo-MoO_2	2.6042E-08 (550°C)	[92, 93]
W-WO_2	3.13E-08 (800°C); 1.97E-11 (550°C)	[94, 95]

Note: Here R=1.986 cal/K/mole

3.4 SUMMARY

Power enhancement of RSOFC and adequate redox-couple selection for ESU are two important elements in the development of SOMARB. The former can improve the overall performance of the SOMARB through reducing resistance whereas the latter can improve via promoting the redox kinetics. Simultaneous achievement of the two can lead to the lowering of SOMARB's operating temperature, thus increasing the reliability and durability. While the power enhancement of RSOFC has been an intensely studied subject in fuel cell research, proper selection of redox couple materials represent a challenge to the SOMARB research. Balancing thermodynamic and kinetic properties of the redox-couple based energy storage materials is deemed a general guidance toward the success. Other properties to be considered include cost, environmental impact, suitability and safety. For my research work, Fe-FeO_x redox couple has been chosen as the baseline for characterizing the performance of the first-generation SOMARB. W-WO_2 and Mo-MoO_2 redox couples are also investigated to fully exploit their thermodynamic and kinetic advantages.

CHAPTER 4

MATERIALS SYNTHESIS, BATTERY ASSEMBLY AND PERFORMANCE EVALUATION METHODOLOGIES

This chapter describes the experimental details in fabricating and testing the new SOMARB.

4.1 MATIRALS SYNTHESIS

4.1.1 The ESU redox couples

4.1.1.1 Co-precipitated and pelletized Baseline Fe-based ESU

Due to its unique thermodynamic and kinetic advantages, Fe-based redox couples are selected as the baseline model ESU for the dissertation work[66]. To prepare a functional and durable Fe/FeO_x redox couple, the initial Fe_2O_3 was intimately mixed with ZrO_2 by a co-precipitation method in a molar ratio of Fe_2O_3:ZrO_2=85:15. The role of ZrO_2 is to mitigate the coarsening of Fe-particles during redox cycles but not interfere with the redox reaction occurring in the system. The nanosized Fe_2O_3 and ZrO_2 mixture powders were prepared by co-precipitating 0.1 M of aqueous solution containing $Fe(NO_3)_3 \cdot 9H_2O$

(Alfa Aeasar, 98.0-101.0%) and $ZrO(NO_3)_2 \cdot xH_2O$ (Alfa Aeasar, 99.9%) with $(NH_4)_2CO_3$. The molar ratio was kept as $n_{(NH_4)_2CO_3} : n_{M^{n+}} = 2.5:1$, where M^{n+} represents the combined Fe and Zr cations. The obtained co-precipitate was then filtered, washed, dried, ground and finally sintered at 600°C for 2h to convert it into the oxides. The decomposed oxide powders were then ball-milled to break up the agglomerates, followed by mixing with a microcrystalline cellulose pore-former (type NT-013, FMC Corp.) in a volume ratio of 1:1. The final pellets were made by pressing the powder into Φ1/2" pellets and sintering at 1000°C for 1 h. All above heat treatments were conducted in open air.

4.1.1.2 CeO_2-modified Fe-based ESU

To study the effect of catalyst on the redox kinetics of Fe-Fe_3O_4, CeO_2 nanoparticles were dispersed into the aforementioned Fe_2O_3/ZrO_2 granules by solution infiltration technique. To be specific, a 2.0 M aqueous solution of $Ce(NO_3)_3 \cdot 6H_2O$ mixed with a dispersant Triton-X100 (3 wt%) was impregnated into the porous Fe_2O_3/ZrO_2 under a vacuum condition for 8 times. For each impregnation, there was a 100°C-drying and 500°C-calcination step. The final CeO_2 nanoparticles dispersed Fe_2O_3/ZrO_2 was obtained by firing the mixture at 600°C in air for 1 h. The final weight pickup was estimated around 4.5%[96].

4.1.1.3 ZrO_2-supported Fe-based ESU

The effect of surface area of active metals on the redox kinetics was also investigated. To

acquire fine particles of Fe, an aqueous solution of $Fe(NO_3)_3$ was infiltrated into a commercial porous ZrO_2 catalyst support (Alfa Aesar, surface area: $51g/m^2$) using a modified one-step infiltration procedure [97, 98]. Specifically, a 2 M $Fe(NO_3)_3$ aqueous solution was first mixed with Triton-X100 (3 wt%) in DI water, into which the porous ZrO_2 pellets were immersed. During the soaking, the solution was gradually heated to 80^oC while the air trapped in the porous ZrO_2 pellets was driven out of the solution, allowing the maximum loading of Fe into the pores of ZrO_2. When no bubbles were visible and the solution finally became viscous, the ZrO_2 pellets filled with $Fe(NO_3)_3$ were then removed, followed by drying at RT and finally calcining at 600^oC for 2 h. The final weight gain in term of Fe was estimated to be 10% [96].

4.1.1.4 Carbothermic reaction derived Fe-based ESU

The Fe-based ESU was also synthesized by conventional carbothermic reaction as described as follows. To distinguish this ESU with the baseline ESU, the new ESU was termed Fe/C-ESU, and the corresponding battery is termed solid oxide Fe/C-air redox battery (SOFeCARB). The starting materials for the reaction are the co-precipitated Fe_2O_3-ZrO_2 powder and carbon black (Fisher Scientific). The two powders were first intimately mixed in an atomic ratio of Fe:C=1:4.2, followed by ball milling in alcohol. The excess stoichiometry of C was intentional to ensure a full reduction of Fe_2O_3 to Fe. The mixed/milled powders were then dried, and pressed into pellets. The pellets were then reacted at 1000^oC for 10h in a flowing N_2 at 100sccm. The final product contains Fe, C, and

ZrO_2 as verified by XRD and SEM/EDS to be shown in Chapter 5.

The iron carbothermic reaction can be described as follows:

$$C + Fe_2O_3 = Fe + CO_2 \quad (4.1)$$

$$CO_2 + C = 2CO \quad (4.2)$$

An Ellingham diagram is constructed from thermodynamic data and shown in Figure 4.1. It is evident that a temperature above 750°C would lead to a full reaction of carbon with iron oxides, resulting in metallic iron. The reaction temperature of 1000°C employed in this study is sufficiently high to reduce iron oxide into metallic iron by carbon. In addition to the solid products, CO and CO_2 are the gaseous products constantly removed by the carrier gas N_2 during the reaction.

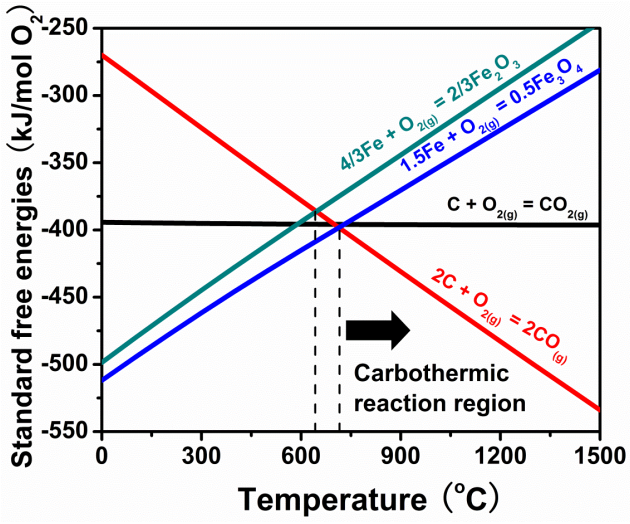

Figure 4.1 Ellingham diagram of Fe-C-O system.

To determine the carbon contents in a Fe/C-ESU, either as-synthesized or tested, a simple chemical analysis method was used. The sample was first weighed and then soaked

in a diluted nitric acid (20 vol %) in a beaker. After approximately one week, all Fe were sure to completely dissolve in the acid, only ZrO_2 and C were left on the bottom of the beaker. After a thorough rinsing with DI water, the residual solids were dried and weighed again. Since the ratio between Zr and Fe was previously known, the content of C in the original sample can then be easily calculated out. The determined C content in the as-synthesized Fe/C-ESU was 37%. After test, there was roughly 15% C less in the ESU. A thermodynamic analysis of the equilibrium compositions of the system seems to support the observation. Figure 4.2 shows that an oxidation of C into CO and CO_2 could occur at above 450°C.

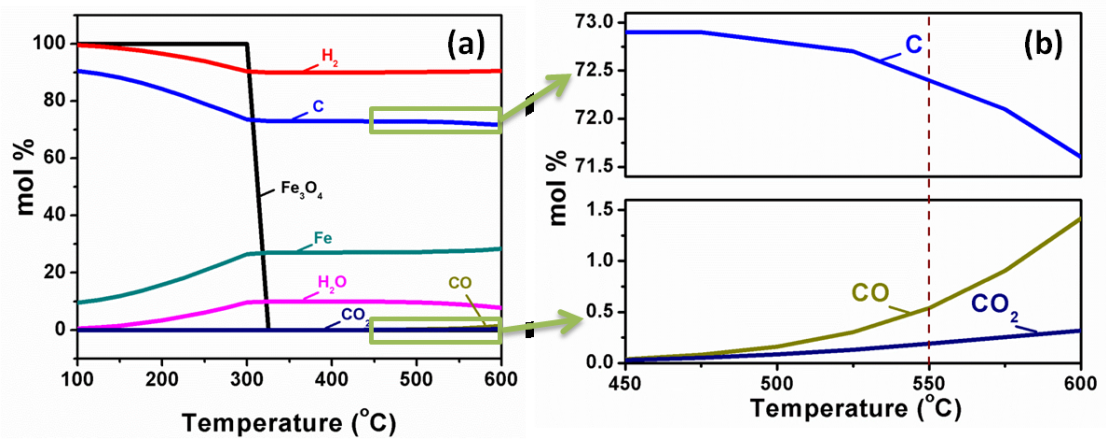

Figure 4.2 Equilibrium compositions as a function of temperatures of (a) all the relevant components and (b) carbon-related components in a simulated environment to the Fe/C-air battery

4.1.1.5 W-based ESU

The functional redox precursor WO_3 in the W-based ESU was from a commercial source (Fisher Chemicals). The commercial WO_3 was first ball-milled into fine particles,

followed by mixing with a microcrystalline cellulose pore-former (type NT-013, FMC Corp.) in a volume ratio of 1:1. Rectanglar bars were then pressed from the powders and sintered at 1100^{o}C for 2h. All heat treatments were conducted in open air. The sintered bars were broken into granules in 9-16 mm^2 by 2 mm. To compare the W-air redox battery with this W-ESU, we also tested the baseline iron-air battery with the baseline Fe-based ESU as described in 4.1.1.1. The results will be discussed and compared in Chapter 7[99].

4.1.1.6 Mo-based ESU

The functional redox precursor MoO_3 in the Mo-based ESU was taken from commercial Molybdenum Trioxide (MP Biomedicals, LLC). The MoO_3 was first ball-milled into fine particles, followed by mixing with V-006A (Heraeus) to form a paste. The paste was then screen-printed on to a Ni-foil support, and calcined in open air at 650^{o}C for 2h. For comparison purpose, the Fe-based baseline ESU was synthesized from the co-precipitation method as described in 4.1.1.1. Thus obtained Fe_2O_3-ZrO_2 (Fe:Zr=85:15, atomic ratio) powders were then ball-milled to break up the soft agglomeration, followed by mixing with V-006A (Heraeus) to form the Fe-based paste. The paste was then screen-printed on to a Ni-foil support. The paste was finally calcined in open air at 650^{o}C for 2h. After that, CeO_2 nanoparticles were dispersed into the aforementioned Fe-based paste as previously described.

4.1.2 RSOFC functional materials

4.1.2.1 Commercial anode-supported tubular RSOFC

A commercially available anode-supported tubular RSOFC was used in a tubular SOFeARB. The tubular anode Ni-YSZ/YSZ (CoorsTek) has a 10 mm in OD, 1.25 mm in wall thickness and 40 mm in length. The resultant effective cell surface area is 4.78 cm^2. A cross-sectional view of the anode/electrolyte microstructure after reduction is shown in Figure 4.3 (a), where an approximately 25 μm-thick YSZ electrolyte on the anode is shown with a reasonably good porosity and pore size. A composite cathode ink consisting of GDC ($Ce_{0.8}Gd_{0.2}O_2$) and LSCF ($La_{0.6}Sr_{0.4}Co_{0.2}Fe_{0.8}O_{3-\delta}$) (from LSCFGDC-1, Fuel Cell Materials) was then applied to the outer surface of the cell and calcined at 1050°C for 1 h in open air. The currents were collected by silver wires attached on the outer surface of the cathode and the end of anode as shown in Figure 4.3 (b). To ensure good electrical contacts, a layer of silver prepared from silver paste (C8829, Heraeus) was coated prior to attaching the silver wires.

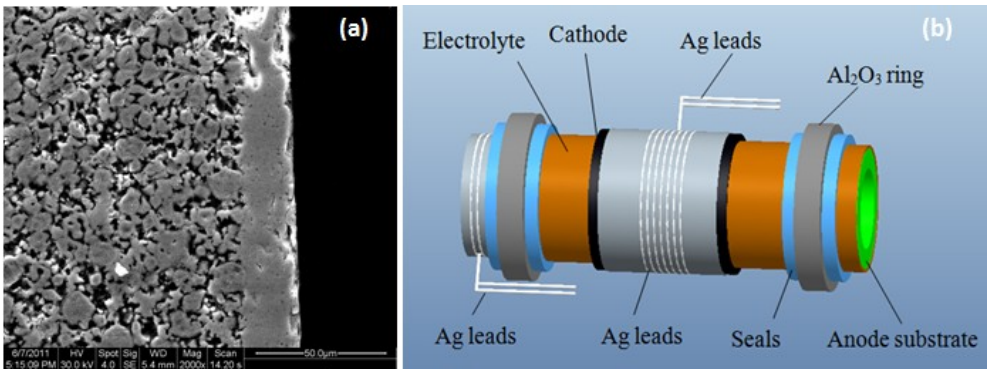

Figure 4.3 (a) Microstructure of an anode-supported tubular RSOFC employed in this study (b) A single battery cell subassembly[68].

4.1.2.2 Commercial electrolyte-supported planar RSOFC

We also examined a planar SOFeARB. Typically, a planar RSOFC outperforms its tubular counterpart due to its shorter current path length. This change also allows us to study the energy storage characteristics at higher current densities. Therefore, a planar SOFeARB is valuable to reveal the key attributes and understand the potentials of the new battery over a broad perspective. Similar commercial planar RSOFC has also been used for SOWARB. The compositions of the RSOFCs from a commercial NextCells as listed in Table 4.1.

Table 4.1 Compositions and dimensions of the commercial NextCells [100]

Component	Composition	Thickness (μm)
Fuel electrode	Ni-YSZ/Ni-GDC (interlayer)	50
Electrolyte	Hionic ZrO_2-based	150(+/-15)
Air electrode	LSM/LSM-GDC(interlayer)	50

4.1.2.3 Composition optimization of the O^{2-} conducting electrolyte

In a SOMARB, the O^{2-} conducting electrolyte is critical to determine the RSOFC performances. In our early work, YSZ-based commercial RSOFCs were employed in the battery tests. However, at intermediate temperatures (550-650^{o}C), the low conductivity of YSZ would lead to high ohmic resistance. Therefore, we have to find a better alternative.

Sr- and Mg-doped $LaGaO_3$ of general formula $La_{1-x}Sr_xGa_{1-y}Mg_yO_{3-(x+y)/2}$ (LSGM) is so far the best fast oxide-ion conductor discovered in perovskite-structured oxides [101-103]. Its oxide-ion conductivity at 600^{o}C is equivalent to that of the state-of-the-art electrolyte 8mol%Y_2O_3-doped ZrO_2 (YSZ) at 800^{o}C, and stable over a broad range of oxygen partial pressures (from pure O_2 to pure H_2), making it an ideal electrolyte for intermediate-temperature solid oxide electrochemical cells (IT-SOECs), including our battery system[96, 104, 105]. However, Ga_2O_3 is an expensive chemical, which can be as high as $10,000/kg for 99.99%'s purity. For an LSGM with the optimal composition (e.g., x=0.20, y=0.17), Ga_2O_3 accounts for nearly one-third of its weight. The concern of Ga_2O_3's high cost and high usage has driven us to lower the cost of LSGM by increasing the doping level of Mg(y) so as to lower the Ga usage. However, too high an Mg-doping level could drastically decrease LSGM's oxide-ion conductivity due to the formation of second phase as well as dopant-vacancy ($2Mg'_{Ga} - V_O^{\bullet\bullet}$) clusters. Our previous study has shown that the optimal stoichiometric Mg-doping level for which a single phase is prevalent and oxide-ion conductivity peaks is at y=0.17[102]. This limitation has prompted the search for alternative approach to lowering the usage of Ga, one of which under consideration in this study is to have Mg doped on Ga-site in an excess ratio, *i. e.*, $La_{1-x}Sr_xGa_{1-y}Mg_{y+z}O_{3-\delta}$.

The practice of nonstoichiometric doping in perovskite structure of ABO_3 has been widely reported in the literature[106-109], thanks to the structural versatility of ABO_3 that allows the host A and B cations to be substituted by a variety of cations with a range of ratios as long as the Goldschmidt's tolerance rule is satisfied[110]. The beneficial effects of

the nonstoichiometric doping have been observed in enhancing conductivity (either ionic or electronic) [107, 108, 110] and promoting sintering[109]. However, the effect of excess Mg-doping on conductivity of LSGM has never been reported.

A concurrent benefit from excess Mg-doping is the potential to improve the mechanical strength of LSGM. Lower mechanical strength of LSGM than YSZ has been previously reported and is another concern for LSGM to be a practically viable electrolyte for commercial devices [111-113]. Among the constituent oxides in LSGM, MgO is the strongest oxide, the elastic modulus of which is ~310 GPa, almost twice as high as that of LSGM[113, 114]. Incorporation of MgO into LSGM, whether into the lattice or along the grain-boundary, is expected to increase the mechanical strength of the final LSGM product. The enhanced mechanical strength of Al_2O_3 by MgO is a convincing example illustrating the role of MgO as a strength reinforcement agent[115]. Since MgO is an inexpensive and widely available ceramic material, and perovskite structure allows for nonstoichiometric doping, it becomes a rational approach to dope excess Mg on the Ga-site to simultaneously lower the cost and increase the strength of an LSGM. In this subchapter, we report a systematic study on the effects of excess Mg-doping on the phase relationship and electrical properties of an LSGM.

Conventional solid-state reaction method was used to synthesize Mg-excess LSGM. The starting materials of La_2O_3 (>99.99% purity, Alfa Aesar), $SrCO_3$ (>99.9% purity, Alfa Aesar), Ga_2O_3 (>99.99% purity, GFI), and MgO (>99.99% purity, Alfa Aesar) were weighed according to the stoichiometry of $La_{0.8}Sr_{0.2}Ga_{0.83}Mg_{0.17+z}O_{3-\delta}$ (z=0.00, 0.03, 0.05,

0.07, 0.10). The selection of $La_{0.80}Sr_{0.20}Ga_{0.83}Mg_{0.17}O_{3-\delta}$ as the baseline material is based on our previous work showing that this composition has the highest oxide-ion conductivity[102]. To ensure the accuracy of the stoichiometry of La and Mg in LSGM, the starting hygroscopic La_2O_3 and MgO were pre-calcined at 1000°C for 5 hours prior to actual weighing to remove any non-oxide components. After pre-calcination, the La_2O_3 and MgO powders were weighted shortly after they were taken out of furnace at 600°C. The weighed powders were then intimately mixed in an agate mortar with the aid of acetone. Pellets were subsequently pressed under a pressure of 200 MPa and fired at 1250°C for 10 hours. The partially reacted samples were then broken up, reground and ball-milled before cylindrical bars (ϕ5 mm in diameter and 10–12 mm in length) were pressed and finally sintered at 1420°C for 5 hours.

In order to reveal grains, grain-boundaries as well as second phases, the sintered samples were first polished (final polishing grid was 1 micron), followed by thermally etching at 1350°C for 1 hour. In some cases, the thermally etched samples were quenched from 800°C to reserve the microstructure at that temperature. A field emission scanning electron microscope (FESEM, Zeiss Ultra) equipped with an EDS capability was employed to observe microstructures and analyze the local chemical compositions of the thermally etched samples. The phase purity of the final products were also examined by powder X-ray diffraction (PXRD) using an X-ray diffractometer (D/max-A, Rigaku, Japan) with graphite-monochromatized CuKα radiation (λ=1.5418 Å). The XRD scan was performed at a rate of 5^o min^{-1} from $2\theta = 20^o$ to 80^o, the spectrum of which was analyzed

with the JADE (MDI) software to identify phase compositions.

The oxide-ion conductivity of the as-sintered bar samples was measured with an impedance cell consisted of a symmetrical electrode configuration. The electrode material of choice for this study is a silver coating prepared from a commercial silver paste (Heraeus C8829). The measuring conditions included a constant flowing air at 50 sccm and temperature range from 350 to 800^{o}C. AC impedance spectroscopy was the primary tool to evaluate the oxide-ion conductivity of LSGM electrolytes. With a Solartron 1260/1287 Electrochemical System, a typical impedance measurement was performed under a frequency range of 0.1Hz - 750kHz and an AC perturbation amplitude of 10mV, the spectrum of which was then used to extract the total and grain-boundary conductivities if possible.

The SEM micrographs of thermally etched $La_{0.80}Sr_{0.20}Ga_{0.83}Mg_{0.17+z}O_{3-\delta}$ (z=0.0-0.1) are shown in Figure 4.4. All of the samples seem to exhibit a well-sintered, dense microstructure. The difference is that the baseline sample, Figure 4.4 (a), shows a cleaner and more distinctive grain boundaries than the Mg-excess samples that, starting from Figure 4.4 (c) to (e), exhibit an increased appearance of the second phase (dark spots) along the grain-boundaries with increasing the level of Mg-excess.

The EDX analysis of regularly furnace-cooled sample (z=0.10) indicates that the second phase on the grain-boundaries is Mg-enriched. However, XRD patterns of all the five Mg-excess LSGM compositions shown in Figure 4.5 failed to discern the second phase, implying that the amount of the second phase in these samples could be below the

detection limit of XRD, *e. g.*, 2 wt%.

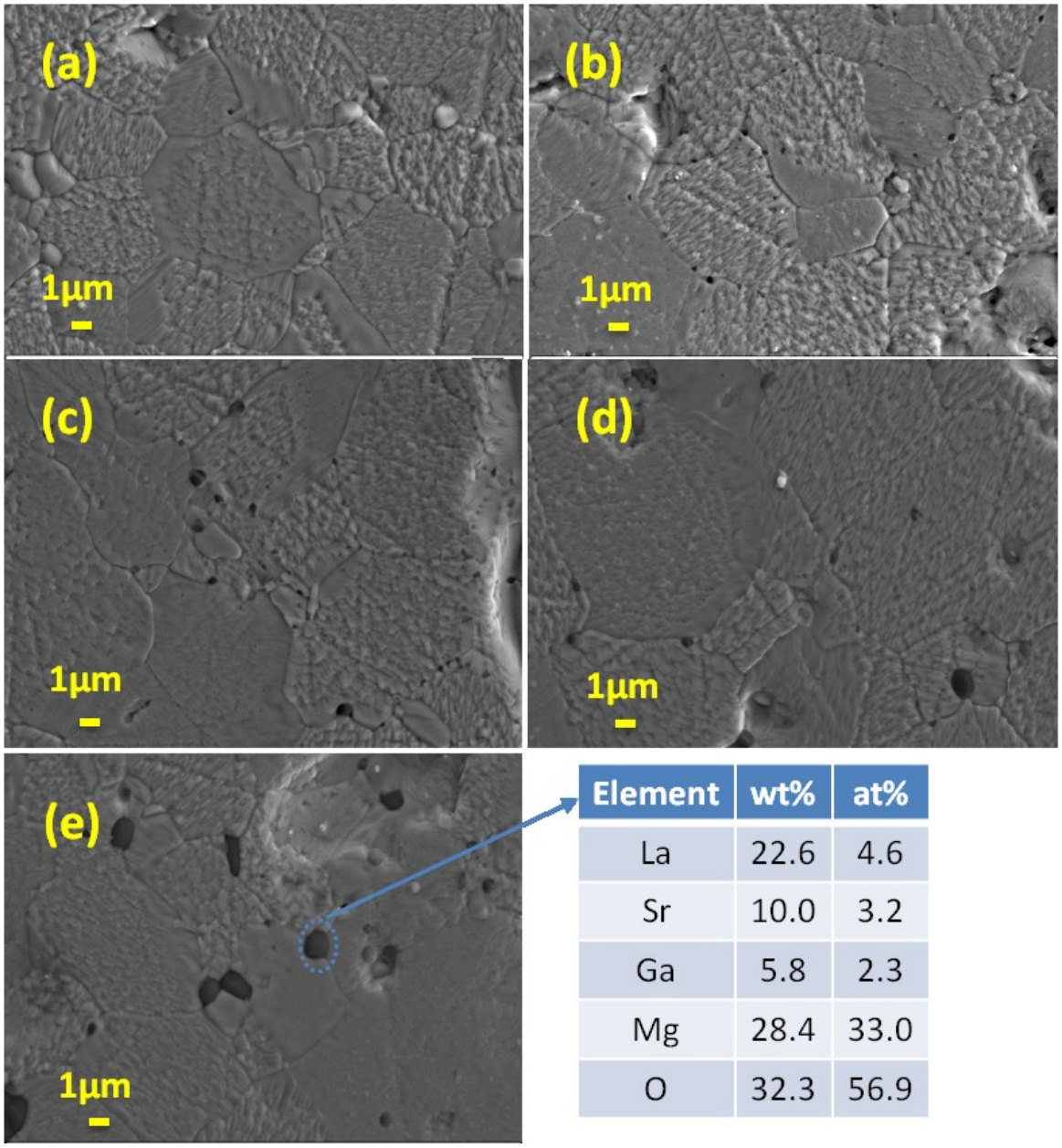

Element	wt%	at%
La	22.6	4.6
Sr	10.0	3.2
Ga	5.8	2.3
Mg	28.4	33.0
O	32.3	56.9

Figure 4.4 SEM micrographs of $La_{0.8}Sr_{0.2}Ga_{0.83}Mg_{0.17+z}O_{3-\delta}$ (a) z=0.00; (b) z=0.03; (c) z=0.05; (d) z=0.07; (e) z=0.10; The EDX analysis was performed on a regularly furnace-cooled sample[116].

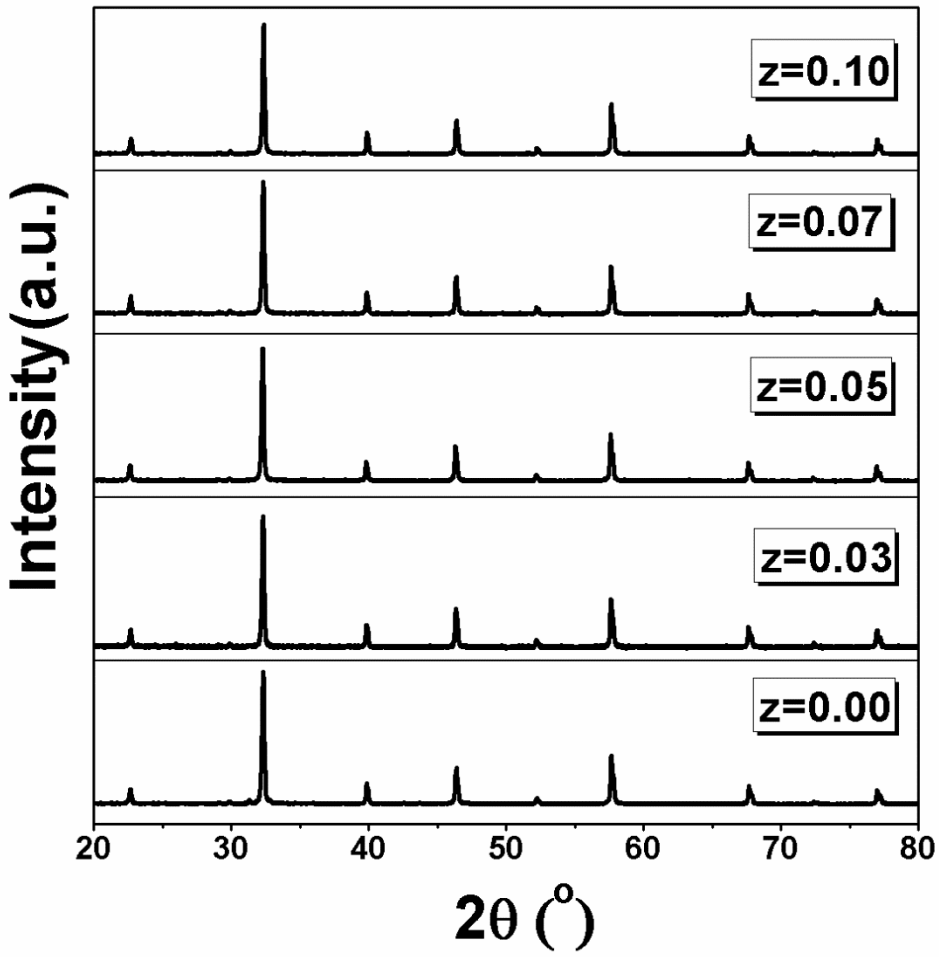

Figure 4.5 Powder XRD patterns of $La_{0.8}Sr_{0.2}Ga_{0.83}Mg_{0.17+z}O_{3-\delta}$[116].

The evolution of AC impedance spectra with temperature of all the samples is shown in Figure 4.6. The overall spectra can be generally characterized by relevant physical/ chemical processes involving inductance, grain, grain-boundary and electrode reaction. The highest-frequency inductance effect with positive imaginary component is a sign of interferences from the measuring leads subject to a magnetic field created by the furnace (a coiled heater), while the lowest-frequency spectrum is related to the O_2/Ag/LSGM electrode interface. The semicircle of intermediate frequency with nonzero intercept on the z'-axis belongs to the "grain boundary effect" in the spectrum, the diameter of which

is the grain-boundary resistance. The higher-frequency intercept of the grain-boundary semicircle represents the grain resistance. What really distinguishes the spectrum is in the intermediate-frequency range where grain and grain-boundary effects are prevalent. For instance, from 417 to 511^{o}C, the grain-boundary effect is clearly visible in a frequency range of 15~750 kHz. Above 602^{o}C, however, this grain-boundary effect becomes less apparent (vanished in some cases). This observation seems to suggest that the Mg-rich grain-boundary material becomes either more conductive or re-dissolved into grains at elevated temperatures. This hypothesis will be used as the basis to interpret the compositional effect on the total conductivity in the following. Since only the total conductivity of samples can be extracted from the spectrum with a greater confidence over the entire temperature range studied, only total conductivity is considered during the discussion.

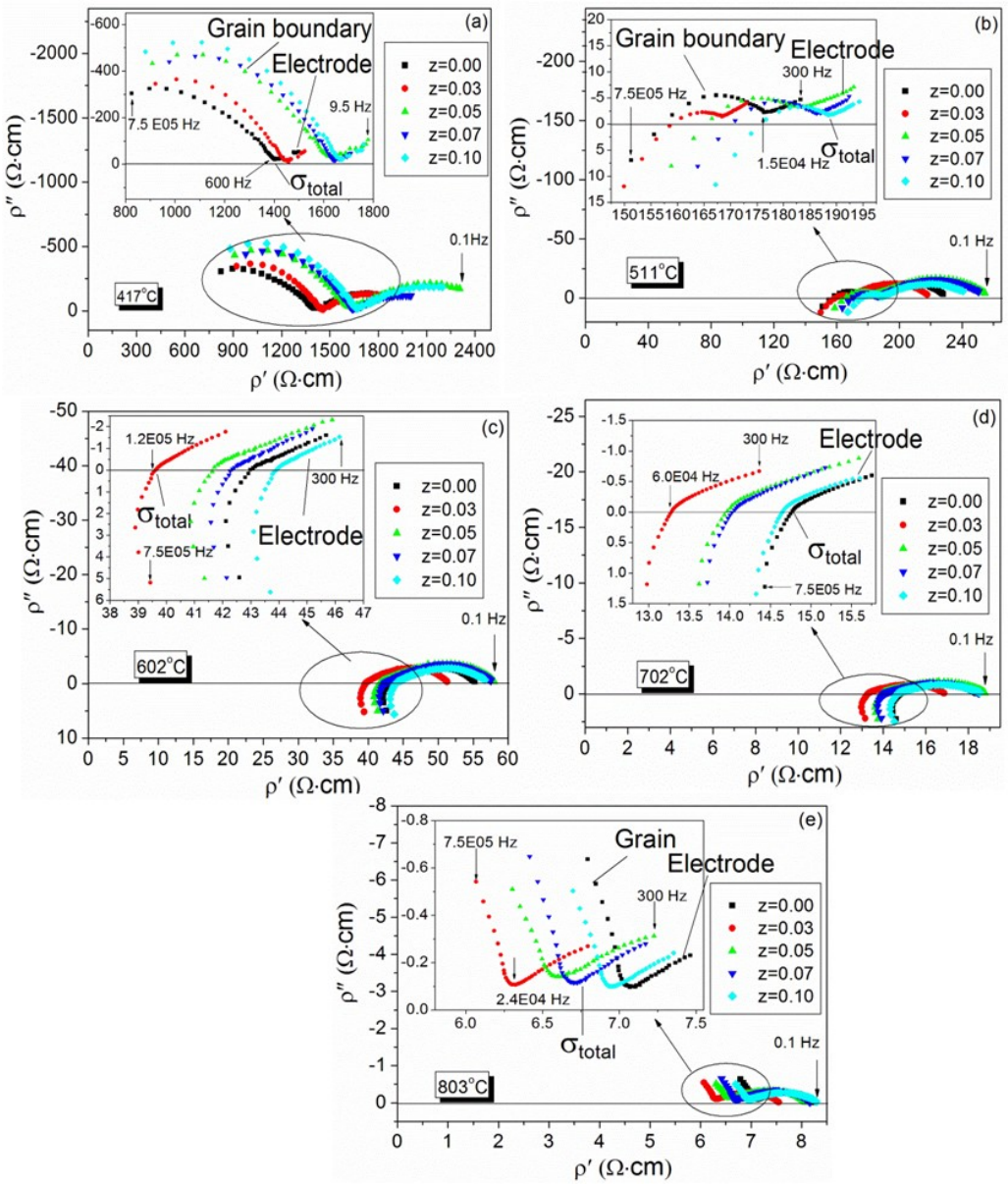

Figure 4.6 AC impedance spectra measured in air and at (a) 417°C, (b) 511°C, (c) 602°C, (d) 702°C and (e) 803°C[116].

The effect of Mg-excess level on the total conductivity σ (or resistivity ρ) is also noticeable from the impedance spectra of Figure 4.6. One clear trend is that the Mg-excess samples become more and more conductive compared to the baseline as the temperature increases. Extracted from Figure 4.6, the total conductivity of LSGM at different z-composition and temperatures is displayed in Figure 4.7. It becomes quite

clear that the order of total conductivity among all the samples varies systematically with the temperature. For example, at 417°C this order is $\sigma_{z=0.00}>\sigma_{z=0.03}>\sigma_{z=0.05}>\sigma_{z=0.07}>\sigma_{z=0.10}$; it changes to $\sigma_{z=0.03}>\sigma_{z=0.00}>\sigma_{z=0.05}>\sigma_{z=0.07}>\sigma_{z=0.10}$ at 511°C and $\sigma_{z=0.03}>\sigma_{z=0.05}>\sigma_{z=0.07}>\sigma_{z=0.00}>\sigma_{z=0.10}$ at 603°C. Above 702°C, the conductivity of all the Mg-excess samples surpasses the baseline (stoichiometric LSGM): $\sigma_{z=0.03}>\sigma_{z=0.05}>\sigma_{z=0.07}>\sigma_{z=0.10}>\sigma_{z=0.00}$. From these data, two questions arise: 1) why does the conductivity of Mg-excess LSGM become systematically higher than the baseline LSGM as the temperature increases? 2) why does z=0.03 composition have the highest conductivity among all the Mg-excess samples?

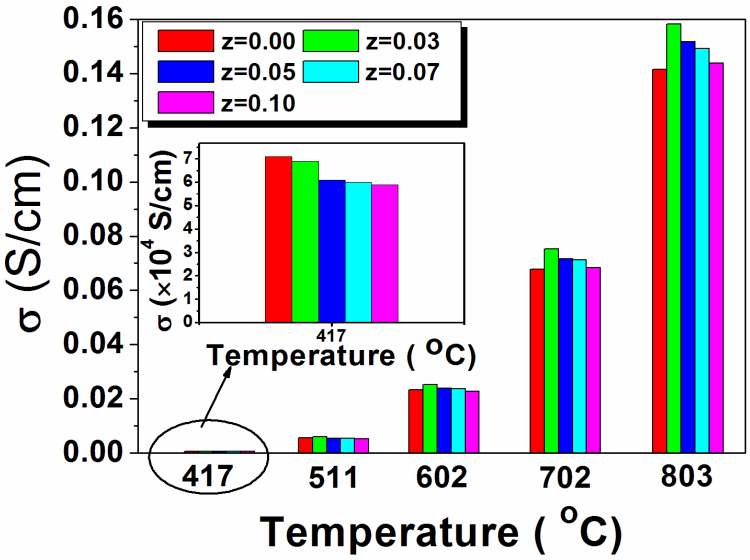

Figure 4.7 Compositional effect of Mg-excess on the total conductivity of LSGM as the temperature changes[116].

To address the first question, we recall Figure 4.6 where a systematic increase of the total conductivity of the Mg-excess samples is accompanied by a gradual disappearance of grain-boundary effect from the impedance spectrum as the temperature increases. This

progressive disappearance of the grain-boundary effect seems to suggest that the Mg-rich grain-boundary phase may re-dissolve into lattice and become more conductive at higher temperatures. To verify this hypothesis, we performed EDX analysis on the samples directly quenched from 800^{o}C, the result of which was then compared with that of regularly furnace-cooled samples. Figure 4.8 shows the microstructures of one Mg-excess LSGM sample, z=0.10, after being quenched from 800^{o}C and furnace-cooled. Other than that the quenched sample exhibits more amorphous appearance in grains than the furnace-cooled sample, there is no apparent difference between the two samples. However, the EDX compositional analysis is much more revealing. Table 4.2 lists the normalized local compositions at three representative areas: Area 1-grain-boundary (dark phase); Area 2-grain with smooth appearance; Area 3: grain with amorphous (wavy) appearance. In general, there are no significant differences in compositions of Area 2 and Area 3 for each individual sample, suggesting that they are the same type of grains in nature. Therefore, no distinction is further made between Area 2 and 3 in the following discussion. However, there exists a great deal of compositional difference in all areas between the quenched and furnace-cooled samples. In Area 1 (the grain-boundary phase), the EDX analysis shows the grain-boundary comprising of a noticeable amount of La, Ga and Mg for the quenched sample whereas mainly Mg for the furnace-cooled sample. This difference strongly suggests that considerable amounts of La, Ga and Mg may interdiffuse across the grain-boundary as the temperature increases. This transient of composition from a more insulating MgO-like substance to a more conductive

LSGM-like material is responsible for the gradual disappearance of grain-boundary effect and progressive increase in total ionic conductivity with the temperature, as observed in Figures. 4.6 and 4.7.

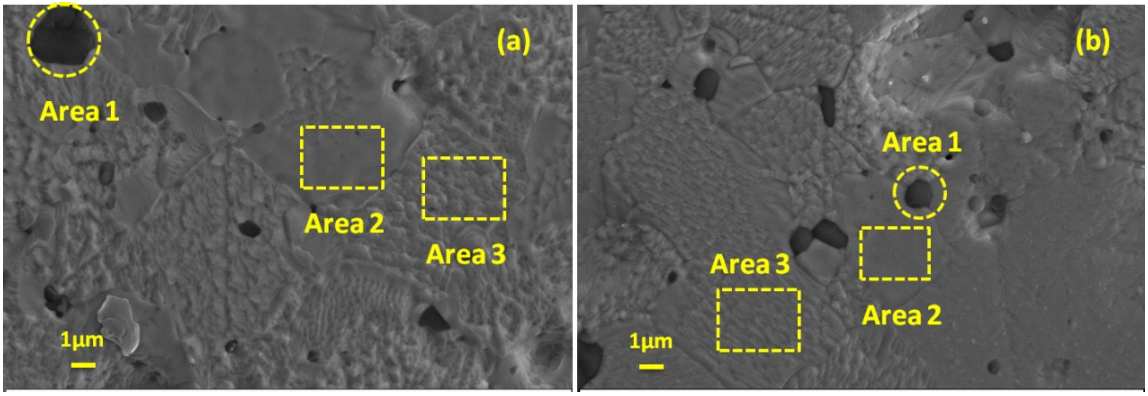

Figure 4.8 Microstructural comparison of z=0.10 Mg-excess LSGM sample after (a) being quenched from 800^{o}C and (b) furnace-cooled. EDX analysis was performed on three representative locations[116].

The above hypothesis is also supported by the change in A/B ratio of the bulk (Area 2 and 3) in the two samples, where A/B ratio refers to as (La+Sr)/(Ga+Mg). For the quenched sample, the averaged A/B ratio is 0.68; it changes to 1.17 for the furnace-cooled sample. The lowered A/B for the quenched sample infers a dominant dissolution of Mg-rich grain-boundary phase into grains (bulk) at higher temperatures whereas the increased A/B for the furnace-cooled sample suggests a precipitation of Mg-rich phase along the grain-boundary when the sample is allowed to cool sufficiently slow.

Table 4.2 Compositions (at%) of z=0.10 Mg-excess LSGM sample after being quenched from 800°C and furnace-cooled[116].

	Quenched, at%			**Furnace-cooled, at%**		
	Area 1	Area 2	Area 3	Area 1	Area 2	Area 3
La	**20.9**	23.9	23.0	**4.6**	8.2	8.2
Sr	**3.4**	4.7	4.7	**3.2**	6.90	5.2
Ga	**32.6**	37.4	36.9	**2.3**	4.10	4.3
Mg	**13.6**	4.6	4.9	**33.0**	8.8	7.1
O	29.5	29.5	30.4	56.9	72.1	75.3

With the fact that the grain-boundary composition changes with the temperature in mind, the question why the total ionic conductivity peaks at z=0.03 could be explained by mechanism of dopant-vacancy interaction, *e. g.*, $2Mg'_{Ga} - V_O^{\bullet\bullet}$ at higher [Mg'_{Ga}], forming a trap (or associate) to oxide-ion vacancies migration and thus reducing the total conductivity. Another possible mechanism is that the composition of z=0.03 produces the most conductive grain-boundary composition, further improving the total conductivity.

The Arrhenius plots of $La_{0.80}Sr_{0.20}Ga_{0.83}Mg_{0.17+z}O_{3-\delta}$ (z=0.0 to 0.10) is shown in Figure 4.9. These plots are consistent with ref. [102] in that there are two straight lines intersected at a critical temperature T*≈ 600°C, dividing the plot into two distinct regions belonging to associate-free (>600°C) and associate-prevalent (<600°C) phenomena. Two sets of activation energies corresponding to these two regions calculated according to ref. [102] show that the Mg-excess samples have generally higher activation energies than that

of the baseline, and the samples with higher Mg-excess level have higher activation energies than those with lower ones. This observation supports the mechanism that the $V_O^{\bullet\bullet}$ defects could become trapped by forming associates with defect $Mg_{Ga}^{/}$ at lower temperatures, thus increasing the activation energy. This assertion is also supported by the modeling prediction presented in ref. [117].

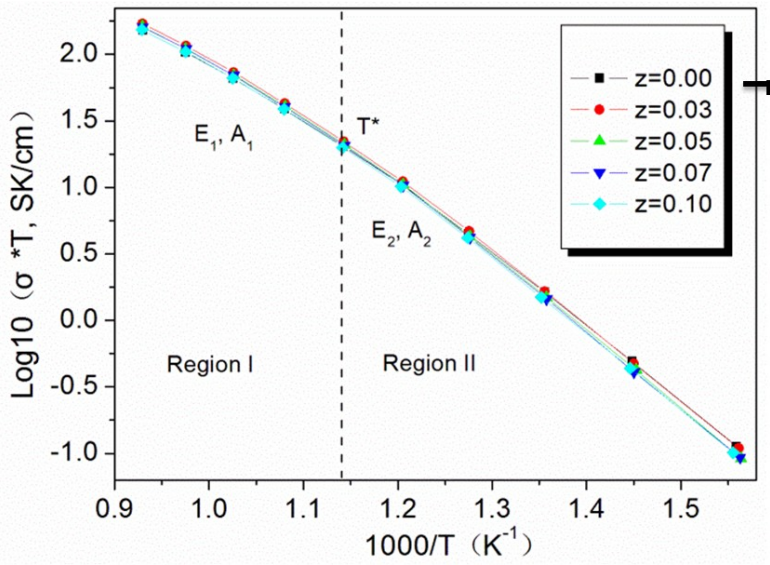

z	E_1, eV	E_2, eV
0.00	0.819	1.105
0.03	0.830	1.125
0.05	0.828	1.144
0.07	0.832	1.144
0.10	0.832	1.134

Figure 4.9 Arrhenius plots of $La_{0.8}Sr_{0.2}Ga_{0.83}Mg_{0.17+z}O_{3-\delta}$[116].

The fact that high ionic conductivity Mg-excess samples also have higher activation energy than the baseline suggests an important role of pre-exponential term played in Arrhenius equation. The pre-exponential term is proportional to concentration of mobile ions and related to crystallographic factors, as predicted by the Random Walk Theory [102]. Higher concentration of mobile ions created by Mg-excess may offset the slightly increased activation energy, resulting in higher ionic conductivity. This hypothesis seems to be in agreement with the proposed Mg-rich phase re-dissolution mechanism.

To sum up, five levels of Mg-excess in $La_{0.8}Sr_{0.2}Ga_{0.83}Mg_{0.17+z}O_{3-\delta}$ (z=0.00, 0.03, 0.05,

0.07 0.10) as solid electrolyte have been synthesized by a solid-state reaction method. The microstructures of all the samples show well-sintered grains and grain-boundaries. As the Mg-excess level increases, the Mg-rich second phase appeared as the dark phase is micro-structurally more pronounced at the grain-boundaries, even though XRD could not discern the presence of this second phase. AC impedance spectroscopy study of these samples surprisingly reveals that as the temperature increases the total ionic conductivity of the Mg-excess samples becomes progressively higher than that of the baseline sample (z=0.0), which is also accompanied by a gradual disappearance of the grain-boundary effect. A mechanism based on the re-dissolution of Mg-rich phase (also diffusion of La, and Ga) along the grain-boundaries at higher temperatures, forming a more conductive grain-boundary phase composition, is proposed to interpret the results. A dopant-vacancy association formation mechanism is also hypothesized to explain the highest conductivity observed at z=0.03. Overall, Mg-excess doping on Ga-site of LSGM show no adversary effects on the total conductivity, thereby can be considered an alternative approach to simultaneously lowering the cost and increasing the strength of LSGM-based SOFCs. After investigating the Mg-excess effect, the optimal LSGM composition for later RSOFC preparation is $La_{0.8}Sr_{0.2}Ga_{0.83}Mg_{0.20}O_{3-\delta}$, in the following subchapters, all the LSGM-based electrolytes applied in my battery tests refer to this composition.

4.1.2.4 Structural optimization of the RSOFC

The structural optimization of planar RSOFCs has experienced three phases, leading

to three generations of RSOFCs. For all the three generations of RSOFCs, the screen-printed fuel electrode consisting of two layers of LDC ($Ce_{0.6}La_{0.4}O_{2-\delta}$)-Ni and GDC ($Ce_{0.8}Gd_{0.2}O_{2-\delta}$)-Ni remained unchanged. The only differences were made on air-electrode and method to make LSGM. In the first generation, the air electrode was screen-printed with Sr- and Co-doped $LaFeO_3$ (LSCF) paste. In the second and third generations, the air electrode was made by infiltrating a prefabricated porous LSGM-scaffold with a mixture of $Sm_{0.5}Sr_{0.5}CoO_{3-\delta}$ and $Sm_{0.2}Ce_{0.8}O_{1.9}$ (SSC/SDC) nitrate solutions for multiple times[118]. The structure of the RSOFC is illustrated in Figure 4.10. Both the first generation and second generation LSGM electrolytes were made of die-pressed pellets. The third generation LSGM electrolyte was made from tape-casting technique. Table 4.3 listed the composition and thickness for all three generations of RSOFCs. The active cell areas for all of these RSOFCs are 1.30cm^2.

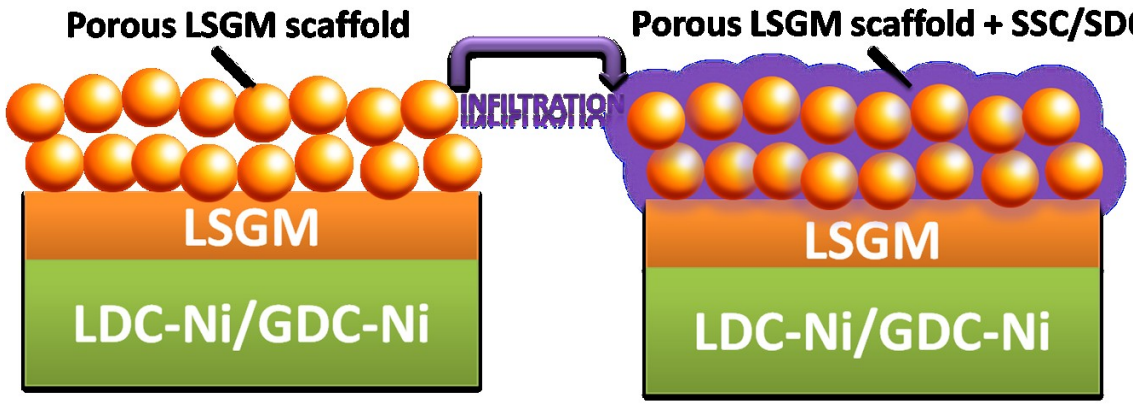

Figure 4.10 Schematic of RSOFC applied in the battery test.

Table 4.3 Summary of the three generations of LSGM-based RSOFCs

Generation	Component	Composition	Thickness (unit: μm)
Gen 1	Fuel electrode	LDC-Ni/GDC-Ni	50
	Electrolyte	LSGM	350
	Air electrode	LSCF	50
Gen 2	Fuel electrode	LDC-Ni/GDC-Ni	30
	Electrolyte	LSGM	350
	Air electrode	Porous LSGM-SSC/SDC	100
Gen 3	Fuel electrode	LDC-Ni/GDC-Ni	30
	Electrolyte	LSGM	180
	Air electrode	Porous LSGM-SSC/SDC	50

Note: LSGM= $La_{0.8}Sr_{0.2}Ga_{0.83}Mg_{0.20}O_{3-\delta}$; LDC=$Ce_{0.6}La_{0.4}O_{2-\delta}$; GDC=$Ce_{0.8}Gd_{0.2}O_{2-\delta}$; LSCF=$La_{0.6}Sr_{0.4}Co_{0.2}Fe_{0.8}O_{3-\delta}$; SSC=$Sm_{0.5}Sr_{0.5}CoO_{3-\delta}$; SDC=$Sm_{0.2}Ce_{0.8}O_{1.9}$

The performance of the three generations of RSOFC were characterized by a Solartron 1260/1287 Electrochemical System. Figure 4.11 shows the electrical performances of the three generations' RSOFCs in an open system with a flowing H_2+3%H_2O measured from 650^{o}C to 550^{o}C. According to Figure 4.11 (a) and (c), the impedance spectra of these two generations battery at each temperature are similar to each other. However, the power performance of Gen 2 battery is better than Gen 1 battery, which is due to the better catalytic performance of SSC/SDC for oxygen reduction at the air electrode than LSCF in

the intermediate temperature; in addition, the porous LSGM infiltrated with SSC/SDC is supposed to provide more active sites for the oxygen reduction process. When comparing the electrical performances of Gen 3 battery (Figs. 4.11(e) and (f)) with the former 2 generations' batteries, the advantages are obvious: the total resistance of Gen 3's RSOFC has decreased to one third of the Gen 1 and Gen 2's RSOFCs, while its power output is more than double than the former two generations. To be more specific, the ohmic resistance of Gen 3's RSOFC is half of Gen 1 and Gen 2's RSOFCs, which is mainly benefit from the decreased thickness of LSGM electrolyte. The polarization decrease is attributed to the decreased air electrode thickness.

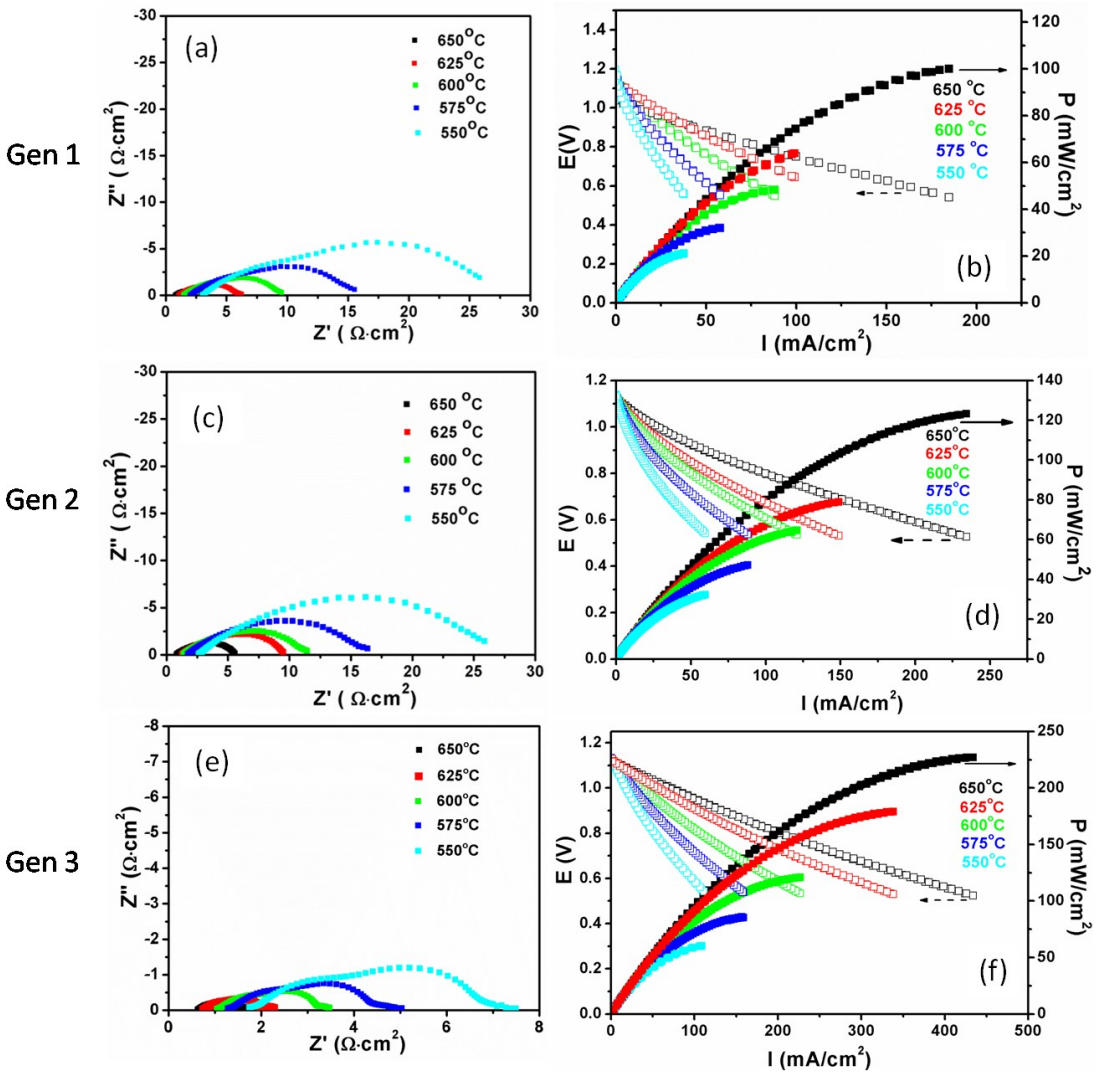

Figure 4.11 Electrical performances of three generations' RSOFCs in an open system with a flowing H_2+3%H_2O measured from 650°C to 550°C. (a) Impedance spectra of Gen 1; (b) P-I and V-I curves of Gen 1; (c) Impedance spectra of Gen 2; (d) P-I and V-I curves of Gen 2; (e) Impedance spectra of Gen3; (f) P-I and V-I curves of Gen 3.

4.2 BATTERY ASSEMBLY

4.2.1 Assembly methods

Two battery assembly configurations were employed in this dissertation study. The first configuration is based on the anode-supported tubular RSOFC. After all the functional

layers were completed as described in 4.1.2.1, two Al_2O_3 rings were attached to the two ends of the cell, which are served as the transitional part. The battery cell was finally cement-mounted onto two long Al_2O_3 tubes in which Fe-based baseline ESU pellets were installed close to the inlet end of the battery cell. The Fe loading was determined to be 0.1064 grams. The volume of the enclosed loop in the fabricated battery cell is approximately 81.5 cm^3. Figure 4.12 shows a schematic view of the assembled anode-supported tubular battery cell.

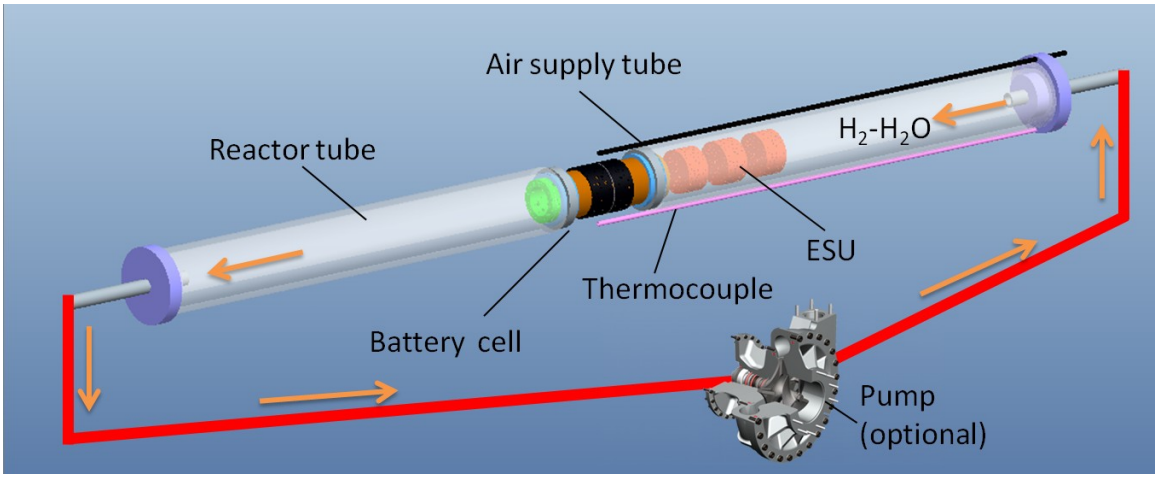

Figure 4.12 A single battery assembly with an anode supported tubular RSOFC and an integrated ESU.

The second configuration is based on the planar RSOFCs, as shown in Figure 4.13. Since the planar configuration allows us to investigate and optimize more conveniently the battery, this configuration has become a standard for all the battery tests following the first tubular battery work. For this kind of configuration, the Fe-, W- or Mo- based ESU materials were packaged underneath the fuel-electrode of ROSFC. A specially formulated glass-ceramic was used as the hermetic sealant for the battery cell. The high

temperature SOFeARB and SOWARB used commercial RSOFCs, while the IT-SOFeARB and IT-SOMoARB employed homemade LSGM-based RSOFCs. Table 4.4 lists the RSOFCs in different homemade IT-SOMARBs.

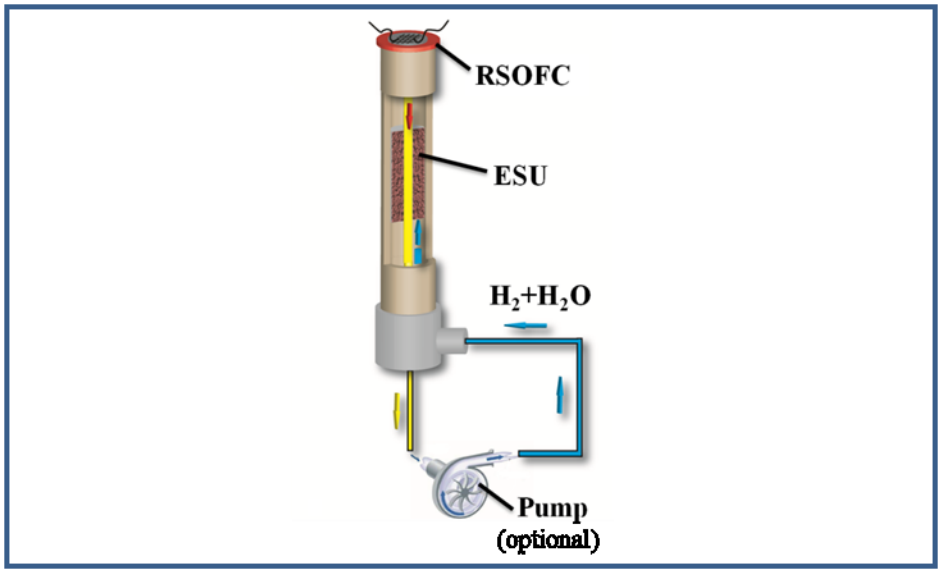

Figure 4.13 Schematic of a planar button SOFeARB configuration[119].

4.2.2 ESU loading effects on RSOFC performance

As a systematic study of the effect of ESU loading onRSOFC performance is also considered. Figure 4.14 shows the EIS spectra measured from batteries with the same type of RSOFC (Gen 3) but different Fe-ESU loading operated at 650^{o}C. The ESU loading seems to mainly effect the intermediate-frequency polarization and ohmic resistance. The trend seems to be rather clear that lower ESU loading leads to lowered battery resistance. While the mechanism is unclear at the present time, the ESU loading in our battery tests have been carefully controled within 0.7-0.9 g of active metal. For energy density evaluation, a similar ESU volume has also been maintained for both

Fe-baseline battery and SOWARB and SOMoARB.

Table 4.4 Battery types, ESU materials and RSOFCs investigated in this research

Battery Type	ESU materials	RSOFC
550°C-SOFeARBs	Baseline Fe-Fe_3O_4	Gen 1
	CeO_2 modified baseline Fe-Fe_3O_4	Gen 1
	ZrO_2-supported Fe-Fe_3O_4	Gen 1
	CeO_2 modified baseline Fe-Fe_3O_4	Gen 3
550°C-SOMoARB vs SOFeARB	Mo-MoO_2	Gen 2
	Baseline Fe-Fe_3O_4	Gen 2
Long term IT-SOFeARBs	Baseline Fe-FeO (650°C) or Fe-Fe_3O_4 (550°C)	Gen 3
	Carbothermic reaction derived Fe-based ESU	Gen 3

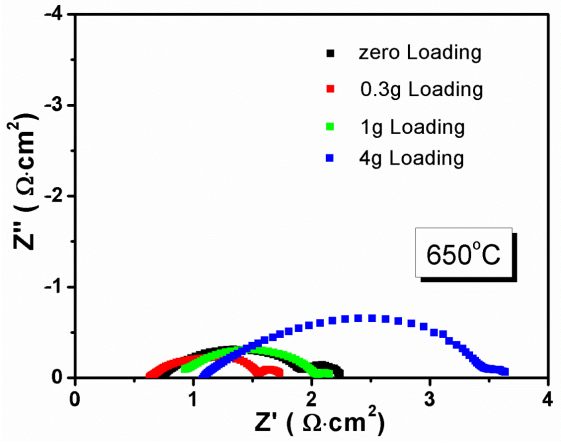

Figure 4.14 ESU loading effects on the impedance spectra of a RSOFC

4.3 PERFORMANCE EVALUATION METHODOLOGIES

4.3.1 Battery testing of tubular battery

The flow block diagram of the battery test setup for the tubular configuration is shown in Figure 4.15. Overall, it consists of three major components: the battery cell, circulating pump, and a set of toggle valves. By turning off and on certain toggle valves, a closed-loop circulation can be created by a pump. The flow rates of all the gases used (N_2, H_2 and Air) were controlled by the mass flow controllers (MFCs). The desirable H_2O contents were obtained by passing the carrier gas N_2 or H_2 through a bubbler heated to a fixed temperature. An on-line humidity sensor (Vaisala model 332) was employed to measure the real-time steam content in the gas phase. To prevent condensation, all pipelines were heat-wrapped and kept at 150^{o}C.

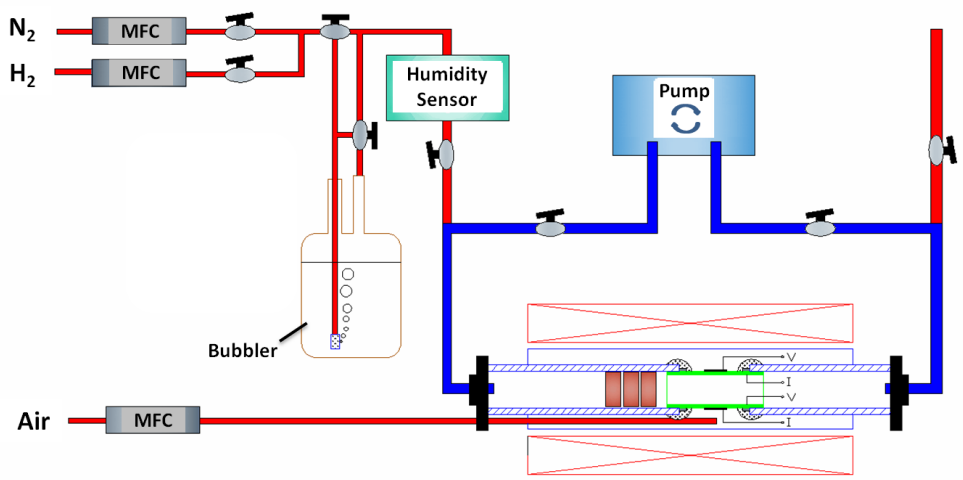

Figure 4.15 A flow block diagram of tubular battery test configuration (the blue loop represents the fuel circulation path)[119].

A typical operation procedure can be described as follows. Pure N_2 is first used to purge the entire pipe system several times to remove any possible residual air in the circulation loop. The battery is then heated up to the target temperature of 800^{o}C with a ramp rate of 3^{o}C/min and 200-sccm air and 90-sccm 5%H_2-N_2 flowing outside and inside of the battery cell, respectively. During this period, the open-circuit voltage is constantly monitored while NiO in the anode and Fe_2O_3 in the redox cycle unit are being at least partially reduced. After reaching 800^{o}C, 5%H_2-N_2 is then gradually switched to 90 sccm dry H_2 to complete the reduction of all Fe_2O_3 into Fe, which becomes the starting point of each battery test. Nitrogen is the primary gas for carrying the steam into the ESU where oxidation of Fe takes place, producing H_2 for the discharge cycle. At each H_2O concentration, testing such as OCV-t, impedance spectroscopy, V-I characteristic and galvanic square wave are conducted before H_2 is introduced to reduce the oxidized Fe back to Fe for the next-round characterization. To ensure no H_2 is left in the pipeline, H_2O-bore N_2 is allowed to purge through for 1 minute (obviously some produced H_2 could be lost during the purge) before the measurement starts. Upon circulation, the outlet and inlet toggle valves are sequentially shutoff, immediately followed by turning on the pump. The pump was set to a pre-calibrated flow rate of 90 sccm.

4.3.2 Battery testing of planar battery

The planar battery testing bed is adopted due to its simplicity in configuration and ease to fabricate in lab. The majority of testing in this dissertation study was based on this

planar geometry.

For the 800°C-SOFeARB and SOWARB, the ESU material, either the Fe_2O_3-ZrO_2 (in 85:15 molar ratio) granules or the WO_3 granules were first reduced with a cover gas of 5% H_2-N_2. Before cycling, a pure H_2 was used to reduce all Fe_2O_3 into metallic Fe or all WO_3 into W. Instead of introducing pure steam to initiate the testing, a small current was applied to oxidize H_2 to H_2O to the extent that Fe becomes equilibrated with FeO or W equilibrated with WO_2 at 800°C, forming the needed Fe-FeO or W-WO_2 redox couple. The RSOFC's EMF was closely monitored during the initial electrochemical oxidation. As soon as EMF reached 0.97 volts for the 800°C-SOFeARB, or 0.99 V for the 800°C-SOWARB, the electrochemical oxidation was stopped, and the system was ready for electrical cycles.

For the 650/550°C-SOFeARBs, 550°C-SOFeCARBs and 550°C-SOMoARBs, the testing protocol is also similar to the aforementioned method. The initial temperature for these IT-batteries was first raised to 650°C in 5%H_2-N_2 atmosphere to melt the sealing glass, after which a pure H_2 was introduced to fully reduce Fe_2O_3 into metallic Fe, or MoO_3 into Mo. This reduction step is not required for the Fe/C-air battery since the ESU contains metallic Fe not Fe oxide. After approximately a half-hour holding to allow the glass to settle, the temperature was then gradually ramped down to the testing temperature. As soon as the temperature was stabilized, the electrochemical oxidation was commenced while the EMF of the battery was constantly monitored. The theoretical EMFs for

650^{o}C-SOFeARB, 550^{o}C-SOFeARB/SOFeCARB, and 550^{o}C-SOMoARB are 1.03 V, 1.07V, and 1.108 V, respectively. The electrochemical oxidation was stopped as soon as these EMFs are obtained, and the system was ready for electrical cycles.

4.3.3 Battery Characterization

The electrochemical performance of all the batteries fabricated was characterized with a Solartron 1260/1287 Electrochemical System. The testing modules include OCV (open circuit voltage)-t, impedance spectroscopy, potential-dynamic and galvanic square wave. A four-probe scheme was used to connect with the instrument.

Other properties of the battery were also evaluated by the relevant techniques. A field emission scanning electron microscope or FESEM (Zeiss Ultra) equipped with an EDS capability was employed to acquire microstructures and analyze the local chemical compositions of the ESU and RSOFC. The phase composition of the ESU material was also examined by PXRD using an X-ray diffractometer (D/max-A, Rigaku, Japan) with graphite-monochromatized CuKα radiation (λ=1.5418 Å). The XRD scan was performed at a rate of 5^{o} min^{-1} from 2θ= 10^{o} to 90^{o}, the spectra of which were analyzed with the JADE (MDI) software to identify phase compositions. The pore characteristics of the porous ESU such as median pore diameter, and porosity were analyzed by a mercury porosimeter (Autopore IV, Micromeritics) in a pressure range of 0.5-30000 psi. The particle sizes of ESU materials were measured by a particle size analyzer (Horiba,

LA950), and the porosities before and after battery tests were analyzed by BET (Micromeritics ASAP 2020 -Surface Area and Porosimetry Analyzer.).

4.4 SUMMARY

The focus of this chapter is the description of experimental details on how materials are synthesized, battery are assembled and tested. The testing platform evolved from early anode-supported tubular geometry to planar geometry for the consideration of simplicity and ease to fabricate. A standard testing protocol has been established through this dissertation work and closely followed by all the tests. In particular, three generations of ROSFCs have also been developed in an effort to enhance the performance of RSOFC, and a variety of synthesis methods were investigated to enhance the performance of ESU. The combination of Gen 3 RSOFC and carbothermic reaction derived ESU produced the best performance of SOFeARB in energy capacity, round-trip efficiency and cyclic durability to be shown in the following chapters.

CHAPTER 5

PERFORMANCE OF SOFEARB – A MODEL SOMARB SYSTEM

Iron-air batteries are an attractive storage mechanism due to its high theoretical energy density, benign environmental impact, rich earth-deposit and low cost [53, 120, 121]. However, traditional room-temperature aqueous iron-air battery suffers from a poor cycle efficiency resulting from irreversible side reactions occurred at the air electrode (e.g., H_2 evolution), electrolyte drainage, and extreme sensitivity to CO_2 present in air [121-123]. In this chapter, we demonstrate that the SOFeARB - a branch of SOMARB - possesses all the merits of traditional low-temperature iron-air batteries along with profound advantages derived from its sound and simple principle and innovative design described in chapter 2. We particularly show testing results obtained from both tubular and planar batteries, elaborating more details about the distinctive energy storage characteristics of this new type of metal-air batteries in the temperature range of 550-800^{o}C.

5.1 SOFEARB OPERATED AT 800^{o}C

5.1.1 Tubular SOFeARB

The charging/discharging characteristic of the tubular SOFeARB is shown in Figure

5.1(a), where two consecutive ten charge/discharge cycles measured at a constant current density of 50 $mAcm^{-2}$ and with a 10-minute single-cycle period are combined as one plot. The characteristic of a rechargeable battery is explicitly observed with stable performance for all the twenty cycles performed. The responses of the battery to the charge and discharge commands are instantaneous. The corresponding specific energy calculated from integration of the voltage-time curve multiplied by the galvanic current is shown in Figure 5.1(b). The battery produces a specific energy of $348W_eh$/kg-Fe averaged from the 20 electrical cycles with a 38.5% Fe utilization. This energy output is compared with the energy input during the charge cycle to yield an averaged round-trip efficiency of η=91.5%. Based on the specific energy attained at 50 mA cm^{-2} and 38.5% Fe utilization, we can project a specific energy of 886 W_ehkg^{-1}-Fe for 100% Fe utilization or full discharge, which comes close to about 95% of the theoretical $932W_ehkg^{-1}$-Fe (or charge specific charge 960Ah/kg-Fe). Such a close agreement favorably supports the validity of experimental data obtained. We anticipate that the charge/discharge time of the battery can be easily scaled-up to hour-level for meaningful practical applications by simply increasing the Fe loading.

The rate of rechargeability (50 mA/cm^2) demonstrated by the SOFeARB is more than one order of magnitude higher than Li-ion battery (~1mA/cm^2) and at a similar magnitude to RFB. However, much higher current density, e. g., 300 mA/cm^2, is very achievable for an RSOFC.

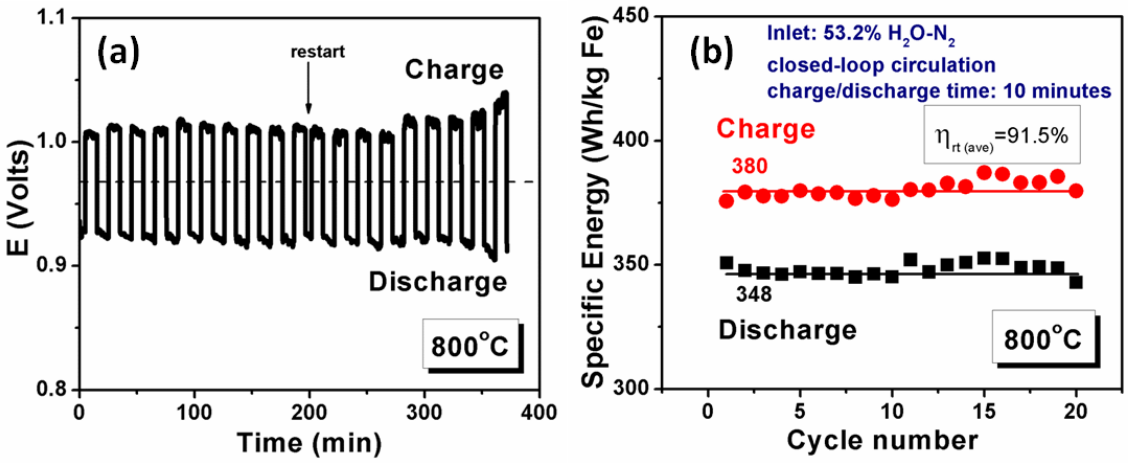

Figure 5.1 (a) Charge and discharge characteristic of the tubular battery at 800°C and j=50 mAcm^{-2}. The break on the curve at ~200 min marks the start of second 10-cycle run; (b) Plot of specific energy as a function of the number of charge and discharge cycles. All data were measured with a close-loop flow of 53.2%H_2O–N_2. Reproduced from Ref.[68].

Figure 5.2 shows the measured EMF (or E_N) *vs* air at 800°C as a function of H_2O content in a closed flow of two different gases, N_2-H_2O and H_2-H_2O. For N_2–H_2O, E_N=0.970 volt is invariant with H_2O content whereas for H_2-H_2O, E_N=0.970 volt only occurs above *ca.* 35% H_2O. The thermodynamic calculations shown in Figure 3.2 predict the equilibrium partial pressure ratio of H_2 and H_2O (pH_2O/pH_2) to be 34.9/65.1 for the steam-iron reaction $Fe + H_2O = FeO + H_2$ occurring at 800°C; the pH_2O/pH_2=34.9/65.1 corresponds to an E_N=0.970 volt vs air for an oxygen concentration cell like ROSFC, see Figure 3.3. The excellent agreement of the experimental data with the thermodynamic calculations indicates that Fe-FeO equilibrium is prevalent in the redox reaction. One important aspect of the SOFeARB is that E_N is virtually controlled by the Fe-FeO equilibrium, resulting in a state-of-the-charge independent EMF. The amount of energy being stored is solely determined by the mass ratio of Fe: FeO in the ESU.

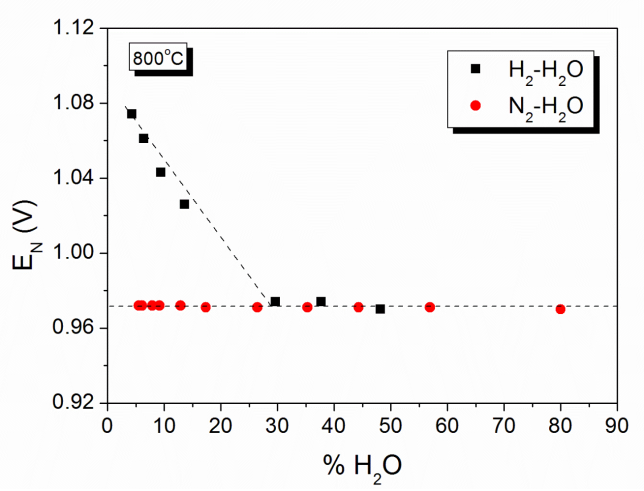

Figure 5.2 Plot of E_N as a function of H_2O content in a closed-loop flow of H_2–H_2O and N_2–H_2[68].

The AC impedance spectra shown in Figure 5.3 (a) and (b) further support the two-phase equilibrium theory by revealing unchanged intermediate-to-low-frequency electrode resistance above *ca*. 35% H_2O in H_2-H_2O mixture and a small systematic reduction of the intermediate-to-low-frequency electrode resistance with increasing H_2O in the N_2-H_2O mixture; the latter apparently results from a reduced N_2-dilution effect while pO_2 is being fixed by the Fe-FeO equilibrium. The systematic reduction in intermediate-to-low-frequency electrode resistance below *ca*. 35% H_2O also confirms that it is an anode-related process with the lowest frequency semicircle likely being related to the gas diffusion process. The V-I characteristic of the battery cell measured under both fuel cell and electrolysis modes, and power performance in a close-loop flow of N_2-x%H_2O are shown in Figure 5.3 (c) and Figure 5.3 (d), respectively. It is evident that the RSOFC exhibited a higher resistance during electrolysis than fuel cell mode. Above ~57%

H_2O, the difference in cell performance is almost indiscernible. The H_2O content used in this study was ~53%, close enough to avoid significant N_2-dilution effect.

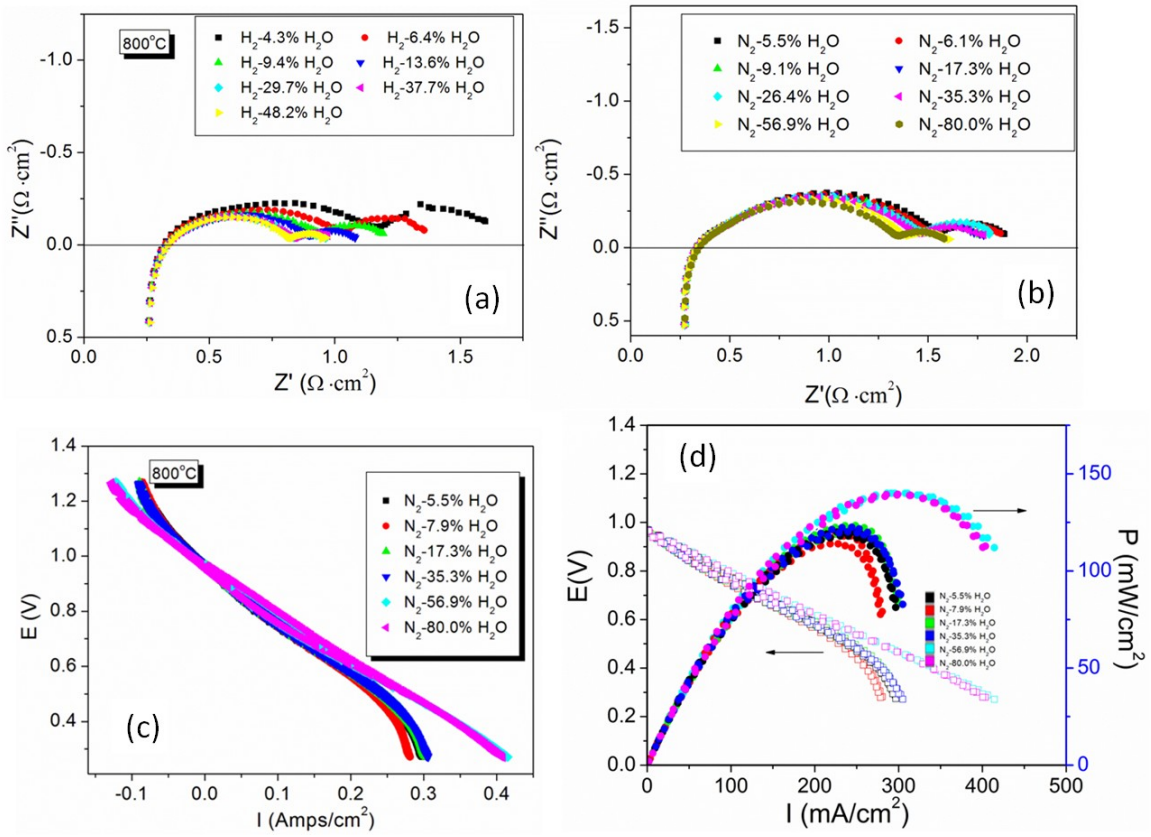

Figure 5.3 AC impedance spectra of the SOFeARB measured under OCV in a closed flow of (a) H_2-H_2O and (b) N_2-H_2O. (c) V-I characteristic of the battery measured under a close-loop flow of N_2-x%H_2O. (d) Power performance of the battery measured with N_2-35.3% H_2O. Reproduced from Ref.[68].

In summary, the 800°C-SOFeARB has been demonstrated in lab with high storage capacity, specific energy, rate-capacity and RTE even at relatively low Fe loading and utilization. Its ability to store a large amount of electrical energy clearly originates from the fundamental discharge and charge reaction that essentially involves the transfer of two electrons in the electrode process. The "in-battery" generation and storage of H_2 via the

in-situ reversible steam-iron reaction is a thermally efficient process than conventional electrolysis/low-temperature H_2 storage approach [124-126]. Therefore, the SOFeARB technology is superior to the conventional RSOFCs involving production and *ex-situ* storage of hydrogen at a very poor energy efficiency.

5.1.2 Planar SOFeARB

With the demonstration of the working principle and key features of the tubular SOFeARB, a simple and easy-to-fabricate planar SOFeARB was later adopted for characterizing energy storage behaviors under different materials and testing conditions.

As previously described, EMF can be conveniently used as an indicator of the phase equilibrium. The EMFs recorded in Figure 5.4 as a function of time during H_2-reduction process at 800^{o}C show several voltage plateaus, each representing a two-phase equilibrium that corresponds to a fixed pO_2 or pH_2O/pH_2 according to Gibbs phase rule. Thermodynamic assessments indicate that these plateaus correspond to the two-phase equilibria of Fe_2O_3-Fe_3O_4 (at ~0.388 volt), Fe_3O_4-FeO (at ~0.938 volt) and FeO-Fe (at ~0.970 volt). The last plateau at ~1.30 volts reflects the pO_2 in the H_2 stream (with a trace amount of H_2O in pure H_2) equilibrating with a metallic Fe phase. Figure 5.4 again verified the theoretical analysis in Figure 3.3 and experimental data in Figure 5.2.

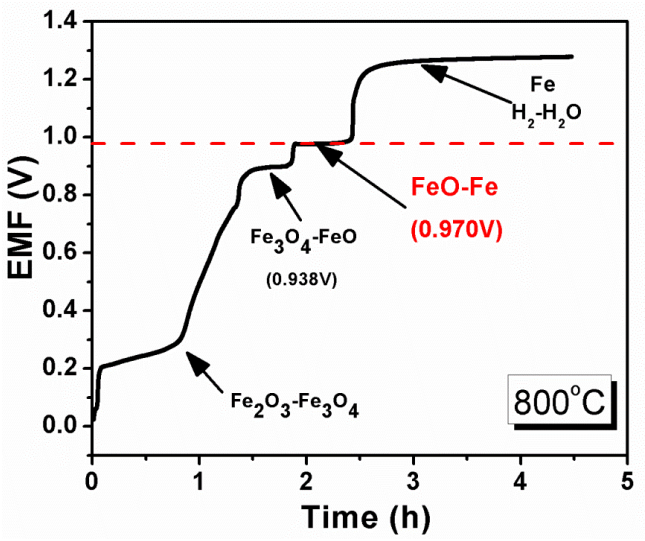

Figure 5.4 EMF recorded during the reduction of Fe_2O_3 by H_2 at 800°C[119].

The energy storage characteristics of the planar 800°C-SOFeARB investigated from 50 to 200mA/cm^2 current density over 10 minutes to 6 hours cycle duration show that the charge storage capacity is strongly dependent on iron utilization (U_{Fe}), a key parameter reflecting the combined effect of operating current and cycle duration (refer to *eq.* (2-17). The variations of battery voltage with charge storage capacities in terms of mAh/g Fe, mAh/L and mAh/cm^2 (specific charge, charge density, and rat capacity) at different U_{Fe} are shown in Figure 5.5; these capacity terms evaluate the ability of the new battery to store electrical charge on the basis of the weight and volume of energy storage material and the active area of the electrode, respectively. The battery explicitly exhibits a higher charge storage capacity at a higher U_{Fe}, but with more pronounced voltage degradation. Given the fact that the kinetic rate (moles/sec/cm^2) of a redox reaction generally decreases with time (a parabolic behavior), the resulting gradual decrease in the production rates of

H_2 (for discharging) and H_2O (for charging) during a deep charge/discharge cycle would essentially increase the actual consumptions of H_2 and H_2O by a RSOFC operating at a constant current, thus lowering voltage as a result of fuel starvation. Other factors such as the loss of surface area of Fe-particles during high-temperature operation could also add to the decline of capacity. Finally, the abrupt drop-off in voltage at U_{Fe}=100% signals the shift of the Fe-FeO equilibrium to the adjacent oxygen-lean FeO-Fe_3O_4 equilibrium; the latter possesses only one-third of the Fe-FeO redox couple's capacity, thus rendering the FeO-Fe_3O_4 equilibrium unfavorable for energy storage.

The relationship between specific energy, round-trip efficiency and U_{Fe} are shown in Figure 5.6. Specific energy follows the theoretical line at low U_{Fe}, but quickly deviates to lower values at higher U_{Fe}. There are two sources of energy loss for the observed deviation: increased voltage losses from ohmic and polarization resistances of the RSOFC at higher current density, and raised consumptions of H_2 and H_2O by the RSOFC due to decreased production rates of H_2 and H_2O over time in the ESU. The relatively low ionic conductivity and thick YSZ electrolyte (150 μm) used in this study is a major cause of the higher energy loss. On the other hand, the observed decrease in round-trip efficiency with regard to U_{Fe} is attributed to the unbalanced energy inputs and outputs resulting from the RSOFC's polarization and the ESU's parabolic kinetics. Overall, the competing trend exhibited between specific energy-U_{Fe} and efficiency-U_{Fe} suggests that the specific energy and efficiency of the new SOFeARB can be balanced with a proper choice of U_{Fe}. One focus of

my research is to optimize the performance of functional materials employed in RSOFC and ESU as an effort to simultaneously achieve high specific energy and efficiency at high U_{Fe}.

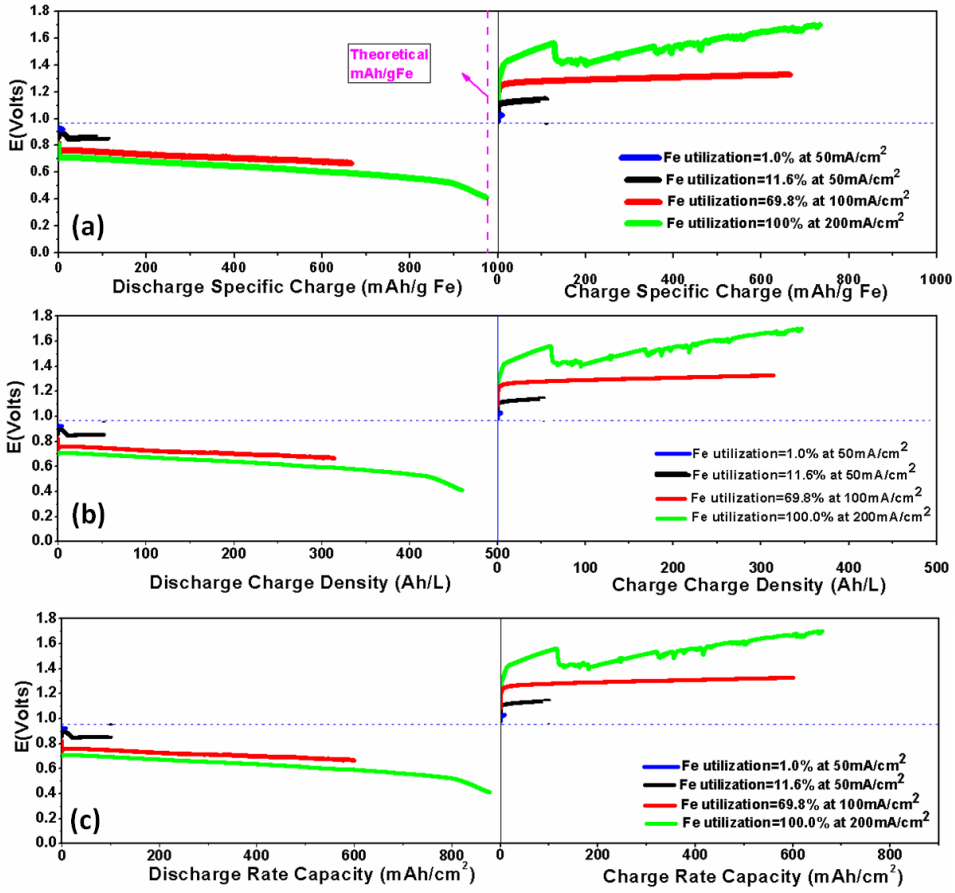

Figure 5.5 Energy storage characteristics measured at different U_{Fe} and 800^{o}C; (a) E vs specific charge (over 0.80g Fe); (b) E vs charge density (over 1.68ml); (c) E vs rate capacity (over 0.88 cm^2 active area of electrode).

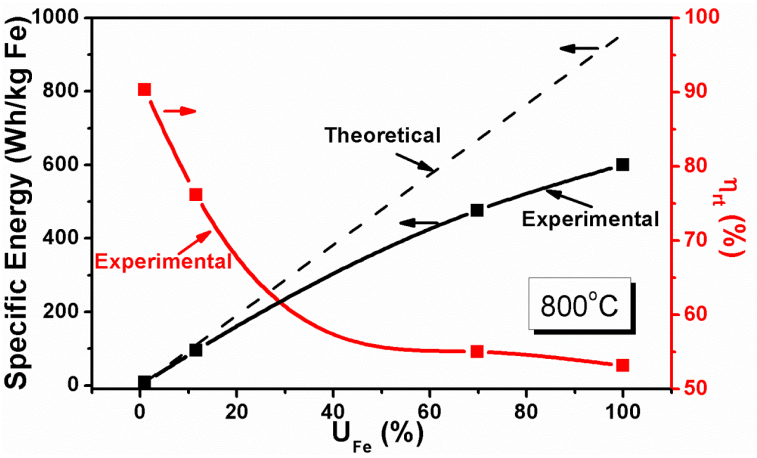

Figure 5.6 Specific energy and RTE as a function of iron utilization[119].

The long-term cycle-ability of the planar battery with pure H_2 as the initial activating gas was studied. The results of 100-cycle performance at a low U_{Fe} (around 1%) are shown in Figure 5.7. Overall, at a fixed current density, there is gradual voltage degradation during repeated charge and discharge cycles. For each single cycle, the increased voltage during charging and decreased voltage during discharging shown in Figure 5.7 (b) are attributed to the performance decay resulted from either RSOFC or redox energy storage couple, or a combination of the two. The averaged RTE of the total 100-cycle shown in Figure 5.7 (c) was ~74% although for the first 20 cycles it was ~88% in Figure 5.7 (d). The normalized specific energy achieved on average was ~ 800Wh/kg Fe.

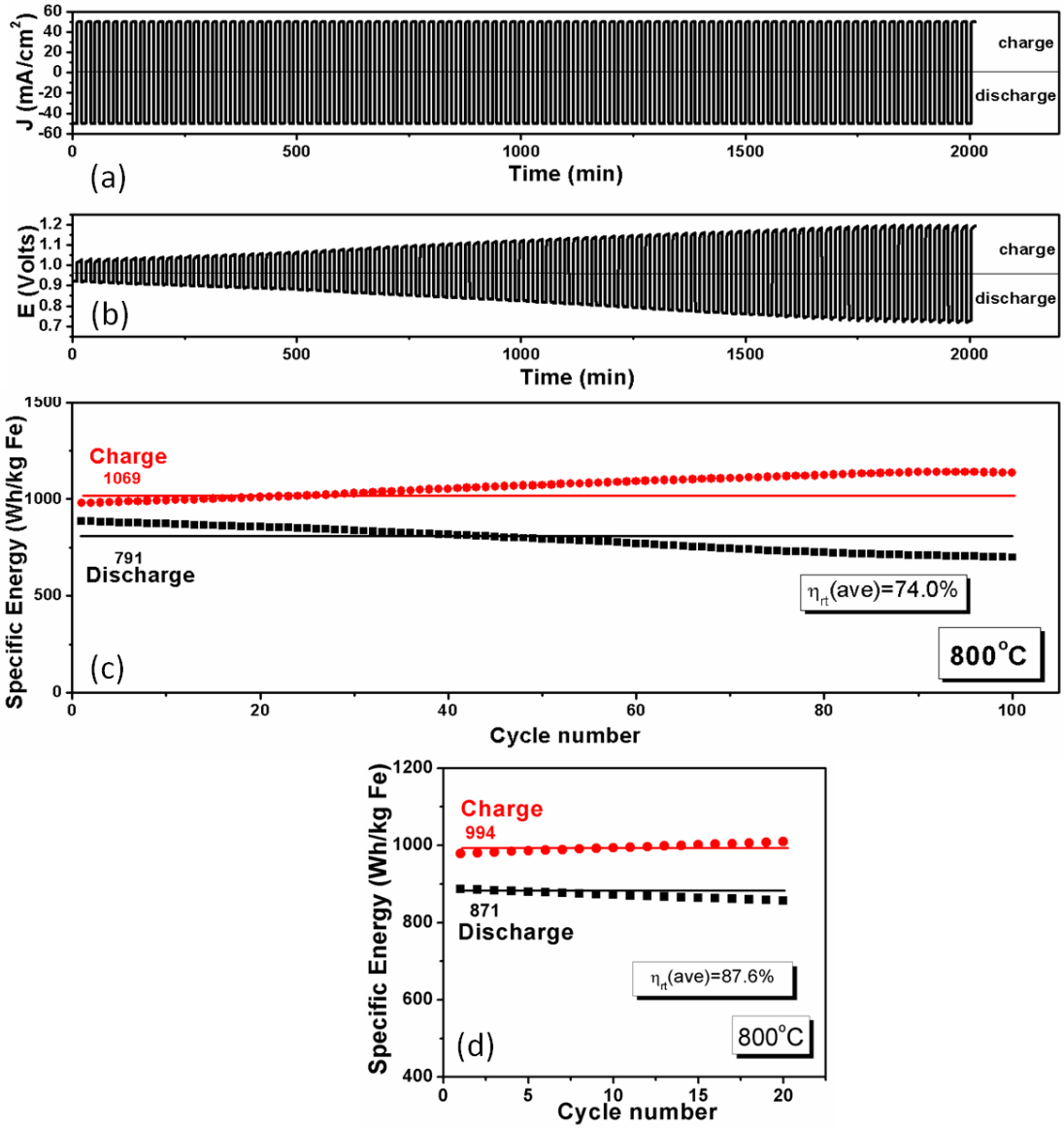

Figure 5.7 Charge and discharge characteristic of the battery at 800°C and J=50mA/cm^2. (a) Cycling current density; (b) voltage variations; (c) RTE averaged from the 100 cycles; (d) specific energy and RTE of the first 20 cycles

The cyclic stability of the battery tested under high current density over ten continuous cycles is shown in Figure 5.8. For each cycle regardless of charge or discharge, the performance appears to be very stable. However, a marked gradual degradation is observed after each charge cycle. The faster degradation of the discharge

compared to the charge in every cycle suggests that a performance-detrimental event has occurred during the charge cycle, which is accountable for the degradation found in the subsequent discharge cycle.

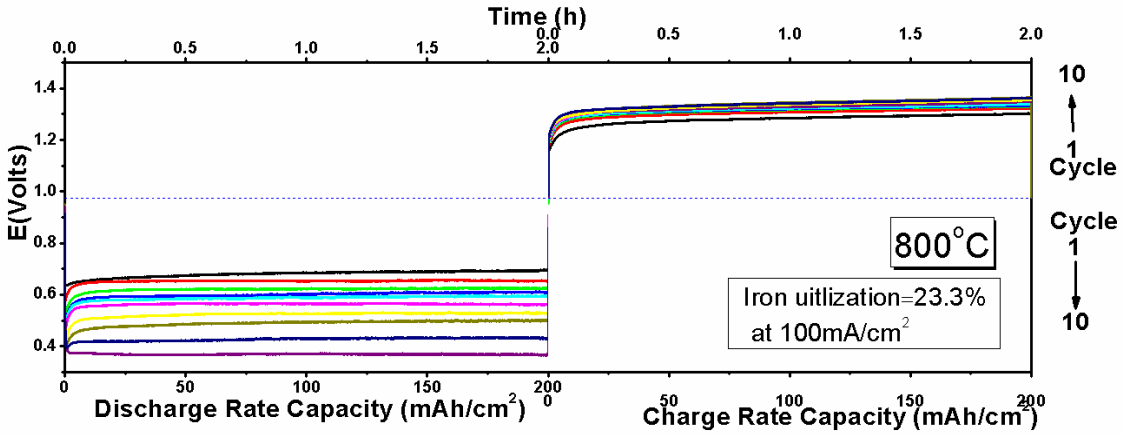

Figure 5.8 Battery voltage variations with energy storage rate capacity at a fixed current density and iron utilization[119].

5.1.3 Degradation mechanism

To investigate the root cause of the degradation, a series of characterizations of the RSOFC and ESU were performed.

Impedance spectra, V-I curves and power performances of RSOFC before and after the test were first investigated. All the initial testing condition was fixed at EMF=0.97V. Figure 5.9 shows the results. It is very clear from Figure 5.9 (a) of impedance spectra that the significant increase in polarization occurred at the anode whereas ohmic and cathode polarization contributions are relatively small. The V-I curves of Figure 5.9 (b) as well as power performance of Figure 5.9 (c) further confirm that the resistance of the battery has

increased considerably. Another general trend is that after reduction with H_2, the battery can be regenerated.

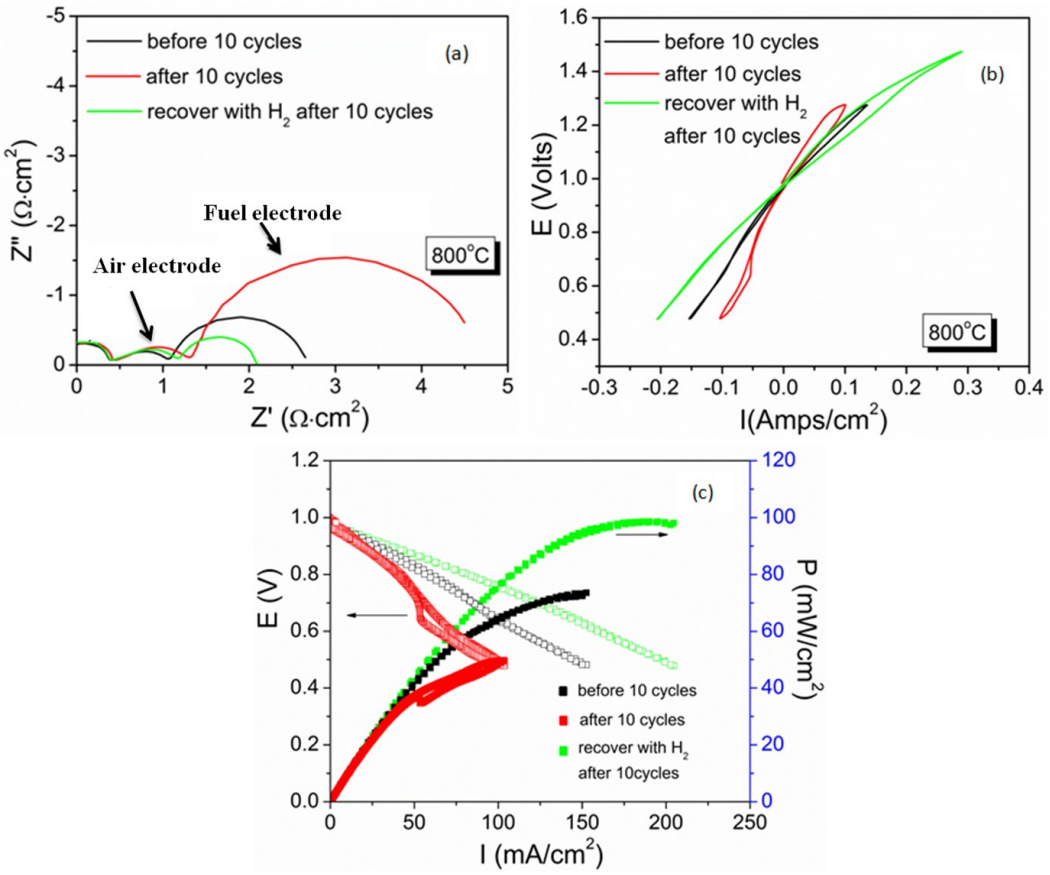

Figure 5.9 Impedance spectra (a) and V-I curves (b) and power performance (c) before and after 10 cycles at U_{Fe}=23.3% and J=100 mA/cm^2.

We also carried out microscopic analysis on the post-test SOFeARB, the cross-sectional view of which as a FESEM image after a 2-week test is shown in Figure 5.10. The fuel electrode interlayer appears to be separated from the electrolyte. While this detachment certainly contributes to the fuel electrode degradation, other reasons such as electrochemical condensation of $FeO_{(s)}$ under a high steam condition could be another possibility. Figure 5.11 shows EDS-analysis results of the fuel-electrode near the

electrolyte/fuel-electrode interface. In addition to the normal constituents of the fuel-electrode, a small amount of Fe (~0.15 at%) was indeed found, indicating Fe diffusion into the fuel electrode/electrolyte interface.

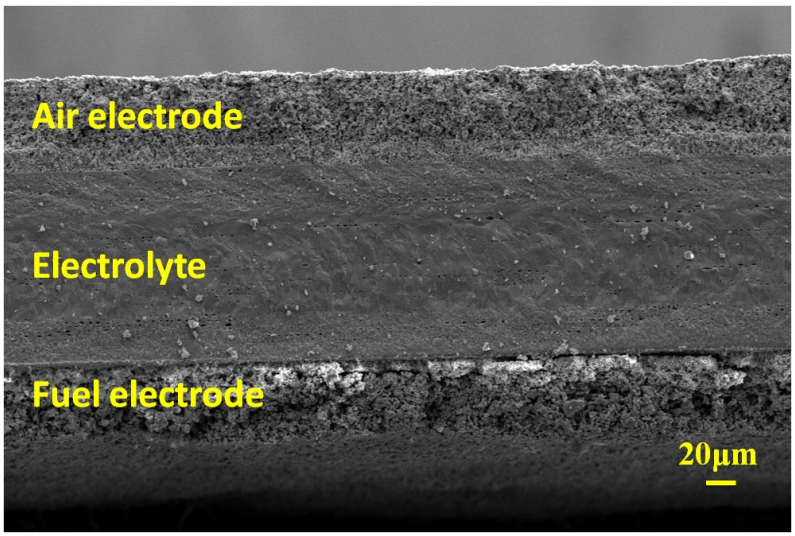

Figure 5.10 FESEM cross-sectional view of RSOFC microstructure after a 2-week test[119].

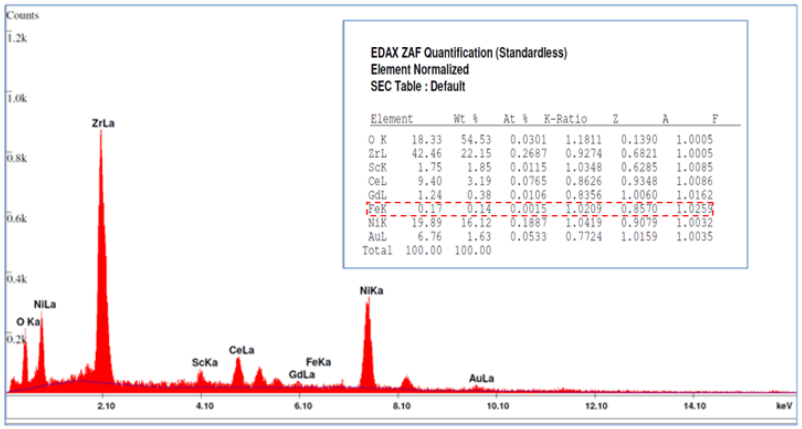

Figure 5.11 EDS spectrum and compositions of the fuel-electrode after test[119].

It has been understood that the overall performance of the SOFeARB is determined not only by RSOFC, but also by Fe-based ESU materials. Therefore, we also performed the

characterization of the microstructure and porosity of Fe-based ESU materials to determine whether the sintering is problematic to a sustainable battery performance. Figure 5.12 shows the morphology of Fe-based redox materials before (a) and after 2-week test (b). It is evident that the microstructures of pre- and post-test samples remained porous. A distinct feature is that many nanoparticles (~200 nm) were observed in the post-test sample (see Figure 5.12 (d)). The EDS analysis of these nanoparticles shows a chemical composition primarily comprising of Fe-oxide with a proportional amount of Zr-oxide. The formation of those nanoparticles is likely to originate from the H_2/H_2O-mediated redox process.

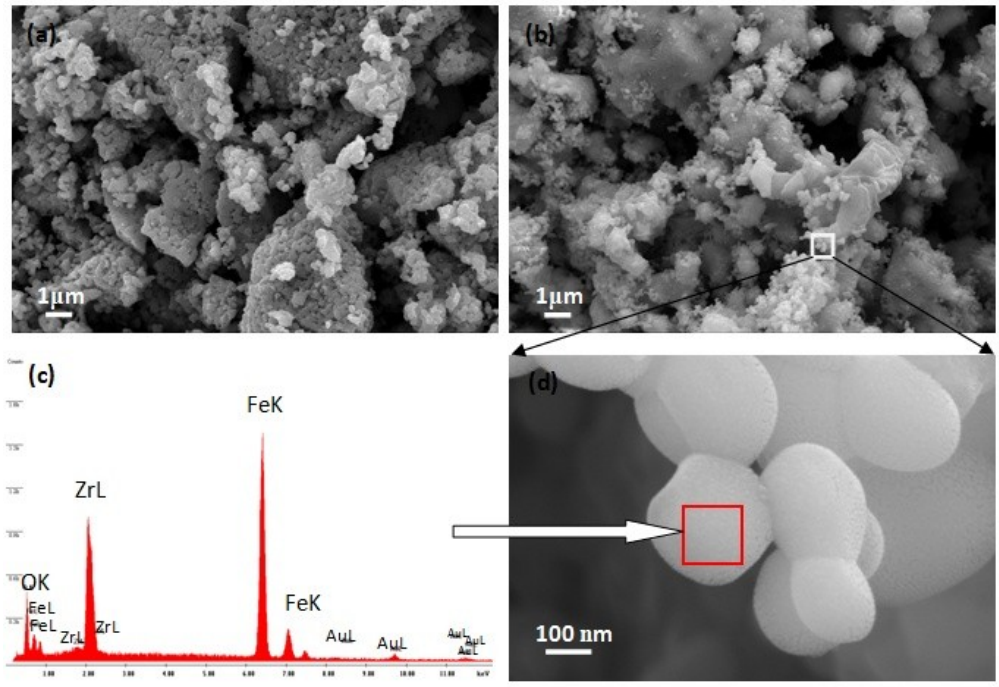

Figure 5.12 Morphology of Fe-based ESU materials (a) pre-test; (b) post-test; (c) EDS spectrum; (d) a close look into the morphology of nanoparticles[119].

The microstructural parameters measured by mercury porosimetry method of the Fe-based ESU materials are given in Table 5.1. After the test, the average pore diameter

was significantly increased, along with a slight increase in the porosity. These results indicate that no obvious sintering has occurred even after a 2-week test.

Table 5.1 Microstructural parameters of Fe-based redox materials loaded in the ESU measured from mercury porosimetry[119]

	Pre-test	**Post-test**
Average Pore diameter, μm	0.692	2.244
Porosity, %	71	76

Figure 5.13 compares the phase compositions present in the samples before and after the 2-week test. Before test, Figure 5.13 (a), it contains two phases Fe_2O_3 and ZrO_2, in the ESU material. After the test, Figure 5.13 (b), it contains Fe and ZrO_2. Based on these XRD results, it is safe to say that ZrO_2 is stable and inactive during redox reaction. The role of ZrO_2 in the ESU material is to help prevent the coarsening of Fe particles during operation.

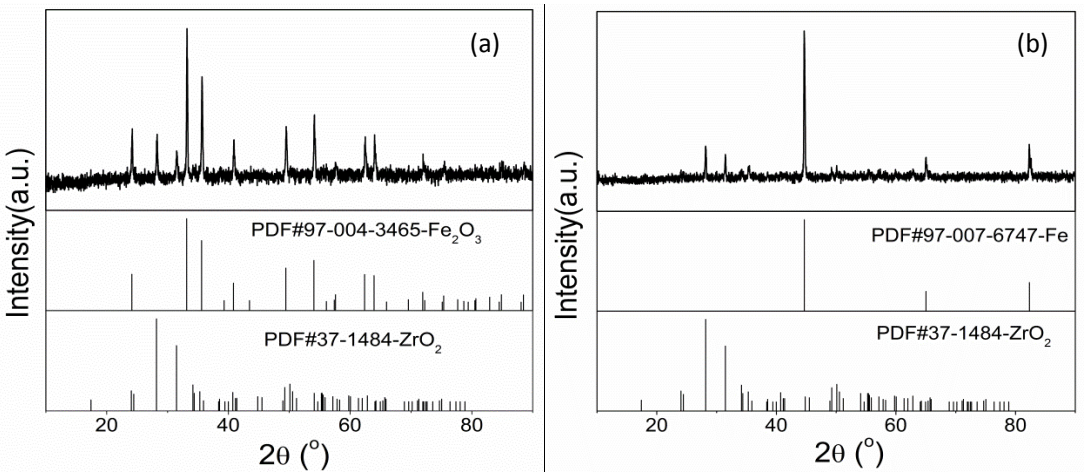

Figure 5.13 XRD analysis of a Fe-based redox material (a) pre-test; (b) post-test. Sample was protected in a 5%H_2-N_2 during shutdown[119].

Based on these results, we postulate that the degradation observed in Figure 5.6 and

Figure 5.7 arises from the RSOFC. We hypothesize the following mechanism to explain the degradation phenomenon. During the discharge cycle, in addition to the dominant reactions (see *e.q.* (1-30)), a parallel reaction between $FeO_{(s)}$ and $H_2O_{(g)}$ also takes place due to its favorable thermodynamics under the battery's operating condition:

$$FeO_{(s)} + H_2O_{(g)} = Fe(OH)_{2(g)} \quad (5.1)$$

The calculated equilibrium partial pressure of $Fe(OH)_{2(g)}$ at 800°C, $pFe(OH)_2$, equals 2.71×10^{-8} atm. During the charge cycle, in addition to the dominant reactions described in eq. (5-1) and (5-2), the gaseous $Fe(OH)_{2(g)}$ can also be reduced at the three-phase boundaries (TPBs) in the fuel-electrode via the following electrochemical reaction:

$$Fe(OH)_{2(g)}+2e^-=Fe_{(s)}+O^{2-}+H_2O_{(g)} \quad (5.2)$$

$$Fe(OH)_{2(g)}+2e^-=FeO_{(s)}+O^{2-}+H_{2(g)} \quad (5.3)$$

A schematic showing such an electrochemical condensation process is given in Figure 5.14. A simple estimation using the equilibrium $pFe(OH)_2=2.71\times10^{-8}$ atm indicates that as high as 0.27 gram $FeO_{(s)}$ per cm^2 can be deposited onto the TPBs for a 2h charge cycle shown in Figure 4-8. With the catalytically inactive $FeO_{(s)}$ accumulating at the TPBs of Ni-based fuel-electrode over every charge cycle, each following discharge cycle will suffer increased resistances of charge-transfer and mass-transfer as a result of decreased catalytic activity and porosity by the condensed $FeO_{(s)}$. This interpretation is consistent with the degradation trend shown in Figure 5.7 of the multi-cycle curves. The AC

impedance spectra and V-I curves of pre- and post-cycle samples shown in Figure 5.9 further supports the mechanism by demonstrating that the degradation is exclusively linked to the increase in the resistance of the fuel-electrode semicircle. Finally, the proposed electrochemical condensation of $FeO_{(s)}$ at the TPBs has also been experimentally confirmed by EDS analysis of the post-test fuel-electrode; Figure 5.11 reveals a 0.14 at% Fe in the fuel electrode. It is also interesting to note from Figure 5.9 that the use of pure H_2 can decrease the battery's resistance to a level even lower than the original one. In line with the proposed model, this improvement can be reasonably understood as a result of freshly reduced fine particles of $Fe_{(s)}$ from the electrochemically condensed $FeO_{(s)}$ and its increased catalytic activity for electrochemical oxidation of H_2 when combined with $Ni_{(s)}$ [127].

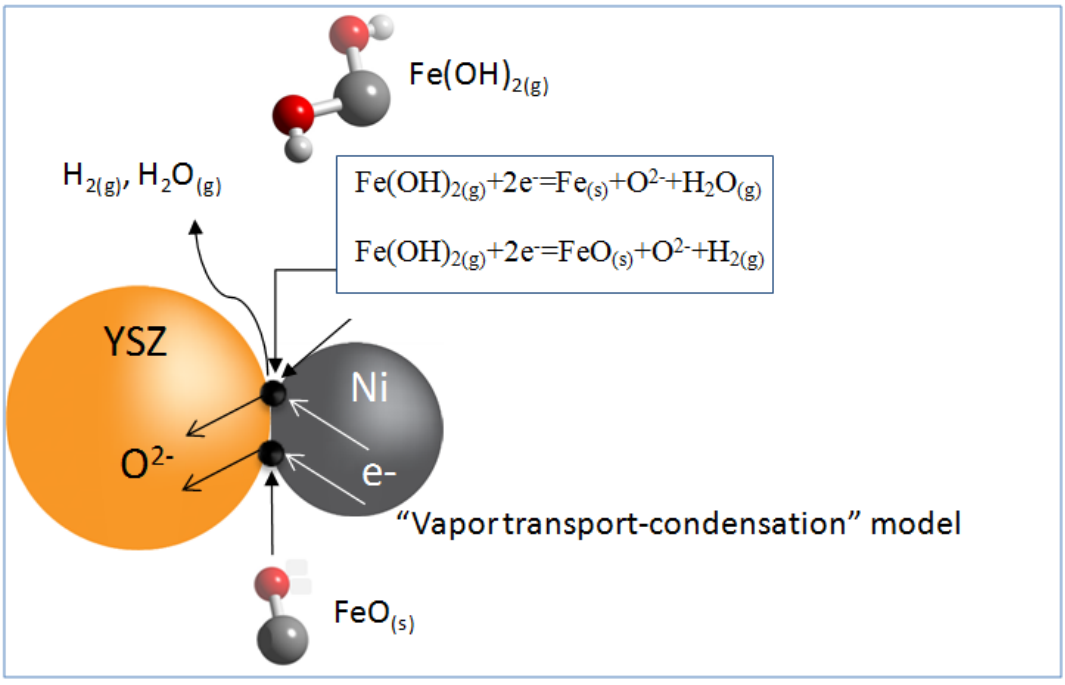

Figure 5.14 A model describing electrochemical condensation of $Fe_{(s)}$ and $FeO_{(s)}$ at

the triple-phase boundaries of the fuel-electrode during battery operation

To summarize, the energy storage characteristics of SOFeARB operated at 800^{o}C was investigated by using a simplified planar cell configuration. The specific energy and efficiency characteristics of this battery are strongly dependent on the degree of iron utilization: higher specific charge and specific energy, but lower round-trip efficiency, can be produced at higher iron utilization, and lower specific charge and specific energy, but higher round-trip efficiency, can be produced at lower iron utilization. Improving electrochemical performance of the RSOFC components and catalytic activity of the ESU materials are attractive approaches to boost efficiency while maintaining high specific energy.

5.2 SOFEARB OPERATED AT 650^{o}C

The novel SOMARB storage battery concept has been successfully demonstrated with 800^{o}C-SOFeARBs as a model SOMARB. Its demonstrated energy storage characteristics have promised this class of new metal air batteries to be a potential next-generation grid EES mechanism. However, a number of challenges still need to be met before it can become a commercially viable energy storage product. First, the operating temperature is too high to be a reliable EES system, although the high operating temperature is an advantage to promote high conductivity in the electrolyte and fast reaction kinetics in electrodes and redox couple. Second, the degradation is still too fast for a commercial product. Therefore, an optimal temperature window that can best

balance kinetics, durability and cost is needed. For the development of RSOFC, a well-accepted temperature window is within 550-650^{o}C where reasonably fast kinetics can be maintained with improved durability and reduced cost. Selection of the same operating temperature window for the SOFeARB and other SOMARB chemistries is also beneficial to the energy storage. As the temperature decreases, the MTSE becomes higher, and more importantly the coarsening of fine metal-particles in the redox-couple can be mitigated, thus extending the lifetime of a SOMARB. It is evident from Figure 3.3 and Figure 3.6 that the Fe-Fe_3O_4 stable at T≤600^{o}C possesses a higher EMF and MTSE than those of Fe-FeO stable at T>600^{o}C. A much higher discharge capacity (>1,000 mAh/g) has indeed been experimentally observed on Fe-Fe_3O_4 as the redox-couple at 600^{o}C [104, 105], although it was H_2 not electricity used to recharge the battery. Since the overall performance of a SOFeARB is primarily determined by RSOFC and ESU, this section examines the performance of SOFeARB operated at 650^{o}C with Fe-FeO as the ESU.

The performance stability was examined by continuously cycling under j=50 mA/cm^2 for 100 times. Each single discharge or charge cycle was set to 10 min. Overall, the cycling performance shown in Figure 5.15 (a) is rather stable, although there is a slight degradation during the first 20 cycles. The degradation for the first 5 cycles is observed for both the discharge and charge cycles, after which the degradation is only seen for the charge cycle from 5 to 20 cycles. After 20 cycles, no obvious degradation can be discerned for all the cycles. The averaged discharge specific energy (DSE) over 100 cycles is 760 Wh/kg-Fe as

shown in Figure 5.15 (b), which is about 77.1% of MTSE (=986 Wh/kg-Fe at 650°C). When compared with the average charge specific energy (CSE) (=1,370 Wh/kg-Fe), the battery cycled at a round-trip efficiency of 55.5%. This performance is better than the Fe-air cell using a YSZ electrolyte at 1000°C, in which the average round-trip efficiency over 10 continuous cycles is only 12%[128].

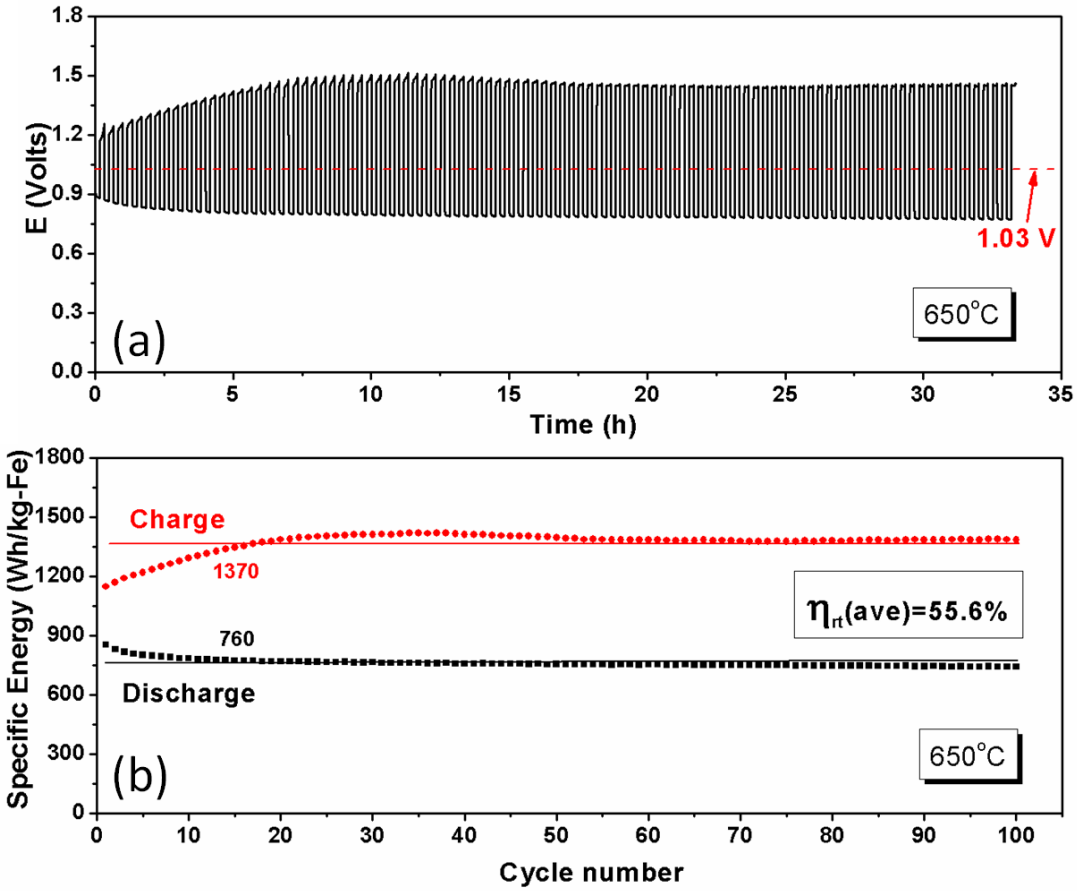

Figure 5.15 (a) Discharge and charge characteristics of the battery at 650°C and j=50mA/cm^2; (b) Plot of specific energy as a function of the number of discharge and charge cycles[129].

The lowered DSE and RTE in comparison to the theoretical values reflect the degree of energy losses to polarizations of the RSOFC and kinetic resistances of the redox reactions.

To investigate the root cause of the degradation, impedance spectra and V-I curves of the RSOFC before and after the test were measured, the results of which are shown in Figure 5.16. The impedance spectra of Figure 5.16 (a) clearly show increases in area-specific resistances (ASRs) of ohm and polarization after 100 discharge/charge cycles. The total ASR of the battery was increased from 3.01 $\Omega \cdot cm^2$ to 5.48 $\Omega \cdot cm^2$. The increase in polarization ASR is much severer than that of ohmic ASR, 2.14 Ωcm^2 *vs* 0.33 Ωcm^2. The V-I curves and the power performances in Figs. 5.16 (b) and (c) further confirm this reduction. The reduction in power density of RSOFC shown in Figure 5.16 (c) corresponds to the increases in ASR found by electrochemical impedance study, decreasing from the original 131 to 60 mW/cm^2 after 100 cycles.

To further investigate why the battery's initial performance has degraded, microscopic examination on the RSOFC was carried out. Figure 5.17 (a) shows the RSOFC consisting of all the three functional layers: air-electrode, electrolyte and fuel-electrode. The contacts between electrolyte and electrodes seem to be intact. Figures.5.17 (b) and (c) show that the bonding between air electrode and electrolyte was not affected after the 100 cycles. Figure 5.17 (d) further shows that the infiltrated SSC-SDC fine particles remain well dispersed in the porous LSGM skeleton after the test. Such an air-electrode structure is deemed beneficial to the retention of battery's performance[118]. The comparison in Figures 5.17 (e) and (f) of the interface between fuel-electrode and electrolyte before and after test appears to suggest that the detachment at

the interface after the cyclic test could attribute to the increase in the total ASR observed. How to make a good fuel electrode of RSOFC under the testing conditions is, therefore, critical to achieve a higher and more stable performance for the battery, according to this study.

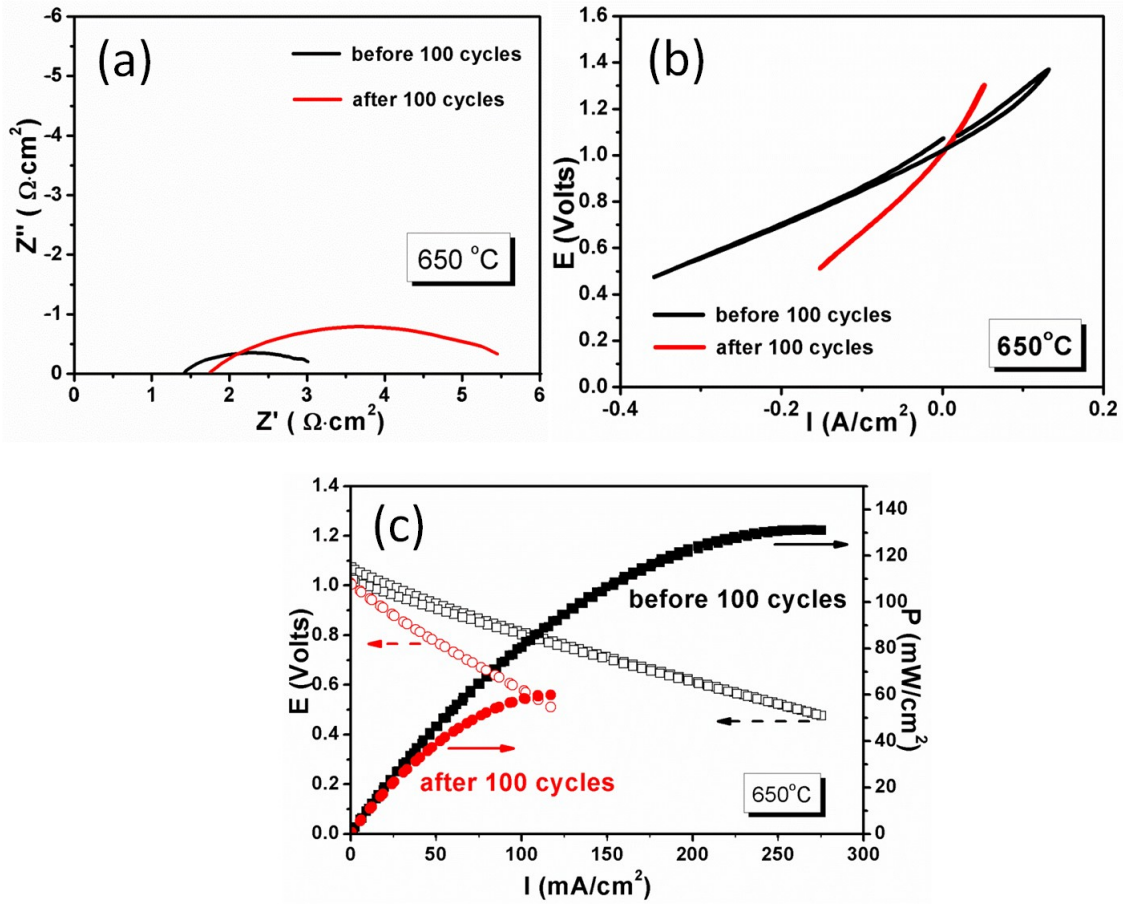

Figure 5.16 Electrical performance of RSOFC measured under the open circuit and 650°C. (a) Impedance spectra; (b) V-I curves and (c) power performances before and after 100 galvanic cycles.

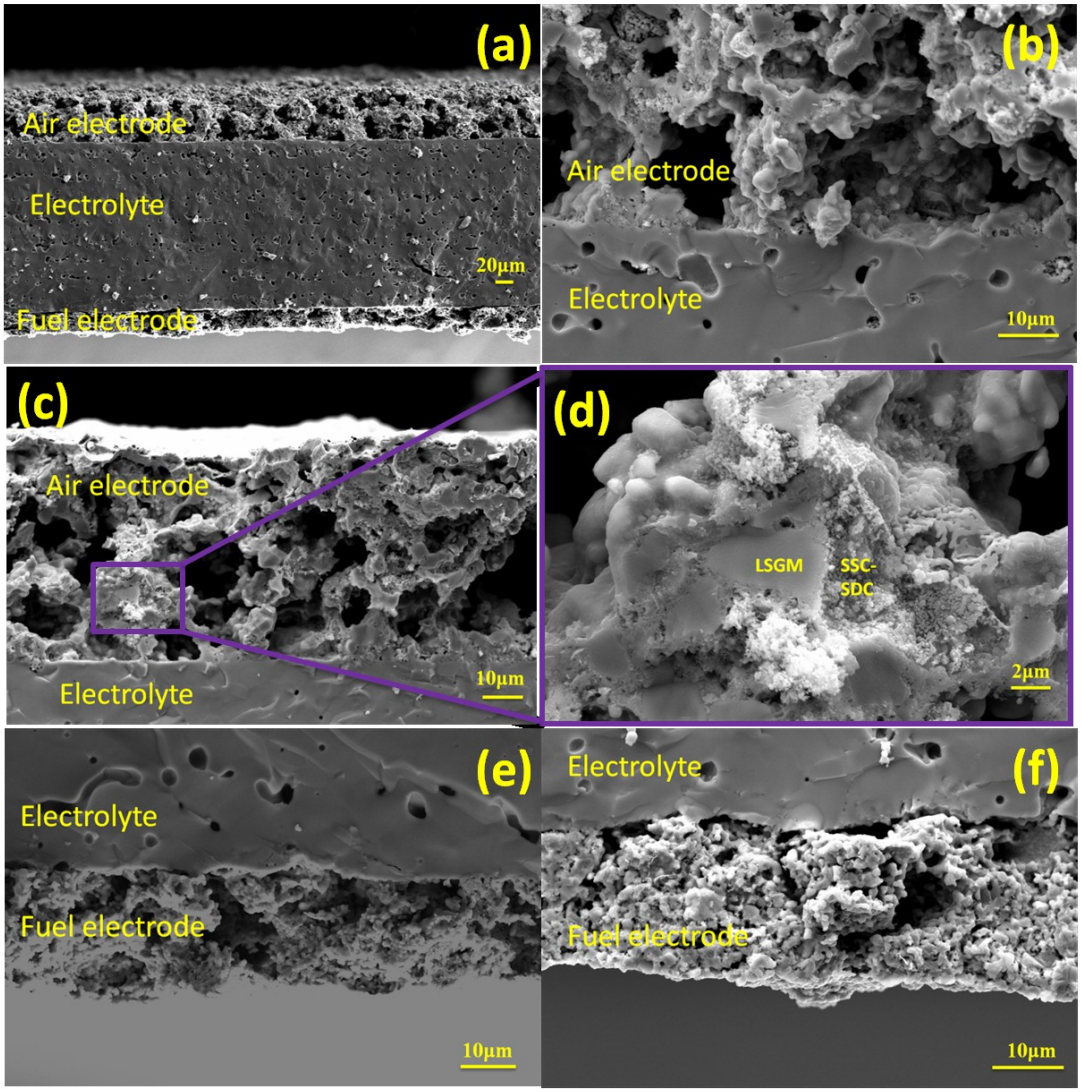

Figure 5.17 Cross-sectional view of the microstructures of a RSOFC: (a) the whole battery; (b) magnified prior-test air-electrode/electrolyte interface; (c) magnified post-test air-electrode/electrolyte interface; (d) magnified post-test air-electrode with porous LSGM infiltrated by SSC-SDC nanoparticles; (e) magnified prior-test fuel-electrode/electrolyte interface and (f) magnified post-test fuel-electrode/electrolyte interface[129].

The overall performance of the battery is determined not only by RSOFC, but also by the Fe-based ESU. Our previous study has shown that the Fe-based ESU is capable of retaining its porosity and grain size even after enduring test at 800^{o}C, mainly benefited from the presence of ZrO_2 as the sintering inhibitor[119]. Figure 5.18 shows that similar

microstructures of the same ESU can also be retained for 650^{o}C. In particular, spherical particles of Fe are seen in Figure 5.18 (b) being uniformly distributed across the ESU after the test. No significant changes in the microstructure of ESU can be found to attribute to the degradation of the battery. Therefore, the degradation shown in the cycle stability test should be mainly originated from the RSOFC.

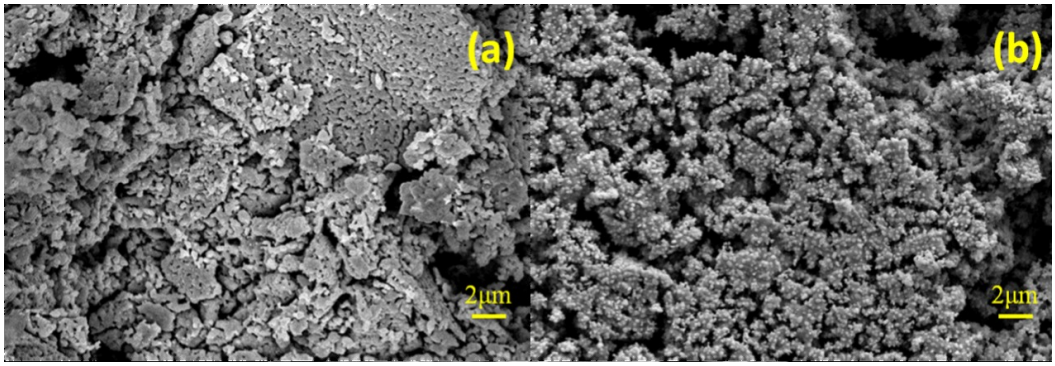

Figure 5.18 Microstructures of the Fe-FeO energy storage medium; (a) prior test and (b) post test[129].

5.3 SOFEARB OPERATED AT 550^{o}C

We further lower the operating temperature of the SOFeARB to 550^{o}C, where the stable redox couple is Fe-Fe_3O_4 other than Fe-FeO. Different from FeO, where ample defects exist, Fe_3O_4 lacks of defects, which is not beneficial for the redox kinetics in the battery. This disadvantage in line with lowered operating temperature poses greater challenges to the kinetics of the whole battery. Therefore, in this work, we studied the effects of catalyst, and porosity of the ESU on the performance SOFeARB operated at 550^{o}C.

5.3.1 550°C-SOFeARB baseline performance

The baseline battery contains the pellets of Fe-Fe_3O_4 redox-couple prepared from the co-precipitation method described in previous chapter 4. Figure 5.19 shows the cycling performance characterized under the conditions of t=550°C, j=10 mA/cm^2 and n=10 continuous 2-h discharge and 2-h charge cycles. The current density necessary to achieve a meaningful cell voltage was largely limited by the performance of the RSOFC operated at this low temperature.

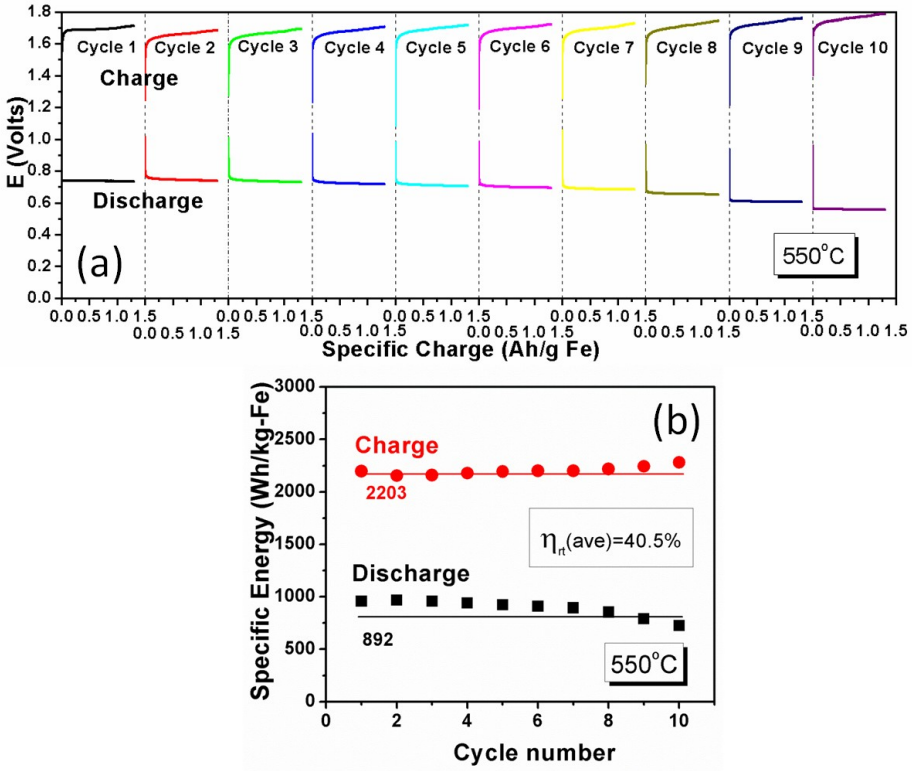

Figure 5.19 The performance of the baseline battery operated at 550°C for 10 continuous cycles with single-cycle duration of 2 hours under a current density of 10 mA/cm^2; (a) E vs specific charge; (b) averaged specific energy vs number of cycles[96].

The DSE was calculated from the amount of Fe consumed by the oxygen flux (or

current density) from the RSOFC, averaging 892 Wh/kg·Fe. Similarly, the CSE was averaged to be 2,203 Wh/kg·Fe, yielding a round-trip efficiency of 40.5%. It should be noted that the normalization of the specific energy to the amount of Fe consumed by the oxygen flux allows for a direct comparison with the MTSE, difference of which reveals the scale of the battery's inefficiency. The obtained DSE is evidently lower than the MTSE=1,360 Wh/kg·Fe calculated from $\Delta G_r^o(550^oC)$ of the iron-oxygen reaction $3Fe + 2O_2 = Fe_3O_4$. This difference (DSE amounts to 65.6% of MTSE) reflects the degree of energy loss to the electrical polarizations of RSOFC and kinetic resistance of Fe/Fe_3O_4 redox couple. Indeed, the RSOFC for the test employed a thick LSGM electrolyte membrane (350 μm, see Table 4.3, Gen 1) and electrode materials that have not been fully optimized for operating at 550^oC. With the use of electrode-supported thin-film electrolytes and more active electrode (particularly air-electrode) materials, the energy loss is expected to be lesser and efficiency to be higher.

The low round-trip efficiency is another sign of energy loss and irreversible redox kinetics. It is known that the total cell resistance of a RSOFC operating under "electrolysis" mode has a tendency to be greater than that of "fuel-cell" mode, which can result in a reduced round-trip efficiency. On the other hand, the lower kinetic rate of Fe_3O_4-reduction to Fe than the oxidation of Fe to Fe_3O_4 also decreases the round-trip efficiency. Overall, the 550^oC Fe/Fe_3O_4 battery has ample rooms to further improve its specific energy and efficiencies by optimizing the components of RSOFC (e.g., use of new cell materials and optimization of microstructure) and promoting the redox kinetics (e.g., use of catalysts, use

of fine-particle active metals).

5.3.2 Performance of 550°C-SOFeARB with CeO_2 modified ESU: effect of catalyst

As a means of promoting the redox kinetics, nanoparticles of CeO_2 were incorporated into the microstructure of Fe-Fe_3O_4 as a catalyst, testing result of which is shown in Figure 5-20. The battery was cycled for 10 times under the conditions of t=550°C, j=10 mA/cm^2 and cycle duration of 2 hours. Compared to Figure 5.19 of the baseline battery, the improvement is evident in discharging cycle: higher and more stable voltage. The DSE reached 1,026 Wh/kg·Fe, yielding a round-trip efficiency of 52.2% when compared to the CSE=1,971 Wh/kg·Fe. These results represent a 15% and 29% improvement in specific energy and round-trip efficiency, respectively, over the baseline battery. It also appears that there was no apparent performance decay over the 10 continuous repeated charge-discharge cycles.

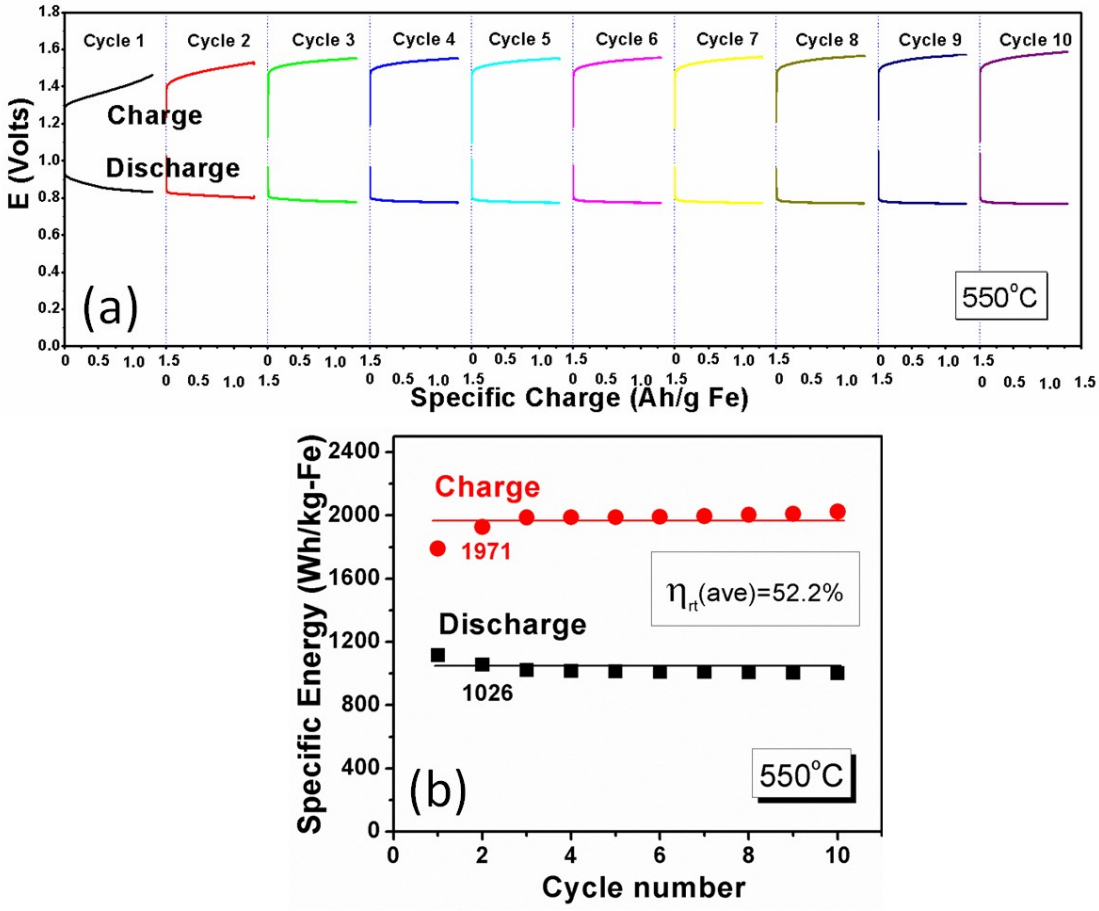

Figure 5.20 The performance of the CeO_2-catalyzed battery operated at 550°C for 10 continuous cycles with single-cycle duration of 2 hours under a current density of 10 mA/cm^2; (a) E vs specific charge; (b) averaged specific energy vs number of cycles[96].

The promotion of redox reaction kinetics by CeO_2 has been well documented in the literature [130-133]. The mixed valence of Ce^{4+}/Ce^{3+} in low partial pressures of oxygen contributes additional catalytic activity to the primary Fe-Fe_3O_4 redox reaction. Previous studies have also reported that Ce can retain the redox activity of Fe-oxides for repeated redox cycles[130]. On the other hand, nanoparticle catalysts can boost the rate of redox reaction by increased surface area. Figure 5.21 shows the morphologies of CeO_2 nanoparticles before and after tests. The original particle sizes of CeO_2 particles were

~50nm, and increased to approximately 60 nm after testing. Although the finely dispersed CeO_2 nanoparticles appear to have been sintered, the adherence of CeO_2 to the Fe/ZrO_2 backbones seems to have little effect on the catalytic activity of CeO_2 as suggested in Figure 5.20.

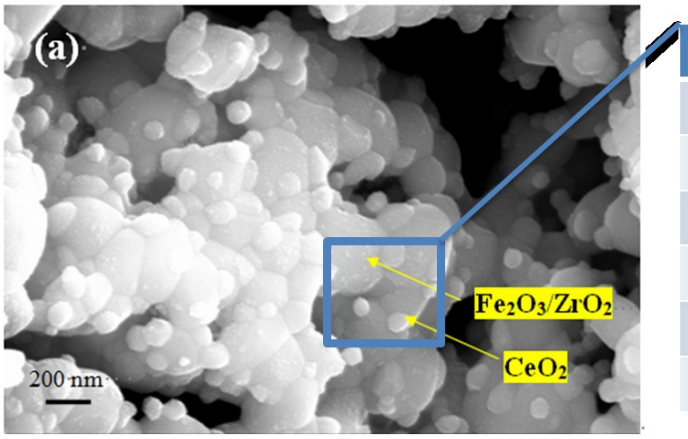

Element	Wt%	At%
OK	32.3	67.19
ZrL	14.83	5.41
CeL	2.83	0.67
FeK	42.79	25.5
AuL	7.27	1.23
Total	100	100

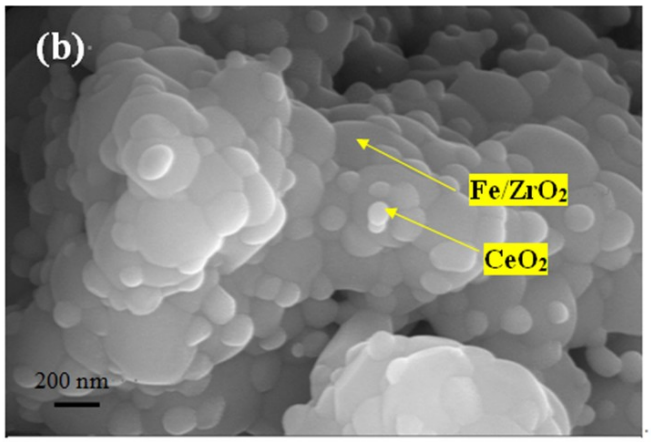

Figure 5.21 SEM images of CeO_2 nanoparticles inside Fe-based energy storage unit before (a) and after (b) tests[96].

5.3.3 Performance of 550°C-SOFeARB with ZrO_2-supported nanoparticle Fe-Fe_3O_4 redox couple: the effect of surface area

The active metal Fe in the form of nanoparticles supported on porous ZrO_2 substrate was also evaluated as the energy storage medium, result of which is shown in Figure 5.22.

The battery was operated at the same condition as the CeO_2-catalyzed battery of Figure 5.20. Compared to Figure 5.19 of the baseline battery, the improvement is also notable. The DSE reached 1,012 Wh/kg·Fe, yielding a round-trip efficiency of 59.9% with CSE=1,695 Wh/kg·Fe. These results represent 13% and 48% improvement in specific energy and round-trip efficiency, respectively, over the baseline battery. When compared to Figure 4-16 of the CeO_2-catalyzed battery, the major improvement is the lowered charging voltage, which is also the reason for the higher round-trip efficiency.

The issue of the nanoparticle redox couple is the poor cycle stability. This is likely caused by the thermal coarsening of these nanoparticles, resulting in a gradual loss of reactive surface area. The morphological change of the Fe nanoparticles in Figure 5.23 seems to support this assertion by showing the flaking morphology of Fe_2O_3 precursor before the test and a cluster of sintered Fe-grains after the test.

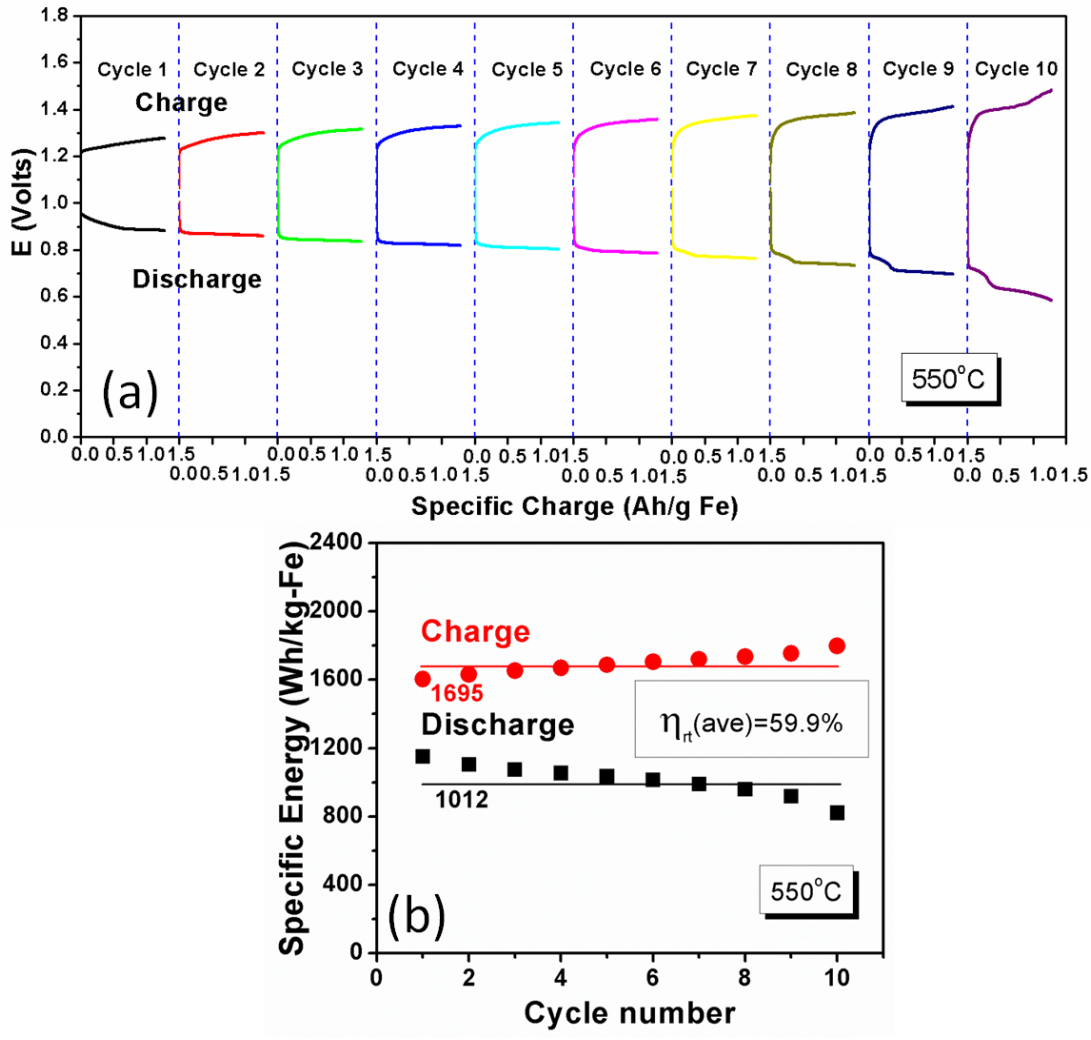

Figure 5.22 The performance of the battery with nanoparticle active Fe supported on porous ZrO_2 operated at 550°C for 10 continuous cycles with single-cycle duration of 2 hours under a current density of 10 mA/cm^2; (a) E vs specific charge; (b) averaged specific energy vs number of cycles[96].

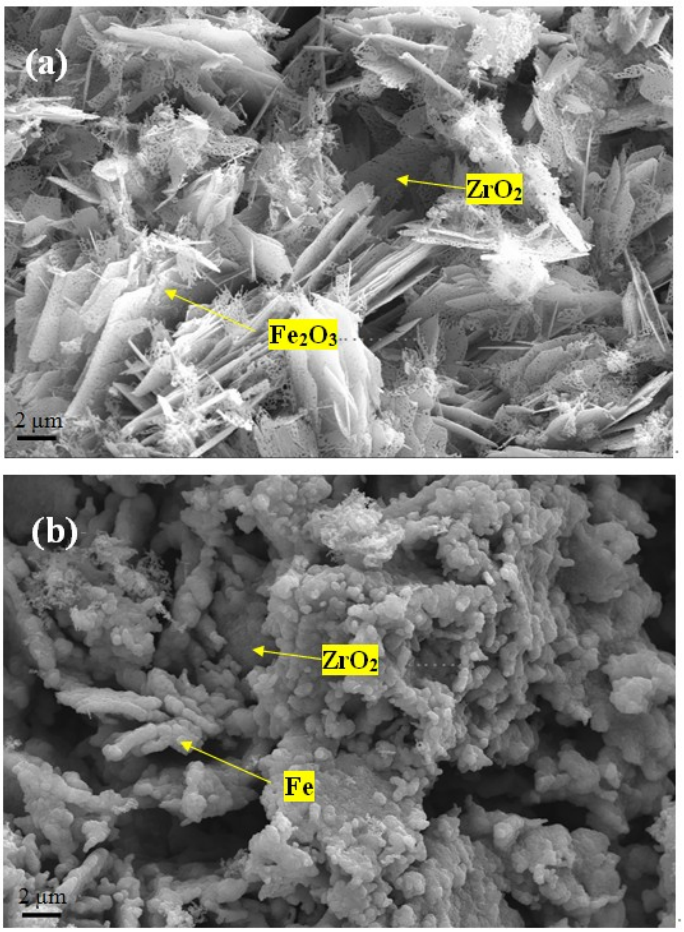

Figure 5.23 SEM images of active Fe nanoparticles inside Fe-based energy storage unit before (a) and after (b) tests

5.3.4 Performance of 550°C-SOFeARB with optimized ESU and RSOFC

The performance of the battery is not only affected by the ESU, but also determined by the RSOFC. Figure 5.24 shows the performance of the baseline battery operated at 550°C for 10 continuous cycles with single-cycle duration of 10 minutes under a current density of 10mA/cm^2. This battery yielded a DSE of 1,119 Wh/kg·Fe, which is up to 82.3% of MTSE, and a RTE of 67.1%, when compared with the CSE=1,669 Wh/kg·Fe.

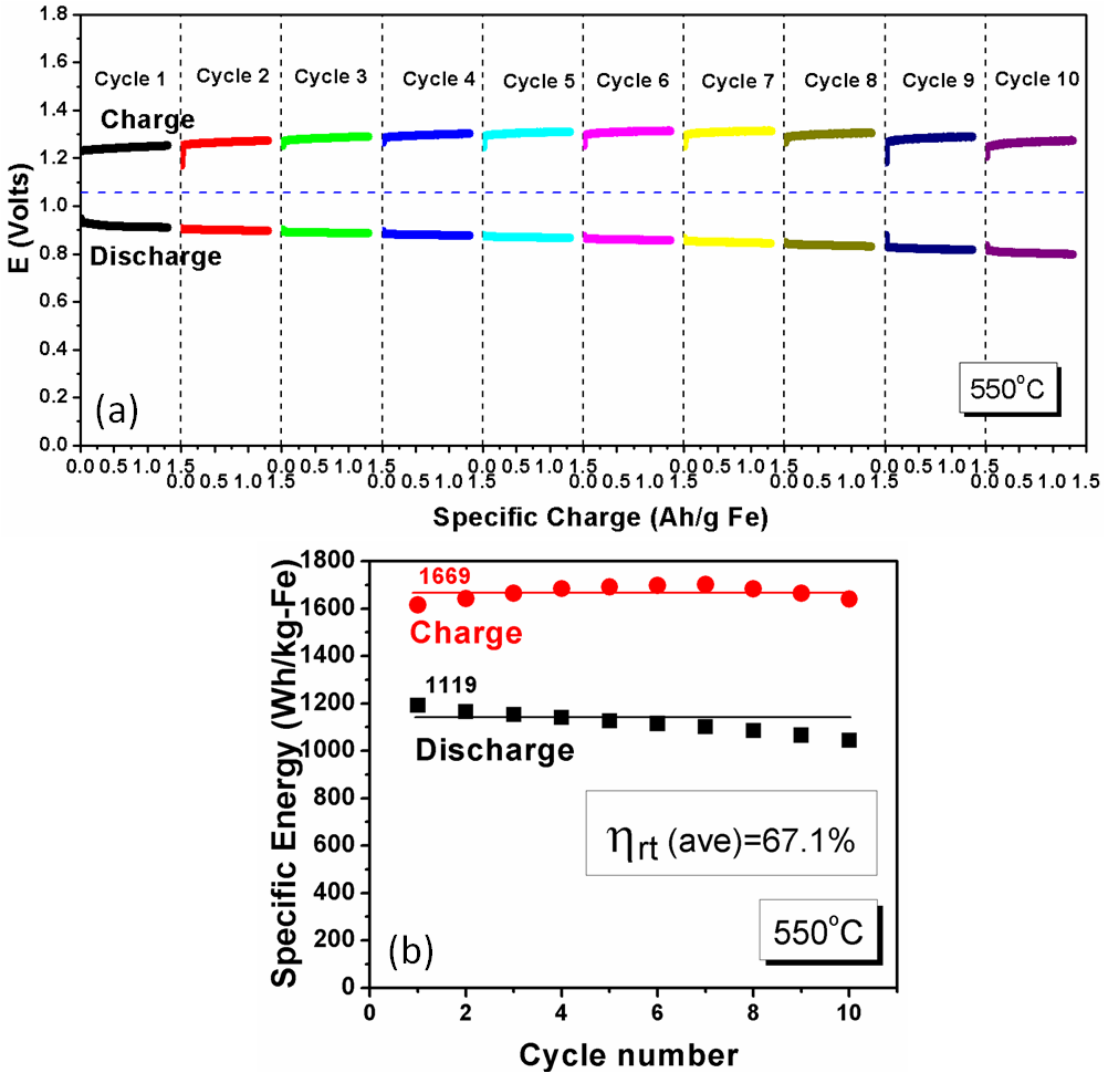

Figure 5.24 The performance of the baseline battery operated at 550°C for 10 continuous cycles with single-cycle duration of 10 minutes under a current density of 10 mA/cm^2 (a) E vs specific charge; (b) average specific energy vs number of cycles

The results of the battery with optimized ESU and optimized RSOFC as shown in Figure 5.25 are more promising. Under the testing conditions of t=550°C, j=10 mA/cm^2 and cycle duration of 10 minutes, the newly developed battery yielded a DSE of 1,237 Wh/kg·Fe, which is up to 91.0% of MTSE, and a RTE of 82.5%, when compared with the CSE=1,500 Wh/kg·Fe.

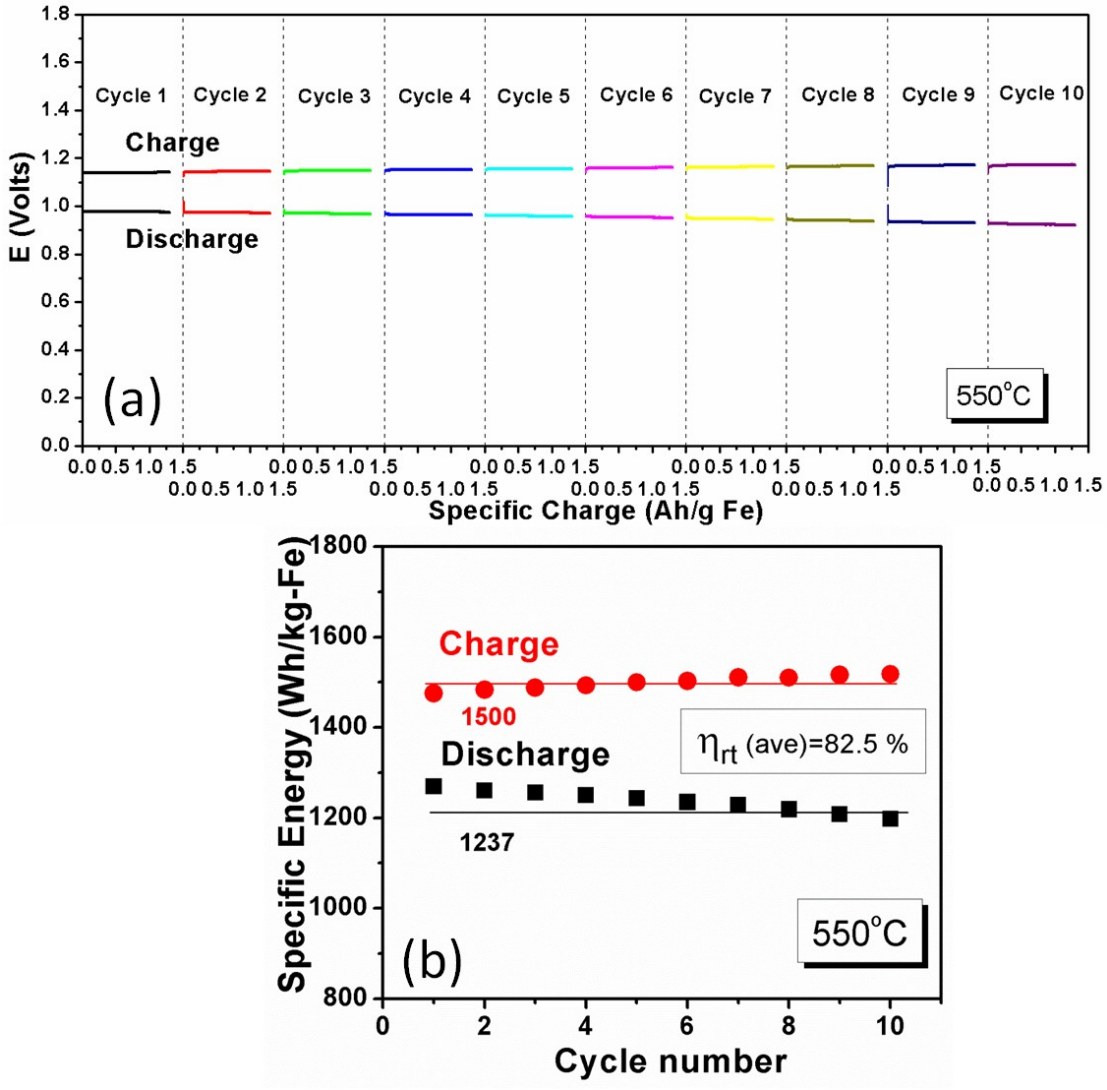

Figure 5.25 The performance of the optimized battery operated at 550°C for 10 continuous cycles with single-cycle duration of 10 minutes under a current density of 10 mA/cm^2 (a) E vs specific charge; (b) average specific energy vs number of cycles[96].

The improved battery performance is a direct result of lowered ASRs of the RSOFC as is shown in Figure 5.26. The initial ASR of the RSOFC is only 40% of the RSOFC used in the baseline battery. After cycling, the ASR increased only 5 Ω·cm^2, much less than 53 Ω·cm^2 observed in the post-tested RSOFC of the baseline battery.

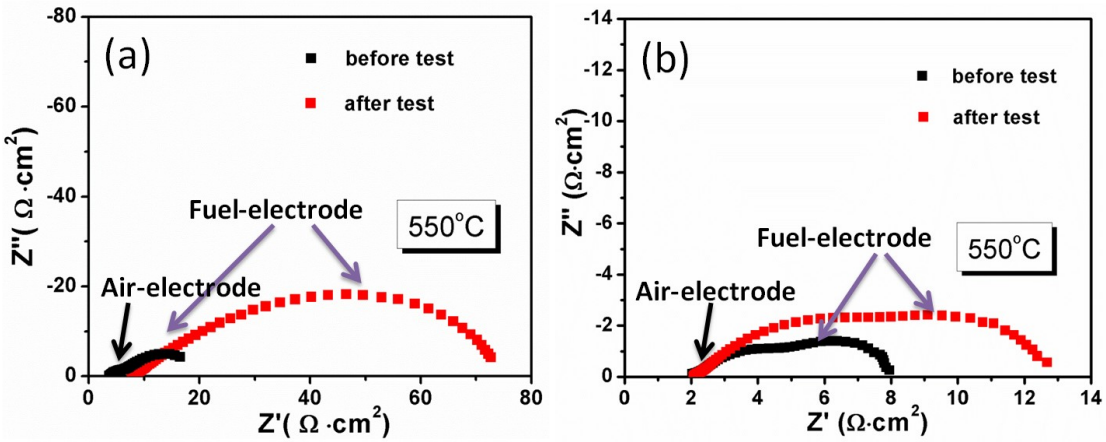

Figure 5.26 Comparison of AC impedance spectra before and after cycling measured from the batteries with Gen 1 RSOFC (a) and with Gen 3 RSOFC (b)[96].

5.3.5 Cyclic stability of 550°C-SOFeARB

The cyclic stability performances of the 550°C-SOFeARBs were also examined. As previously indicated, IT-SOFeARB operated at 550°C uses Fe-Fe_3O_4 redox couple as the ESU while its counterpart at 650°C has Fe-FeO. We examined the performance stability of the baseline battery under the similar testing condition at j=10mA/cm^2. It is evident from Figure 5.27 (a) that the cycling performance of 550°C-battery is less stable than the 650°C-battery as shown in Figure 5.15. The average DSE of this 550°C-battery over 100 cycles is 1056 Wh/kg-Fe as shown in Figure 5.27 (b), which is about 77.6% of the MTSE=1, 360 Wh/kg at 550°C. When compared with the average CSE (=1,765 Wh/kg-Fe), the battery cycled at a round-trip efficiency of 59.8%.

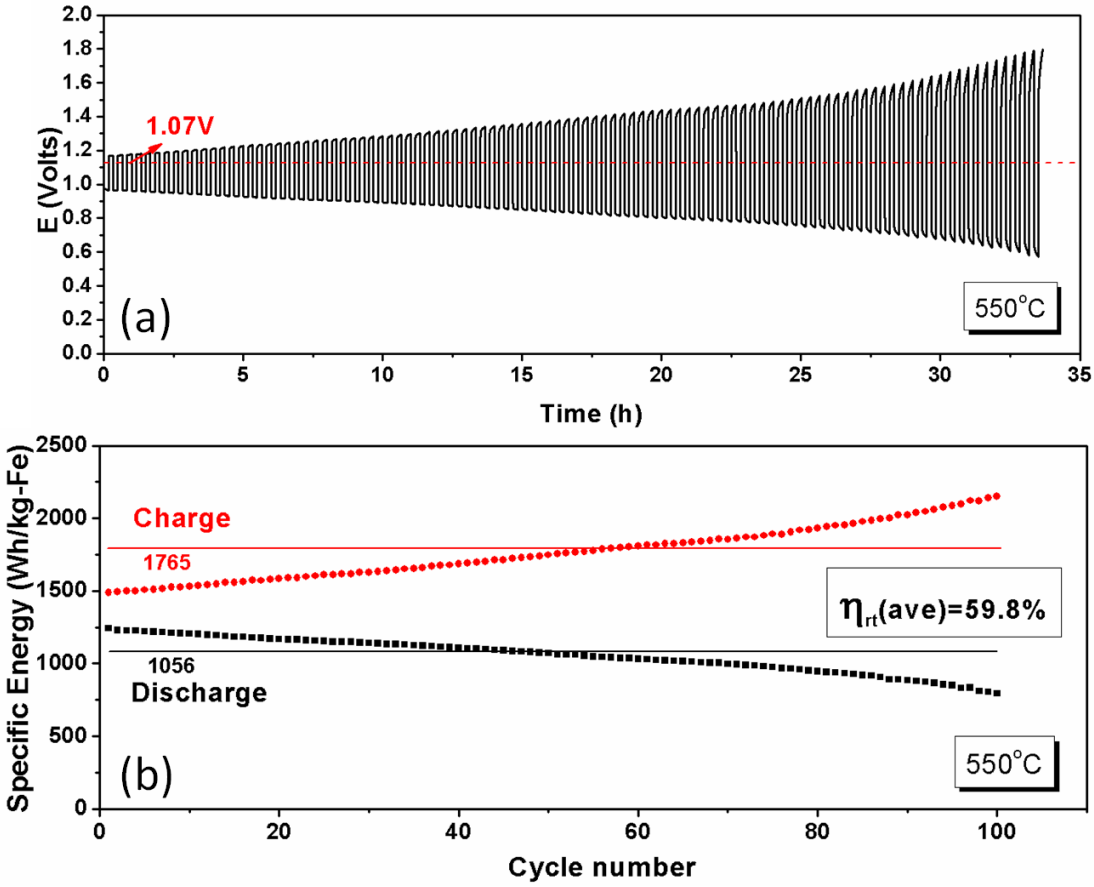

Figure 5.27 (a) Discharge and charge characteristics of the battery at 550°C and j=10mA/cm^2; (b) Plot of specific energy as a function of the number of discharge and charge cycles.

The impedance spectra and V-I curves of the RSOFC before and after the test were also measured, as shown in Figure 5.28. The impedance spectra of Figure 5.28 (a) clearly show increases in area-specific resistances (ASRs) of ohm and polarization after 100 discharge/charge cycles. The total ASR of the battery was increased from 10.23Ω·cm^2 to 54.75Ω·cm^2. The increase in polarization ASR is much severer than that of ohmic ASR, 2.05 Ωcm^2 *vs* 42.47 Ωcm^2. The V-I curves and the power performances in Figures. 5.28 (b) and (c) further confirm this reduction. The reduction in power density of RSOFC shown in Figure 5.28 (c) corresponds to the increases in ASR found by electrochemical impedance

study, decreasing from the original 33.5 to 4.7 mW/cm^2 after 100 cycles. This impedance performance will be later compared with the carbothermic reaction derived Fe/C-air battery.

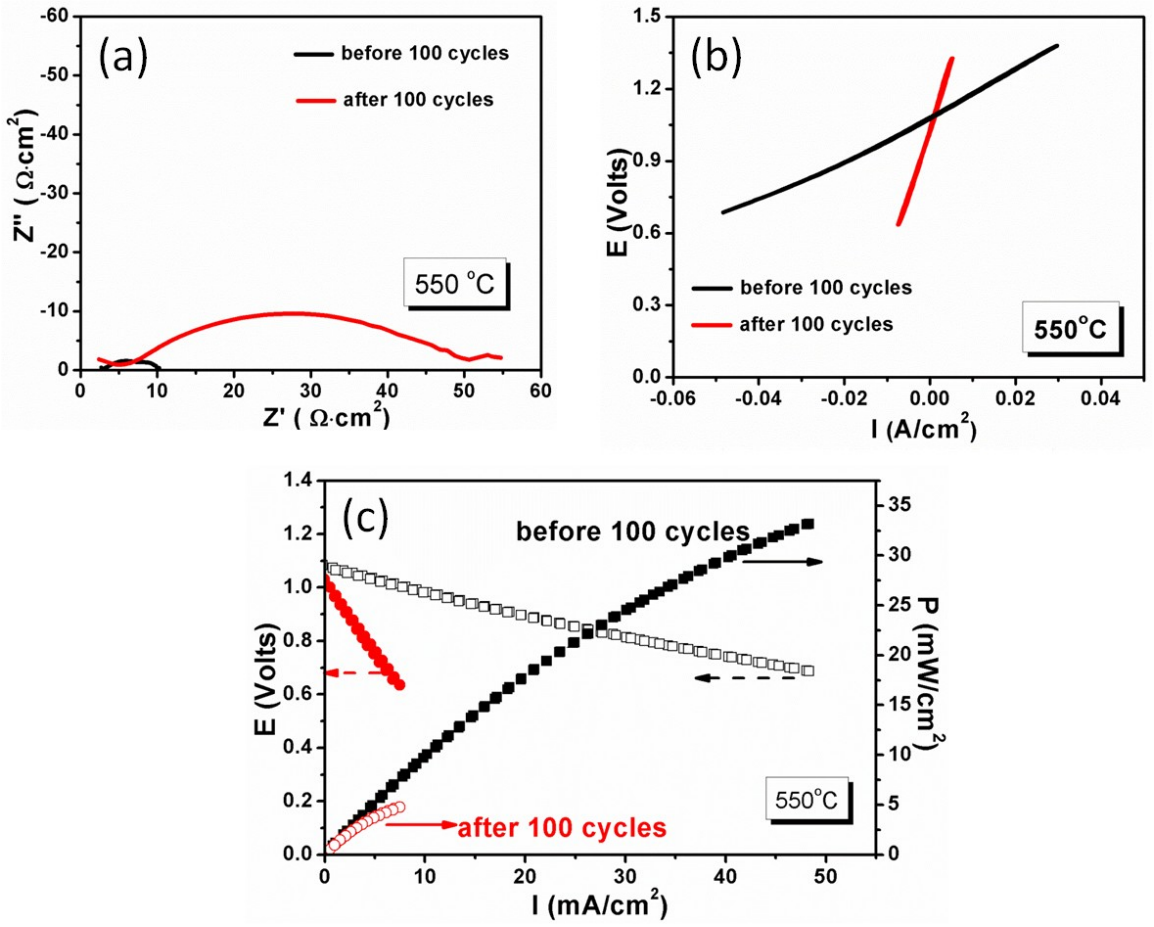

Figure 5.28 Electrical performance of RSOFC measured under the open circuit and 550^{o}C. (a) Impedance spectra; (b) V-I curves and (c) power performances before and after 100 galvanic cycles.

Figure 5.29 shows the post-test microstructures of the RSOFC in the battery tested. Figure 5.29 (a) exhibits the cross sectional view of the whole RSOFC with all the three functional layers. Figure 5.29 (b) shows that the bonding between air electrode and electrolyte was not affected after the 100 cycles. The infiltrated SSC-SDC fine particles

remain similar to that in Figure 5.17 (b). Figure 5.29 (c) shows that the bonding between fuel electrode and electrolyte was completely detached, which may well have happened during the cycles, according to the in-situ impedance spectra recorded in Figure 5.28. Therefore, making a stronger and more durable fuel electrode is critical to ensure the cyclic durability.

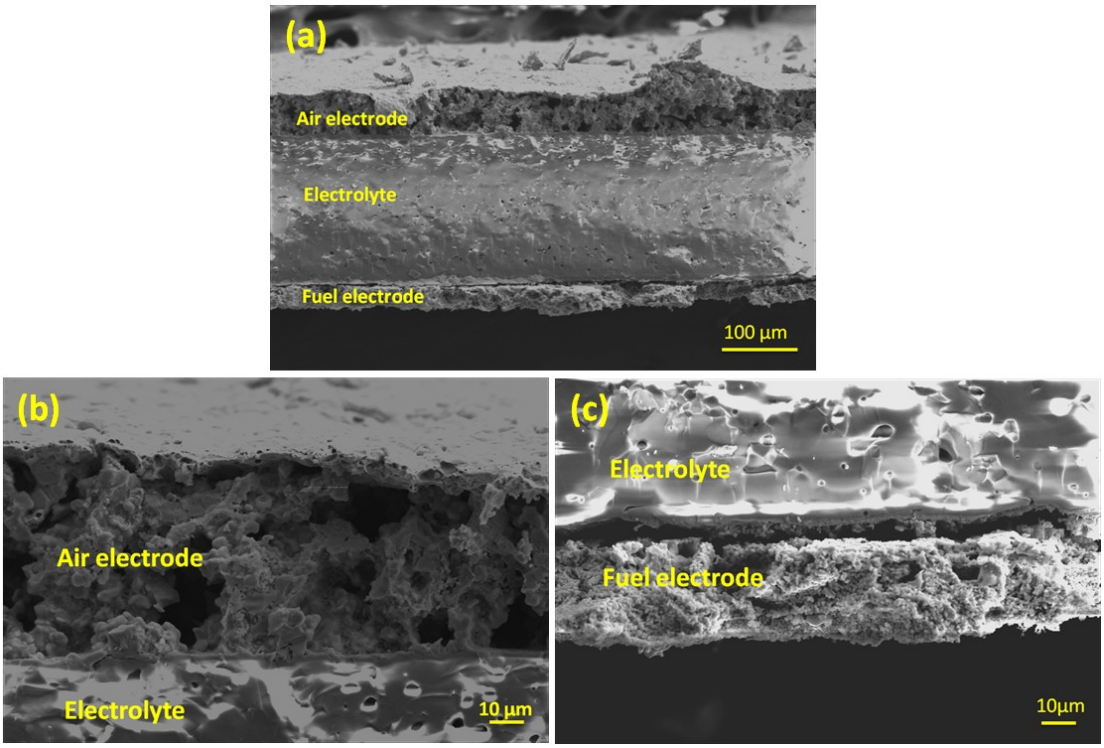

Figure 5.29 Cross-sectional view of the microstructures of the post-test RSOFC in an Fe-air battery: (a) the whole battery; (b) magnified electrolyte/air-electrode interface with porous LSGM infiltrated by SSC-SDC nanoparticles; (c) magnified fuel electrode/electrolyte interface.

5.4 CYCLIC STABILITY OF 550°C-SOFEARB WITH CARBOTHERMIC REACTION DERIVED FE-BASED ESU

The cyclic stability of a 550°C-SOFeARB was also investigated, in which Fe-ESU was synthesized by conventional carbothermic reaction. The unique nanostructures

created by the departure of gaseous products CO and CO_2 are believed beneficial to the redox kinetics of the synthesized ESU. A detailed description of the synthesis method has been given in section 4.1.1.4.

The energy storage characteristic of the battery is shown in Figure 5.30. The battery was continuously cycled at the current density j=10mA/cm^2 for ten consecutive 10-min cycles, producing a constant DSE 1,258 Wh/kg-Fe; it is 93% of the MTSE. The round-trip efficiency (RTE) is 83.3% when compared the DSE with the CSE of 1,510 Wh/kg-Fe. This performance is even better than the optimized 550^oC Fe-air battery shown in Figure 5.25 [96]. No degradation is detectable during the cycle period.

The effects of operating current density (j) and cyclic duration (t) on DSE/CSE and RTE were also evaluated, the results of which are shown in Figure 5.31. It is evident from these plots that the j has a greater impact on DSE/CSE and RTE than cyclic duration (t). This is understandable in that a higher j leads to a greater voltage loss (discharge) or voltage increase (charge) due to battery's internal resistance, resulting in lowered DSE/CSE and RTE. The insensitivity of RTE to t at a fixed j suggests a good reversibility of the Fe/C-ESU. This comparison also infers that operating SOFeARB under a lower j for a longer cyclic duration is a favorable testing approach to achieving a required energy storage rating.

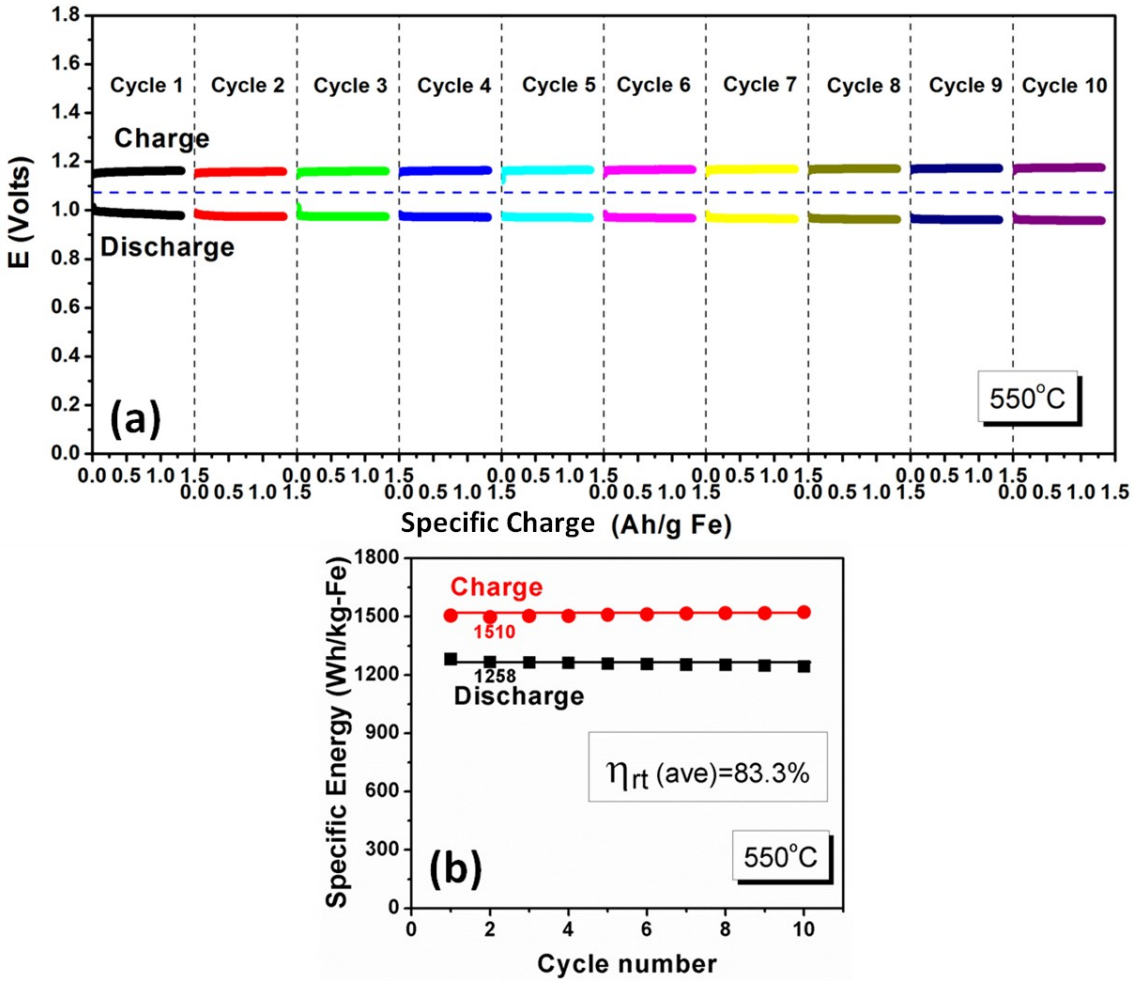

Figure 5.30 Cyclic performance of the SOFeCARB with carbothermic reaction derived Fe-ESU under a current density of 10 mA/cm^2 (a) E vs specific charge; (b) average specific energy vs number of cycles[134].

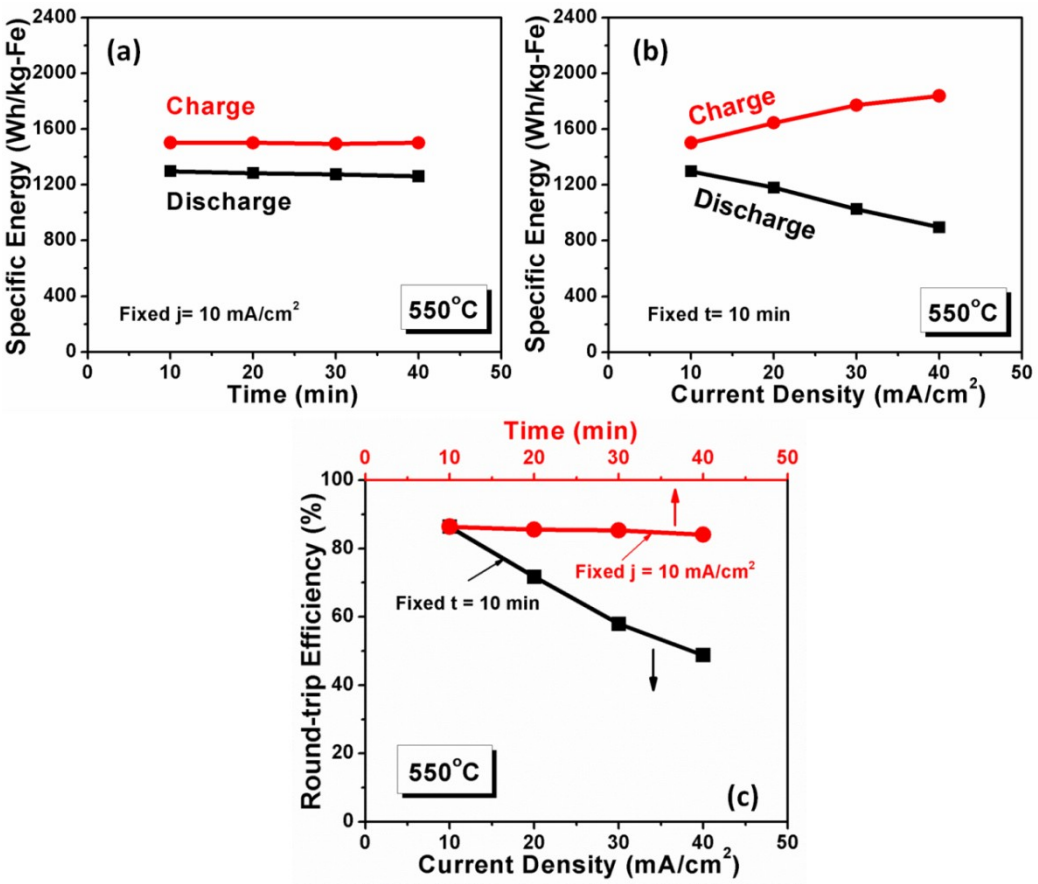

Figure 5.31 Dependence of DSE/CSE and RTE on current density (j) and cyclic duration (t) characterized at 550°C. (a) DSE/CSE vs t at a fixed j=10mA/cm^2; (b) DES/CSE vs current density at a fixed t=10min. (c) RTE-j-t relationship.

The long-term cyclic stability of the Fe/C-air battery under j=10 mA/cm^2 compared with the baseline Fe-air battery at 550°C (see Figure 5.27) for the same 100 cycles is shown in Figure 5.32. Evidently, the Fe/C-air battery shows superior stability over the baseline. The average degradation rate for the Fe/C-air battery is estimated to be 214% lower than the baseline. The DSE and RTE of the Fe/C-air battery averaged from the 100 cycles are 1,188 Wh/kg-Fe and 76.3%, respectively; this level of performance presents a 12.5% and 27.6% improvement over the baseline (1,188 vs 1,056 and 76.3% vs 59.8%); The lowered DSE and RTE for the 100-cycle test than the initial 10-cycle study shown in Figure 5.30

(1,188 vs 1,258 Wh/kg-Fe and 76.3% vs 83.3%) reflect the degree of degradation throughout the 100-cycle test. To investigate the root causes for the performance difference observed in the Fe/C-air and Fe-air batteries, we studied the EIS spectra from both batteries before and after 100 cycles, discovering that the resistance of Fe/C-air battery is consistently lower than the baseline after the test. Figure 5.33 shows that impedance spectra of the two batteries prior to cyclic testing are similar. It is not surprising that they used the same RSOFCs. After the 100- cycle, the total ASR of the RSOFC with Fe/C ESU only increased by 11.5 $\Omega \cdot cm^2$, much less than 44.5 $\Omega \cdot cm^2$ for that with Fe ESU. After reduction by H_2, both RSOFCs showed signs of recovery, but only the RSOFC with Fe/C ESU restored close to its initial performance. The ASR of RSOFC with the baseline ESU was ~22 Ωcm^2, nearly twice the initial value. These comparisons suggest that ESU has an effect on the performance of RSOFC. Faster redox kinetics and better oxygen shuttling between ESU and RSOFC can support a faster mass transfer and charge transfer in the fuel electrode of the RSOFC. Therefore, it can be concluded that the new Fe/C-ESU has a better redox kinetics.

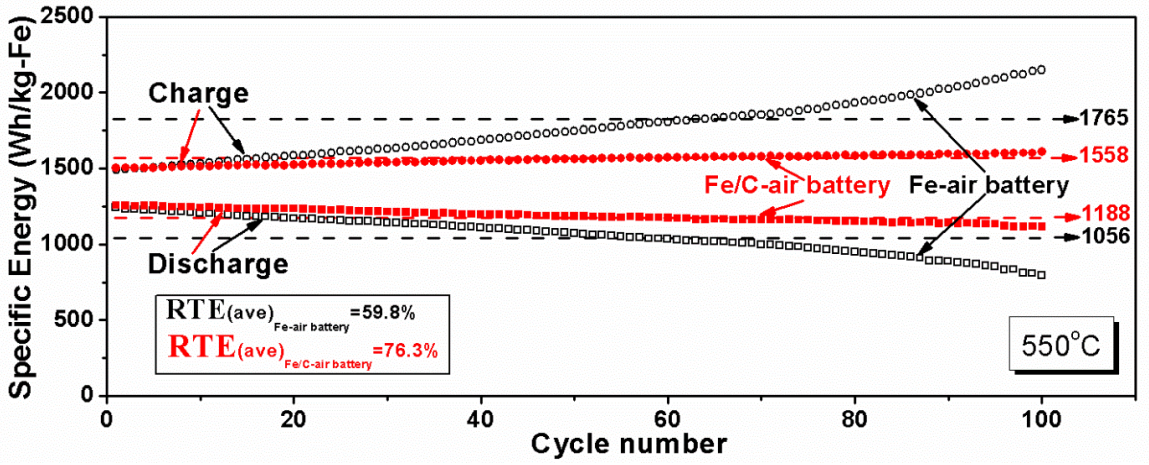

Figure 5.32 Cyclic stability comparison between SOFeCARB and SOFeARB under 550°C and j=10mA/cm^2[134].

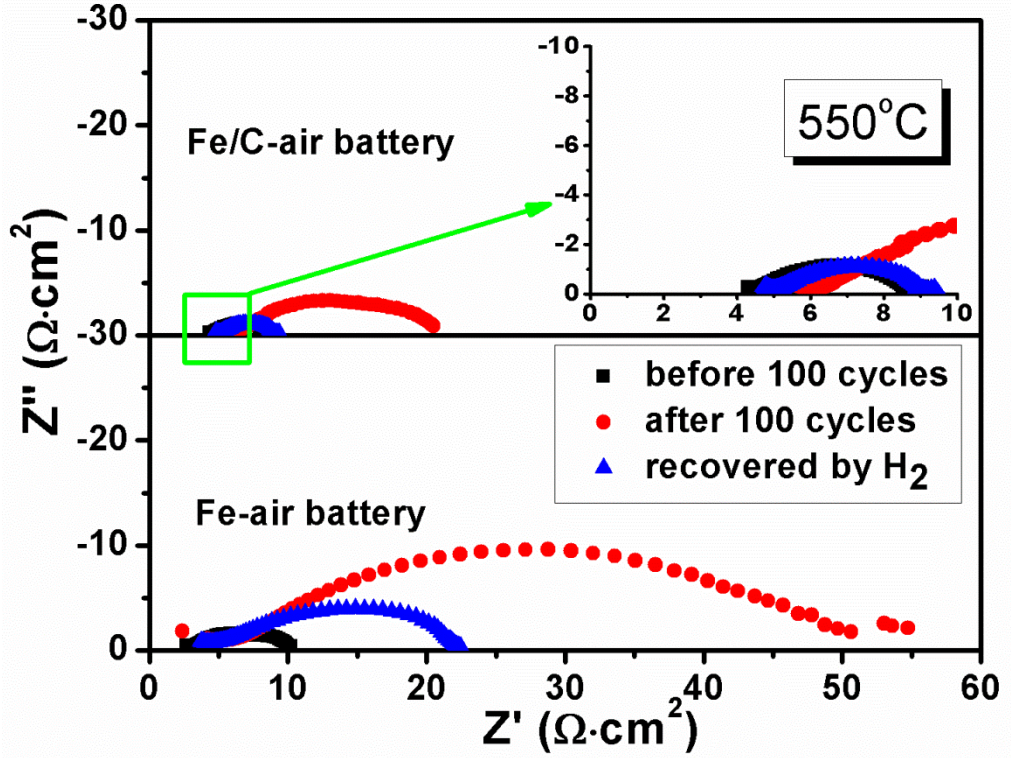

Figure 5.33 Comparison of EIS spectra measured from the baseline Fe-air and Fe/C-air batteries under different states[134].

The voltage as a function of state-of-charge was also investigated. The battery's state-of-charge is represented by the utilization of metal (discharge) or metal-oxide

(charge). To show a wider range of state-of-charge, a longer cyclic duration is needed to have appreciable amount of metal or metal oxide utilized. Since the SOMARB exhibits an EMF fixed by the thermodynamic equilibrium existed between metal and metal-oxide [68, 96, 119], its operating voltage should be independent of the state-of-charge under a galvanic mode until all the active metals or metal-oxides are depleted. In other words, the amount of metal loading determines the storage capacity of a SOMARB.

A single-cycle plot of voltage vs a wide range of metal/metal-oxide utilization measured under j=10mA/cm^2 and 550^{o}C is shown in Figure 5.34. The discharge and charge were cycled between 0.80 V and 1.80 V under a constant j=10mA/cm^2. The total discharge time reached 23 h at which 60% of Fe was utilized with relatively stable voltage, Approximately 10 h was consumed for the charge cycle to reach ~40% utilization of Fe_3O_4 with stable voltage prior to an abrupt increase in the charging voltage, a sign of Fe_3O_4/H_2O depletion. The battery produced a DSE=1,132 Wh/kg-Fe at a RTE=93.7% when compared with a CSE=1,208 Wh/kg-Fe. The asymmetrical discharge-charge curve in Figure 5.34 signals that reduction of Fe_3O_4/H_2O could be a slower process than the oxidation of Fe or H_2O production. This could be a simple concentration effect since the ratio of equilibrium partial pressures H_2 to H_2O, pH_2/pH_2O, is 79/21 at 550^{o}C, a condition favorable for the discharge.

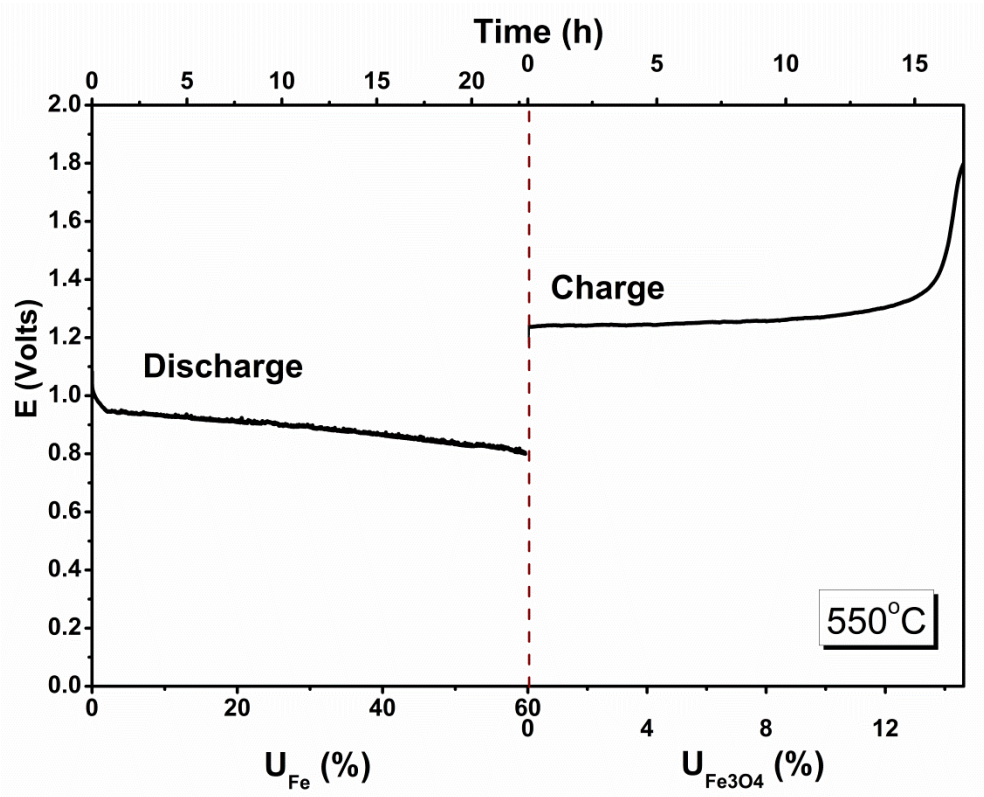

Figure 5.34 Effect of state-of-charge (metal/metal-oxide utilization) on electrochemical behavior of the SOMARB[134].

The prior-test SEM microstructures and XRD patterns of the Fe/C ESU are shown in Figure 5.35. Before test, the particles are clearly uniform in a size of ~100nm. EDS analysis reveals that the bulk (zone-1 and -2) as well as the surface (zone-3) contains elements of Fe, C, Zr and O, but with the surface exhibiting a slightly higher C content. It appears that a "core-shell" (zone-2) structure has been formed after the reaction. We failed to study further the internal structure of "core-shell" with TEM owing to concerns of potential damage to the lens due to magnetism present in the iron particles.

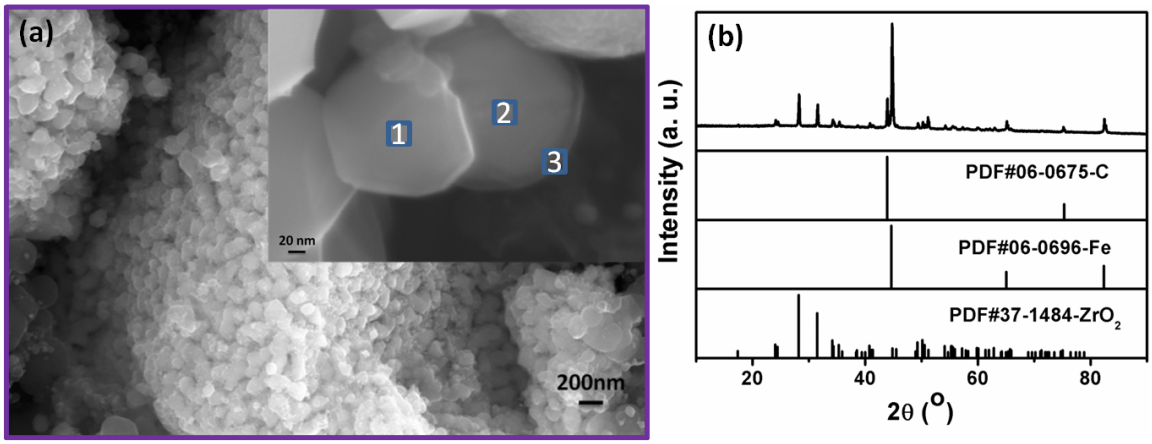

Zone 1

Element	Wt%	At%
C K	17.95	44.50
O K	14.25	26.52
Zr L	34.63	11.30
Fe K	33.17	17.68
Total	100	100

Zone 2

Element	Wt%	At%
C K	18.08	44.45
O K	14.56	26.87
Zr L	33.80	10.94
Fe K	33.56	17.74
Total	100	100

Zone 3

Element	Wt%	At%
C K	19.39	49.24
O K	9.14	17.41
Zr L	26.83	8.97
Fe K	44.65	24.38
Total	100	100

Figure 5.35 Microstructure and composition of the Fe/C-ESU obtained by the iron carbothermic reaction; (a) morphology and (b) XRD pattern[134].

The microstructure and XRD pattern of Fe/C ESU after test are shown in Figure 5.36. Compositionally, there seems to be no significant difference between the darker and lighter particles (zone-1 vs zone-2), but carbon is clearly observed to concentrate on the surface (zone-3), although no crystalline carbon was found from the XRD pattern. The BET surface area of this post-test Fe/C-ESM is 10.5m^2/g, slightly smaller than the initial value of 12.5m^2/g, suggesting little agglomeration of Fe-particles occurred during the battery test.

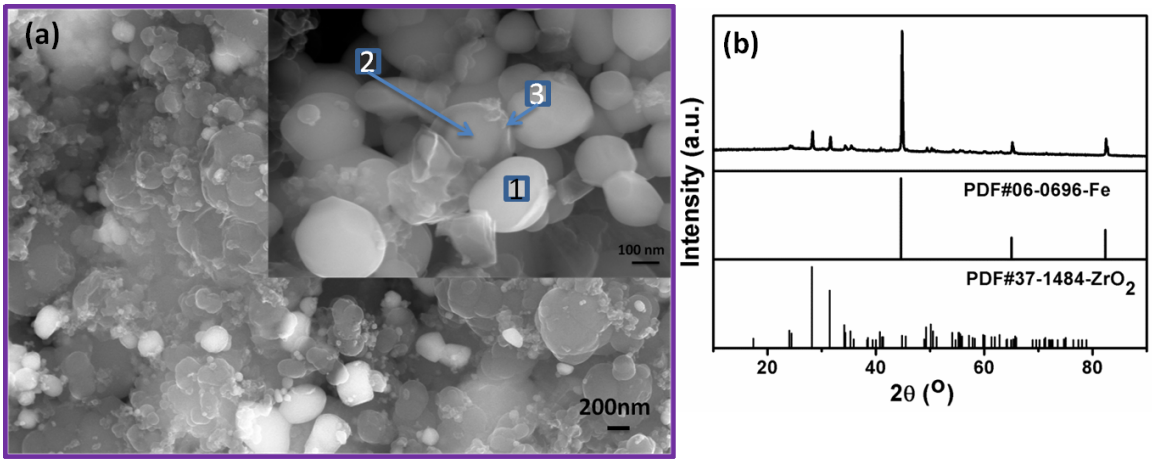

Zone 1

Element	Wt%	At%
C K	41.46	62.14
O K	25.83	29.07
Zr L	14.01	2.76
Fe K	18.70	6.03
Total	100	100

Zone 2

Element	Wt%	At%
C K	41.48	62.54
O K	25.06	28.37
Zr L	14.04	2.79
Fe K	19.42	6.30
Total	100	100

Zone 3

Element	Wt%	At%
C K	54.41	82.44
O K	5.62	6.39
Zr L	14.66	2.93
Fe K	25.30	8.25
Total	100	100

Fig 5.36 Microstructure and composition of the post-tested Fe/C-ESM obtained by the iron carbothermic reaction; (a) morphology and (b) XRD pattern[134].

The microstructures of the post-test RSOFC in the Fe/C-air battery are shown in Figure 5.37, in which (a) depicts the three functional layers: air-electrode, electrolyte and fuel-electrode. The contacts between electrolyte and electrodes are continuous and intact. Figure 5.37 (b) further shows that the bonding between air electrode and electrolyte was not affected after the 100 cycles, and the infiltrated SSC-SDC fine particles remain well dispersed in the porous LSGM skeleton after the test. Such an air-electrode structure is deemed beneficial to the retention of the battery's performance. Figure 5.37 (c) shows that the bonding between fuel electrode and electrolyte was not affected either. This feature is different from what was observed in an Fe-air battery tested for 100 cycles at 650^{o}C where

there was clearly a detachment between fuel-electrode and electrolyte [129]. Figure 5.37 (d) shows that the double-layer anode still maintains a good porous structure with no detachment discerned.

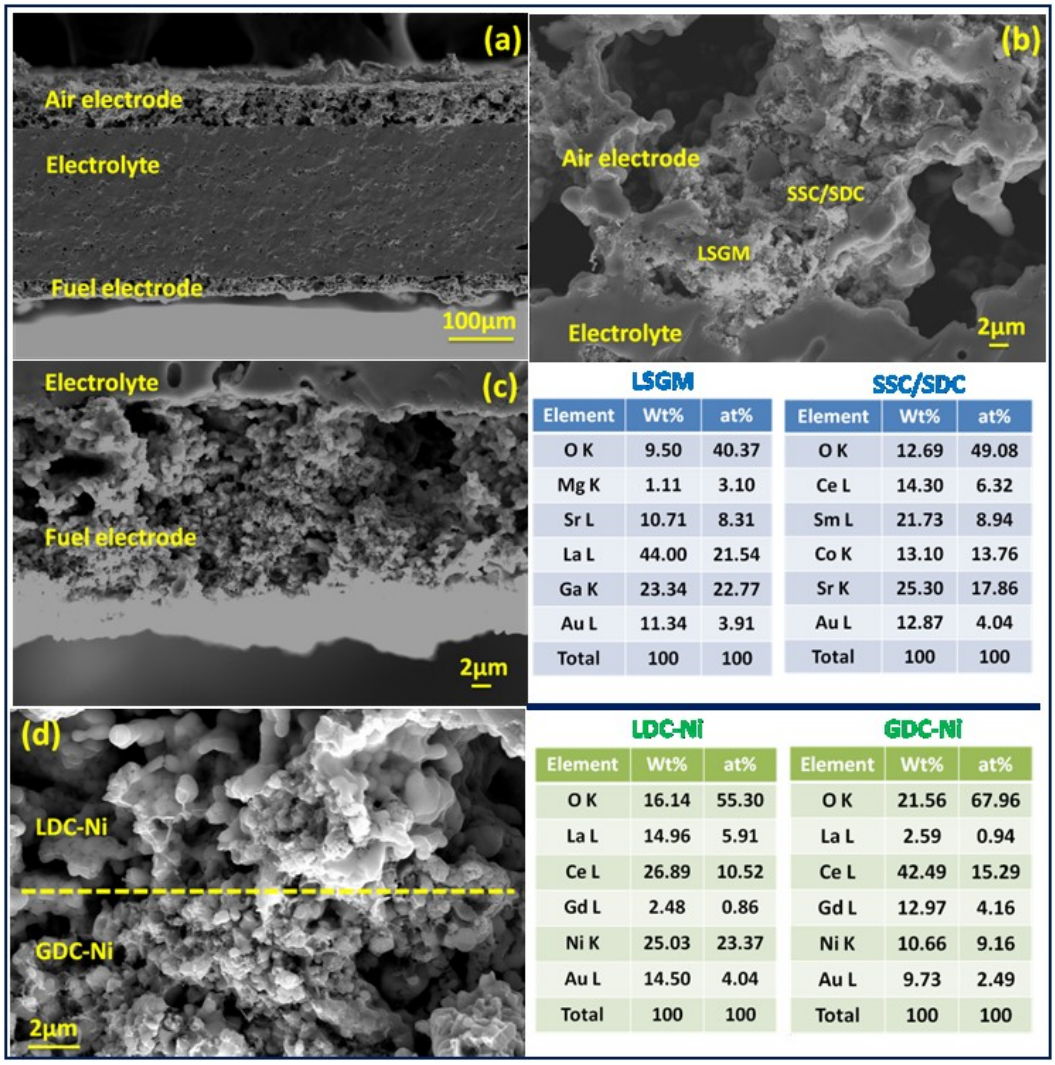

LSGM

Element	Wt%	at%
O K	9.50	40.37
Mg K	1.11	3.10
Sr L	10.71	8.31
La L	44.00	21.54
Ga K	23.34	22.77
Au L	11.34	3.91
Total	100	100

SSC/SDC

Element	Wt%	at%
O K	12.69	49.08
Ce L	14.30	6.32
Sm L	21.73	8.94
Co K	13.10	13.76
Sr K	25.30	17.86
Au L	12.87	4.04
Total	100	100

LDC-Ni

Element	Wt%	at%
O K	16.14	55.30
La L	14.96	5.91
Ce L	26.89	10.52
Gd L	2.48	0.86
Ni K	25.03	23.37
Au L	14.50	4.04
Total	100	100

GDC-Ni

Element	Wt%	at%
O K	21.56	67.96
La L	2.59	0.94
Ce L	42.49	15.29
Gd L	12.97	4.16
Ni K	10.66	9.16
Au L	9.73	2.49
Total	100	100

Figure 5.37 Cross-sectional view of the microstructures and compositional analysis of the post-test RSOFC in the Fe/C-air battery: (a) whole battery; (b) electrolyte/air-electrode interface; (c) current collector/fuel-electrode/electrolyte interface; (d) fuel electrode with LDC-Ni and GDC-Ni dual layers (Note: the compositions given represent the highlighted zones)[134].

5.5 SUMMARY

The SOFeARB has been used as a model SOMARB in this research for a thorough understanding of the energy storage characteristics. These fundamental results can be summarized as follows.

- The specific energy can be as high as 80-90% of the MTSE
- The RTE can be in the range of >90%
- The long-term cyclic stability over 100 cycles has been significantly improved by using carbothermic reaction derived Fe-ESU
- The battery's voltage is independent of state-of-charge, a favorable trait for a rechargeable battery. Metal utilization is the indicator of state-of-charge for SOMARB
- Metal utilization or state-of-charge must be properly selected to best optimize the specific energy and RTE
- Operating a SOMARB at relatively lower current density for a longer duration is a good strategy to realize energy storage capacity required
- The battery's EMFs determined by the stable metal/metal-oxide redox couple is in excellent agreement with the theoretical values

CHAPTER 6

A MULTI-PHYSICS MODEL FOR SOFEARB

As experimental studies on the characteristics of the new battery are currently being carried out in our group, it becomes increasingly clear that a fundamental understanding of the complex physical, chemical, mechanical, and electrochemical phenomena involved in the system would greatly benefit the development of the battery. Physics-based mathematical modeling would be an ideal tool to meet this demand. So far, very little modeling work on this type of battery has been reported. In 2012, Ohmoti *et al* [135] proposed a 1D Fick's diffusion model with the simplest configuration to study the battery's characteristics. However, that model has at least two major limitations. First, the geometries for most practical designs should be beyond 1D. Second, the transport phenomena in the concentrated gas phase are far more complicated than the Fick's diffusion. Therefore, the major objective of this work is to develop a more rigorous multi-physics model than the Ohmoti's 1D model, which would encompass most of the transport and kinetic processes involved in the solid oxide redox flow batteries. The theoretical basis for the model development is the fundamentals in the reaction engineering and chemical reactor design[136]. The outcome of the constructed model is also compared

with the measured experimental results.

6.1 MATHEMATICAL MODEL

6.1.1 Model Configuration

Our multi-physics model presented here is developed for a close-loop tubular battery reactor with a planar RSOFC working at 800^{o}C. According to the schematic illustrated in Figure 6.1, this flow battery system includes a cylindrical tubular reactor that carries out the battery's functionality and a gas manifold that includes a "T"-shape tube and a returning tubing that allow the gas mixture leaving and circulating back to the tubular reactor. The tubular reactor can be regarded as the combination of a RSOFC and an Fe/FeO-ESU. The RSOFC has a planar disk configuration and is sealed at the top of the tubular reactor with the anode (negative electrode) facing the interior space of the tubular reactor. Right below the RSOFC is the ESU, a packed-bed containing porous Fe-based redox-couple pellets. The circulating gas is a mixture of H_2 and H_2O, and the direction of close-loop flow is shown by the green arrows in Figure 6.1. The working principle was described in subchapter 2.2. Here for the modeling purpose, we reiterate it one more time:

At the anode of RSOFC, the following electrochemical reaction occurs between the hydrogen and the steam:

$$H_2 + O^{2-} \underset{\text{charge}}{\overset{\text{discharge}}{\rightleftharpoons}} H_2O + 2e^- \tag{6.1}$$

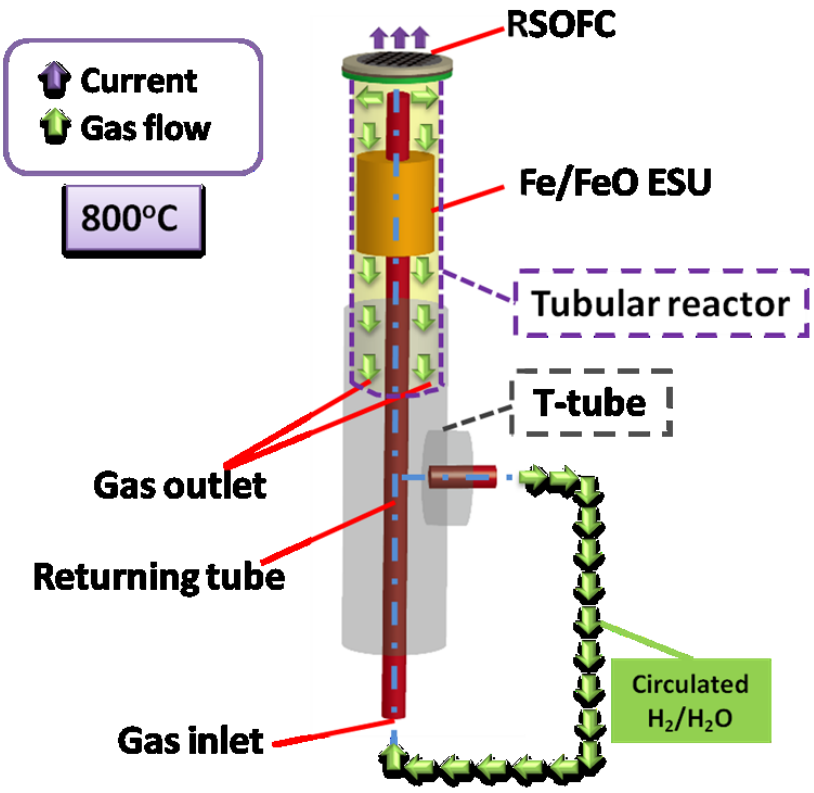

Figure 6.1 Configuration and operating principle for the solid oxide redox flow battery[137].

The cathode (positive electrode) of the RSOFC is an air electrode facing the outside of the tubular reactor, and the following electrochemical reaction occurs at the cathode:

$$\frac{1}{2}O_2 + 2e^- \underset{\text{charge}}{\overset{\text{discharge}}{\rightleftharpoons}} O^{2-} \tag{6.2}$$

In the ESU, the following reversible homogeneous reaction occurs between the solid and gas phases:

$$H_2O + Fe \underset{\text{charge}}{\overset{\text{discharge}}{\rightleftharpoons}} H_2 + FeO \tag{6.3}$$

The gas leaves the tubular reactor from the bottom (the gas outlet) and is collected in

the T-tube; then the gas is recirculated back to the tubular reactor through the returning tube.

As shown above, the gaseous species are consumed at the RSOFC and regenerated in the ESU, and then re-supplied to the battery system. Therefore, the capacity of this flow battery is theoretically limited only by the total loading of the redox couple Fe/FeO.

6.1.2 Basic Assumptions and the Model Simplification

In this work, a mathematical model was developed for the system using COMSOL 4.3 multi-physics software. The whole system is regarded as isothermal, and therefore, the thermal diffusion of the gaseous species and the heat transfer are neglected. The transport phenomena in the model include the computational fluid dynamics (CFD) and the convective mass transfer of concentrated species [138, 139], and the gas flow is assumed to be laminar. For a complete model, the T-tube has to be treated as a 3D fluid domain due to the asymmetric geometry; however, this would make this model computationally too expensive. To avoid the large computation loads and make the simulations more efficient, we simplified the model by regarding the T-tube as a continuous-stirred tank (CST). The gas phase in the CST is well-stirred under a constant pressure; therefore, the species in the gas phase can be assumed to have uniformly-distributed concentration profiles throughout the volume of CST. The mass balance for the CST is thus reduced to lumped sub-models. Therefore, the mass and momentum distributions treated by the simplified model include

only the tubular reactor and the returning tube.

6.1.3 Computational Domains and Model Settings

As the tubular reactor and the returning tube are co-axial cylinders, the computational domains of this model can be built on a two-dimensional axial-symmetric plane. The schematic for the in-plane cross-section of the modeling domains is presented in Figure 6.2 and the full 3D geometry for the tubular reactor and the returning tube can be obtained by revolving this cross-section for 360^{o} around the symmetric axis. In order to improve the gas recirculation in the tubular reactor, corner fillets are applied for ESU domain and small space is also left between the exterior vertical boundary of the ESU and the wall of the tubular reactor.

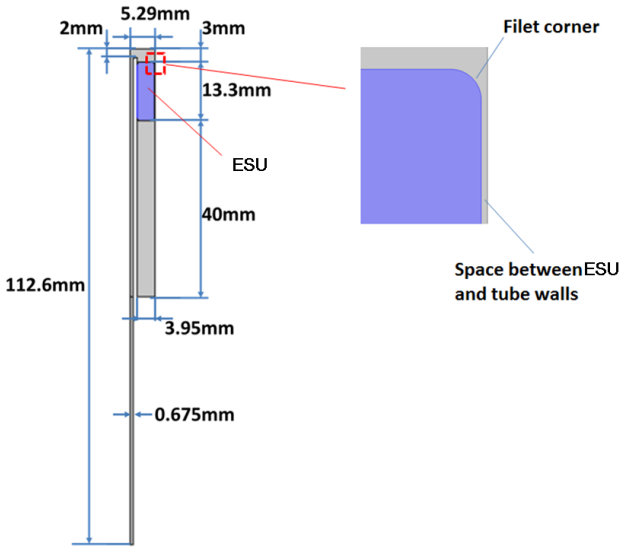

Figure 6.2 Cross-section of the modeling domains for the flow battery in a 2D plane[137].

Figure 6.3 (a) shows the settings of physical sub-models for different domains and

boundaries. Regions outside the ESU contain only the gas phase and are set as free-flow domains. The ESU domain, which includes both solid and gas phases, is regarded as a porous media in which the transport properties are scaled by the porosity and the tortuosity. As the regenerative homogeneous redox reactions occur in the ESU domain, volumetric mass sources are coupled to the transport equations. Due to the small thickness, the RSOFC is regarded as a reacting boundary where the mass flux of the gas phase species is proportional to the anode electrochemical current density. The voltage-current characteristic of the RSOFC is governed by the electrochemical sub-models. The gas circulation through the "T"-tube is simplified into a lumped sub-model that formulates the gas phase compositions in the inflow and outflow. The walls of the tubular reactor and the returning tube are set as no-slip and insulated boundaries, and the central axis is set as a symmetric boundary. The meshing of the model domains are presented in Figure 6.3 (b); to ensure sufficient computation accuracy, extremely fine meshing is used in this work and the discretized domains include totally 24,611 domain elements and 1,635 boundary elements. Quadrilateral mesh was selected for the near-wall boundary layers and triangular mesh was applied for all the other regions. The derivations of the model equations are presented in the following subsections.

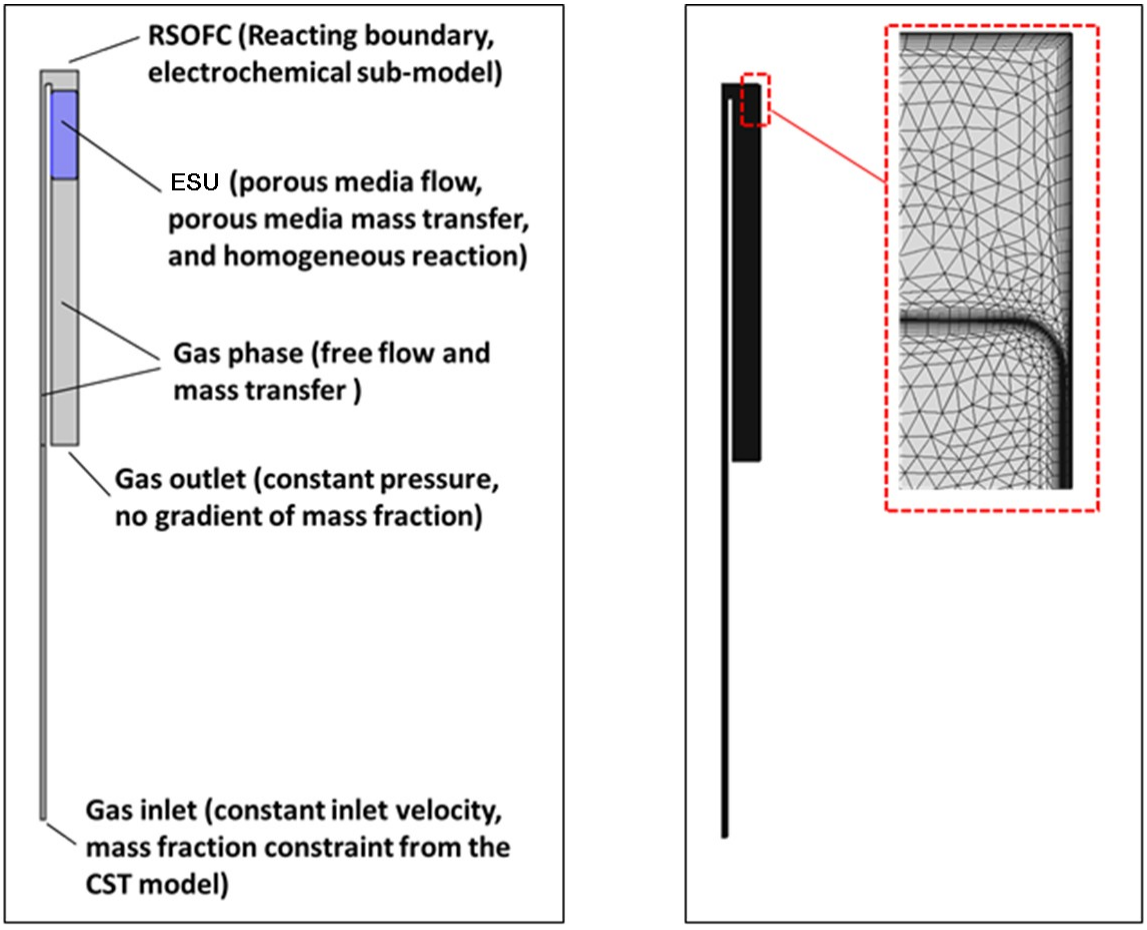

Figure 6.3 Basic model settings: (a) physical sub-models for computational domains and boundaries, (b) the meshing patterns[137].

6.1.3.1 The mass and momentum transports in the free-flow phase

In the free-flow phase, the multi-component mass transfer for concentrated species is governed by the Maxwell-Stefan diffusion and convection, and the governing equation is as follow:

$$\rho\frac{\partial\omega_i}{\partial t}+\nabla\cdot\underline{\mathbf{j}}_i+\rho(\underline{\mathbf{u}}\cdot\nabla)\omega_i=0 \qquad (i=1,2) \tag{6.4}$$

where ω_i is the mass fraction of species i, ρ is the density of gas phase, $\underline{\mathbf{j}}_i$ is the diffusive mass flux vector for species i, $\underline{\mathbf{u}}$ is the velocity vector of the fluid flow, and the subscript $i=1$ stands for hydrogen and $i=2$ stands for steam. The expression for diffusive mass flux vector, $\underline{\mathbf{j}}_i$ (in the unit of $\mathrm{kg}\cdot\mathrm{m}^{-2}\cdot\mathrm{s}^{-1}$), is as follow:

$$\underline{\mathbf{j}}_i = -\rho\omega_i \sum_k \widetilde{D}_{i,k}\underline{\mathbf{d}}_k \qquad (i=1,\ 2 \text{ and } k=1,2) \tag{6.5}$$

Where $\widetilde{D}_{i,k}$ are the multi-component Fick's diffusivities, $\underline{\mathbf{d}}_k$ (in the unit of 1/m) is the diffusive driving force acting on species k, and subscript k is a dummy index for species. According to ref. [138], the values of $\widetilde{D}_{i,k}$ can be calculated from the multi-component Maxwell-Stefan diffusivities, $D_{i,j}$ (where $i \neq j$ and $D_{i,j} = D_{j,i}$); therefore for this binary system, only the value of $D_{1,2}$ is needed to implement the model. In this work, the hydrogen/steam mixture is regarded as ideal gas and the diffusive driving forces are expressed as:

$$\underline{\mathbf{d}}_k = \nabla x_k + \frac{1}{p_A}\left[\left(x_k - \omega_k\right)\nabla p_A\right] \tag{6.6}$$

where x_k is the mole fraction of species k and p_A is the absolute pressure. The mole fraction x_k can be calculated as:

$$x_k = \frac{\omega_k}{M_k} M_n \tag{6.7}$$

$$M_n = \left(\sum_k \frac{\omega_k}{M_k} \right)^{-1} \tag{6.8}$$

where M_k is the Molar mass for species k and M_n is the mean Molar mass for the gas mixture. The total mass flux of species i, $\underline{\mathbf{N}}_i$, is the combination of the diffusive flux and the convective flux:

$$\underline{\mathbf{N}}_i = \underline{\mathbf{j}}_i + \rho \underline{\mathbf{u}} \omega_i \qquad (i = 1, 2) \tag{6.9}$$

The fluid dynamics in the free-flow phase [140] are described by the Navier-Stokes equations:

$$\rho \frac{\partial \underline{\mathbf{u}}}{\partial t} + \rho (\underline{\mathbf{u}} \cdot \nabla) \underline{\mathbf{u}} = \nabla \cdot \left\{ -p \underline{\underline{\mathbf{I}}} + \mu \left[\nabla \underline{\mathbf{u}} + (\nabla \underline{\mathbf{u}})^T \right] - \frac{2}{3} \mu (\nabla \cdot \underline{\mathbf{u}}) \underline{\underline{\mathbf{I}}} \right\} \tag{6.10}$$

and the continuity equation:

$$\frac{\partial \rho}{\partial t} + \nabla \cdot (\rho \underline{\mathbf{u}}) = 0 \tag{6.11}$$

where μ is the viscosity of the gas phase, $\underline{\underline{\mathbf{I}}}$ is the identity matrix, and p is the modified pressure which is defined as:

$$p = p_A - p_{\text{ref}} \tag{6.12}$$

and in this work, the reference pressure, p_{ref}, is set at 1 atm.

6.1.3.2 The Mass and Momentum Transports in the ESU Domain

In the ESU domain, the gas phase is regarded as reacting-flow in a porous media, and the mass transfer governing equations in the gas phase are as follow:

$$\varepsilon_p \rho \frac{\partial \omega_i}{\partial t} + \nabla \cdot \underline{\mathbf{j}}_i + \rho \left(\underline{\mathbf{u}} \cdot \nabla \right) \omega_i = R_i \qquad \left(i = 1, 2 \right) \tag{6.13}$$

$$\underline{\mathbf{j}}_i = -\rho \omega_i \sum_k \widetilde{D}_{i,k}^{\text{eff}} \underline{\mathbf{d}}_k \qquad \left(i = 1, 2 \text{ and } k = 1,2 \right) \tag{6.14}$$

where ε_p is the porosity of ESU and $\widetilde{D}_{i,k}^{eff}$ are the effective multi-component Fick's diffusivities, and R_i is the volumetric mass source of species i. The expressions for effective diffusivities are as follow:

$$\widetilde{D}_{i,k}^{\text{eff}} = D_{i,k} \varepsilon_p^{3/2} \qquad \left(i = 1, 2 \text{ and } k = 1,2 \right) \tag{6.15}$$

According to the reaction eq. (6.3), the rate for this multi-phase chemical reaction depends on the concentrations of reactants in both the gas phase (hydrogen and steam) and the solid phase (Fe and FeO). Let ξ_{Fe} stand for the conversion of Fe to FeO, it can be easily found that the molar fractions of Fe and FeO are respectively proportional to $1-\xi_{Fe}$ and ξ_{Fe}. Assuming that the reaction orders equal the stoichiometric coefficients in eq. (6.3), the volumetric molar reaction rates for hydrogen and steam, r_1 and r_2, can thus be expressed as:

$$r_1 = k\left(1-\xi_{Fe}\right)c_2 - k^{-1}\xi_{Fe}c_1 \tag{6.16}$$

$$r_2 = -r_1 \tag{6.17}$$

where c_1 and c_2 are the molar concentrations of hydrogen and steam, and k and k^{-1} (in units of 1/s) are respectively the rate constants for the forward and reverse reactions. For species i, the volumetric mass source terms, R_i, is the molar reaction rate scaled by the Molar mass, M_i:

$$R_i = r_i M_i \qquad (i = 1, 2) \tag{6.18}$$

According to the ideal gas properties, the molar concentrations of species i can be calculated from the mole fraction:

$$c_i = \frac{x_i p_A}{RT} \qquad (i = 1, 2) \tag{6.19}$$

where T is temperature (K) and R is the universal gas constant. The governing equation for the mass balance in the solid phase is as follow:

$$c_{Fe} \frac{\partial \xi_{Fe}}{\partial t} = r_1 \tag{6.20}$$

where c_{Fe} is the total amount of Fe and FeO per unit bulk volume of ESU. Therefore, c_{Fe} is expressed as:

$$c_{Fe} = \frac{n_{Fe} + n_{FeO}}{V_{\text{ESU}}} \tag{6.21}$$

where n_{Fe} and n_{FeO} (in the unit of mole) are the amounts of Fe and FeO, and V_{ESU} is the

bulk volume of ESU. As the conversion between Fe and FeO is equal-molar, the value for $n_{Fe}+n_{FeO}$ remains constant and is equal to the total number of mole of Fe and FeO in the initial ESU loading. As Fe and FeO have different molar volume values, the porosity of ESU, ε_p, may change with the progress of reaction (6.3), and the correlation between ε_p and ξ_{Fe} is derived as follow:

$$\varepsilon_p = \varepsilon_{p,0} + c_{Fe}\left(\frac{M_{Fe}}{\rho_{Fe}} - \frac{M_{FeO}}{\rho_{FeO}}\right)\left(\xi_{Fe} - \xi_{Fe,0}\right) \tag{6.22}$$

where $\varepsilon_{p,0}$ is the initial porosity of ESU, $\xi_{Fe,0}$ is the initial conversion of Fe to FeO, M_{Fe} and M_{FeO} are the Molar masss of Fe and FeO, and ρ_{Fe} and ρ_{FeO} are the densities of Fe and FeO, respectively.

The fluid dynamics of the gas phase in the ESU domain are described by the Brinkman equations[141] for flow in a packed-bed:

$$\frac{\rho}{\varepsilon_p}\left[\frac{\partial \underline{\mathbf{u}}}{\partial t} + \left(\underline{\mathbf{u}}\cdot\nabla\right)\frac{\underline{\mathbf{u}}}{\varepsilon_p}\right] = \nabla\cdot\left\{-p\underline{\underline{\mathbf{I}}} + \mu\left[\nabla\underline{\mathbf{u}} + \left(\nabla\underline{\mathbf{u}}\right)^{\tau}\right] - \frac{2}{3}\frac{\mu}{\varepsilon_p}\left(\nabla\cdot\underline{\mathbf{u}}\right)\underline{\underline{\mathbf{I}}}\right\} - \left(\frac{\mu}{\kappa_{br}} + \frac{Q_{br}}{\varepsilon_p^2}\right)\underline{\mathbf{u}} \tag{6.23}$$

$$\frac{\partial\left(\varepsilon_p\rho\right)}{\partial t} + \nabla\cdot\left(\rho\underline{\mathbf{u}}\right) = Q_{br} \tag{6.24}$$

where κ_{br} is the permeability of porous media and Q_{br} is the volumetric mass source for the gas phase. Obviously, Q_{br} equals to the sum of volumetric mass sources for all individual species in the gas phase:

$$Q_{br} = \sum_{k} R_k \qquad (k = 1, 2) \tag{6.25}$$

6.1.3.3 The electrochemical sub-model at the RSOFC boundary

The mass flux of the gas phase species at the RSOFC boundary are coupled to the electrochemical current density, i_n:

$$-\underline{\mathbf{n}} \cdot \underline{\mathbf{N}}_1 = -\frac{i_n M_1}{2F} \tag{6.26}$$

$$-\underline{\mathbf{n}} \cdot \underline{\mathbf{N}}_2 = \frac{i_n M_2}{2F} \tag{6.27}$$

where $\underline{\mathbf{n}}$ is the unit normal vector pointing out of the RSOFC boundary, i_n is the anode current density of the RSOFC, and F is the Faraday's constant. We assume that the mass transfer of O^{2-} ions from the cathode to the anode of the RSOFC during discharge is sufficiently fast due to the small thickness of the RSOFC, so the concentration of O^{2-} ions in the RSOFC can be regarded as a constant. The anode current density of anode, i_n, is governed by the Butler-Volmer equation [142]:

$$i_n = i_{n,0}\left\{\exp\left[\frac{2\alpha_a F}{RT}\left(\phi_n - E_{\mathrm{eq},n}\right)\right] - \exp\left[-\frac{2(1-\alpha_a)F}{RT}\left(\phi_n - E_{\mathrm{eq},n}\right)\right]\right\} \tag{6.28}$$

where ϕ_n is the solid phase electric potential of the anode, $E_{\mathrm{eq},n}$ is the equilibrium potential of the anode, $i_{n,0}$ is the exchange current density for the anode, and α_a is the anodic transfer coefficient for the anode. As the concentration of O^{2-} ions is a constant, the exchange current density of the anode depends only on the composition of the gas

phase species through the following expression:

$$i_{n,0} = i_{n,0}^{\text{ref}} x_1^{1-\alpha_a} x_2^{\alpha_a} \tag{6.29}$$

where $i_{n,0}^{\text{ref}}$ is the reference-state (where $x_1 = 1$ and $\alpha_a = 0$) exchange current density. The equilibrium potential of the anode follows the Nernst equation:

$$E_{\text{eq},n} = E_{\text{eq},n}^{\theta} + \frac{RT}{2F} \ln\left(x_2 / x_1\right) \tag{6.30}$$

where $E_{\text{eq},n}^{\theta}$ is the equilibrium potential at the standard state. The solid phase materials of electrodes usually have large electrical conductivities, so the solid phase electric potential of anode, ϕ_n, can be regarded as a function that depends on time only and can be solved by the limiting electrical equation:

$$\frac{1}{A_{\partial\Omega_E}} \iint_{\partial\Omega_E} i_n dS = -i_{\text{app}} \tag{6.31}$$

where i_{app} is the applied current density on the RSOFC, $\partial\Omega_E$ is the symbol of the RSOFC boundary, and $A_{\partial\Omega_E}$ is the area of the RSOFC boundary. In this paper, i_{app} is defined as positive for charging and negative for discharging.

Similar to the anode, the cathode current density is also governed by the Butler-Volmer equation:

$$i_p = i_{p,0} \left\{ \exp\left[\frac{2\beta_a F}{RT} \left(\phi_p - E_{\text{eq},p} \right) \right] - \exp\left[-\frac{2\left(1-\beta_a\right) F}{RT} \left(\phi_p - E_{\text{eq},p} \right) \right] \right\} \tag{6.32}$$

where β_a is the anodic transfer coefficient for the cathode, and other symbols have the same physical meanings as in equation (6-28). The limiting electrical condition for the cathode is:

$$\frac{1}{A_{\partial\Omega_E}} \iint_{\partial\Omega_E} i_p dS = i_{\text{app}} \tag{6.33}$$

In this work, the cathode of the RSOFC works under constant oxygen partial pressure; therefore the exchange current density ($i_{p,0}$) and equilibrium potential ($E_{\text{eq},p}$) of the cathode are both constants. When a constant current density is applied to the battery, the value of ϕ_p is obtained as a constant from eqs. (6.32) and (6.33). The voltage of the battery, E, is defined as the difference of solid phase electrical potentials between the cathode and the anode of the RSOFC:

$$E = \phi_p - \phi_n \tag{6.34}$$

while the full-cell Nernst potential, U, is expressed as:

$$U = E_{\text{eq},p} - E_{\text{eq},n} \tag{6.35}$$

and the overvoltage of the battery, η, is defined as

$$\eta = E - U \tag{6.36}$$

6.1.3.4 The Gas Circulation

According to the assumption made previously, the "T"-tube is simplified to a CST

where the pressure is constant and gas phase composition is uniform; therefore, the mass fraction gradients are zero at the boundary of the gas outlet and the absolute pressure at the gas outlet boundary is set at p_{ref}. The mass balance for a CST is described by the following lumped model [136]:

$$\frac{d\bar{c}_i}{dt} = \frac{1}{\tau}\left(c_{i,f} - \bar{c}_i\right) \qquad (i = 1, 2, \ldots, n) \tag{6.37}$$

where $\bar{c}_i$ is the mean molar concentration of species i in the CST, $c_{i,f}$ is the mean molar concentration of species i at the gas outlet boundary, and τ is the mean residence time of the CST. In this model, τ is expressed as:

$$\tau = \frac{V_R}{Q_f} \tag{6.38}$$

where V_R is the volume of the CST, and Q_f is the volumetric flow rate of the gas phase at the gas outlet boundary. The mass fractions of species in the circulated gas flow are same as those in the CST; therefore, the inflow condition at the gas inlet boundary of the venting pipe is set as:

$$\omega_i\big|_{\partial\Omega_{in}} = \bar{c}_i \frac{M_i}{M_n}\left(\frac{RT}{p_A}\right) \tag{6.39}$$

where $\partial\Omega_{in}$ is the symbol for the gas inlet boundary. The normal inflow velocity at the gas inlet boundary, U_0, is set as a constant.

6.1.3.5 Model Inputs

Values for the parameters involved in eq. (6.4) through (6.39) are listed in Table 6.1. The value for the binary diffusivity, $D_{1,2}$, is obtained from ref.[143]. According to ref.[68], the full-cell Nernst potential, U, is measured as 0.970 [V] at the mole fraction ratio $x_1 / x_2 = 0.65 / 0.35$, therefore, it can be calculated that $E^{\theta}_{\text{eq},n} = -0.941$ [V] vs $E_{\text{eq},p}$. In this work, $E_{\text{eq},p}$ is set to 0 as the reference electric potential.

Table 6.1 Parameters used for the simulations[137]

Parameter	Value	Unit
$D_{1,2}$	7.6×10^{-4}	m^2/s
$E^{\theta}_{\text{eq},n}$	-0.941	V
$E_{\text{eq},p}$	0	V
F	96487	C/mol
$i_{p,0}$	78.96	A/m^2
$i^{\text{ref}}_{n,0}$	4.623×10^{3}	A/m^2
k	10	$1/s$
k^{-1}	5.38	$1/s$
p_{ref}	1.0	atm
R	8.3143	J/mol/K
T	800	°C
V_R	5.63×10^{-6}	m^3

α_a	0.5	
β_a	0.5	
κ_{br}	1.18×10^{-11}	m^2
μ	1.0×10^{-4}	$Pa\cdot s$
ρ_{Fe}	7.8×10^{3}	kg/m^3
ρ_{FeO}	5.5×10^{3}	kg/m^3
$\varepsilon_{p,0}$	0.7	

6.2 THE ELECTROCHEMICAL RESULTS

A discharge processes at $i_{app} = -200\ mA/cm^2$ was simulated to compare with the experimental data. The RSOFC applied in the experiment is a commercially available NextCell Electrolyte Supported Button Cell (Fuel Cell Materials, Ohio, USA), as shown in Table 4.1. Other numerical results from the simulation are used for the extended studies of this flow battery's electrical and chemical behavior. The ESU in the experimental battery has an initial Fe loading of 0.907g and an initial porosity of 0.7, and the operating temperature for the system is 800°C. The end-of-discharge condition in our simulation is set at $E = 0.24V$ and the velocity of inflow, U_0, is set at 0.1 m/s. The initial mass fractions of hydrogen and steam are $\omega_1 = 0.999$ and $\omega_2 = 0.001$, respectively. Discharges at other current densities were also simulated as case studies.

The simulated *vs* experimental voltage profiles under $i_{app} = -200\ mA/cm^2$ discharge

are presented in Figure 6.4 (a). It is evident that the model produces results in good agreement with the measured data. The full discharge continues for about 4.5 hour to reach the stop condition. According to the plots, the battery voltage decreases almost linearly for the depth of discharge (DOD) ranging between 0 and 80%, beyond which the voltage falls sharply as a result of the depletion of hydrogen at the anode of the RSOFC. The profiles for the surface-averaged full-cell Nernst potential (note that even the battery is not really under open-circuit, U can still be calculated from Nernst equation) and overvoltage *vs* time are shown in Figure 6.4 (b). At the beginning of discharge, the full-cell Nernst potential, which is a logarithmic function of partial pressures of H_2O and H_2 according to the Nernst equation, drops very quickly because the sensitivity $\partial U / \partial x_2$ is infinitely large in magnitude when the mole fraction of steam, x_2, is close to zero. For a similar reason, the overvoltage of the battery, which is an inverse hyperbolic function of applied current density according to the Butler-Volmer equation, increases quite sharply as the discharge begins and counterbalances the drop in the full-cell Nernst potential. As a result, the voltage of battery only changes slightly at the beginning of the discharge. According to Figure 6.4 (b), the calculated internal resistance of this battery at $i_{\text{app}} = -200$ mA/cm^2 is about $1.8\,\Omega\cdot\text{cm}^2$. It is noted that from the beginning to the end of this discharge, the voltage of the battery drops by 0.48 V while the overvoltage of the battery has a magnitude of 0.35V. Obviously, the discharge profiles will change significantly at different applied current densities. The end-of-discharge distributions of the full-cell Nernst potential and the electrochemical current density on the surface of the RSOFC anode are presented in

Figure 6.5; the non-uniformities of these electrochemical variables are caused by the distributions of the gas-phase species concentrations on the electrode surface.

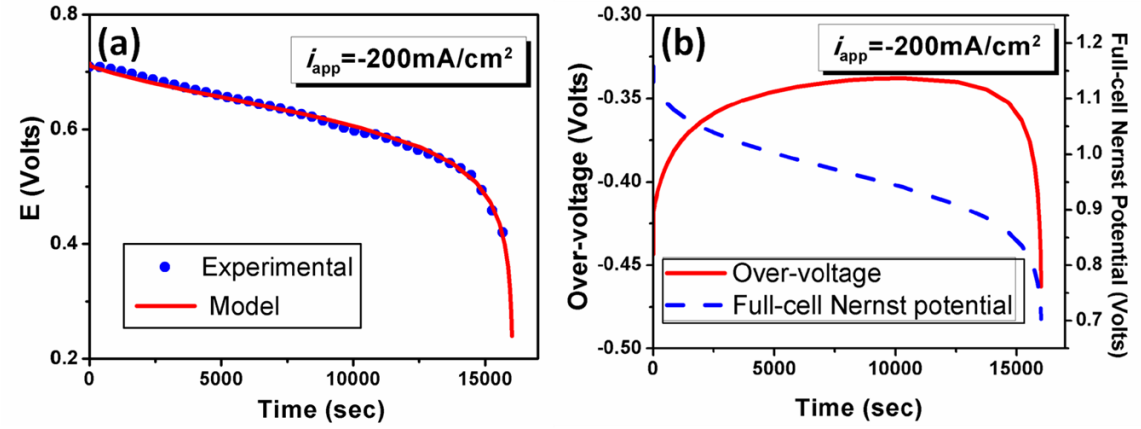

Figure 6.4 Results from the electrochemical sub-model: (a) The simulated vs experimental voltage of RSOFC operated at i_{app}=-200 mA/cm^2, (b) The simulated surface-average over voltage and full-cell Nernst potential of RSOFC[137].

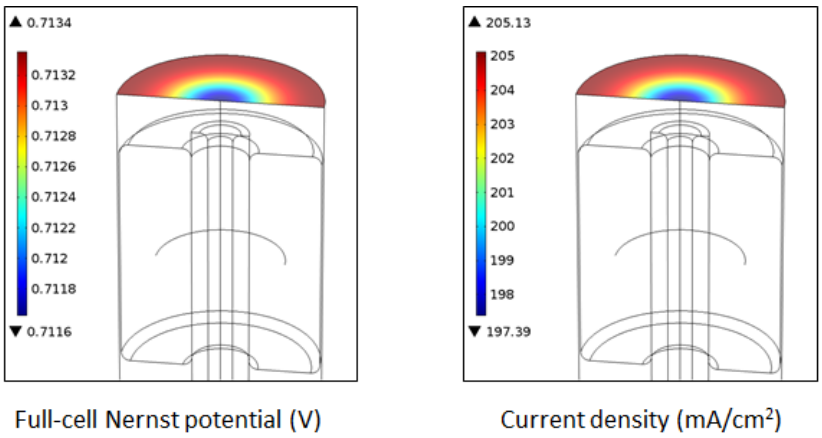

Figure 6.5 End-of-discharge distribution of full-cell Nernst potential and electrochemical current density[137].

6.3 THE CFD RESULTS

The end-of-discharge distribution of the fluid velocity fields throughout the tubular

reactor and the upper part of the returning tube is presented in Figure 6.6 (a). The velocity magnitude changes significantly when the gas flow leaves the narrow returning tube and enters the large space of the tubular reactor. The direction of the gas flow in the top regions of the tubular reactor are shown by the 2D streamline plots in Figure 6.6 (b); the main stream of the gas flow travels through the space between the ESU and the tube wall while only a small part of the gas phase enters the ESU. The distribution of the modified pressure in the gas phase is shown in Figure 6.6 (c), the pressure drops significantly through the ESU domain because of the resistive forces in the porous phases.

6.4 THE MASS TRANSFER RESULTS

The end-of-discharge distributions of the hydrogen and steam mole fractions are presented in Figure 6.7 (a) and (b), and the profile for distributed Fe-to-FeO conversion in the ESU is presented in Figure 6.7 (c). As shown in these plots, both the hydrogen and the Fe have about 98% conversions at the end of discharge. As steam is generated through the electrochemical reaction at the RSOFC boundary, the mole fraction of steam at the top of the tubular reactor is larger than that at the bottom by about 0.025; and the molar fraction of hydrogen has an opposite distribution profile. In accordance with the distributions of the gas-phase species, the Fe-to-FeO conversion at the top of the ESU is slightly higher than that at the bottom because a larger steam/hydrogen ratio drives the reaction (6.3) to the right hand.

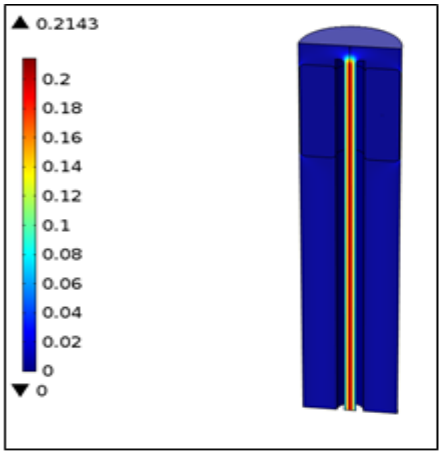

(a) Magnitude of velocity (m/s)

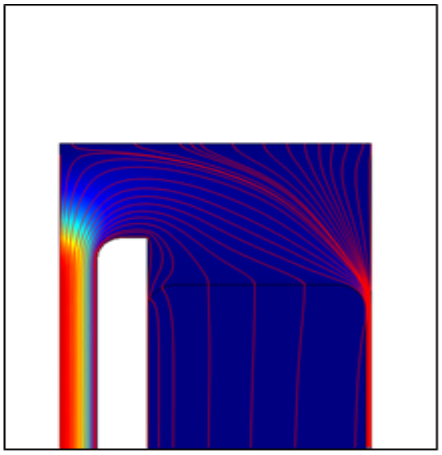

(b) 2D streamline plot for velocity field

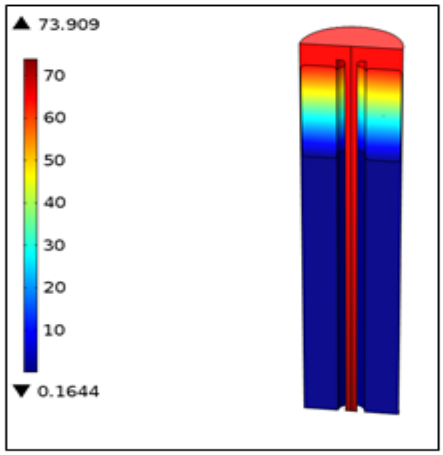

(c) Modified pressure (Pa)

Figure 6.6 The end-of-discharge distributions of the velocity and pressure of the gas flow[137].

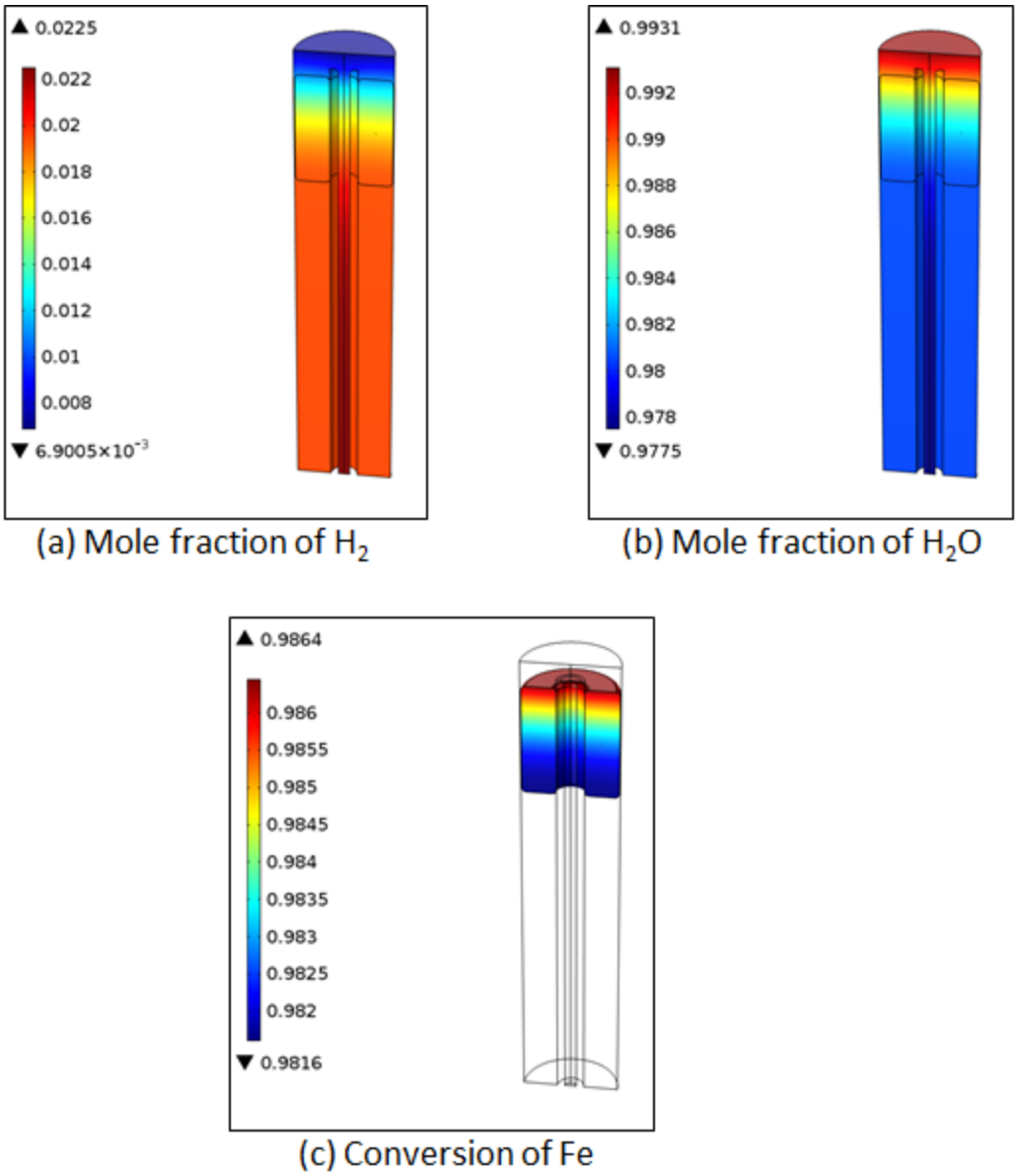

Figure 6.7 End-of-discharge distributions of (a) molar fraction of hydrogen, (b) molar fraction of steam, and (c) conversion rate of Fe[137].

The overall generation rate of hydrogen in the ESU and the overall consumption rate of hydrogen at the RSOFC anode are compared in Figure 6.8 (a). As shown in this plot, the generation rate of hydrogen is comparatively small at the beginning of discharge due to the low concentration of steam, but increases very quickly to catch the consumption rate of

hydrogen. The overall material balance in the gas phase is close to a pseudo-steady state (PSS) where the generation and consumption rates are equal for both hydrogen and steam. As the hydrogen-generating ESU is located close to the hydrogen-consuming RSOFC and the gas phase diffusivity at high temperature is large (7.6×10^{-4} m^2/s), the mass transfer between the ESU and the RSOFC is sufficiently fast and the overall mass balance of the system is limited by the reactions except for the initial stage in which the concentration gradients in gas phase are not fully developed; therefore, after short time delay, the gas phase stays in the PSS until the end of discharge. As a result of the PSS in the gas phase, the volume-average Fe conversion and porosity in the ESU change linearly with time (see Figure 6.8 (b)). However, as shown in Figure 6.8 (c), the average molar fractions of gaseous species in the ESU change with time in nonlinear profiles. According to eq. (6.16), during the PSS, the reaction rate r_1 is close to a constant, while ξ_{Fe} is a linear function of time and the total molar concentration of gas mixture, $c_1 + c_2$, is close to a constant due to the equal-molar conversion between hydrogen and steam; it can be easily derived that c_1 and c_2 change with time through the hyperbolic correlations.

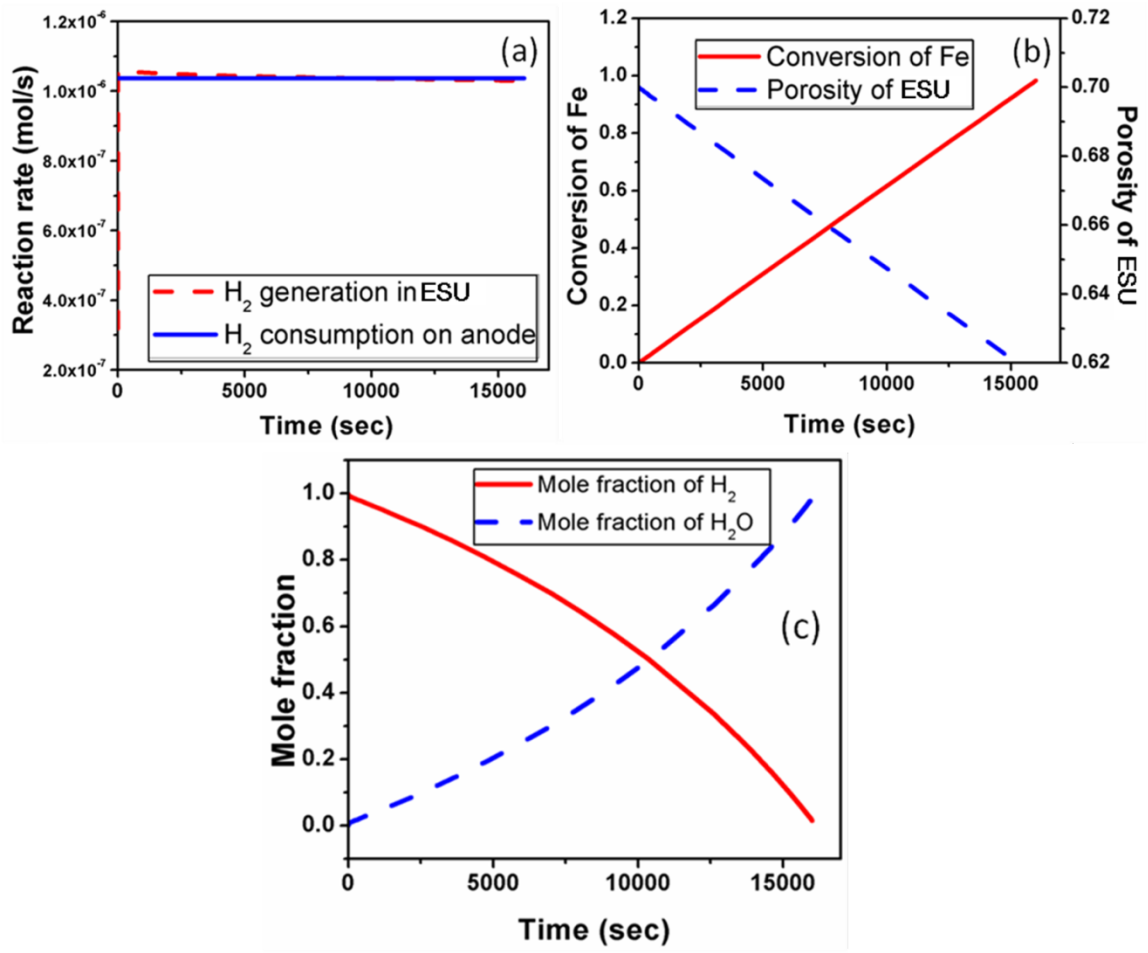

Figure 6.8 Mass transfer behavior of the battery (a) overall generation/consumption rates of hydrogen, (b) volume-average molar fractions of hydrogen and steam in the ESU, (c) volume-average Fe conversion and porosity in the ESU[137].

6.5 THE DISCHARGE PROFILES AT DIFFERENT CURRENT DENSITIES

Discharge profiles of this battery at i_{app} =-50, -100, -200, and -500 mA/cm^2 are compared in Figure 6.9; in these simulation results, the battery was fully discharged (program stops when the mole fraction of hydrogen at the RSOFC boundary drops to 0.001). The plateaus of the discharge curves drop by 0.30 V as the applied current density changes from -50 to -500 mA/cm^2, which is consistent with the analysis made in the

section for the electrochemical results. As the theoretical capacity of the battery is limited only by the loading of the Fe material, the change of applied current does not cause big differences in the full-discharge capacity. However, in practical operations, the batteries are often set under voltage control; therefore, the discharge capacities may shift significantly with the input current.

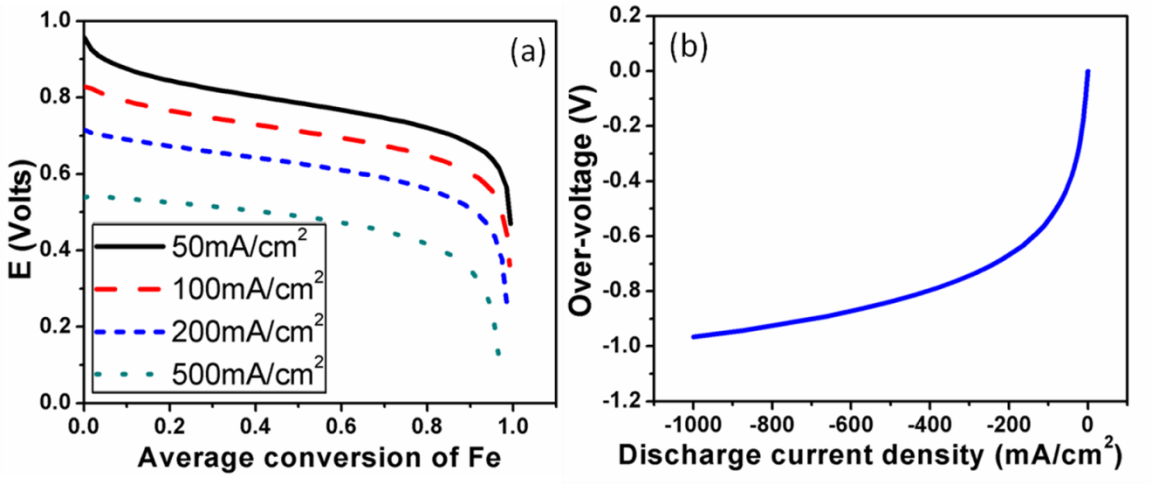

Figure 6.9 Discharge profiles of the battery at different applied current densities (a) and the dependency of initial over-voltage on applied discharge current density (b)[137].

6.6 SUMMARY

In this work, a rigorous multi-physics model for a solid oxide redox flow battery system was developed based on the fundamental theories of reaction engineering. The major functioning part of the battery is treated as a tubular packed-bed reactor combined with a working planar disk electrochemical cell. The gas circulation system of the battery is simplified to a continuous-stirred tank described by lumped material balance sub-models. The developed model shows is suitable for studying electrical and chemical behavior of

this new flow battery system, and can be extended to other battery configurations. The simulated voltage profile under a 200 mA/cm^2 discharge agrees well with the experimental data.

CHAPTER 7

SOMARBS WITH OTHER METAL AIR CHEMISTRIES

As discussed in Chapter 2, one of the key features of the SOMARB is the decoupled design of electrodes and ESU, which not only avoids volume expansion-contraction of electrodes during electrical cycles, but also allows the new metal-air chemistry to be explored conveniently by simply changing the redox couple in ESU. In this chapter, we take the latter advantage to explore two other metal-air chemistries, viz. W-O and Mo-O, in search for better performing SOMARBs. Thus constituted SOMARBs are therefore termed solid oxide tungsten air redox battery or SOWARB and solid oxide molybdenum air redox battery or SOMoARB. The selection of W-O and Mo-O systems for ESU is largely supported by their favorable kinetics indicated by prior studies and high thermodynamic energy density as a result of their high mass densities.

7.1 SOLID OXIDE TUNGSTEN AIR BATTERY (SOWARB)

7.1.1 Energy Storage Characteristics of SOWARB at 800^{o}C

The energy storage characteristic of the all solid-state tungsten-air battery measured at 800^{o}C is shown in Figure 7.1(a). To illustrate the advantage of SOWARB in energy

density, volumetric energy and charge are primarily evaluated herein. The battery was continuously cycled under j=100mA/cm^2 for three consecutive 2-hour cycles, producing a discharge charge-density of 5.36 kAh/L and discharge energy-density of 3.55kWh/L with a round-trip efficiency of 53%. The operating current density j=100mA/cm^2 is well below the j_{max}=500mA/cm^2 of W-WO_2 predicted in Figure 2.7(c) for a 2-h cycle, which ensures that the rate of redox kinetics is fast enough to sustain the battery's current density. Similarly, the SOFeARB with the same ESU volume was cycled under the same conditions, but producing a lower discharge charge-density of 4.45 kAh/L, discharge energy-density of 2.90 kWh/L, and RTE of 50% than the SOWARB, see Figure 7.1 (b). The roughly 22% higher energy-density of the SOWARB than the SOFeARB is evidently the result of the higher specific density of tungsten considering the fact that the SOWARB in fact exhibits a lower operating voltage than SOFeARB. The slightly higher round-trip efficiency of the SOWARB appears to benefit from faster redox kinetics as suggested in Figure 2.7. Note that the energy densities shown in Figure 7.1 are normalized to the metal-oxide volume that is equivalent to an oxygen flux needed to sustain the redox reaction. Such normalization allows for comparison with theoretical values such as those shown in Figure 2.7. The comparisons clearly indicate that the achieved energy density only represents 67% of the theoretical value, which implies that a portion of energy has been lost to RSOFC polarization reactions and ESU redox kinetic resistances.

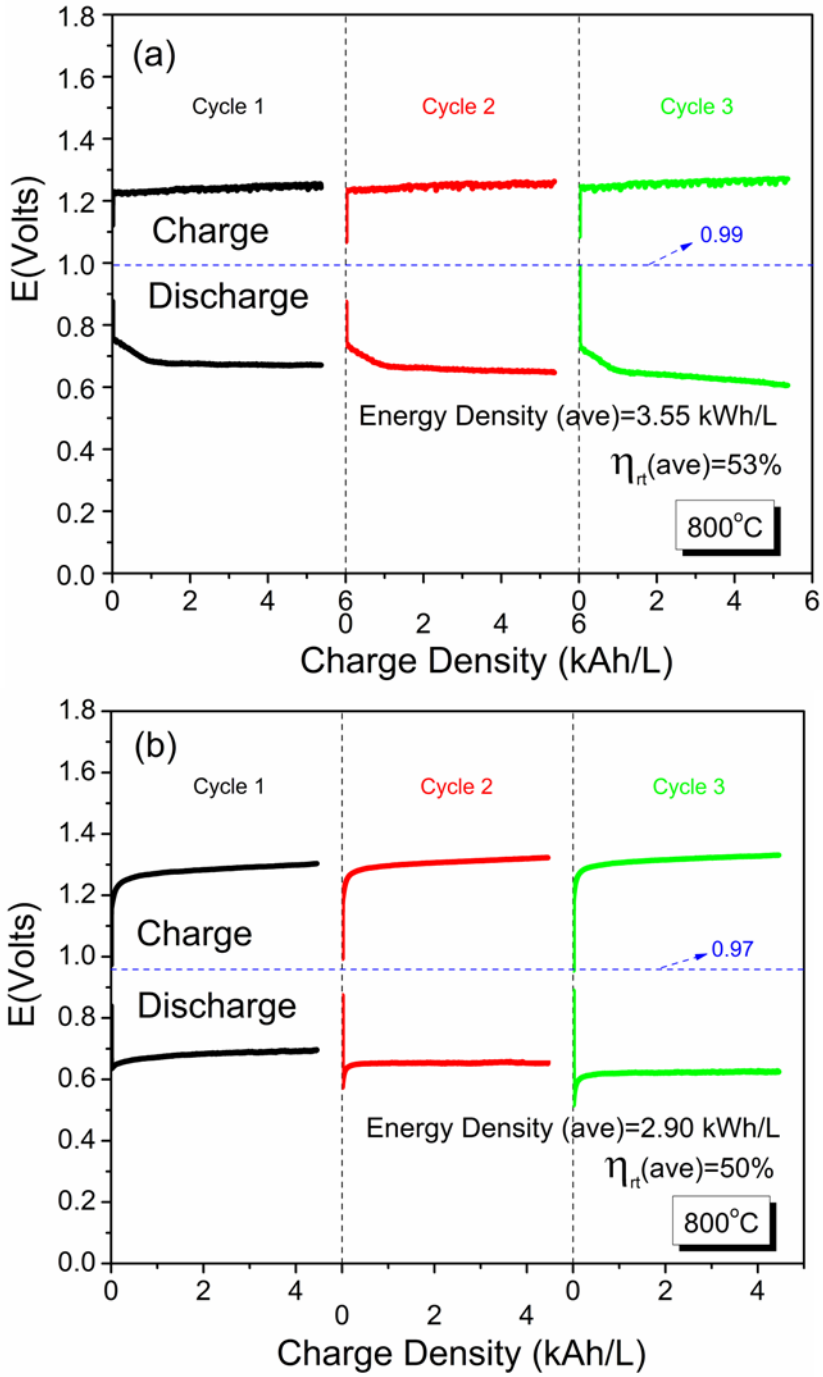

Figure 7.1 Battery voltage as a function of charge-density for (a) SOWARB; (b) SOFeARB; operating current density j=100mA/cm^2[99].

7.1.2 Characterization of RSOFC

To understand the origin of the energy loss, impedance spectra, V-I curves and power performances of RSOFC within SOWARB before and after the test were investigated. All the initial testing condition was fixed at 0.99V. Figure 7.2 shows the results. It is very clear from Figure 7.2 (a) of impedance spectra that the significant increase in polarization occurred at anode along with slight increase in ohmic resistance. The increase of cathode polarization is negligible. The V-I curves of Figure 7.2 (b) as well as power performance of Figure 7.2 (c) further confirm that the resistance of the battery has increased considerably. Same as the recoverable feature of the SOFeARB, H_2 can help regenerate the battery to some degree whereas the regenerated battery does not exhibit smaller resistance than the initial battery, as shown in the three types of plots in Figure 7.2.

We also carried out microscopic analysis on the post-test SOWARB, the cross-sectional view of which as a FESEM image is shown in Figure 7.3. Obviously, there is a delamination between the fuel electrode and electrolyte, which is more obvious than the post-test SOFeARB, as shown in Figure 4.10.

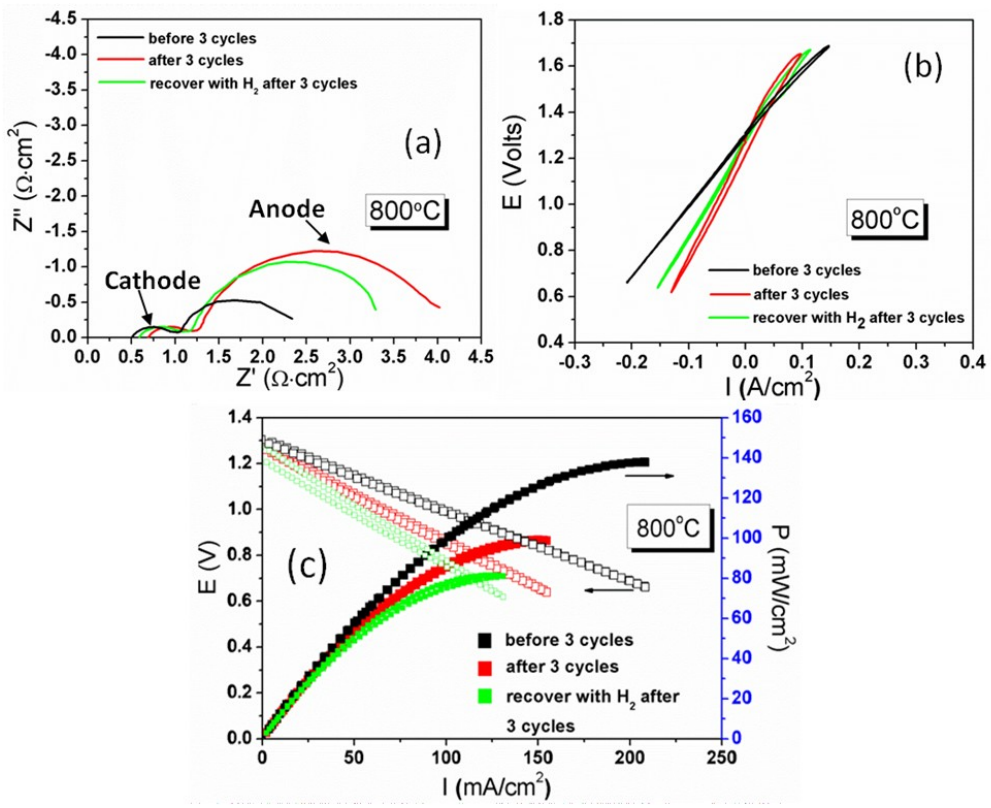

Figure 7.2 Impedance spectra (a) and V-I curves (b) and power performance (c) before and after 3 cycles at j=100 mA/cm^2, single cycle duration= 2h.

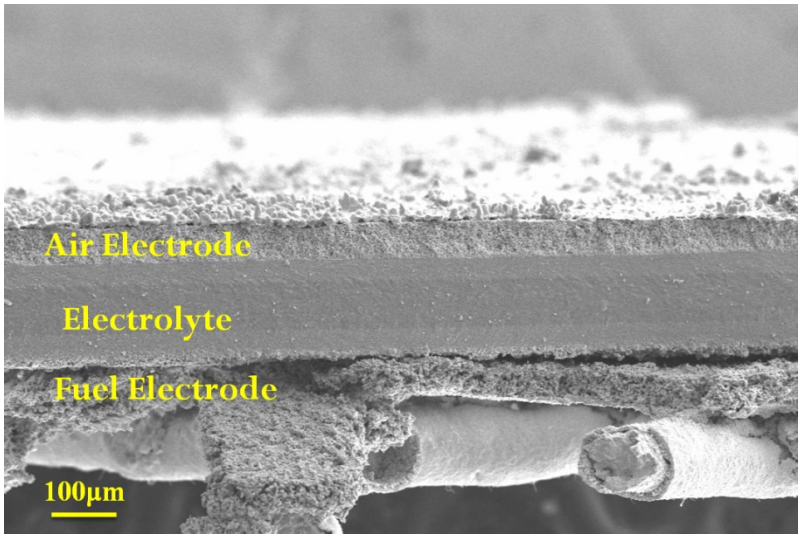

Figure 7.3 FESEM cross-sectional view of RSOFC microstructure after 3 cycles test[99].

We first examine whether a "vapour-transport-condensation mechanism" similar to

that proposed for the SOFeARB is attributed to the delamination in the following.

During the discharge cycle, in addition to the dominant reactions, a parallel reaction between $WO_{2(s)}$ and H_2O may take place to produce some by products, for example, $WO(OH)_{2(g)}$:

$$WO_{2(s)} + H_2O_{(g)} = WO(OH)_{2(g)} \quad (7.1)$$

During the charge cycle, in addition to the dominant reactions, the gaseous $WO(OH)_{2(g)}$ can also be reduced at the TPBs in the fuel-electrode via the following electrochemical reaction:

$$2WO(OH)_{2(g)} + 2e^- = 2WO_2 + O^{2-} + H_{2(g)} + H_2O_{(g)} \quad (7.2)$$

The thermal expansion mismatch between WO_2 (thermal expansion coefficient α=9.3 ppm/^{o}C) and the fuel electrode materials (e.g. GDC: α=13.4 ppm/^{o}C,SDC:=12.7ppm/^{o}C) may cause the detachment of fuel electrode from the electrolyte during cooling process.

However, the calculated equilibrium partial pressure of $WO(OH)_{2(g)}$ at 800^{o}C, $pWO(OH)_2$, equals 4.75×10^{-16} atm, which is eight orders of magnitude lower than the $Fe(OH)_2$ counterpart. The EDS-analysis results carried out near the electrolyte/fuel-electrode interface, as shown in Figure 7.4, also rule out this possibility as no trace of W can be detected besides the normal constituents of the fuel electrode and electrolyte. Therefore, the delamination caused by "vapour transport and condensation" mechanism is unlikely. Another possibility for the delamination is the damage induced during battery's disassembly. In addition, it also explains why H_2 cannot regenerate the SOWARB to a better performance since no additional catalytic benefits gained as the

SOFeARB did.

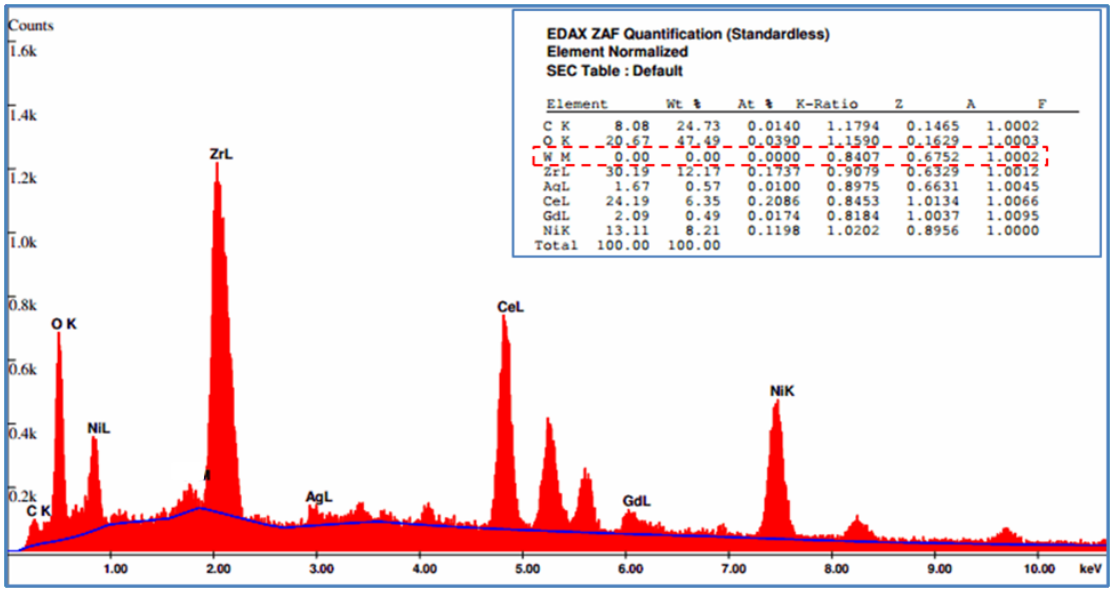

Figure 7.4 EDS spectrum and compositions of the fuel electrode after cycles test[99].

7.1.3 Characterization of ESU

Figure 7.5 shows the morphologies of W-based ESU before (a) and after test(b). It is evident that both pre-and post-test redox materials were porous. The post-tested ESU is a mixture of W and WO_x ($WO_{2-\delta}$), as indicated by the XRD analysis (c). A distinct feature is that the grain size of post-test redox materials is smaller, which can be further confirmed by Table 7.1, in which the microstructural parameters were measured by mercury porosimetry method. The fine grains are likely to originate from the H_2/H_2O-mediated redox reaction.

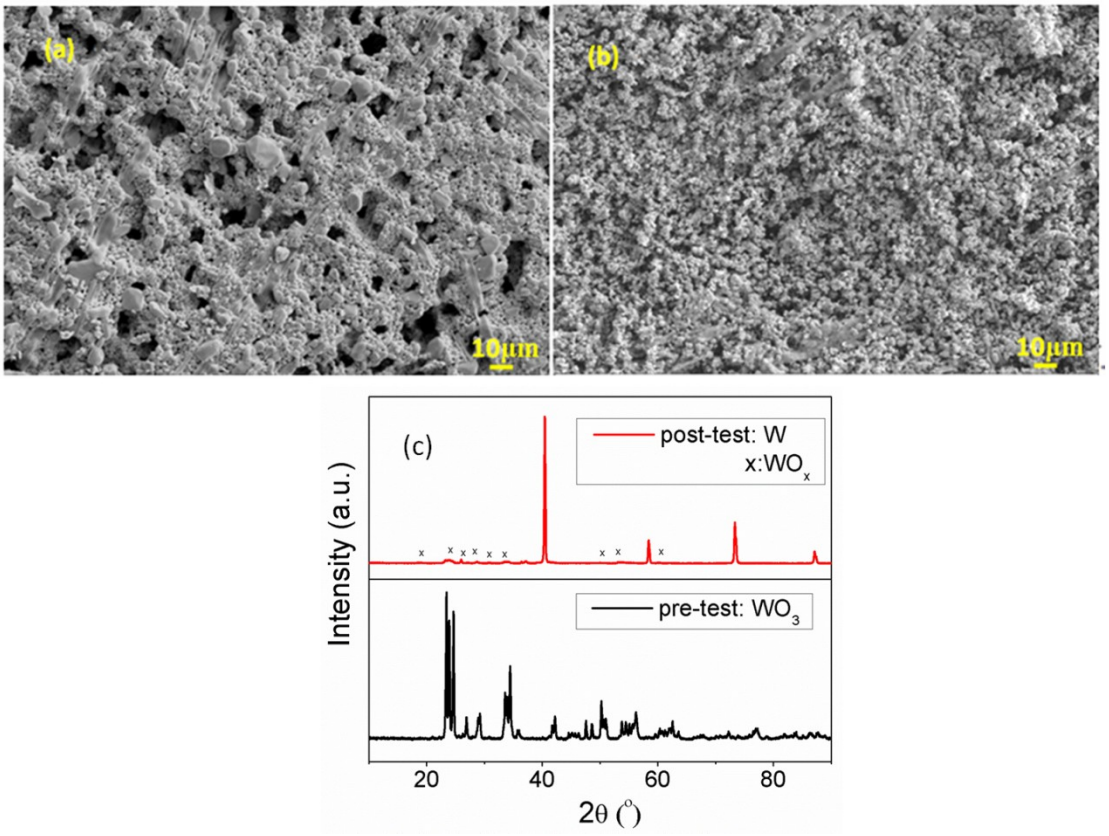

Figure 7.5 Morphologies of W-based ESU (a) pre-test; (b) post-test and (c) XRD analysis of pre-tested and post-tested W-based redox materials.

Table 7.1 Microstructural parameters of W-based redox materials loaded in the ESU measured from mercury porosimetry[99]

	Pre-test	**Post-test**
Average Pore Diameter, µm	6.281	0.984
Porosity, %	31%	74%

7.2 SOLID OXIDE MOLYBDENUM AIR REDOX BATTERY (SOMoARB)

7.2.1 Energy Storage Characteristics of SOMoARB Operated at 550^{o}C

The energy storage characteristics of the Mo-air redox battery operated at 550^{o}C are shown in Figure 7.6. To demonstrate proof-of-concept, the battery was continuously cycled at j=10mA/cm^2 for 10 consecutive cycles. For each single discharge or charge cycle, the duration is kept for 10 min. According to Figure 7.6 (a), the battery produces an average specific charge of 1,117 Ah/kg-Mo, which is 45% higher than the primary Mo-air batteries[144, 145]. Figure 7.6 (b) further shows that the battery has an average discharging specific energy of 974Wh/kg-Mo, which is roughly 78.5% of the MTSE. The measured EMF is 1.108V, which agrees precisely with the theoretical value (=1.108V). The average RTE is 61.7% over ten continuously discharge and charge cycles when compared to the charging specific energy (=1,578Wh/kg-Mo). No significant degradation is observed during the 10-cycles period. The lower round-trip efficiency and lower specific energy in relative to the MTSE suggest the occurrence of energy loss to the polarization of RSOFC and kinetic resistance of the Mo-MoO_2 redox reactions.

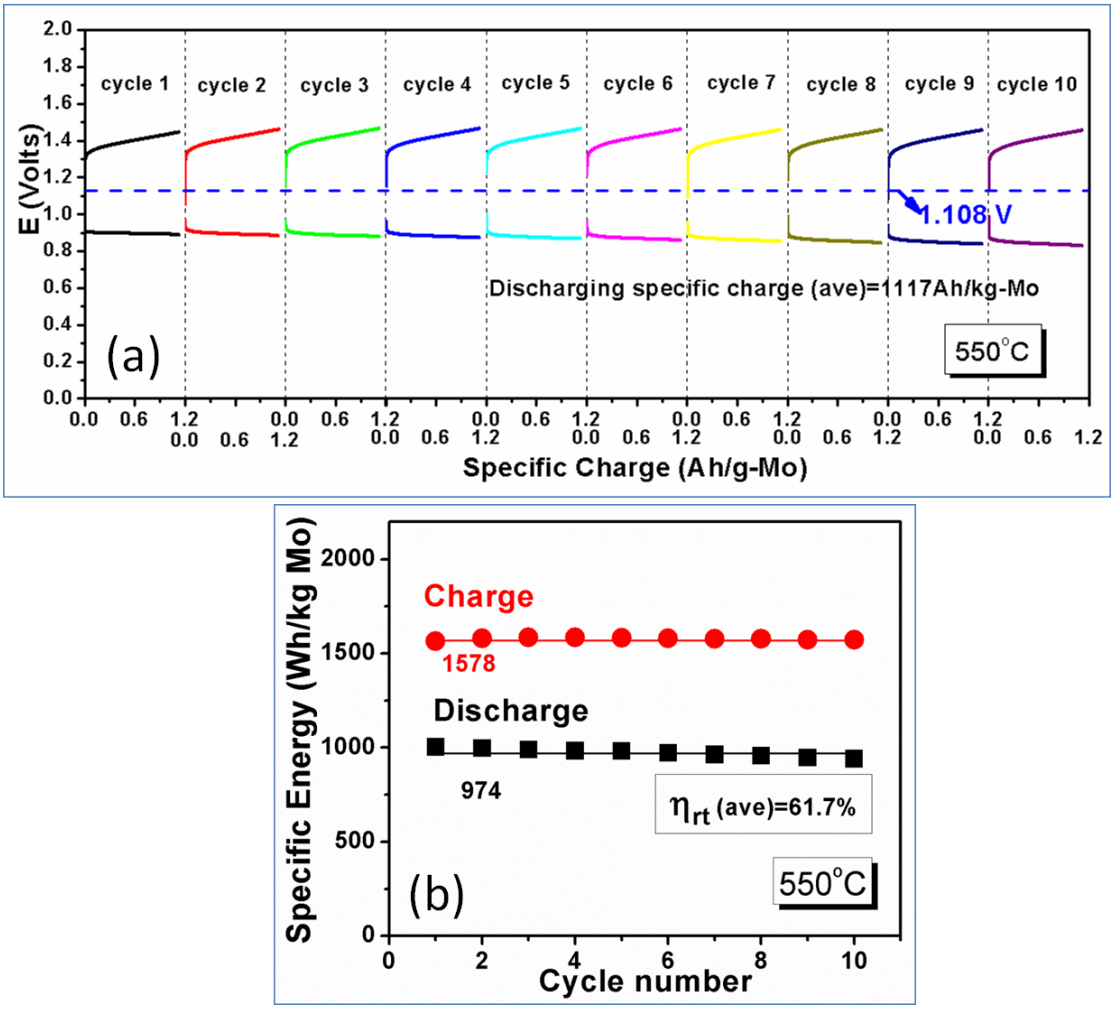

Figure 7.6 Electrochemical performance of the rechargeable Mo-air redox battery operated at 550°C for 10 continuous cycles with single discharge or charge duration of 10 min under a current density of 10mA/cm^2. (a) Voltage vs specific charge; (b) average specific energy vs number of cycles[146].

The higher charge/energy density of the Mo-air redox battery than the standard Fe-air counterpart is further illustrated in Figure 7.7. The average charge density of the Mo-air redox battery is 11.5 kAh/L-Mo, which is 13.9% higher than that of the Fe-air battery (=10.1 kAh/L-Fe). Similarly, the average energy density of the Mo-air redox battery shows 24.5% higher than the Fe-air redox battery. Not shown in Figure 7.7 are the average round-trip efficiency and EMF of Fe-air battery, which are 60.9% and 1.067V,

respectively. The higher energy density, round-trip efficiency and EMF of the Mo-air battery are consistent with the thermodynamic and kinetic predictions presented in Figure 2.6 and 2.7.

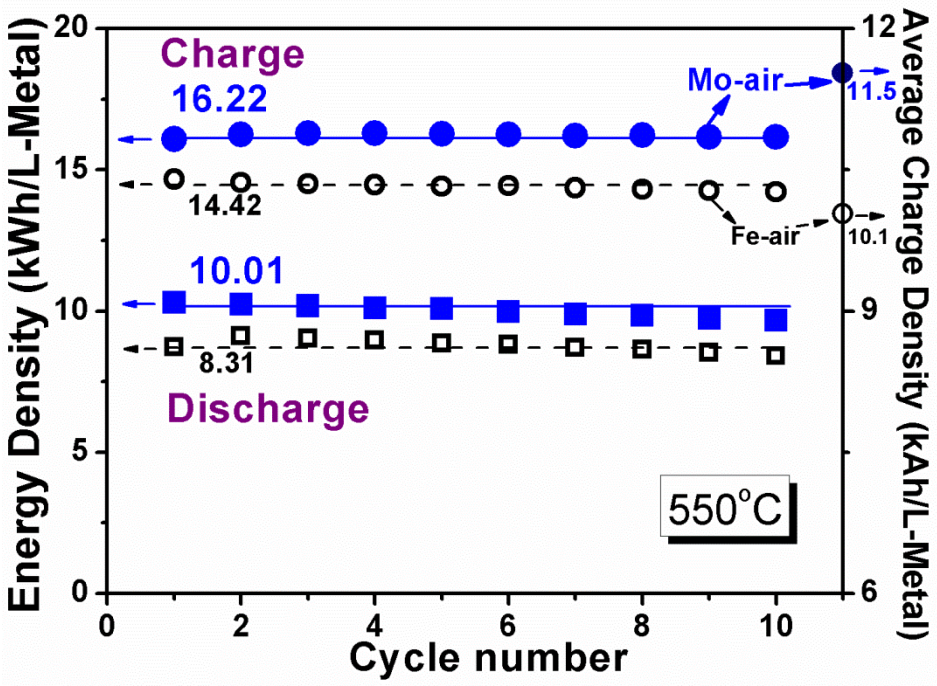

Figure 7.7 Comparison of energy density and charge density as a function of number of cycles for the Mo-air and Fe-air redox batteries[146]. BLUE: Mo-air; BLACK: Fe-air

7.2.2 Characterization of RSOFC

Impedance spectra, V-I curves and power performances of RSOFC within SOMoARB before and after the test were investigated. All the initial testing condition was fixed at 1.108 V. Figure 7.8 shows the results. It is very clear from Figure 7.8 (a) of impedance spectra that the significant increase in polarization occurred at anode along with negligible increase in ohmic resistance. The V-I curves of Figure 7.8 (b) as well as power performance of Figure 7.8 (c) further confirm that the resistance of the battery has

increased considerably. Same as the recoverable feature of the SOFeARB, H_2 can help regenerate the battery to some degree whereas the regenerated battery does not exhibit smaller resistance than the initial battery, as shown in the three types of plots in Figure 7.8.

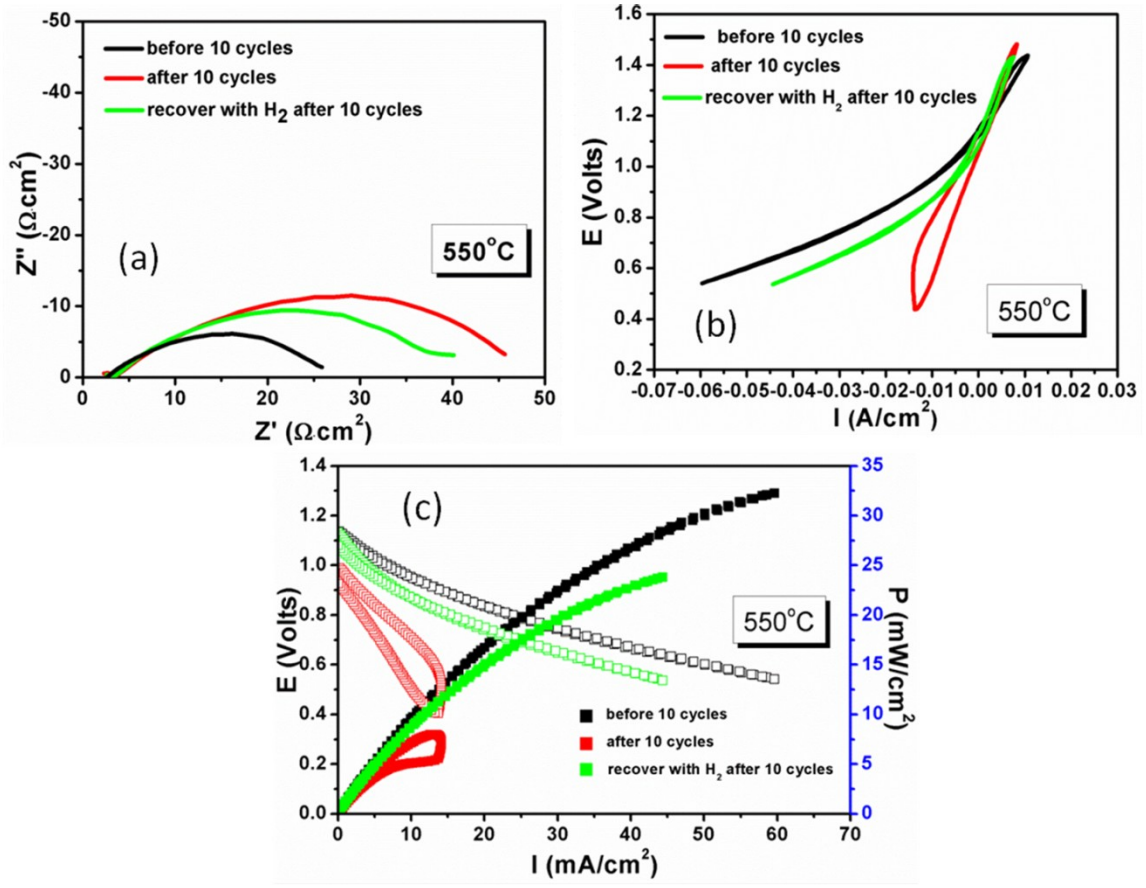

Figure 7.8 Impedance spectra (a) and V-I curves (b) and power performance (c) before and after 10 cycles at j=10 mA/cm^2, single cycle duration= 10min.

Figure 7.9 shows the cross-section of the post-tested RSOFC, including all three functional layers. The contacts between electrolyte and electrodes shown in Figure 7.9 (a) are well maintained, showing no delamination occurred during the battery test. Figure 7.9 (b) shows that the infiltrated SSC/SDC particles remain finely dispersed in the porous

LSGM after test, while Figure 7.9 (c) also indicates a porous structure of the fuel electrode after test.

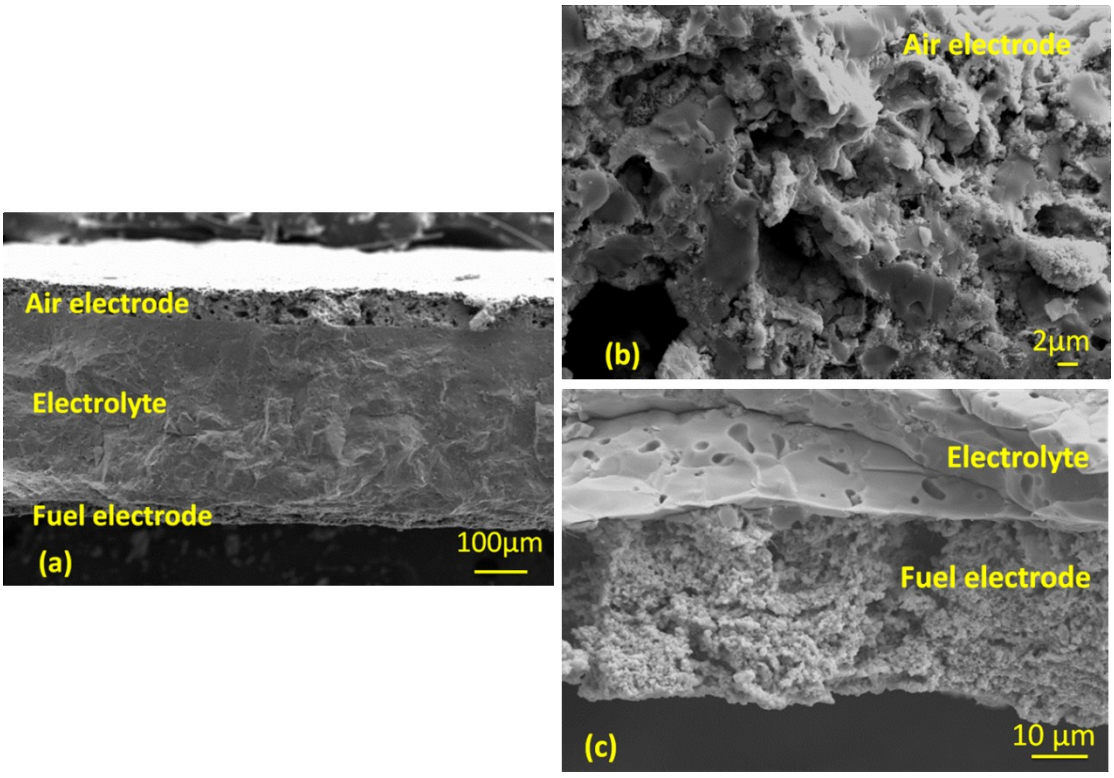

Figure 7.9 Cross-section view of a post-tested Gen 2 RSOFC (a) whole battery (b) magnified cathode and (c) magnified fuel electrode with electrolyte

7.2.3 Characterization of ESU

Figure 7.10 shows the morphologies of Mo-based ESU before (a) and after test (b). It is evident that both pre-and post-test redox materials were porous. After test, the porous structures become less uniform with needle-like morphologies appearing in various sizes. The XRD in Figure 7.10 (c) further confirms that the final product after test consisted of Mo and MoO_2 even though the starting material is MoO_3. This is consistent with the phase diagram that predicts the same Mo-MoO_2 as the stable redox couple at 550^{o}C. The EDX

analysis of Figure 7.10 (d) shows the areas with finer needles are oxygen-rich, which are more likely to be MoO_2. The bigger needles may be ascribed to the grain growth of metallic Mo in 550°C during testing.

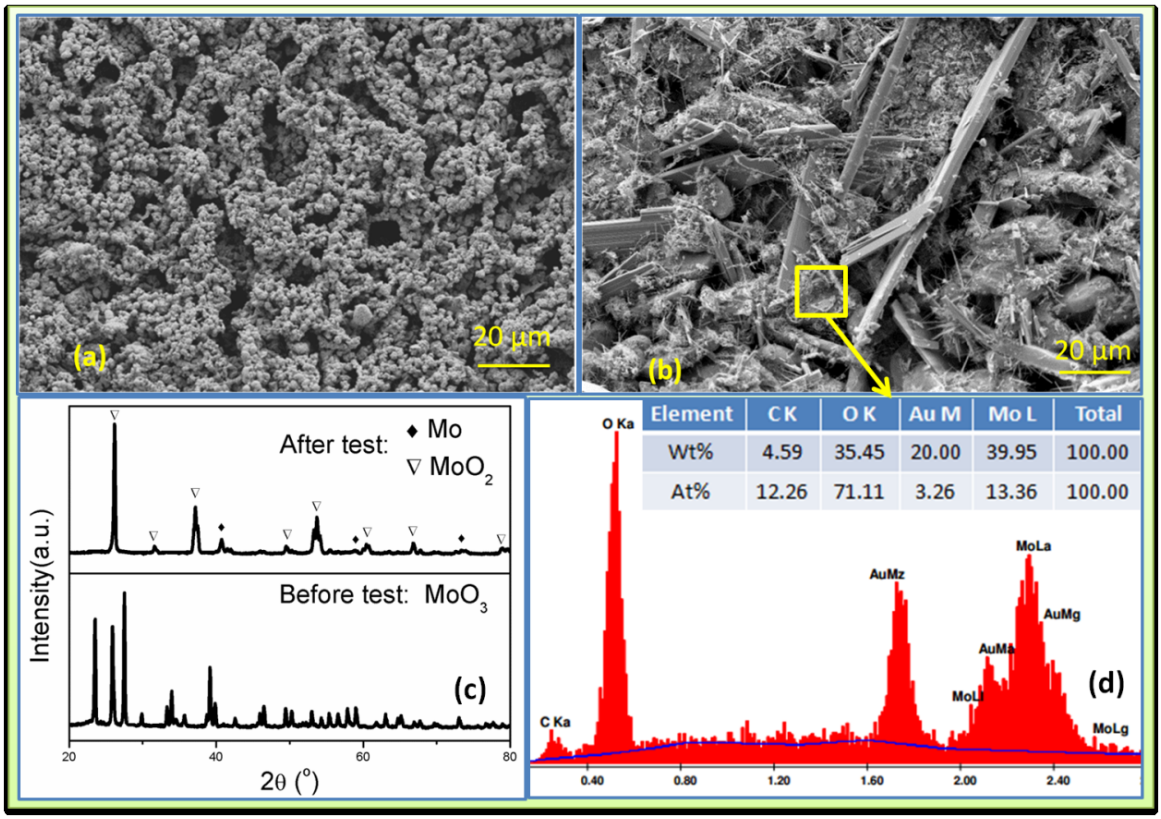

Figure 7.10 Morphologies of Mo-based ESU (a) pre-test; (b) post-test; (c) XRD-revealed phase evolution before and after test; (d) EDX analysis of post-tested Mo-based ESU[146].

7.3 SUMMARY

The heavy nature of W and Mo entitles the SOWARB and SOMoARB with higher energy densities than the SOFeARB baseline. The electrochemical testing shows that the SOWARB exhibits 22% higher energy density than the SOFeARB at 800°C, and the SOMoARB shows 24.5% higher energy density than the SOFeARB at 550°C. These

better performances are consistent with the theoretical predictions based on thermodynamics and kinetics, further demonstrating the importance of theoretical guidance in finding enabling materials.

CHAPTER 8

CONCLUDING REMARKS

Cost-effective and large-scale energy storage systems are the enabling technology for the integration of renewable energy and realization of efficient and reliable grid. Rechargeable batteries have great potential to play critical role in future large-scale EES systems due to their higher energy density, faster response, better efficiency, smaller footprint, more diverse designs and many more. This PhD research project investigates the energy storage characteristics of a new class of rechargeable solid oxide metal-air redox batteries (SOMARBs) that combines a regenerative solid oxide fuel cell (RSOFC) and hydrogen chemical-looping. This new battery inherits the merits of both the conventional metal-air batteries and traditional redox flow batteries, while circumventing their shortcomings by adopting all solid state components. One of the distinctive features of the new battery from conventional storage batteries is the ESU that is physically separated from the electrodes of RSOFC, allowing it to freely expand and contract without impacting the mechanical integrity of the entire battery structure. This feature also allows an easy change in the chemistry of the battery. Other features include state-of-charge independent EMF, O^{2-}-enabled high rate and high capacity storage, independent design of power and energy, scalability, sustainability and safety.

The materials selection for ESU is critical to achieve high energy capacity, round-trip efficiency and cost effectiveness of the new battery. Me-MeO_x redox couples with favorable thermodynamics and kinetics are highly preferable. Phase diagram, thermodynamic and kinetic principles are consistently applied in this research to guide the selection process of Me-MeO_x redox couples. This has led to the demonstrations of SOFeARBs, SOWARBs and SOMoARBs.

The SOFeARB has been investigated as a model system for the SOMARB technology. The demonstration of SOFeARB was given by two primary geometries: tubular and planar. The tubular SOFeARB produced an energy capacity of 348Wh/kg-Fe and RTE of 91.5% over 20 stable cycles at 800^{o}C. The planar SOFeARBs based on either commercial YSZ RSOFC or homemade LSGM RSOFC further confirmed that SOMARB is a high energy capacity, high RTE and high rate capacity technology for advanced energy storage. The study further revealed that metal utilization, an indicator of state-of-charge, is a crucial factor in balancing the energy capacity achievable with the efficiency desirable. Increasing metal utilization increases energy capacity produced, but at an expense of lowered RTE. From an engineering perspective, a strategy can be laid out to operate the battery at a low metal utilization (e.g., overloading the low-cost Fe-based ESU materials) as a means of achieving the required energy/power rating while retaining a high RTE.

The fundamental studies on the energy characteristics of the new SOMARB have also be complemented by computational modeling. A multi-physics-based model has been constructed to consider mass transport and charge transport during operation of a

SOFeARB. The results are satisfactorily verified by the experimental results obtained under pertinent conditions.

To enhance the performance of SOFeARB in the IT range, two major efforts were implemented: 1) use of thick film tape casted LSGM electrolyte and nanostructured air-electrode; 2) use of innovative synthesis methods for Fe-ESU. The first effort has led to the development of three generations of RSOFCs. The SOFeARB consisted of a Gen 3 RSOFC and CeO_2-modified Fe-ESU has been demonstrated with a RTE as high as 82.5% and specific energy 91% of the theoretical value at 550^{o}C.

The study also demonstrated that specific energy, RTE and cyclic stability (100 cycles) of the SOFeARB can be further improved by 12.5%, 27.8% and 214%, respectively, through the use of a low-cost carbothermic reaction derived Fe-ESU. A more thorough investigation shows that current density has a more pronounced effect on the round-trip efficiency than the cycle duration, implying that operating a SOFeARB under a relatively lower current density for a longer cyclic duration is a favorable testing condition to achieve a required energy storage capacity.

Two new metal-air chemistries, viz. SOWARB and SOMoARB, have also been investigated in this dissertation work. The selection of W and Mo as the redox metals is based on their favorable thermodynamic and kinetic attributes over the SOFeARB baseline model. The results explicitly show that these heavy metals based SOMARBs can indeed produce higher energy density (capacity per unit volume) than the baseline battery SOFeARB by allowing more mass loading and higher oxygen storage capacity. The better

kinetic rates also lead to a higher cycle efficiency and cycle stability.

To conclude, this dissertation work demonstrates a new energy storage mechanism that has great potential for stationary applications. The new storage battery has been studied in the perspectives of materials development, parametric optimization, and testing methodology. As a result of these systematic investigations, a set of standard testing and characterization protocols has been established for future testing of larger systems. Thermodynamics and kinetics have constantly been employed to guide materials selection and electrochemical testing. The experimental results are often found consistent with the theoretical predictions.

REFERENCE

[1] Annual Energy Outlook 2012, (2012).

[2] International Energy Outlook 2011, (2011).

[3] J. Yang, N. Cai, Z. Li, Energy & Fuels, 22 (2008) 2570-2579.

[4] Z. Yang, J. Zhang, M.C.W. Kintner-Meyer, X. Lu, D. Choi, J.P. Lemmon, J. Liu, Chemical Reviews, 111 (2011) 3577-3613.

[5] J.P. Barton, D.G. Infield, Energy Conversion, IEEE Transactions, 19 (2004) 441-448.

[6] P. Poizot, F. Dolhem, Energy & Environmental Science, 4 (2011) 2003-2019.

[7] T.R. Cook, D.K. Dogutan, S.Y. Reece, Y. Surendranath, T.S. Teets, D.G. Nocera, Chemical Reviews, 110 (2010) 6474-6502.

[8] F. Díaz-González, A. Sumper, O. Gomis-Bellmunt, R. Villafáfila-Robles, Renewable and Sustainable Energy Reviews, 16 (2012) 2154-2171.

[9] C. J. Yang, R.B. Jackson, Renewable and Sustainable Energy Reviews, 15 (2011) 839-844.

[10] H. Chen, T.N. Cong, W. Yang, C. Tan, Y. Li, Y. Ding, Progress in Natural Science, 19 (2009) 291-312.

[11] D. Connolly, University of Limerick, October, 2010, (2010).

[12] U.S.Department of Energy-Energy Efficiency and Renewable Energy, Wind and

Hydropower Technologies Program, (2006).

[13] http://www.pangeaexploration.com/compressed_air_energy_storage.htm.

[14] R. Saidur, N.A. Rahim, M. Hasanuzzaman, Renewable and Sustainable Energy Reviews, 14 (2010) 1135-1153.

[15] B. Bolund, H. Bernhoff, M. Leijon, Renewable and Sustainable Energy Reviews, 11 (2007) 235-258.

[16] X. Xue, K. Cheng, D. Sutanto, Superconductor Science and Technology, 19 (2006) R31-R39.

[17] B. Baxter, A Nontechnical Guide, PennWell Corporation, Oklahoma, (2006).

[18] W.V. Hassenzahl, D.W. Hazelton, B.K. Johnson, P. Komarek, M. Noe, C.T. Reis, Proceedings of the IEEE, 92 (2004) 1655-1674.

[19] H. Pan, J. Li, Y. Feng, Nanoscale Research Letters, 5 (2010) 654-668.

[20] M. S. Halper, J.C. Ellenbogen, MITRE Nanosystems Group, (2006).

[21] A.W.C. van den Berg, C.O. Arean, Chemical Communications, (2008) 668-681.

[22] B. Sakintuna, F. Lamari-Darkrim, M. Hirscher, International Journal of Hydrogen Energy, 32 (2007) 1121-1140.

[23] M. Cabo, S. Garroni, E. Pellicer, C. Milanese, A. Girella, A. Marini, E. Rossinyol, S. Suriñach, M.D. Baró, International Journal of Hydrogen Energy, 36 (2011) 5400-5410.

[24] M.A. de la Casa-Lillo, F. Lamari-Darkrim, D. Cazorla-Amorós, A. Linares-Solano, The Journal of Physical Chemistry B, 106 (2002) 10930-10934.

[25] S. Tedds, A. Walton, D.P. Broom, D. Book, Faraday Discussions, 151 (2011) 75-94.

[26] H. Wu, W. Zhou, T. Yildirim, Journal of the American Chemical Society, 129 (2007) 5314-5315.

[27] T. Borodina, D. Grigoriev, H. Mohwald, D. Shchukin, Journal of Materials Chemistry, 20 (2010) 1452-1456.

[28] R. Bardhan, A.M. Ruminski, A. Brand, J.J. Urban, Energy & Environmental Science, 4 (2011) 4882-4895.

[29] C.D. Wood, B. Tan, A. Trewin, H. Niu, D. Bradshaw, M.J. Rosseinsky, Y.Z. Khimyak, N.L. Campbell, R. Kirk, E. Stöckel, A.I. Cooper, Chemistry of Materials, 19 (2007) 2034-2048.

[30] N.L. Rosi, J. Eckert, M. Eddaoudi, D.T. Vodak, J. Kim, M. O'Keeffe, O.M. Yaghi, Science, 300 (2003) 1127-1129.

[31] M. Xue, S. Ma, Z. Jin, R.M. Schaffino, G.-S. Zhu, E.B. Lobkovsky, S.-L. Qiu, B. Chen, Inorganic Chemistry, 47 (2008) 6825-6828.

[32] L.M. Gandía, R. Oroz, A. Ursúa, P. Sanchis, P.M. Diéguez, Energy & Fuels, 21 (2007) 1699-1706.

[33] A.J.B. S. Motupally, J. W. Weidner, J. Electrochem. Soc., 149 (2002) D63-D71.

[34] A. Hauch, S.D. Ebbesen, S.H. Jensen, M. Mogensen, Journal of Materials Chemistry, 18 (2008) 2331-2340.

[35] S.C. R. O'hayre, W. Colella, F. B. Prinz, Fuel Cell Fundamentals,Wiley, John Wiley & Sons, Inc., (2009).

[36] D. H. Doughty, P. C. Butler, A. A. Akhil, Nancy H. Clark, J.D. Boyes, The

Electrochemical Society Interface, (2010).

[37] D.E. Reisner, A.J. Salkind, P.R. Strutt, T.D. Xiao, Journal of Power Sources, 65 (1997) 231-233.

[38] A. Weber, M. Mench, J. Meyers, P. Ross, J. Gostick, Q. Liu, Journal of Applied Electrochemistry, 41 (2011) 1137-1164.

[39] P. Zhao, H. Zhang, H. Zhou, B. Yi, Electrochimica Acta, 51 (2005) 1091-1098.

[40] C.P. de Leon, A. Frias-Ferrer, J. Gonzalez-Garcia, D.A. Szanto, F.C. Walsh, Journal of Power Sources, 160 (2006) 716-732.

[41] T. Oshima, M. Kajita, A. Okuno, International Journal of Applied Ceramic Technology, 1 (2004) 269-276.

[42] R.C.Galloway, J. Electrochem. Soc., 134 (1987) 256-257.

[43] C.H. Dustmann, Journal of Power Sources, 127 (2004) 85-92.

[44] R.A. Huggins, Springer New York Heidelberg Dordrecht London, (2010).

[45] H. Shimotake, G.L. Rogers, E.J. Cairns, Industrial & Engineering Chemistry Process Design and Development, 8 (1969) 51-56.

[46] E.J.Cairns, H. Shimotake, Science, 164 (1969) 1347-1355.

[47] D.J. Bradwell, H. Kim, A.H.C. Sirk, D.R. Sadoway, Journal of the American Chemical Society, 134 (2012) 1895-1897.

[48]http://www.geekwire.com/2012/mit-spinout-liquid-metal-battery-lands-15m-bill-gates/.

[49] K.F. Blurton, A.F. Sammells, Journal of Power Sources, 4 (1979) 263-279.

[50] B. Sun, B. Wang, D. Su, L. Xiao, H. Ahn, G. Wang, Carbon, 50 (2012) 727-733.

[51] F. Cheng, J. Chen, Chemical Society Reviews, 41 (2012) 2172-2192.

[52] G. Yu. Aleshin, D.A. Semenenko, A.I. Belova, T.K. Zakharchenko, D.M. Itkis, E.A. Goodilin, Y.D. Tretyakov, Solid State Ionics, 184 (2011) 62-64.

[53] S.R. Narayanan, G.K.S. Prakash, A. Manohar, B. Yang, S. Malkhandi, A. Kindler, Solid State Ionics, 216 (2012) 105-109.

[54] M. Nestoridi, D. Pletcher, R.J.K. Wood, S. Wang, R.L. Jones, K.R. Stokes, I. Wilcock, Journal of Power Sources, 178 (2008) 445-455.

[55] J.S. Lee, S. Tai Kim, R. Cao, N.-S. Choi, M. Liu, K.T. Lee, J. Cho, Advanced Energy Materials, 1 (2011) 34-50.

[56] Y.C. Lu, E.J. Crumlin, G.M. Veith, J.R. Harding, E. Mutoro, L. Baggetto, N.J. Dudney, Z. Liu, Y. Shao-Horn, Sci. Rep., 2 (2012).

[57] S.A. Freunberger, Y. Chen, N.E. Drewett, L.J. Hardwick, F. Bardé, P.G. Bruce, Angewandte Chemie International Edition, 50 (2011) 8609-8613.

[58] B.D. McCloskey, A. Speidel, R. Scheffler, D.C. Miller, V. Viswanathan, J.S. Hummelshøj, J.K. Nørskov, A.C. Luntz, The Journal of Physical Chemistry Letters, 3 (2012) 997-1001.

[59] E.C.A. Center, 2010 Energy Storage, (2010).

[60] C.F. Schönbein, Philosophical Magazine, 17 (1840) 293-294.

[61] H.P. E. Bauer, Z.Elektrochem., 43 (1937).

[62] C. Wagner, Naturwissenschaften, 31 (1943) 265-268.

[63] W. Doenitz, R. Schmidberger, International Journal of Hydrogen Energy, 7 (1982) 321-330.

[64] M. Thaler, V. Hacker, International Journal of Hydrogen Energy, 37 (2012) 2800-2806.

[65] M.F. Bleeker, H.J. Veringa, S.R.A. Kersten, Industrial & Engineering Chemistry Research, 49 (2009) 53-64.

[66] L.G.V. Vargas, Dissertation, The Ohio State University, (2007).

[67] R.J.R. Arnold O. Isenberg, United States Patent: 5,492,777, (1996).

[68] N. Xu, X. Li, X. Zhao, J.B. Goodenough, K. Huang, Energy & Environmental Science, 4 (2011) 4942-4946.

[69] S.A. Freunberger, Y. Chen, Z. Peng, J.M. Griffin, L.J. Hardwick, F. Bardé, P. Novák, P.G. Bruce, Journal of the American Chemical Society, 133 (2011) 8040-8047.

[70] M. Kowalski, P.J. Spencer, CALPHAD: Comput. Coupling Phase Diagrams Thermochem., 19 (1995) 229-243.

[71] X. Zhao, N. Xu, X. Li, Y. Gong, K. Huang, ECS. Trans., 50 (2013) 115-123.

[72] H.A. Wriedt, Bulletin of Alloy Phase Diagrams, 10 (1989) 368-384.

[73] B. Philips, L.L.Y. Chang, Trans. Metal. Soc. AIME, 233 (1965) 1433-1436.

[74] M. Pajunen, J. Kivilahti, Z. Metallkd, 83 (1992) 17-20.

[75] M.P. Arbuzov, N. T. Bugaichuk, B.V. Khaenko, Inorg. Mater., 17 (1981) 300-302.

[76] Ya. I. Ol'shanskii, V.K. Shlepov, Dokl. Akad. Nauk. SSSR, 91 (1953) 561-564.

[77] M. S. Wang, B. Sundman, Metall. Trans. B, 23B (1992) 821-831.

[78] L. A. Zabdyr, O.B. Fabrichnaya, CALPHAD: Comput. Coupling Phase Diagrams Thermochem., 28 (2004) 293-298.

[79] J. R. Taylor, A.T. Dinsdale, Z. Metallkd, 81 (1990) 354-366.

[80] E. Gebhardt, W. Obrowski, Z. Metallkd, 45 (1954) 332-338.

[81] S.R.J. Saunders, M. Monteiro, F. Rizzo, Progress in Materials Science, 53 (2008) 775-837.

[82] T. Hurlen, Journal of the Institute of Metals, 89 (1960) 128-136.

[83] E.A. Gulbransen, K.F. Andrew, Journal of the Electrochemical Society, 97 (1950) 396-404.

[84] O. Kubaschewski, A. Schneider, Journal of the Institute of Metals, 75 (1949) 403-416.

[85] Y. Matsunaga, Japan Nick. Rev., 1 (1933) 347.

[86] C.A. Phalnikar, E.B. Evans, W.M. Baldwin, Journal of the Electrochemical Society, 103 (1956) 429-438.

[87] G. R. S., B.W. M., Trans. Metal. Soc. Metals, 42 (1950) 308.

[88] K. Hopkins, Oxidation of Metals and Alloys, New York, 1953.

[89] E.A. Gulbransen, K.F. Andrew, Journal of the Electrochemical Society, 98 (1951) 241-251.

[90] A. Preece, G. Lucas, Journal of the Institute of Metals, 81 (1952) 219-&.

[91] E.A. Gulbransen, K.F. Andrew, Journal of the Electrochemical Society, 104 (1957) 451-454.

[92] E.A. Gulbransen, K.F. Andrew, F.A. Brassart, Journal of the Electrochemical Society,

110 (1963) 952-959.

[93] E.A. Gulbransen, K.F. Andrew, F.A. Brassart, Journal of the Electrochemical Society, 110 (1963) C178-C178.

[94] E.A. Gulbransen, K.F. Andrew, Journal of the Electrochemical Society, 107 (1960) 619-628.

[95] E.A. Gulbransen, K.F. Andrew, Journal of the Electrochemical Society, 107 (1960) C73-C73.

[96] X. Zhao, Y. Gong, X. Li, N. Xu, K. Huang, J. Electrochem. Soc., 160 (2013) A1241-A1247.

[97] X. Li, N. Xu, X. Zhao, K. Huang, Journal of Power Sources, 199 (2012) 132-137.

[98] N. Xu, X. Li, X. Zhao, H. Zhao, K. Huang, Electrochem. Solid-State Lett. , 15 (2011) B1-B4.

[99] X. Zhao, X. Li, Y. Gong, N. Xu, K. Romito, K. Huang, Chemical Communications, 49 (2013) 5357-5359.

[100] http://www.fuelcellmaterials.com/pdf/NextCell%2005-09.pdf.

[101] T. Ishihara, H. Matsuda, Y. Takita, Journal of the American Chemical Society, 116 (1994) 3801-3803.

[102] K. Huang, R.S. Tichy, J.B. Goodenough, J. Am. Ceram. Soc., 81 (1998) 2565-2575.

[103] M. Feng, J.B. Goodenough, Eur. J. Solid State Inorg. Chem., 31 (1994) 663-672.

[104] A. Inoishi, S. Ida, S. Uratani, T. Okano, T. Ishihara, Physical Chemistry Chemical Physics, 14 (2012) 12818-12822.

[105] A. Inoishi, S. Ida, S. Uratani, T. Okano, T. Ishihara, RSC Advances, 3 (2013) 3024-3030.

[106] S. Tanasescu, N.D. Totir, D.I. Marchidan, Electrochimica Acta, 43 (1998) 1675-1681.

[107] T. Koslowski, Physical Chemistry Chemical Physics, 1 (1999) 3017-3023.

[108] M. Oishi, K. Yashiro, J.-O. Hong, Y. Nigara, T. Kawada, J. Mizusaki, Solid State Ionics, 178 (2007) 307-312.

[109] S. M. Haile, G. Staneff, K.H. Ryu, J. Mat. Sci., 36 (2001) 1149-1160.

[110] V.M. Goldschmidt, Naturwissenschaften, 14 (1926) 477-485.

[111] Y. Du, N. M. Sammes, G.. A. Tompsett, D. Zhang, J. Swan, M. Bowden, J. Electrochem. Soc., 150 (2003).

[112] N. Liu, M. Shi, Y. Yuan, S. Chao, J. Feng, P. Majewski, F. Aldinger, International Journal of Fatigue, 28 (2006) 237-242.

[113] S. Pathak, D. Steinmetz, J. Kuebler, E. Andrew Payzant, N. Orlovskaya, Ceramics International, 35 (2009) 1235-1241.

[114] J. B. Wachtman, W. R. Cannon, M.J. Matthewson, Mechanical Properties of Ceramics, A John Wiley & Sons, Inc., New York (2009).

[115] A. Rittidech, L. Portia, T. Bongkarn, Materials Science and Engineering: A, 438–440 (2006) 395-398.

[116] X. Zhao, X. Li, N. Xu, K. Huang, Solid State Ionics, 214 (2012) 56-61.

[117] M.S. Khan, M.S. Islam, D.R. Bates, The Journal of Physical Chemistry B, 102 (1998)

3099-3104.

[118] Z. Zhan, D. Han, T. Wu, X. Ye, S. Wang, T. Wen, S. Cho, S.A. Barnett, RSC Advances, 2 (2012) 4075-4078.

[119] X. Zhao, N. Xu, X. Li, Y. Gong, K. Huang, RSC Advances, 2 (2012) 10163-10166.

[120] W.A. Bryant, Electrochimica Acta, 24 (1979) 1057-1060.

[121] L. Öjefors, L. Carlsson, Journal of Power Sources, 2 (1978) 287-296.

[122] D.A.J. Rand, Journal of Power Sources, 4 (1979) 101-143.

[123] M. Bursell, Academic Press, London, (1981).

[124] A.V. G. Tao, DOE hydrogen program annual progress report, (2006) 24-28.

[125] C. Miliken, Proc. 2001 DOE hydrogen program review, (2001) 570-30535.

[126] T. Lipman, US DOE officie of energy efficiency and renewable energy. Washington DC, May, 2011, (2011).

[127] H. Kan, H. Lee, Catalysis Communications, 12 (2010) 36-39.

[128] A. Inoishi, Y.W. Ju, S. Ida, T. Ishihara, Journal of Power Sources, 229 (2013) 12-15.

[129] X. Zhao, Y. Gong, X. Li, N. Xu, K. Huang, J. Electrochem. Soc., 160 (2013) A1716-A1719.

[130] K. Otsuka, T. Kaburagi, C. Yamada, S. Takenaka, Journal of Power Sources, 122 (2003) 111-121.

[131] H. Kaneko, T. Miura, H. Ishihara, S. Taku, T. Yokoyama, H. Nakajima, Y. Tamaura, Energy, 32 (2007) 656-663.

[132] K. Sohlberg, S.T. Pantelides, S.J. Pennycook, Journal of the American Chemical

Society, 123 (2001) 6609-6611.

[133] H. Kaneko, H. Ishihara, S. Taku, Y. Naganuma, N. Hasegawa, Y. Tamaura, J. Mater. Sci., 43 (2008) 3153.

[134] X. Zhao, X. Li, Y. Gong, K. Huang, Chemical Communications, (2013), **DOI**: 10.1039/C3CC47673A.

[135] H. Ohmori, S. Uratani, H. Iwai, Journal of Power Sources, 208 (2012) 383-390.

[136] J.B. Rawlings, J.G. Ekerdt, Chemical Reactor Analysis and Design Fundamentals.,Nob Hill Pub., (2002).

[137] M. Guo, X. Zhao, R. E. White, K. Huang, J. Electrochem. Soc., 160 (2013) A2085-2092.

[138] Chemical Reaction Engineering Module User's Guide (for COMSOL 4.3b), (2013) 202-209.

[139] C.F. Curtiss, R.B. Bird, Industrial & Engineering Chemistry Research, 38 (1999) 2515-2522.

[140] F.M. White, Viscous Fluid Flow (3rd edition), Tata McGraw-Hill Education, (1974).

[141] M. L. Bars, M. Worster, Journal of Fluid Mechanics, 550 (2006) 149-173.

[142] P. Geoffrey, Electrochemical engineering priciples 1(1991).

[143] W. He, K.J. Yoon, R.S. Eriksen, S. Gopalan, S.N. Basu, U.B. Pal, Journal of Power Sources, 195 (2010) 532-535.

[144] D. Chu, R. Jiang, J. Walker, J.C.W. Walker, US 20100255375 A1, (2010).

[145] D. Chu, R. Jiang, J.C.W. Walker, US 8148020 B2, (2012).

[146] X. Zhao, Y. Gong, X. Li, N. Xu, K. Huang, Journal of Materials Chemistry A, (2013), **DOI**: 10.1039/C3TA12726E.